

**TWO-PHASE CFD ANALYSES IN FUEL ASSEMBLY
SUB-CHANNELS OF PRESSURIZED WATER REACTORS
UNDER SWIRL CONDITIONS**

**(ZWEIPHASIGE CFD-ANALYSEN IN UNTERKANÄLEN VON
BRENNEMENTEN VON DRUCKWASSERREAKTOREN
UNTER DRALLBEDINGUNGEN)**

Von der Fakultät Maschinenwesen

der

Technischen Universität Dresden

zur

Erlangung des akademischen Grades

Doktor-Ingenieur (Dr.-Ing.)

genehmigte Dissertation

von

Dipl.-Ing. (FH) Salnikova Tatiana

geboren am 9. November 1980 in Moskau

Tag der Einreichung:

Dresden, 13. August 2008

Tag der Verteidigung:

Dresden, 18. Dezember 2008

Gutachter:

Prof. Dr.-Ing. habil. Jörg Huhn

Prof. Dr.-Ing. Wolfgang Lischke

Prof. Dr.-Ing. Simon Lo

Dr.-Ing. Franz Wehle

Vorsitzender der Prüfungskommission:

Prof. Dr.-Ing. habil. Jochen Fröhlich

Acknowledgements

I owe many thanks to Professor Jörg Huhn (TU Dresden) for his outstanding initiative to set up this research project. Due to his support throughout the whole project in all areas, including administrative and scientific tasks, it has been possible for me to achieve the milestones within a reasonable time frame.

In regards to all aspects of the work, it was Professor Wolfgang Lischke (HS Zittau/Görlitz), who was responsible for the scientific and general support that I required during all stages of the accomplished work. Thanks to his wise guidance and the support from Professor Frank-Peter Weiß (Forschungszentrum Dresden-Rossendorf) and Professor Wolfgang Hansen (TU Dresden), the achieved results have been presented to the international community during the conference ICONE-15 in Nagoya.

At the beginning of this project it was Professor Jürgen Knorr (TU Dresden), who motivated and guided my work in promising directions. I am also grateful to Professors Günter Lohnert and Eckart Laurien from TU Stuttgart, as well as Professors from Moscow Power Engineering Institute, Vasilij Dmitrievich Kuznezov and Viktor Vladimirovich Jagov for the helpful discussions.

The continuous encouragement of Reinhart Zimmermann and Fritz Burtak with regard to two-phase CFD calculations and my reimbursement through AREVA NP, demonstrated once again the very well established collaboration between AREVA, TU Dresden and the University of Applied Sciences Zittau/Görlitz.

The local management and direction of the work was perfectly organized and guided by Rudi Reinders (AREVA NP). He was the one who introduced me to CFD programs and encouraged me to study numerical results with open eyes. His brilliant advice in handling detailed problems arising from calculations was always very helpful. Due to his outstanding knowledge and great sense of humor, the time I spent working with him was both very productive and pleasant.

I also thank Franz Wehle (AREVA NP) greatly for the support provided during the years of my Ph.D.-Studies, both as my reviewer and someone who believed in the successful closure of this work, always having a positive word for me.

The whole department of Thermohydraulik (Fuel-Sector) is acknowledged for the warm welcome it provided me. I would like to express special thanks to the “CFD-team” and in particular to Klaus Vogel for his support during Mesh-generating and Norbert Alleborn for the in-depth correction of the manuscript (“opus magnum”) during the final phase of the work, both from a stylistic, as well as scientific point of view.

Acknowledgements

Thanks to the advice of Markus Glück (AREVA NP) and the experimental results, courtesy of Fabrice François (CEA/Grenoble), it was possible to begin the CFD validation studies that became an important part of the performed work.

A special thanks to Jörg Peucker, who made a large contribution to the corrections of the here presented manuscript. I am also thankful to Hans Kemner, Markus Pöhlmann, Juris Kronenberg and Jochen Heinecke for the stimulating discussions and helpful suggestions during the preparation of the thesis.

The work was perfectly integrated into the Fuel-Sector worldwide through the international CHF-working group. This close attachment with this international group of commercial, as well as scientific experts, allowed me to think about potential applications of the work presented here already in its development stage.

The rewarding companionship of CD-adapco assured that the work performed was in accordance to the latest releases of the STAR-CD two-phase software. In particular I am pleased to acknowledge my debt to Professor Simon Lo for his interest in my work, good advice and cooperation, and especially for making a review on my thesis in such a short time. I also want to mention Frits Put, who supported the generation of the mesh, as well as corrections to the manuscript.

The computer software and hardware were continually upgraded by the IT-department, which was very helpful for my work as I required a large computer capacity.

I am also extremely grateful to the new colleagues at the Engineering Services-Department (Plants-sector) and especially to Uwe Stoll and Ulrich Waas for their generous support in finishing this work in the framework of my new challenge at AREVA.

Thanks a lot to the Ph.D. board of examiners (TU Dresden) as well as to all those who showed their interest in my work and came to see my Ph.D.-presentation.

I want to thank my friends, music-band and dance-company as well for their support and understanding for my absence during the time I spent preparing this thesis.

With all my heart, I want to thank my parents, Igor and Irina, who set a good example with their own Ph.D. theses carried out 25 years ago and were always interested in details of my work, as well as my grandparents Valentina, Petr and Zinaida, who always tried to support me, each in their own way.

Finally, I would like to express my deeply-felt thanks to my husband Andrey, who stood by me during this whole demanding time, as well as doing all he could to let me concentrate on the progression of this thesis. I also want to thank him for the scientific discussions and for keeping me grounded in every situation.

The publication of this thesis was kindly made possible by the funding of AREVA NP.

Erlangen, August 2009



Tatiana Salnikova

Index of contents

Nomenclature and abbreviations	VIII
Abstract	XIV
Kurzfassung	XV
Краткое резюме	XVI
Summary	XVII
Zusammenfassung	XIX
1. Introduction	1
1.1 Preface and motivation	1
1.2 Literature overview and assessment.....	5
1.2.1 Simple geometry without swirl	5
1.2.2 Simple geometry under swirl conditions	8
1.2.3 Sub-channel geometry without swirl	9
1.2.4 Sub-channel geometry under swirl conditions	10
1.3 Objectives of this work	16
1.4 Numerical tool	17
1.5 Thesis outline	18
2. Physical phenomena of single-phase flow	20
2.1 Introduction	20
2.2 Governing equations	20
2.3 Turbulence modeling	24
2.4 Numerical treatment	29
2.4.1 General approach	29
2.4.2 Mathematical formulation and discretization methods	29
2.4.3 Initial and boundary conditions.....	35
2.4.4 Solution method.....	37
3. Physical phenomena of two-phase flow	38
3.1 Definition	38
3.2 Governing equations	40
3.3 Inter-phase momentum transfer.....	40
3.3.1 Drag force	41
3.3.2 Turbulent drag (dispersion) force.....	43

Index of contents

3.3.3	Lift force	44
3.3.4	Virtual mass force.....	46
3.3.5	Wall lubrication force.....	46
3.4	Turbulence.....	47
3.4.1	Turbulence equations.....	47
3.4.2	Response coefficient C_t	49
3.5	Heat and mass transfer	50
3.5.1	Flow and heat transfer regimes	50
3.5.2	Interphase heat transfer (Boiling model)	52
3.5.3	Wall heat transfer model (Heat partitioning model).....	57
3.5.4	Sources for conservation equations.....	63
3.6	Two-phase physical properties of fluids	64
3.6.1	General assumptions.....	64
3.6.2	Evaluation of the specific heat	65
3.6.3	Inlet temperature	72
3.7	Alternative formulation (Enhanced heat partitioning model).....	74
4.	Validation	77
4.1	Validation basis of STAR-CD two-phase modeling.....	77
4.1.1	Overview.....	77
4.1.2	Discussion and conclusions.....	86
4.2	Radial void fraction distribution in a vertical pipe flow	88
4.2.1	Description of experiment with R12. Scaling for water-steam application.....	88
4.2.2	Numerical method	93
4.2.3	Results and discussion	96
4.2.4	Conclusions.....	104
4.3	Critical heat flux considerations based on pipe flow	106
4.3.1	Theoretical background and motivation	106
4.3.2	Numerical method	110
4.3.3	Results and discussion	113
5.	Flow in sub-channels under swirl conditions	118
5.1	Introduction and motivation	118
5.2	Simplified model with defined rotational inlet flow. Quarter of the sub-channel ..	119
5.2.1	CFD Model: geometry, inlet and boundary conditions	119
5.2.2	Numerical analyses.....	121
5.2.3	Results and discussion.....	121
5.3	Simplified vanes in the single sub-channel geometry.....	129
5.3.1	CFD Model: geometry, inlet and boundary conditions	129
5.3.2	Numerical results and discussion. Coarse model	130
5.3.3	Numerical results and discussion. Fine mesh	132
5.4	Simplified swirl promoter in single channel geometry around the rod.....	136

5.4.1	CFD Model: geometry, inlet and boundary conditions	136
5.4.2	Numerical results and discussion	137
5.5	Simplified vanes in the 2x2 sub-channel geometry	139
5.5.1	CFD Model: geometry, inlet and boundary conditions	139
5.5.2	Numerical results and discussion	140
5.6	Conclusions	143
6.	Closure	145
6.1	Conclusions	145
6.2	Suggestions for future work	148
	Appendix A	151
	Appendix B	155
	Appendix C	162
	Appendix D	164
	Bibliography	171

Nomenclature and abbreviations

Latin symbols:

Symbol	Unit	Description
A		Coefficient matrix
A	m^2	Area
A_i	m^{-1}	Specific interfacial area
A_d	m^2	Projected area of the particle in the flow direction
A_c	—	Condensation or non-boiling area of influence
A_e	—	Boiling area of influence
a_i	m^{-1}	Specific drag area
D	m	Pipe or rod diameter
d	m	Diameter
d	m	Distance between cell-node centers
d_b	m	Bubble bulk diameter
$d_0; d_1$	m	Bubble diameters at two subcoolings in Kurul formulation
d_w	m	Bubble departure diameter
c_p	J/(kgK)	Specific heat at constant pressure
E	J	Energy
F	N/m^3	Force per unit volume
F_j	W	Diffusion energy flux in direction x_j
f	N	Force
f	—	Convective or diffusive component of the flux vector orthogonal to the face of the Control Volume (CV)
f	Hz	Bubble departure frequency
G	$kg/(ms^3)$	Rate of generation of turbulence energy (production term)
	$kg/(m^2s)$	Volumetric mass flow rate, mass flux
g	m/s^2	Gravitational acceleration, 9.806
h	J/kg	Specific enthalpy
h	$W/(m^2K)$	Heat transfer coefficient
h^*	$W/(m^2K)$	Heat transfer coefficient, taken into account area of influence
h_{fg}	J/kg	Latent heat
k	m^2/s^2	Turbulent kinetic energy
L	m	Length
l	m	Turbulent length
M	N/m^3	Interfacial transfer of the momentum per unit volume
m	kg	Mass
\dot{m}	kg/s	Mass flow rate, mass flux
n	—	Unit vector orthogonal to S_{CV} and directed outwards
n''	m^{-2}	Nucleation site density
n_b	m^{-3}	Number of bubbles per unit volume (in CV)
p	bar	Pressure

pt	m	Pitch
Q	J	Energy Heat transfer
\dot{Q}	W	Heat transfer rate
\dot{q}	W/m ³	Heat tranfer rate per unit volume
\dot{q}''	W/m ²	Uniform heat flux
$R; r$	mm	Radius
S	m ²	Surrounding area of the system or element
S	—	Source term in the generic two-phase transport equation
s	—	Source term in the generic single-phase transport equation
T	K	Absolute temperature
t	C	Celsius Temperature
t	s	Time, Periode
t_{wt}	s	Waiting time
t_{ct}	s	Contact time
t_{cycle}	s	Cycle periode
t_i	m/s	Tangential vector from velocity field
U	m/s	Superficial velocity
u_i	m/s	Velocity in i direktion
\bar{u}	m/s	Resultant velocity parallel to the wall
u_τ	m/s	Resultant friction velocity
x	m	Coordinate
x	—	Dynamic quality
x_{th}	—	Thermalhydraulic quality
y^+	—	Dimensionless normal distance from the wall

Greek symbols:

Symbol	Unit	Description
α		Volume fraction
ε	m ² /s ³	Dissipation rate of turbulence kinetic energy
η	m ² /s	Molecular viscosity
Φ	—	Corresponding extensive property to ϕ
ϕ	—	Any conserved intensive property
Γ	—	Diffusion coefficient in the transport equation
Γ_k	kg/(ms)	Diffusion coefficient for k
Γ_ε	kg/(ms)	Diffusion coefficients for ε
μ	kg/(ms)	Molecular dynamic viscosity
μ^t	kg/(ms)	Turbulent eddy-viscosity
τ	N/m ²	Shear stress
λ	W/(mK)	Thermal conductivity
ρ	kg/m ³	Density
Ω	m ³	Voulme
σ	N/m	Surface tension coefficient
δt	s	Arbitrary time step

Nomenclature and abbreviations

Dimensionless Numbers, coefficients and constants:

Symbol	Description
β	Dimensionless coefficient (<i>e.g.</i> for C_t -model)
C_d	Drag coefficient
C_{lg}	Interfacial drag coefficient
C_L	Lift coefficient
C_{VM}	Virtual mass coefficient
$C_{w1}; C_{w2}$	Wall lubrication force coefficients
C_t	Turbulence response coefficient
E	Roughness parameter
$E\ddot{o}$	<i>Eötvös</i> number
F_A	Boiling model constant (used in STAR-CD)
Nu	<i>Nusselt</i> number
π	Constant
Pr	<i>Prandtl</i> number
Re	<i>Reynolds</i> number
St	<i>Stanton</i> number
κ	<i>von Kármán</i> constant
θ	Transition variable
γ	<i>Barnett</i> number
Ψ_σ	Dimensionless number defined by <i>Ahmad</i>

Subscripts:

Symbol	Description
0	Reference values
<i>add</i>	Additive
<i>b</i>	Bubble
<i>c</i>	Carrier phase and
<i>c</i>	Condensation
<i>cf</i>	Index of the cell faces
<i>C</i>	Centrifugal
<i>CV</i>	Control Volume
<i>CM</i>	Control Mass
<i>ch</i>	Characteristic
<i>d</i>	Dispersed phase
<i>D</i>	Drag
<i>diff</i>	Differential
<i>E</i>	East cell node of a CV
<i>e</i>	East cell face of a CV and evaporation
<i>eq</i>	Equivalent
ϕ	Any conserved intensive property
<i>g</i>	Gas phase
<i>gl</i>	From gas to liquid
<i>gi</i>	From gas to interface
<i>given</i>	Initial values
<i>eq</i>	Equilibrium
<i>h</i>	Heated

<i>i</i>	Interface
<i>i</i>	Related to inter-phase mass or heat transfer due to ΔT
<i>i</i>	Index for the cell number
<i>i</i>	Internal
<i>inlet</i>	Entrance conditions
<i>K</i>	Kinetic
<i>k</i>	Phase index
<i>l</i>	Liquid phase or laminar
<i>lg</i>	From liquid phase to gas phase
<i>li</i>	From liquid phase to interface
<i>L</i>	Lift
<i>LF</i>	Shear-induced
<i>mix</i>	Mixture
<i>par</i>	Parameter used in STAR-CD
<i>r</i>	Relative
<i>s</i>	Saturation conditions
<i>sub</i>	Sub-cooling
<i>sup</i>	Superheating
<i>t</i>	Turbulent
<i>th</i>	Thermalhydraulic
<i>tr</i>	Transition condition
τ	Tangential component
<i>VM</i>	Virtual Mass
<i>w</i>	Wall conditions
<i>wt</i>	Waiting
<i>water</i>	Water
<i>WK</i>	Wake-induced
<i>R12</i>	R12 (CCl ₂ F ₂ /Freon 12)

Superscripts:

Symbol	Description
<i>D</i>	Drag
<i>d</i>	Differential
<i>h</i>	Enthalpy or related to energy conservation equation
<i>i</i>	Interface
<i>L</i>	Lift
<i>l</i>	Laminar
<i>m</i>	Mean
<i>mass</i>	Related to mass conservation equation or mass transfer
<i>mom</i>	Related to momentum conservation equation
<i>n</i>	Time step level
<i>STAR</i>	Values or parameter used in STAR-CD code
<i>T</i>	Turbulent drag
<i>t</i>	Turbulent
<i>VM</i>	Virtual Mass
<i>W</i>	Wall lubrication
<i>+</i>	Near wall
<i>*</i>	Value of <i>S</i> with $\alpha_d \rightarrow 0$

Nomenclature and abbreviations

Oversymbols for any variable S:

Symbol	Description
\bar{S}	Mean value
\vec{S}	Vector
\vec{S}'	Fluctuations above the mean value of vector \vec{S}
S'	R.m.s. of fluctuations above the mean value of vector \vec{S}
S''	Second spatial derivative $\frac{\partial S}{\partial x \partial y}$
\dot{S}	First time derivation $\frac{dS}{dt}$
\tilde{S}	Transposed
$(S)^T$	Transposed

Operators and other symbols:

Symbol	Description
∇	Nabla operator
:	Dyadic product
$\frac{D}{Dt}$	Material derivative

Abbreviations:

Abbreviation	Description
adapco	Analysis and design company
ANL	Argonne National Lab
ANS	American Nuclear Society
1-D, 2-D, 3-D	One-, two-, three-dimensional
BFBT	BWR Full-size fine-mesh Bundle Test
BDS	Backward Difference Scheme
BWR	Boiling Water Reactor
CAE	Computer-Aided Engineering
CD	Computational Dynamics
CDS	Central Difference Scheme
CFD	Computational Fluid Dynamics
CHF	Critical Heat Flux
CM	Control Mass
CV	Control Volume
DoE	United States Department of Energy
ECL	École Centrale de Lyon
FA	Fuel Assembly
FDS	Forward Difference Scheme
GUI	Graphical User Interface
IPP	Initiatives for Proliferation Prevention
JSME	Japan Society of Mechanical Engineers
LWR	Leight Water Reactor

NUPEC	Nuclear Power Engineering Corporation of Japan
ONB	Onset of Nucleate Boiling
ONSB	Onset of Nucleate Significant Boiling
OVG	Onset of Vapor Generation
PWR	Pressurized Water Reactor
r.m.s	Root mean square
RPI	Renslaer Polytechnic Institute
SIMPLE	Semi-Implicit Method for Pressure-Linked Equations
STAR	Simulation of Turbulent flow in Arbitrary Regions
VNIIEF	Vserossijskij Nauchno Issledovatel'skij Institut Eksperimentalnoj Fiziki (All-Russian Research Institute of Experimental Physics)
VOF	Volume Of Fluid
UDS	Upwind Difference Scheme

Abstract

Single-phase CFD calculations are already widely applied in nuclear industry for the thermal-hydraulic design optimization of fuel assemblies (FA). In contrast, two-phase CFD-applications are still in the state of development. The work presented in this thesis shows contributions towards the detailed two-phase modeling of boiling flows under swirl conditions in sub-channel geometries of pressurized water reactors (PWR) FAs, including a realistic description of the critical heat flux (CHF)-phenomena and identification of two-phase indicators characterizing CHF-phenomena. The numerical simulations were conducted with a 3-D CFD code (STAR-CD) for various types of swirl generating components in FA. New insights regarding local void distribution in sub-channels under swirl conditions were obtained, which are relevant for CHF (“bubble pockets”). Furthermore, an enhanced wall partitioning model provides a more realistic description of the steep increase of the rod temperature due to CHF. Presented validation studies showed good agreement with the available experiments under PWR conditions for the radial void distributions at non-CHF conditions as well as for the CHF prediction. The results performed in this thesis show the incentives and chances of two-phase CFD applications for the development of thermal-hydraulically optimized PWR spacer grids with regard to heat transfer and improvement to the CHF behaviour.

Keywords: *PWR, sub-channel geometry, two-phase CFD modeling, swirl flow, CHF*

Kurzfassung

Einphasige CFD Analysen stellen für typische thermohydraulische Fragestellungen aus dem Kernkraftwerksbereich bereits jetzt ein wichtiges Werkzeug für die Brennelement (BE)-Auslegung dar. Die zweiphasige CFD-Modellierung befindet sich dagegen in der Entwicklungsphase. Die in dieser Dissertation präsentierten Arbeiten zeigen Fortschritte für die detaillierte zweiphasige Modellierung drallbehafteter Strömungen im Unterkanal eines BEs des Druckwasserreaktors (DWR) einschließlich der realistischen Beschreibung des kritischen Wärmestroms (CHF) sowie die Bestimmung zweiphasiger Indikatoren, welche das Auftreten von CHF-Phänomen beschreiben. Verschiedene drallerzeugende Komponenten im BE wurden mit dem 3-D CFD-Code STAR-CD modelliert. Es wurden neue Erkenntnisse zur lokalen Blasenverteilung in Unterkanälen unter Drallbedingungen gewonnen, die für CHF relevant sind (“bubble pockets”). Durch eine Modifikation des Wärmeübergangsmodells (heat partitioning model) wird der starke Anstieg der Stabtemperatur infolge CHF realistischer beschrieben. Die durchgeführten Validierungen zeigen eine gute Übereinstimmung mit verfügbaren Experimenten unter DWR-Bedingungen für die radialen Blasenverteilungen und für die Bestimmung von CHF. Die vorliegenden Ergebnisse dieser Dissertation verdeutlichen den Nutzen und die Möglichkeiten von zweiphasigen CFD-Anwendungen für die Entwicklung und die thermohydraulische Optimierung von DWR-Abstandshaltern bezüglich des Wärmeübergangs und der Verbesserung des CHF-Verhaltens.

Schlüsselwörter: *DWR, Unterkanalgeometrie, zweiphasige CFD Modellierung, Drall, kritischer Wärmestrom*

Краткое резюме

Модели однофазовой среды в вычислительной гидродинамике (англ. CFD) являются уже сейчас важным инструментом для решения типичных термогидравлических задач в ядерной энергетике, например, при конструировании тепловыделяющих сборок (ТВС). Двухфазовое моделирование, в сравнении с однофазовым, находится на сегодняшний момент в стадии развития. Данная диссертация связана с совершенствованием двухфазовой модели в направлении улучшения детализации вихревого течения внутри ячейки ТВС в условиях работы двухконтурного ядерного реактора (тип PWR). Также в работе показана возможность более реалистичного описания феномена кризиса теплоотдачи и определения двухфазовых индикаторов, характеризующих критический тепловой поток (англ. CHF). Комплекс расчетов выполнен для различных интенсификаторов теплоотдачи, размещенных на дистанционирующих решетках ТВС. Расчеты производились с помощью программного обеспечения STAR-CD, позволяющего моделировать трехмерные гидродинамические системы. Полученные новые данные о локальном распределении пузырьков в ячейках с вихревым течением дали важную информацию для идентификации критического теплового потока. Усовершенствование модели теплоотдачи на поверхности тепловыделяющего элемента (ТВЭЛ) позволило более реалистично описать резкое повышение температуры на поверхности ТВЭЛа при достижении критических условий. Полученные результаты численного моделирования для радиальных распределений пузырьков при нормальных условиях работы PWR и также для определения критического теплового потока показали хорошее совпадение с известными экспериментальными данными. Представленные в диссертации результаты показывают возможности применения двухфазовых CFD-расчетов для разработки и термогидравлической оптимизации дистанционирующих решеток с целью улучшения теплообмена и характеристик критического теплового потока в двухконтурном ядерном реакторе типа PWR.

Ключевые слова: *PWR, геометрия ячейки, двухфазовое моделирование, CFD, вихревое течение, критический тепловой поток*

Summary

The major goals of a modern thermal-hydraulic design of advanced fuel assemblies (FA) for pressurized water reactors (PWR) and boiling water reactors (BWR) are to improve the efficiency of the nuclear power plant and to increase operating flexibility and plant reliability. One of the most important phenomena regarding these goals is the critical heat flux (CHF). Flow directing components (e.g. spacer grids with swirl inducing vanes) can improve the CHF performance of the FA by homogenizing the temperature in the sub-channel and improving the mixture between the adjacent sub-channels. Single-phase CFD calculations are already widely applied in the nuclear power industry for the design optimization of the FA (e.g. pressure drop calculations) as they can take into account the influence of the geometry without additional experiments. Two-phase CFD modeling is still in a state of development, with the long-term goal of the reliable prediction of CHF for FA designs.

The reviewed literature dedicated to CFD applications in the nuclear field clearly shows the lack of two-phase flow analyses for various sub-channel geometries under swirl conditions for PWR applications, as well as of detailed validations based on reliable two-phase experiments. This insight additionally motivated the research work presented in this thesis, which was carried out with CFD code STAR-CD. The two-phase methodology used in STAR-CD was analyzed with respect to sub-channel applications under high pressure. The origin and several limitations of the applied models are pointed out. The validations available in the literature for the current two-phase STAR-CD version are summarized and reviewed, showing the applicability of the current two-phase models for various two-phase problems. Validations of the radial flow distributions for water-steam flow at high pressures are not available from literature.

In this work, contributions are made towards an improved flow boiling model under PWR conditions by carrying out detailed CFD analyses based on experimental data of radial void distributions in heated pipes. The experiment was carried out by *Garnier et al.* [50] with a refrigerant (Freon) as working fluid and was scaled to water-steam PWR conditions by applying an appropriate scaling model (*Ahmad* [2]). A parameter sensitivity study of the most important two-phase parameters in the standard STAR-CD two-phase model shows the large influence of the formulation used for bubble bulk diameter on radial void distribution. Improvements for

Summary

describing both, high sub-cooled flow and saturated flow boiling, are achieved by using two parameter sets for the physical models with a modified formulation for the variable bubble bulk diameter (function of the sub-cooling *Kurul* and *Podowski* [86]), respectively.

An enhanced mechanistic wall heat transfer partitioning model is applied to CHF conditions and shows improvements regarding the realistic description of the CHF phenomena validated by CHF experiments. A new model for the heat transfer for big bubbles in contact with heated surfaces allows steam superheating for bubbles and a steep increase of the wall temperature under CHF conditions. The boiling curve (“*Nukijama-curve*”) is modeled by two-phase CFD, applying this enhanced model. The proposed method to obtain CHF from the calculated boiling curve provides CHF-values for the two analysed cases that are in good agreement with CHF-values obtained from the empirical correlation of *Doroshchuk* [34].

An important contribution is made in the present work towards the detailed modeling of boiling in fuel assembly geometries under swirl conditions. The performed two-phase CFD simulations show phase separation, explained by distribution of the local centrifugal force, in the form of bubble accumulations in the center of the sub-channel and “bubble pockets” on the lee side of the rod surface (due to the change of sign for the curvature of the stream lines).

A completely deterministic method for CHF predictions in sub-channel geometries, based on two-phase CFD analyses is not yet available; thus trends of CHF for different designs have to be assessed based on relevant physical parameters. In the present work, possible two-phase indicators of CHF are identified and used for optimization studies on the vane geometry. For such CFD analyses a simplified model with a generic swirl (with a defined flow at the inlet) was chosen. Swirl, pressure loss, accumulations of bubbles in the center of the sub-channel and on the rods, as well as wall superheating (applying a new partitioning model) were taken as optimization parameters with respect to CHF.

Further calculations are performed for a single sub-channel model with 4 simplified vanes for a more realistic description of the swirl flow, as well as for different types of swirl promoters (swirl induced around the rod) to show the influence of the geometry. Detailed calculations are carried out for a 2x2 sub-channel geometry with split vanes to show the influence of the cross flow between the adjacent sub-channels.

The results of the performed analyses indicate that two-phase CFD can play a significant role in designing PWR spacer grids for improved CHF performance. This will not only decrease the duration for design evaluation cycles, but also the number of expensive experiments needed.

Zusammenfassung

Die Ziele der thermohydraulischen Entwicklung fortschrittlicher Brennelemente (BE) für Druckwasserreaktoren (DWR) und für Siedewasserreaktoren (SWR) sind die Verbesserung der effizienten Energieerzeugung sowie die Erhöhung der Betriebsflexibilität und Verfügbarkeit. Bezüglich dieser Verbesserungsziele ist der kritische Wärmestrom (CHF) einer der wichtigsten Phänomene. Drallerzeugende Konstruktionselemente, wie z.B. Abstandhalter mit Fahnen, können durch Vergleichmäßigung der Temperatur von benachbarten Stäben und Vermischung zwischen Unterkanälen das CHF-Verhalten des BEs verbessern. Einphasige CFD-Analysen stellen für typische einphasige Fragestellungen (z.B. Druckverlustberechnungen) bereits jetzt ein wichtiges Werkzeug für die BE-Auslegung dar, weil damit der Einfluss geometrischer Änderungen ohne zusätzliche Experimente bewertet werden kann. Die zweiphasige CFD-Modellierung befindet sich in der Entwicklungsphase mit dem langfristigen Ziel, das CHF-Verhalten für die BE-Auslegung vorherzusagen.

Die untersuchte Literatur zu CFD-Anwendungen im Nuklearbereich zeigt einen Mangel sowohl an Untersuchungen zur drallbehafteten Strömung unter hohem Druck in der BE-Geometrie als auch an dazugehörigen verlässlichen Experimenten bzw. deren Nachrechnungen. Diese Tatsache bildete eine zusätzliche Motivation für die mit dem CFD-Code STAR-CD durchgeführte Dissertation. Die zweiphasigen CFD-Standard-Modelle werden für Unterkanal-Anwendungen unter hohem Druck betrachtet, und deren Ursprung und Anwendungsbeschränkungen werden analysiert. Eine Zusammenstellung der mit aktueller Version der STAR-CD durchgeführten Validierungs-rechnungen zu verschiedenen Experimenten hat gezeigt, dass die verwendeten zweiphasigen Modelle unterschiedliche zweiphasige Problemstellungen gut beschreiben können. Nachrechnungen von radialen Wasserdampf-Strömungen unter hohem Druck sind in der betrachteten Literatur bisher nicht verfügbar.

In dieser Arbeit werden Beiträge zur verbesserten Beschreibung des Verdampfungsvorgangs unter hohem Druck durch detaillierte zweiphasige CFD Nachrechnungen von radialer Blasenverteilung im beheizten Rohr dargestellt. Die Experimente wurden von *Garnier et al.* [50] mit einem Kältemittel (Freon) als Arbeitsfluid durchgeführt und anschließend auf das

Zusammenfassung

Verhalten von Wasserdampf unter DWR-Bedingungen mit Hilfe der Ähnlichkeitstheorie skaliert (*Ahmad* [2]). Durch Variation der zweiphasigen Parameter im CFD-Modell wird der Einfluss des Blasendurchmessers in der Hauptströmung gezeigt. Mit einer Modifikation der für Blasendurchmesser verwendeten Formulierung (Blasendurchmesser als Funktion der Unterkühlung *Kurul* and *Podowski* [86]) auf Basis physikalischer Gesetzmäßigkeiten wird die radiale Blasenverteilung sowohl für stark unterkühlte als auch für gesättigte Flüssigkeiten unter Verwendung zweier Parametersätze besser modelliert.

Ein verbessertes mechanistisches Modell zur Aufteilung des Wärmestroms an der Wand wird unter kritischen Bedingungen angewendet und durch CHF Experimente validiert. Dabei werden die Verbesserungen bezüglich einer realistischen Beschreibung des CHF-Phänomens aufgezeigt. Durch eine neue Modellierung des Wärmeübergangs bei großem Dampfgehalt in Wandnähe, steigt die Wandtemperatur unter kritischen Bedingungen steil an. Die Siedekurve (“*Nukijama-Kurve*”) wird mit zweiphasigen CFD-Rechnungen unter Verwendung des verbesserten Modells simuliert. Die vorgeschlagene Methode zur Bestimmung des kritischen Wärmestroms aus dieser Kurve liefert einen Wert, der mit den Ergebnissen der *Doroshchuk-Korrelation* [34] übereinstimmt.

Ein deutlicher Fortschritt wird für die detaillierte Modellierung der drallbehafteten siedenden Strömung im Unterkanal des DWRs erreicht. Die Simulationen zeigen eine Separation der Phasen, wie etwa eine Blasenansammlung im Zentrum des Unterkanals und an der Staboberfläche (“*bubble pockets*”). Die berechneten lokalen Blasenverteilungen können qualitativ sehr gut mit der Verteilung der lokalen Zentrifugalkraft begründet werden. Einerseits ist diese Kraft der Grund für die Blasenanhäufung im Zentrum des Unterkanals, andererseits führt die Änderung des Vorzeichens bei der Krümmung der Strömungslinien an der Brennstaboberfläche zur Ansammlung der Blasen an der abströmenden Seite des Stabs.

Eine vollständig deterministische Methode zur Vorhersage vom CHF in Unterkanälen, basierend auf zweiphasigen CFD Analysen, existiert derzeit noch nicht. Deswegen sollen relevante Strömungsparameter den CHF-Trend für verschiedene Designs zeigen. In dieser Arbeit werden mögliche zweiphasige Indikatoren festgelegt, welche das Auftreten des kritischen Wärmestroms beeinflussen sollten und für die Optimierung der Fahngeometrie, in diesem Fall des Fahnenwinkels, verwendet. Für solche Rechnungen wird ein vereinfachtes Modell mit vorgegebenem Drall am Eintritt gewählt. Die festgelegten Kriterien für die Optimierung sind die Intensität des Dralles, der Druckverlust und zwei neue Kriterien: Blasenansammlung im Zentrum des Kanals und an der Staboberfläche. Durch die neue

Modellierung, die eine Überhitzung des Dampfes zulässt, ist die Temperatur der Wandoberfläche ein zusätzliches Kriterium für den Optimierungsprozess.

Weitere Rechnungen werden mit einem CFD-Modell durchgeführt, das vier Fahnen abbildet, um die Strömung realistischer zu beschreiben. Darüber hinaus wurde eine andere Art von drallerzeugenden Komponenten (mit dem Drall um den Stab) simuliert, um den Einfluss dieser Geometrie zu zeigen. Detaillierte CFD-Rechnungen werden für ein 2x2 Unterkanal-Modell mit "Split"-Fahnen durchgeführt, um die Einflüsse von Querströmungen zwischen benachbarten Kanälen zu untersuchen.

Die Ergebnisse dieser Forschungsarbeit zeigen die erhebliche Bedeutung und das große Potenzial von detaillierten zweiphasigen CFD-Rechnungen für das DWR BE-Design hinsichtlich des verbesserten CHF-Verhaltens. Dadurch könnten nicht nur Entwicklungszyklen verkürzt werden, sondern auch die Anzahl notwendiger und kostspieliger Experimente verringert werden.

1. Introduction

1.1 Preface and motivation

Nuclear fuel assemblies for Pressurized Water Reactors (PWRs) consist of square arrays of 14x14 to 18x18 fuel rods. An individual PWR reactor core consists of 121 to 241 fuel assemblies (FA). Fuel rods are cylindrical tubes manufactured from zirconium alloy (Zircaloy), which encapsulate the ceramic pellets of the enriched uranium dioxide (UO_2) and are backfilled with gas (Helium) to improve the heat transfer across the pellet-to-cladding gap and to reduce the cladding creep-down due to external pressure [155].

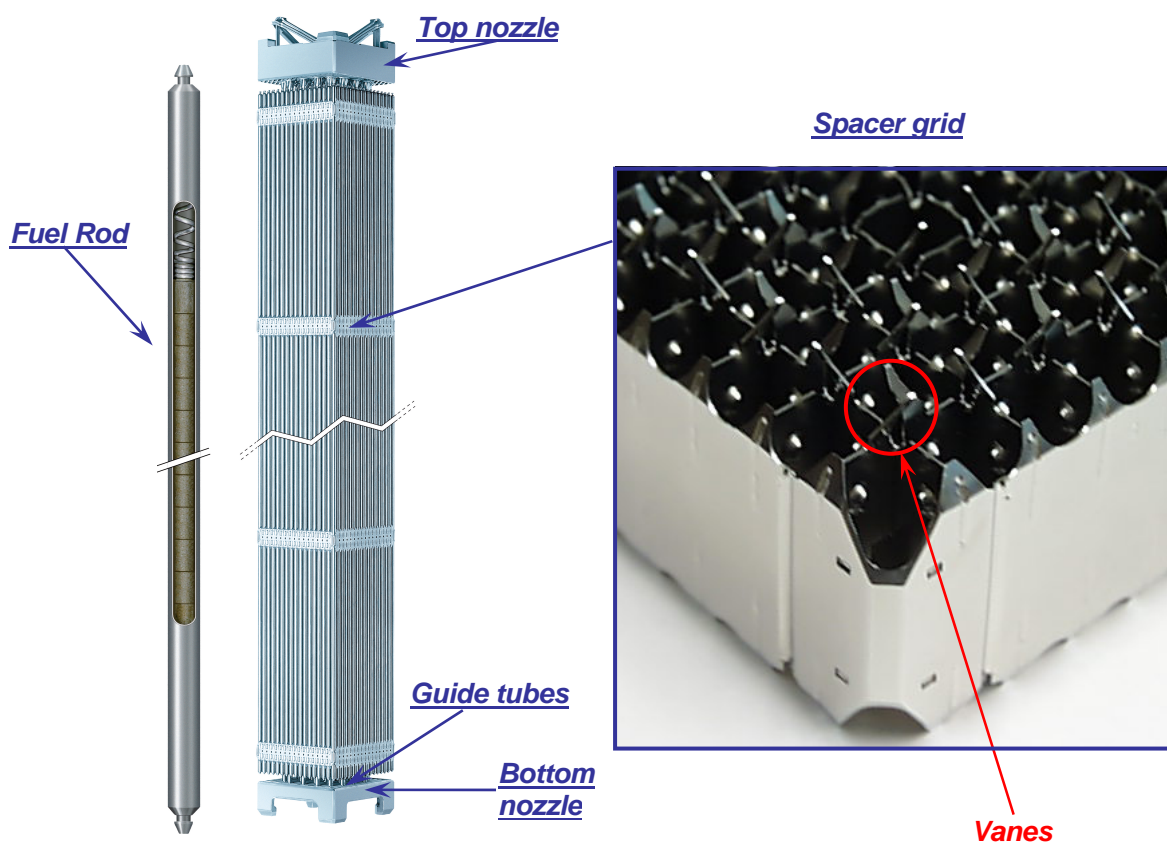


Figure 1.1 Typical advanced FA-design with split vane spacer grid (courtesy of AREVA)

A typical fuel rod has a diameter of about 10 mm and a total length of about 4 m. Top and bottom nozzles fix the axial and radial position of the guide tubes, which are additionally supported by spacer grids that are arranged vertically within approximately 0.5 m of each other (spacer span). Fuel rod supports (springs and hard stops) are used to hold the fuel rods in

1 Introduction

position in the spacer grids. Moreover, control rods can be inserted from the top of the PWR fuel assembly directly into the guide tubes e.g. to shut-down the reactor. An example of a PWR fuel assembly is presented in Figure 1.1, which shows details of a fuel rod and a spacer grid.

The thermal-hydraulic design of a light-water reactor is limited by “boiling crisis” i.e. *Critical Heat Flux (CHF)* at normal reactor operation, as well as at transient conditions. By ruling out CHF the integrity of the fuel rod cladding, which is the first barrier against the release of fission products, is maintained. The CHF behavior of fuel assemblies is measured in specific tests. These tests are used to develop adequate CHF correlations, where the CHF of a specific fuel assembly is represented as a function of the local flow conditions: pressure, mass flux and enthalpy as well as geometry.

The design basis of the thermal-hydraulic core and the FA-design in PWRs is the avoidance of *Departure from Nucleate Boiling (DNB)*, which is the most important mechanism of the CHF for PWR. The occurrence of DNB at the rod surface is associated with the formation of a vapor film between cladding and coolant, which may significantly degrade the heat transfer to the coolant, causing the cladding temperature to reach such high values that the cladding integrity of the rod would be lost (*burnout*).

As the critical heat flux is influenced by the geometry of the FA, one of the design goals of the PWR fuel assemblies is the improvement of the geometry with respect to CHF. This would increase the safety margins, or lead to better economic efficiency of the nuclear plant enlarging the radial and axial peaking, improving the fuel utilization or enhancing the reactor power.

The design of the spacer grid (see Figure 1.1) and its axial spacer span has significant influence on the heat transfer and CHF behavior of the fuel assembly. To improve the CHF performance, various types of swirl generating devices (e.g. vanes) were developed and integrated in the spacer grids to superpose a swirl component on the vertical flow of the coolant. Especially such devices as split vanes induce cross-flow between sub-channels as well as swirl and enhanced turbulence in the sub-channel. Together these effects lead to better heat transfer between cladding and coolant and, as can be shown from experiments e.g. [127] or [30], to a higher measured critical heat flux. A typical split vane for commercial nuclear fuel assembly is marked with a red circle in Figure 1.1.

According to the published literature dedicated to CHF of light water reactors, no physical model is available to accurately describe the critical boiling phenomena for the full range of the reactor flow conditions. Therefore, predictions of the CHF performance as well as of void fraction distribution and of local pressure losses in the sub-channels of the fuel assembly are

based on sub-channel codes and on empirical correlations developed from experimental results at various conditions. For such correlations the typical prediction accuracy is in the order of 5 % in the ranges of parameters covered by the CHF tests. Applying the correlation beyond the parameter range validated by the tests may degrade the accuracy to about 30 % [4]. Transient conditions are even more challenging. The development of such correlations for both design and licensing purposes requires large experimental series of high quality tests to develop the CHF correlation, which is very cost-intensive.

CHF correlations for PWR fuel assemblies are based on CHF experiments in 5x5 rod bundle test assemblies. Thereby, following parameters are given: spatial power distribution (uniform and/or non-uniform in axial and radial direction), the respective spacer grid, and adequately heated length and guide tubes.

To save electrical power required for CHF experiments under PWR conditions, some correlations were developed based on CHF experiments carried out with coolant fluids, having a lower latent heat compared to water, e.g. a refrigerant such as Freon. Special fluid-to-fluid scaling laws based on dimensionless numbers characterizing the two-phase flow provide the flow conditions for the model fluid. An additional important advantage of using Freon as a model fluid is its lower pressure resulting from the scaling procedure, allowing easier handling. The CHF correlations developed from tests with model fluids at scaled conditions are considered to be well applicable to water data, e.g. in [2] or [74].

With the table look-up method originally developed by *Doroshchuk et al.* [34] and further extended for instance by *Groeneveld et al.* [53], [55], CHF data in vertical tubes with uniform heat-flux can be obtained. This method has a very wide range of application and a high accuracy. Therefore it is also used as a basis for the prediction of CHF in rod bundle geometries including the appropriate correction factors e.g. in [64] or [92].

Avoidance of CHF in the thermal-hydraulic design of PWR is achieved by keeping the DNB ratio (DNBR), which is defined as the ratio of “CHF (predicted by the correlation)”/“Local heat flux”, high enough to prevent the occurrence of DNB. In normal reactor operation, a typical DNBR of 2.20 is achieved, compared to a minimum limiting DNBR of about 1.2.

Any design change that may influence the CHF performance, e.g. the mixing vane shape or pattern, requires new test series to demonstrate that the existing correlation is applicable; more tests may be required for the development of a new correlation. Therefore, the important long-term goal of thermal-hydraulic design of nuclear fuel assemblies is the development of reliable and approved methods for the prediction of the flow distribution and in the final stages of the

1 Introduction

CHF for any geometry variation. In this way, the design cycles could be reduced or even the replacement of these expensive CHF experiments could be envisaged.

As *Computational Fluid Dynamics (CFD)* is developing very fast, the achievement of such a goal looks promising for the future. Nowadays CFD can analyze complex engineering systems including fluid flow and heat transfer by means of computer-based simulations. Though CHF prediction is still a big challenge, first important steps toward this aim have already been performed.

Single-phase flow CFD simulations are widely applied to the design of fuel assemblies. The detailed modeling of sections of a fuel assembly is now possible for single-phase flow applications, allowing the thermal-hydraulic process to be described more adequately. Additionally, the continuously further developed experimental methods provide data on flow and turbulence distribution for validation of the single-phase CFD codes.

Two-phase flow (here water/steam) CFD simulations for nuclear applications are commonly carried out using the *Eulerian two-fluid* model with both phases treated as continua. The conservation equations are obtained by an averaging procedure and use various mechanistic constitutive models to achieve the closure of the conservation equations. This two-phase methodology includes inter-phase exchange terms for condensation and evaporation. For heated surfaces a heat partitioning model is applied to distribute the incoming defined heat flux at the surface into evaporation, convection and quenching. Though the mentioned models include adjusted coefficients matching experimental data and therefore have some limitations, bubbly boiling flow in simplified geometries was mostly successfully modeled and widely validated under non-CHF conditions primarily for low pressures. First attempts to use this two-phase methodology for flow prediction under non-CHF conditions in sub-channel geometries showed promising results compared to the available experiments.

For the application of the two-phase CFD code to FA-design optimization with respect to CHF, the code has to be validated for flow boiling in real geometries and under real thermal-hydraulic conditions. For this purpose, three important needs are defined to be solved in parallel:

- enhanced physical models (replacement of the empirical correlations by mechanistic models) for both non-CHF and CHF conditions,
- improved description of the geometry (avoiding simplifications),
- validations with suitable and reliable experiments, e.g. radial void distribution.

In this thesis, each of these needs is analyzed and further developed in the frame of the possibilities of the applied commercial CFD code, computational time and power.

In the remainder of this chapter, the recent state of knowledge for CFD calculations with respect to nuclear applications for PWRs is summarized. CFD applications are arranged into groups depending on the used geometry (simplified or sub-channel), flow configuration (with/without swirl) and applied conditions (non-CHF / CHF). The research tasks with respect to the long-term goal of CHF prediction for flow boiling in real fuel assembly geometry and under real thermal-hydraulic conditions are identified and the objectives of the performed work are pointed out. The commercial CFD software package STAR-CD applied in this work is shortly described. Finally, the thesis structure is outlined.

1.2 Literature overview and assessment

A substantial amount of literature concerning two-phase CFD calculations in general is available. A summary on all of them is beyond the scope of the present thesis and would be a large challenge due to a great number of conferences and publications in this field. The present overview is focused on some of the existing works that play an important role for the long-term goal, the prediction of the CHF performance for the realistic PWR fuel assembly by means of the two-phase CFD calculation, pointing out the modeling needs and challenges. Additionally, a wide range of papers are mentioned in the remainder of this thesis describing e.g. the two-phase modeling methodology of the STAR-CD with respect to sub-channel applications (Section 3.3) or performed validations of the STAR-CD two-phase model carried out as joint projects of CD-adapco and some national labs (Section 4.1).

1.2.1 Simple geometry without swirl

Correct prediction of the flow distribution in two-phase flow by CFD code was a topic of research of many numerical studies in the past. Many of them used the *Eulerian two-fluid* framework that was developed e.g. by *Ishii and Mishima* [71] and based on the averaged transport equations for mass, momentum and energy with additional source terms describing the phase interaction across the interface. For the turbulence modeling the standard high *Reynolds* number $k - \varepsilon$ model proposed by *Launder and Spalding* [91] is used very often. A large number of the CFD calculations were carried out in geometries such as pipes, annuli or triangular or rectangular ducts, because of their simple form and available experiments for validations.

➤ *Two-phase flow CFD calculations at non-CHF conditions*

Among the first flow regimes that were modeled by two-phase methodology were water-air adiabatic flows and sub-cooled boiling followed by saturated boiling. The aim of the calculations was prediction of the flow distribution e.g. void, velocity. Many authors validated the axial flow distribution.

1 Introduction

Kurul in 1991 [85] and *Anglart* in 1993 [3] calculated the axial channel averaged void fraction and temperature for sub-cooled boiling in a vertical channel using the two-fluid model of PHOENICS and FLOW3D CFD code, respectively. The computational results were compared with experimental data of *Bartolomei* and *Chanturiya* for a heated vertical pipe at 45 bar [14]. Good agreement was achieved in [85] and the advantage over 1-D calculations was shown. In [3] void fraction was overpredicted in the bulk flow, but the calculated void fraction at the wall was similar to experimental values.

In 2003, *Krepper* [82] summarized the existing models for sub-cooled boiling and validated the axial void distribution calculated with the CFX two-phase model against the experimental data of *Bartolomei* at various conditions, showing good agreement for axial void distribution for a pressure range of 15 to 50 bar.

In 2007, a new version including adequate near-wall treatment, based on the analytical temperature wall function, showed a good agreement for pressures between 30 and 110 bar. However, at PWR conditions (~150 bar) the calculated axial profile was still underpredicted along most of the heated length [84].

Parallel to works devoted to axial profiles the radial flow distribution was evaluated, but mostly for atmospherical pressure and water-air experiments.

In 1991, *Antal et al.* [9] used a finite element method to describe the two-phase fully- developed adiabatic laminar air-water flow in a vertical tube at 1 bar and introduced the wall lubrication force keeping the bubbles away from the pipe wall. Here, the radial distributions of the void fraction and liquid velocity showed good agreement with experiments.

In 1993, *Anglart et al.* [6] simulated the adiabatic air-water flow and the saturated boiling in rectangular channels with the CFD code PHOENICS. The radial flow distribution was evaluated and the results of the adiabatic calculation were compared with experimental data at 1 bar ([128] and [164]). Thereby, a high peak in the void profile was observed near the wall for low void fractions and the vapor phase tends to flow toward the center of the channel at high voids in experimental and calculated results.

The fully developed void and velocity distribution in a pipe and in a non-axisymmetric triangular duct was modeled by *Lopez de Bertodano et al.* [102] in

1994 using CFD code PHOENICS. Various experiments for air-water flow at 1 bar were simulated, see e.g. [164]. Two-phase parameters e.g. lift coefficient and bubble bulk diameter were tuned to achieve good agreement with experiments for all tests.

In 1996, *Anglart* and *Nylund* [5] analyzed the two-phase bubbly sub-cooled and saturated boiling flow in a vertical annulus with heated inner tube (single-rod model) at a system pressure of 45 bar . The void fraction was measured in three radial zones at only one altitude [113] and was compared with calculations of the CFDS-FLOW3D code. Agreement with a calculation for the case with high sub-cooling at the inlet was achieved. The calculations for low sub-cooling at the inlet (saturated boiling) showed a large discrepancy with experimental results.

Later, the detailed radial void distribution was validated at low pressure. In 2003, the two-fluid model of the CFX code was combined with a population balance for bubble diameter by *Tu* and *Yeoh* [157] and validated in an annulus geometry at $\sim 1.4\text{ bar}$ [93]. The inner pipe of the annulus was heated and the validation of the radial flow distribution for sub-cooled boiling was carried out. Calculated radial void profiles and liquid velocities showed good agreement, but less good agreement was found for gas velocities. Additionally, the calculation of the radial distribution of the bubble diameter was very promising compared to experimental data.

➤ *Two-phase flow CFD calculations at CHF conditions*

In 1997, *Podowski* and co-workers ([1], [118]) combined the two-fluid model with a mechanistic DNB model of *Weisman* and *Pei* [166] that predicts temperature increase when the local void fraction exceeds a predetermined value in the near-wall bubbly layer. Such model was proved by *Rao et al.* in 2000 [122] in annular geometry leading to an error of the DNB prediction of 20 % for more than 40 cases.

➤ *Conclusions: No sufficient validations of the two-phase CFD model for flow boiling under normal operation PWR conditions were found, even for simplified geometries. Detailed validations for lateral void fraction distributions are currently not available. The simulation of the CHF conditions with two-phase CFD model for simple geometry showed a large need for improvement due to the inaccuracy of CHF predictions.*

1 Introduction

1.2.2 Simple geometry under swirl conditions

Swirl, i.e. flow with axial and azimuthal velocity components is introduced to various technical solutions to achieve better thermal mixing and to improve the heat transfer. To generate swirl, special components, e.g. fixed vanes or helical tube bundles have to be integrated. These also induce an additional pressure drop, which is a disadvantage that comes along with the mentioned positive effects. Among other simple geometries the impact of the swirl on turbulent flow in a pipe was commonly studied experimentally as well as a lot of single-phase CFD codes and turbulence models are validated on such flow due to the challenge of its modeling. Two-phase CFD applications are comparatively rare; one example of combined single and two-phase validation is presented here.

➤ *Single-phase flow* CFD calculations

In 2006, *Mimouni et al.* [110] validated the single-phase liquid water calculation using the NEPTUNE CFD code for flows in a single heated tube with swirl induced by three mixing blades. The computed lateral liquid velocities downstream of the mixing vane were compared with experiments (AGATE-mixing experiment [43]), showing qualitatively good agreement. Quantitatively, the predicted lateral velocities were underestimated. Operating conditions were not stated in this paper.

➤ *Two-phase flow* CFD calculations at non-CHF conditions

In the same paper [110] the applicability of the two-phase NEPTUNE_CFD model to describe the sub-cooled boiling under swirl conditions was proven by the Freon boiling tests (DEBORA-mixing experiment [44]). The calculated void fraction profile downstream of the mixing blades was compared with the measured values showing good agreement near the wall and overprediction in the bulk region. It has to be mentioned that the presented validation case had very small local void fractions (< 4 %) and measured results were available for only one altitude at a long distance downstream from the vanes.

➤ Conclusions: *Though CFD is used in many studies to model single-phase flow in simple geometries under swirl conditions and the results are quite successfully validated, the impact of the swirl on the two-phase flow in simple geometries is not studied enough in terms of CFD calculation. Experimental results with details on void distribution as well as CFD two-phase calculations at CHF conditions were not found.*

1.2.3 Sub-channel geometry without swirl

Two-phase CFD applications describing flow in sub-channels exist already for more than one decade. Subsequently the models became more detailed, e.g. with respect to the spacer design, and the comparison with experiments has been more successful.

➤ *Two-phase flow CFD calculations at non-CHF conditions*

In 1996, *Anglart* and *Nylund* [5] predicted void fraction in a cylindrical vessel with six heated rods at ~ 50 bar using the CFDS-FLOW3D code. Utilizing the symmetry of the bundle $1/10^{\text{th}}$ of the cross-section was modeled. The modeled regimes were sub-cooled and saturated boiling. Special focus was drawn to the calculated axial and lateral distribution of the void fraction, which was zone-wise compared to the experimental data (3 radial zones at 4 axial positions). Though in general the computed results were in a good agreement with the experiments within the measurement uncertainty, the mean values of the void fraction over the whole bundle were overpredicted probably due to an underprediction of condensation. Additionally, *Anglart et al.* [7] investigated in 1997 the effect of the spacers (either the equivalent parallel plate geometry approach was used to model the spacer or two-sections of the spacer were directly modeled) on both the phase distribution between cylindrical rods and the pressure drop along the rods. The results were in accordance with the experimental observations.

Later, *In et al.* in 2005 [68] evaluated two-phase flow models with CFX for the sub-cooled boiling flow in the same cylindrical vessel with six heated rods. For axial and radial void profiles the model showed better agreement with experiments than the previous work [5] and the bubble bulk diameter together with lift force showed to have a significant impact on the lateral flow distribution. Need for validations at various operation conditions was pointed out.

In 2001, *Windecker* and *Anglart* [169] validated the CFX prediction of the radial and axial flow in a vessel with six adiabatic rods and one heated central rod at 30 bar. The spacer grids were not modeled, but their influence was integrated as sources (pressure loss) in momentum and turbulence equation. Good agreement with measurement was achieved for radial distribution at low void fractions. With increased bundle averaged void fraction, discrepancies occurred, showing that the prediction of the void drift is a challenge for two-phase CFD [8]. The axial values were compared with results of sub-channel code and measurements. The CFD results were better than those achieved with a sub-channel code, but were nevertheless underpredicting the axial void fractions.

1 Introduction

The same authors evaluated the sub-channel averaged and local void fraction for sub-bundles containing 24 heated rods with different power distributions at 70 bar. The applied heat flux was low enough to assure the bubbly flow regime. Promising results were achieved showing the main trends of the experiments.

In 2006, *Anglart et al.* [8], summarizing the current needs and challenges for thermal-hydraulic design of fuel assemblies, pointed out one more challenge for two-phase CFD. The prediction of the pressure losses is still a difficult task due to the lack of a proper law-of-the-wall closure for two-phase flow.

- *Conclusions: In the literature related to two-phase calculations for sub-channel geometry with/without spacer grids mostly only hydraulic CFD predictions at non-CHF conditions are compared with experiments. Though the available experimental data is not very detailed and many improvements are needed for two-phase modeling, such predictions seem to be promising. At the same time the literature related to the two-phase CFD thermal predictions for fuel assembly geometry is extremely sparse. It has to be mentioned that none of the works found related to two-phase CFD modeling in sub-channel geometry, which include any kind of validations were carried out under PWR conditions. CFD two-phase calculations at CHF conditions for such flow were not found at all.*

1.2.4 Sub-channel geometry under swirl conditions

The main topic of the performed work described in this thesis is the sub-channel flow under swirl PWR conditions. Therefore, the literature overview of the existing CFD applications and used experimental data related to this subject is presented here in detail.

- *Single-phase flow CFD calculations*

During the past decades single-phase CFD has become an established tool for the prediction of the flow pattern, mixing performance and the pressure drop for fuel assembly with spacer grids including swirl generation features. These studies have been performed parallel to the improvement of the measurement techniques used for the experimental analyses, which have been carried out over several decades to investigate the effect of the swirl generating components on the flow field and the heat transfer downstream of such components (e.g. [28], [31], [62], [73], [171]). The experimental results have been used for the validation of several CFD codes.

For example, in 1995 *Karoutas et al.* [73] validated calculated axial and radial velocity profiles in the single sub-channel geometry of one span length for several spacer

designs, including split vanes and squeezed tubes, against Laser Doppler Velocimeter (LDV) measurement results along sub-channels in a 5x5 rod bundle cold water test loop at about 5 bar. The results of the simulation of the single-phase turbulent flow carried out with the CFDS-FLOW3D code showed relatively good agreement with experiments. The deviations were explained by neglecting rod support features, infinite thin thickness of the spacer strap and the influence of the next spacer. Additionally, the swirl factor was defined as a qualitative indicator for the impact of the spacer grid on the DNB performance. This factor was evaluated for calculations and experimental results for split vanes showing good agreement. Other designs were compared using this indicator.

In 2001, the CFX code was validated by *In* [67] in terms of the published measurements for the FA with spacer grids including split vanes at low pressure: velocity profiles [73] and the turbulent kinetic energy [171]. The computation model was a single sub-channel with a length of one spacer span. The overall characteristics of coolant mixing were well represented. Large discrepancies found in the region near the spacer were also explained by not modeling the rod support features and the assumption of an infinite thin spacer strap. The performance of four different types of the vanes was investigated comparing the simulated swirl and cross flow downstream of the spacer grid.

In 2002, in the frame of the bachelor thesis of the present author [129] the single-phase flow under swirl conditions in the single sub-channel geometry was simulated with the STAR-CD code at high pressure. The model was a quarter of the sub-channel using cyclic boundary conditions with the length of about one spacer span. A horizontal velocity component was superposed to the vertical flow component at the inlet to simulate the swirl induced by vanes. The damping behavior of the swirl in the sub-channel was studied. The inlet horizontal velocity was optimized with respect to the swirl near the outlet and the pressure loss. The value of a “declination angle” was defined and an optimum found. The declination angle of vanes used in real fuel assemblies was in agreement with the result of the simple optimization study.

In 2003, *Cui* and *Kim* [33] used the LDV experimental data of *Karoutas et al.* [73] to validate the lateral velocity distribution calculated with CFX-TASCflow code with various turbulence models for split vanes. From this the standard $k - \varepsilon$ turbulence model was selected as an optimum model. Different designs of the mixing vanes with different twist angles were numerically compared with commercialized split vanes, showing the

1 Introduction

twist angle of the vane to be an important factor for cross-flow between sub-channels.

Later, *Kim and Seo* in 2005 [75] validated the lateral velocity computed by the CFX code against measurements with split vanes [73] with a maximum underestimation of about 30 % and afterwards optimized the shape of the mixing vane for PWR fuel assemblies numerically. The chosen geometry included two adjacent sub-channels with a modeled length of one spacer span. The thickness of the spacer grid straps was taken into account but the rod support elements were still missing for model simplification.

In 2005, *Campbell et al.* [22] applied the CFD code FLUENT to predict pressure drop and rod wall temperature for the PWR grid spacer at various conditions. The experimental data [127] was achieved for full length 7x7 rod bundles with mixing vane grids representing the actual PWR 17x17 grid and missing only the rod support features (e.g. springs). The CFD model had a detailed spacer geometry (2x2 rod model with transverse and translational symmetry and cyclic boundary conditions) and showed good agreement with experiments.

For about three decades the heat-transfer enhancement caused by a mixing vane spacer was evaluated by various single-phase heat transfer correlations. For example, *Yao et al.* in 1982 [172] analyzed the governing heat transfer mechanisms near spacer grids with and without swirl at different flow conditions. They developed a single-phase heat transfer correlation to predict the local heat transfer rate downstream of a vaned spacer grid. The enhancement was identified to be caused by swirling flow (swirl factor) and the turbulent wakes behind the spacer grid (blockage ratio). Due to missing experimental heat-transfer data for single-phase flow in rod bundles with vaned spacer grid, the correlation was validated on tube experiments with a swirl generator [108], showing good agreement for the decay of the averaged *Nusselt* number with a fitted value of blockage ratio for the swirl generator.

Later, *Cui and Kim* (in 2003) [33] compared the results of this empirical correlation [172] with results of single-phase CFD calculation carried out with CFX-TASCflow for various designs of the mixing vanes with constant blockage ratio at low Re-number. A single sub-channel was modeled and cyclic boundary conditions were used to allow cross-flow between the channels. The increased twist angle in the CFD model of the mixing vane provided increased calculated cross flow. The effect of the twist angle can be shown only by CFD as the correlation only includes 2-D effects. The heat transfer downstream of the vane was shown by calculation to be influenced significantly by the

cross-flow factor and turbulence intensity, which both are not used in the correlation.

Recently, *In et al.* (in 2007) [69] benchmarked the single-phase CFX-10 simulation of turbulent heat transfer in a fully heated 5x5 array of a rod bundle including spacer grids with split vanes at a low *Reynolds* number under atmospheric pressure and then compared the thermal-hydraulic performance of two different types of mixing vanes: split and hybrid-vane at normal operation PWR conditions. The CFD geometry includes a 5x5 rod bundle with two spacers, a spacer span typical for PWR and the modeled length after the second spacer long enough to assure a fully developed flow at the outlet. For the benchmarking two experiments [31], [62] and the results of two correlations [62], [172] were chosen. The authors pointed out that the initial heat transfer enhancement directly downstream of the top of the vanes as measured in the experiment with the partially heated rod-bundle data [62] is similar to the CFD result achieved by using analogous structure (without rod support features on grid). The decay of the averaged *Nusselt* number for the experiment with fully heated rods [31] and for the results achieved with correlation of *Yao et al.* [172] showed fairly good agreement with CFD calculation, except for the region close to the spacer grid. Overestimations are explained by the different length of the vanes and the applied turbulence model. The calculations under PWR conditions proved that the spacers with vanes significantly enhance the overall heat transfer.

Conclusions: Single-phase CFD has been widely validated for single-phase flow in sub-channel geometries and used for purposes of the spacer grid design with mixing vanes. In these analyses it was shown that swirl, turbulence intensity and cross flow have a positive impact with respect to heat transfer. The geometry used for single-phase calculations became more detailed with time: beginning with a single sub-channel with one spacer grid including vanes (without modeled strap thickness and without rod supports) and ending with 5x5 rod bundle geometry with two spacer grids and more detailed modeling of the grids. Hence, CFD calculations at normal operation PWR conditions including all geometrical details of the real fuel assembly are still object of future work. This can be achieved e.g. by improving the meshing technique, numerical methods, increasing the computational power and using higher order turbulence models. Additionally, the experimental data at such pressures is needed for validations. For reliable conclusions with respect to CHF the two-phase calculations at both normal operation and CHF conditions are needed.

1 Introduction

➤ Two-phase flow CFD calculations at non-CHF conditions

In 2003, while defining the goals for this work, the diploma thesis of the present author [130] was the only available simulation of the two-phase flow carried out in sub-channel geometry under swirl conditions applying a two-fluid CFD model. The main part of the work described in this thesis was carried out with the *Euler-Lagrangian technique* (at that moment the only available technique by STAR-CD), describing the behavior of air bubbles in water and of droplets in air flow. The calculations were carried out in a simplified sub-channel geometry with disperse particles homogeneously distributed over the model inlet, where the rotational flow is additionally defined. The influence of parameters as bubble diameter, void fraction and swirl intensity on the phase separation was investigated. But finally, the first isothermal calculation using *Euler-Euler technique* was possible with a beta version of STAR-CD, showing first promising details of the void distribution with respect to CHF, in particular the “bubble pocket” at the rod surface.

Later, *Krepper* [84] proved the capability of CFX to support fuel rod bundle design by means of the same simplified sub-channel geometry with swirl flow generated at the entrance, also showing the accumulation of the bubbles on the rod surface. However the calculated maximum wall temperature for the case without inlet swirl was slightly lower than the one calculated with the defined swirl at inlet.

In 2006, *Boucker et al.* [19] presented the first computation of a real fuel assembly geometry including a spacer grid with mixing vanes by means of NEPTUNE-CFD code. The performed calculation was carried out at typical PWR core conditions, but the vapor production at the wall was very moderate leading to very small local void fractions and the applied mesh seems to be too coarse.

Conclusions: *The efforts undertaken, e.g. by Salnikova [130], towards the two-phase modeling of the isothermal flow in a simplified sub-channel geometry under swirl conditions showed the potential of the two-phase calculations with respect to the design optimization of the fuel assembly. Hence, the enhanced two-phase model applied to more detailed (e.g. adjacent sub-channels with heated rods and spacer grids with mixing vanes) or even real geometry under normal operation PWR conditions as needed for more reliable flow predictions in the context of heat transfer optimization.*

➤ CHF conditions

Conventionally the CHF performance and other two-phase information of the fuel

assemblies with spacer grids including mixing vanes were achieved through 1-D analyses carried out with *sub-channel codes* using integrated correlations based on measurements, which depend on geometry and flow parameters. Today the correlations used for industrial application are based on large representative CHF data bases. The dependence of CHF on geometry and operating conditions results in additional expensive measurements for each geometry variation (e.g. *Hwang et al.* [64] correction for non-uniform heating of the DNB correlation, which was proved among other geometries for rod bundles). Additionally, several attempts to use *single-phase CFD* calculations at CHF conditions to draw conclusions with respect to CHF performance of fuel assemblies have been reported in the literature.

For example, *Ikeda K. et al.* [66] (in 2006) used STAR-CD to model single-phase flow in a 5x5 fuel rod bundle of PWR with spacer grid including detailed mixing and support structures. One span length of the bundle with axial cyclic conditions was modeled to simulate the full length element. One limitation was the use of a constant heat flux along the rod (average values of the axial modeling domain in the test) instead of a realistic cosine shape with central peaking. The radial difference in the heating of the rods was taken into account. This single-phase calculation was used to deduce the location of the highest risk of DNB occurrence for one water DNB test at 103 bar and with low quality, which was chosen to minimize the impact of two-phase effects. It was shown that there was a correlation between local velocity and enthalpy distribution around the rod surface, which were both assumed to determine the initial conditions for the two-phase structure. The rod with a high potential of CHF found in the simulation agreed with the experimental results, thus showing the potential of single-phase analyses.

Conclusions: CHF performance of the fuel assembly is described today by CHF correlations. CFD has only recently started to play a role with respect to the CHF. The single-phase CFD analyses of detailed fuel assembly geometries showed a potential of the single-phase CFD for the designing the spacer grids. But there are large limitations: with increased quality two-phase phenomena such as e.g. generation of bubbles at the rod surface or increased pressure drop due to a two-phase flow and bubble-induced turbulence will influence the flow distribution. Therefore two-phase CFD modeling is needed and some two-phase indicators have to be found with respect to the CHF. Until today the CHF cannot yet be predicted in the real fuel assembly geometry at real conditions.

1.3 Objectives of this work

The research presented in this thesis was carried out in the frame of a cooperation between AREVA NP GmbH (Thermal-Hydraulic department FDWT), the Technical University (TU) Dresden and the University of Applied Sciences Zittau/Görlitz. It is concerned with two-phase swirl flow in sub-channels modeled by the commercial CFD code STAR-CD. The CFD results achieved by the author in terms of CFD in previous bachelor [129] and diploma [130] theses were very promising and have been an important motivation for further work. They described single-phase flow and two-phase isothermal flow in a simplified sub-channel geometry under swirl conditions (without modeling the vanes). The main goal of thermal-hydraulic design optimization analyses, presented in detail in Section 1.1, is an improved CHF performance of the fuel assembly. The literature overview showed the state of the art and allowed to identify research tasks towards this goal as well as to further define the objectives of the work presented in this thesis.

The aim of this work is to provide a better understanding of the flow with respect to the thermal-hydraulic optimization of the spacer grid design by improvement of the two-phase CFD modeling, using detailed geometries and performing detailed validations under high pressures as found in normal PWR operation. The result of this work aims to be a significant step towards a reliable two-phase CFD modeling applicable to realistic geometries under CHF conditions.

The analyses of two-phase flow under swirl conditions in sub-channel geometry are to be carried out with main focus on the general aspects such as swirl decay along the sub-channel or bubble distribution near the rod surface. The relevant conclusions of such analyses are to be some indicators with respect to the CHF behavior of fuel assemblies under conditions of the PWR. The simulation of any particular design is not subject of this work.

First of all the two-phase flow models used in STAR-CD are to be summarized and the presented validations that show the range of applicability of these models with respect to the sub-channel analyses under non-CHF and CHF conditions are to be overviewed. For the missing validations, important for applications under PWR conditions, the required experimental data is to be found and compared with calculated results. Possible improvement of the two-phase flow model for sub-channel flow under high pressure for both non-CHF and CHF conditions is to be carried out.

Next, the CFD analyses under swirl conditions for different sub-channel geometries and types of vanes are to be performed.

Thereby the following aspects are to be taken into account:

- Influence of the swirl in sub-channels on the CHF,
- Local void fraction distributions and possible new criteria for CHF,
- Mixing between coupled sub-channels.

The analysed two-phase regimes are predominantly bubbly flows.

1.4 Numerical tool

Computer-aided analysis techniques play an important role in many areas, notably in the field of structural analysis. There are also a number of software packages available that solve fluid flow problems, based on *Computational Fluid Dynamics (CFD)* method. However, the market of CFD codes is not as large as structural mechanic codes. CFD is the analysis of engineering systems involving fluid flow, heat transfer and associated phenomena e.g. two-phase flow, by means of computer-based simulations, solving equations for mass, momentum, energy, turbulence and concentration. Among the various numerical solution methods the so called *finite volume method* is the most used. Possible replacement of cost-intensive experimental studies and empirical correlations is the main long term goal of CFD codes and its applications, leading to their wide and quick development.

In this work the CFD software package STAR-CD was applied, provided by CD-adapco, developed with an ISO 9001:2000 accredited code development environment. It is a multipurpose code that can assist the user through the complete design and development process. The system includes the solver STAR and pre-/post-processor, PROSTAR, with its Graphical User Interface (GUI). STAR-CD provides the tools that are needed to build a new model, set up analyses and post-process the results. With help of the GUI it is possible to create/import, check and fix the grid, to specify boundary locations and conditions, to select the thermo-physical model, material properties and finally to set up solution controls. The models from other computer-aided engineering (CAE) systems can be also imported to STAR-CD [135]. The results can be evaluated and presented by options for plotting, animation and data graphs. STAR-CD has been applied to many flow problems: Aerospace, Automotive, Mechanics, Nuclear Engineering etc. [135].

At the moment of the definition of the goals for this research work the commercially available two-phase package of STAR-CD was in its initial development phase. While the research work was being carried out, the two-phase modeling was continuously further developed by CD-adapco and new versions were applied for the performed calculations. In cooperation with CD-adapco some improvements of the STAR-CD code were achieved.

1.5 Thesis outline

The remainder of the thesis has the following structure:

Chapter 2 presents general modeling of single-phase physical phenomena by CFD codes with special focus on sub-channel analyses in fuel assemblies. This chapter starts by stating the governing equations. Then, the fundamentals of the turbulence modeling with focus on the $k-\varepsilon$ model used in this work are presented. Finally, the numerical treatment is discussed by presenting the discretization process, boundary conditions and the applied solution algorithm.

Chapter 3 includes a detailed overview of changes and additional terms needed for two-phase modeling. Here, the Euler-Euler technique is presented, which is then utilized in the following Chapters to model the two-phase flow. The description of the mathematical model starts with the governing equations, followed by closure laws and constitutive equations. The formulations of inter-phase momentum, heat and mass transfer as well as of two-phase turbulence modeling used for the performed STAR-CD calculations were discussed in detail using various literature sources. Additionally, the choice of appropriate physical properties, which are to be set constant in the present two-phase STAR-CD modeling, is discussed and an improved approximation method is proposed. In the last section of this chapter an extended heat partitioning model formulation for the steam phase in a direct contact with a heated wall is introduced.

Chapter 4 summarizes the whole range of validations carried out for the current two-phase STAR-CD model. In the first section the review of the already published validations is presented, discussed and required additional validations are pointed out. In the second section, an experiment providing detailed results for local void distribution in a heated vertical tube with Freon as working medium and scaled to water-steam PWR conditions was chosen to investigate the currently implemented two-phase model. The most important two-phase parameters were varied and two sets of parameters for the physical model were found to fit best the experimental data for low void and high void fractions, respectively. In the third section, the potential of the recent STAR-CD version in two-phase modeling of CHF is shown exemplarily on the pipe flow. The possibilities for an improved modeling by utilizing the new model from Chapter 2 are presented here.

Chapter 5 is dedicated to CFD analyses of sub-channel flow under swirl conditions. It starts with a generic swirl model with a defined rotational flow at the inlet. Further on, a more detailed description of the flow in a single sub-channel is presented by a CFD model with a simplified vane geometry inducing swirl within the sub-channel. Additionally, the same single sub-channel geometry is compared with another type of the swirl generating component

inducing swirl around the rod. Finally, a non-isothermal two-phase calculation for complex geometries such as real vanes in connected sub-channels is performed. For these models, possible optimization criteria for fuel assembly spacer grids are outlined. Analyses of such parameters as swirl, pressure loss, accumulation of bubbles on the rods and wall temperature are presented, including an optimization study of the declination angle of the vanes. Additionally, an application of an extended heat partitioning model under swirl conditions is shown.

In Chapter 6 general conclusions are drawn and suggestions for future work are listed for each studied topic.

2. Physical phenomena of single-phase flow

2.1 Introduction

To better understand the modeling of physical phenomena with special focus on sub-channel analyses in fuel elements by CFD codes, first of all the single-phase approach is presented in this chapter. The mathematical description of the flow physics and turbulence modeling are gathered in Sections 2.2 and 2.3 respectively. The general ideas of numerical treatment can be found in Section 2.4. The detailed information about changes and additional terms needed for the two-phase modeling (Euler-Euler approach) is presented in Chapter 3. The numerical treatment of two-phase flow is essentially based on the same principles as for single-phase flows (a detailed description is beyond the scope of this work).

2.2 Governing equations

The physical laws governing the motion of fluids are stated in terms of mass and momentum balances. Further balance equations can be set up for scalar properties such as energy. In the frame of the present work the mean free path of the molecule is much smaller than the characteristic dimension of the considered system; so that a *continuum approach* can be applied i.e. the fluid is treated as a continuum (infinite set of material points).

For 3-D single-phase flow the motion can be specified by five partial differential equations: one continuity equation, three momentum equations (*Navier-Stokes equations* for *Newtonian fluids*) and one energy equation. In addition, constitutive equations are required e.g. to correlate fluxes with gradients. For turbulent flow, models with different levels of approximation are available. One of the frequently used methods is the *k - ε turbulence model*, with two additional scalar transport equations for kinetic energy of turbulence *k* and the rate of dissipation *ε*.

In the following, the governing equations and computational methods for fluid dynamics are introduced based on the international well-established textbook of *Ferziger and Peric* [46]. The governing conservation equations for fluid motion can be derived from the classical physical laws for the motion of solid bodies. These main laws deal with the amount of matter or so-called control mass (CM) of the solid bodies and its *extensive* properties (dependent on the CM) such as mass, momentum and energy:

- **The law of mass/matter conservation** (or the *Lomonosov/Lavoisier law*) states that the mass of a body can neither be created nor destroyed, although it may change form:

$$\frac{dm}{dt} = 0. \quad (1)$$

- **Newton's second law** of motion states that the rate of change of momentum of a body (CM) equals the sum of the forces \vec{f} acting on it:

$$\frac{d(m\vec{u})}{dt} = \sum \vec{f}. \quad (2)$$

- **The first law of thermodynamics** states that energy can neither be created nor destroyed; it can only change form. The balance for energy can be formulated as follows: the rate of change of the total energy of a body equals the work done by the external forces on the body (CM) W plus the rate of heat energy added to the body \dot{Q} :

$$\frac{d(E_K + E_I)}{dt} = W + \dot{Q}, \quad (3)$$

with E_K and E_I kinetic and internal energy, respectively.

For the application of the governing equations to the fluid motion, the control volume approach will be used. This approach deals with fluid elements or so-called control volumes (CVs) enclosing the CM, and is related to its intensive variables (independent from the considered CM): such as density, velocity and enthalpy. For derivation of the fluid conservation laws for fluids the transition from extensive to intensive variables and from CM to CV is needed [46]:

- **transition of variables**

For any conserved intensive property ϕ per unit mass (for conservation of mass $\phi = 1$, for conservation of momentum $\phi = \vec{u}$, for conservation of a scalar e.g. energy conservation $\phi = k$), the corresponding extensive property Φ can be defined as integral over the volume occupied by the CM Ω_{CM} :

$$\Phi = \int_{\Omega_{CM}} \rho \phi d\Omega. \quad (4)$$

- **transition of application domain**

The left-hand side of each conservation equation can be written in form of *Reynold's* transport theorem allowing the needed transition from CM to CV. Changing the extensive property in the control mass is described as change within the control volume, Ω_{CV} (time dependent) and its net-flux through the surface enclosing CV S_{CV} , due to fluid motion relative to CV boundary (convective term):

2 Physical phenomena of single-phase flow

$$\frac{d}{dt} \int_{\Omega_{CM}} \rho \phi d\Omega = \frac{d}{dt} \int_{\Omega_{CV}} \rho \phi d\Omega + \int_{S_{CV}} \rho \phi (\vec{u} - \vec{u}_{CV}) \cdot \vec{n} dS, \quad (5)$$

with \vec{n} denoting the outward facing normal unit vector to the surface element dS . For fixed i.e. non-moving and not deforming CV, which is the case for all presented calculations in this thesis, $\vec{u}_{CV} = 0$ and the first derivative on the right hand side becomes a local (partial) derivative.

$$\frac{d}{dt} \int_{\Omega_{CM}} \rho \phi d\Omega = \frac{\partial}{\partial t} \int_{\Omega_{CV}} \rho \phi d\Omega + \int_{S_{CV}} \rho \phi \vec{u} \cdot \vec{n} dS. \quad (6)$$

Mass conservation (Continuity equation):

The differential form of the continuity equation applied to a fluid element (CV) can be derived from the Law of mass/matter conservation Eq. (1) and is presented here in detail.

The integral form of the mass conservation equation for any fluid element (CV) can be obtained applying *Reynolds's transport theorem* Eq. (5) by setting $\phi = 1$:

$$\frac{d}{dt} \int_{\Omega_{CM}} \rho d\Omega = \underbrace{\frac{\partial}{\partial t} \int_{\Omega_{CV}} \rho d\Omega}_{\text{Time depended term}} + \underbrace{\int_{S_{CV}} \rho \vec{u} \cdot \vec{n} dS}_{\text{Convection term}} = 0. \quad (7)$$

Accounting a fixed CV and a continuous integrand the *Leibniz rule* can be applied to the time dependent term:

$$\frac{\partial}{\partial t} \int_{\Omega_{CV}} \rho d\Omega = \int_{\Omega_{CV}} \frac{\partial}{\partial t} \rho d\Omega. \quad (8)$$

Due to *Gauss's divergence theorem* applied to the convection term, the surface integral over the boundary of the CV can be replaced by a volume integral over the CV:

$$\int_{S_{CV}} \rho \vec{u} \cdot \vec{n} dS = \int_{\Omega_{CV}} \nabla \cdot (\rho \vec{u}) d\Omega. \quad (9)$$

Eq. (7) using Eqs. (8) and (9) can be written as:

$$\int_{\Omega_{CV}} \left(\frac{\partial \rho}{\partial t} + \nabla \cdot (\rho \vec{u}) \right) d\Omega = 0. \quad (10)$$

Taking into account that the integrand is continuous and that the domain of integration may be any CV, the integrand has to be equal to zero. The coordinate-free differential form of the continuity equation can be written in the following form:

$$\frac{\partial \rho}{\partial t} + \nabla \cdot (\rho \vec{u}) = 0, \quad (11)$$

with $\frac{\partial \rho}{\partial t}$ - time depended changes of the density (specific mass) within CV,

$\nabla \cdot (\rho \vec{u})$ - net mass flow through the surface enclosing CV.

Due to definition of the divergence operator, for a Cartesian coordinate system using *Einstein summation convention* (repeated subscripts denote summation - also everywhere later) in index notation Eq. (11) becomes:

$$\frac{\partial \rho}{\partial t} + \frac{\partial(\rho u_i)}{\partial x_i} = 0. \quad (12)$$

If any mass source s^{mass} exists in the control volume Eq. (12) can be extended as:

$$\frac{\partial \rho}{\partial t} + \frac{\partial(\rho u_i)}{\partial x_i} = s^{mass}. \quad (13)$$

Momentum conservation:

The momentum balance for a fluid element (CV) can be derived from *Newton's second law* of motion Eq. (2), applying *Reynold's transport theorem* Eq. (5) to the left-hand side of Eq. (2) by setting $\phi = \vec{u}$ [46]. At the same time the right-hand side of the equation has to be expressed in terms of intensive properties over the CV. The considered forces are surface and body forces. Body forces considered in STAR-CD are buoyancy and rotational force. In differential form with Cartesian tensor notation it gives the following expression [136]:

$$\frac{\partial(\rho u_i)}{\partial t} + \frac{\partial}{\partial x_j}(\rho u_j u_i - \tau_{ij}) = -\frac{\partial p}{\partial x_i} + s_i^{mom}, \quad (14)$$

with s_i^{mom} momentum source components, including body forces and other external forces, if present.

For solving these *Navier-Stokes equations* the stress tensor components τ_{ij} have to be determined by a constitutive equation, which depends on the type of the flow.

- **laminar flow**

For *laminar flow* of a *Newtonian fluid* the stress tensor components τ_{ij} are related to the velocity gradients as:

$$\tau_{ij}^l = \mu \left[\frac{\partial u_i}{\partial x_j} + \frac{\partial u_j}{\partial x_i} - \left(\frac{2}{3} \cdot \frac{\partial u_k}{\partial x_k} \right) \delta_{ij} \right], \quad (15)$$

according to *Stokes' hypothesis* from 1845 [142], with the molecular dynamic viscosity μ and the *Kronecker* symbol δ_{ij} ($\delta_{ij} = 1$ if $i = j$ and $\delta_{ij} = 0$ otherwise). This expression is often denoted in literature as laminar stress tensor. For laminar flow the conservation equations together with known flow properties and sources, defined inlet and boundary conditions and the constitutive relation described before, provide a closed system of equations for the unknown velocity vector u_i and pressure p . Such a system can be numerically solved after spatial and temporal discretization.

2 Physical phenomena of single-phase flow

- **turbulent flow**

The relation for the stress tensor component τ_{ij} for *turbulent flow* is obtained in Chapter 2.3, describing turbulence modeling for single-phase flow.

Energy conservation:

The energy conservation equation for a fluid element (CV) can be derived from the energy balance Eq. (3). If the conserved property representing the energy is the thermal enthalpy, the energy conservation equation in differential form for any fixed CV with Cartesian tensor notation is written in the STAR-CD methodology manual [136] as:

$$\frac{\partial(\rho h)}{\partial t} + \frac{\partial}{\partial x_j}(\rho h u_j + F_j^h) = \frac{\partial p}{\partial t} + u_j \frac{\partial p}{\partial x_j} + \tau_{ij} \frac{\partial u_i}{\partial x_j} + s^h, \quad (16)$$

with F_j^h the diffusion energy flux in direction x_j and s^h energy sources.

For the diffusion energy flux F_j^h an additional constitutive relation has to be specified, which will also be dependent on the flow type.

- **laminar flow:**

Due to *Fourier's law* the diffusion energy flux F_j^h for laminar flow is defined as:

$$F_j^h = -\lambda \frac{\partial T}{\partial x_j}, \text{ with } \lambda \text{ thermal conductivity.} \quad (17)$$

- **turbulent flow:**

The relation of the diffusion energy flux F_j^h for *turbulent flow* will be given in the following section, which describes turbulence modeling for single-phase flow.

2.3 Turbulence modeling

The time-averaged equations for the turbulent flow are derived from the *Navier-Stokes equations* by an averaging operation, in which it is assumed that there are fluctuations p' , h' and u'_i about the mean value (time averaged) \bar{p} , \bar{h} and \bar{u}_i , respectively. The used mathematical technique is called *Reynolds decomposition*, yielding the following formulation for pressure, thermal enthalpy and velocity vector:

$$p = \bar{p} + p', \quad h = \bar{h} + h' \quad \text{and} \quad u_i = \bar{u}_i + u'_i. \quad (18)$$

The resulting conservation equations are called *Reynolds Averaged Navier-Stokes (RANS) equations* and due to their non-linearity by the averaging operation, additional terms are arising, the so-called *Reynolds stresses*, turbulent diffusion flux, etc, for which appropriate closure laws or models are required.

Stress tensor components for turbulent flow:

Assuming all occurring dependent variables to be ensemble or time (for steady state situation) averaged, stress tensor components τ_{ij} for *Newtonian turbulent flow* can be obtained from:

$$\tau_{ij} = \underbrace{\mu \left[\frac{\partial u_i}{\partial x_j} + \frac{\partial u_j}{\partial x_i} - \left(\frac{2}{3} \cdot \frac{\partial u_k}{\partial x_k} \right) \delta_{ij} \right]}_{\tau_{ij}^l} + \underbrace{\left(-\bar{\rho} \cdot \overline{u'_i u'_j} \right)}_{\tau_{ij}^t}, \quad (19)$$

where the term $\bar{\rho} \cdot \overline{u'_i u'_j}$ describes the additional *Reynolds stresses*, due to the turbulent motion, also defined as an additional turbulent stress tensor τ_{ij}^t . This term has the form of a symmetrical tensor of second order and leads to the occurrence of six additional unknown variables. During the averaging process no new equations have been introduced.

Diffusion energy flux for turbulent flow:

Assuming all dependent variables occurring in the diffusion energy flux to be time averaged, the flux for turbulence flow can be written as:

$$F_j^h = -\lambda \frac{\partial T}{\partial x_j} - \bar{\rho} \cdot \overline{u'_j h'}, \quad (20)$$

where the term $\bar{\rho} \cdot \overline{u'_j h'}$ characterizes the turbulent diffusion energy flux, leading to three additional unknown variables also without any newly introduced equation.

Due to these additional unknown variables, RANS equations for averaged velocity, pressure and enthalpy can not be solved. This fact is called in the literature *closure problem of turbulence*. Therefore, turbulence modeling has to close the system of equations by providing suitable constitutive equations for the unknown terms. It can be done with the help of empirical or semi-empirical correlations. A widely used type of the turbulence model is a *two-equation eddy-viscosity* model. The “standard” *High Reynolds number k-ε model* proposed by *Launder and Spalding* [140] is the most commonly used variant of this model.

As all *eddy-viscosity* models it uses the *Boussinesq eddy-viscosity assumption* [21] postulating that the momentum transfer caused by turbulent eddies can be modeled with a turbulent eddy-viscosity, in analogy to momentum transfer due to molecular motion described by molecular viscosity.

According to this assumption, the correlation of *Reynolds stresses* and also scalar-fluxes with the averaged flow variables gets a similar form as the laminar stress tensor components and is given in the STAR-CD methodology manual [136] as:

2 Physical phenomena of single-phase flow

$$-\bar{\rho} \cdot \overline{u'_i u'_j} = \mu^t \left[\frac{\partial u_i}{\partial x_j} + \frac{\partial u_j}{\partial x_i} - \left(\frac{2}{3} \cdot \frac{\partial u_k}{\partial x_k} \right) \delta_{ij} \right] - \left(\frac{2}{3} \cdot \rho k \right) \delta_{ij} \quad \text{and} \quad (21)$$

$$-\bar{\rho} \cdot \overline{u'_j h'} = \frac{\mu^t}{Pr_h^t} \frac{\partial h}{\partial x_j}, \quad (22)$$

with turbulent eddy-viscosity μ^t , turbulent *Prandtl* number Pr_h^t and kinetic energy of turbulence k . To achieve the closure of the system of equations, the turbulent eddy-viscosity has to be estimated. *Prandtl* [119] proposed to define it as a product of a characteristic turbulent velocity u_{ch}^t and a characteristic turbulent length scale l_{ch}^t . The “standard” *High Reynolds* number *k-ε model* uses the following assumptions for u_{ch}^t and l_{ch}^t :

$$u_{ch}^t = C_\mu^{1/4} k^{1/2}, \quad (23)$$

$$l_{ch}^t = C_\mu^{3/4} k^{3/2} / \varepsilon. \quad (24)$$

Using *Prandtl*'s proposal and Eqs. (23) and (24), the turbulent molecular eddy-viscosity for *k-ε model* results in:

$$\mu^t = \rho \cdot u_{ch}^t \cdot l_{ch}^t = \rho \cdot C_\mu k^2 / \varepsilon, \quad (25)$$

with the empirical constant C_μ , that has been determined by a numerical fit.

The *k-ε model* belongs to the *two-equation* class of turbulence models, according to the number of introduced additional differential equations. For this model two additional transport equations for kinetic energy of turbulence k and dissipation rate of turbulence ε have to be solved:

- **transport equation for k**

The first equation for the kinetic energy of the fluctuating motion k , defined as

$$k = \frac{\overline{u'_i u'_i}}{2}, \quad (26)$$

can be written in the following form:

$$\frac{\partial}{\partial t} (\rho k) + \frac{\partial}{\partial x_i} (\rho u_i k) = \frac{\partial}{\partial x_i} \left(\Gamma_k \frac{\partial k}{\partial x_i} \right) + G - \rho \varepsilon, \quad (27)$$

with G the rate of generation of turbulence energy or production term

$$G = \mu^t \left[\frac{\partial u_i}{\partial x_j} + \frac{\partial u_j}{\partial x_i} \right] \cdot \frac{\partial u_i}{\partial x_j}, \quad G = f(\text{velocity changes}) \quad (28)$$

and with Γ_k the diffusion coefficient for the kinetic energy

$$\Gamma_k = \mu + \frac{\mu^t}{Pr_k^t}. \quad (29)$$

- **transport equation for ε**

A similar differential equation governs the dissipation rate of turbulence ε , defined as

$$\varepsilon = \frac{\mu}{\rho} \cdot \overline{\left(\frac{\partial u'_i}{\partial x_k} \frac{\partial u'_i}{\partial x_k} + \frac{\partial u'_i}{\partial x_k} \frac{\partial u'_k}{\partial x_i} \right)}, \quad (30)$$

but it can not be exactly derived from the *Navier-Stokes equation* [51]. Therefore, some parameters are needed to be adjusted for turbulent flow situation [61]:

$$\frac{\partial}{\partial t}(\rho\varepsilon) + \frac{\partial}{\partial x_i}(\rho u_i \varepsilon) = \frac{\partial}{\partial x_i}(\Gamma_\varepsilon \frac{\partial \varepsilon}{\partial x_i}) + \frac{\varepsilon}{k}(C_{\varepsilon 1}G - \rho C_{\varepsilon 2}\varepsilon), \quad (31)$$

with Γ_ε the diffusion coefficients for ε

$$\Gamma_\varepsilon = \mu + \frac{\mu^t}{Pr_\varepsilon^t}. \quad (32)$$

Turbulent boundary layer:

For numerical simulation of the turbulent flow a special algebraic formulation (boundary condition) for the shear stress at the wall, based on so-called “*wall functions*”, which represent the local profiles of velocity in the wall boundary layer is used. This practice is applied to avoid detailed meshing and modeling of the boundary layer; because these models are not valid in regions within the layer where molecular and turbulence effects are of comparable magnitude.

The universal law of the wall [57] is a correlation between shear stress at the wall τ_w , resultant velocity parallel to the wall $\bar{u} = u - u_w$ and the dimensionless normal distance from the walls

$y^+ = \frac{\rho u_\tau y}{\mu}$, based on experimental data for pipe flow dating back to 1920. It is presented as

curve 2 in Figure 2.1 and can be expressed for a smooth wall as:

$$u^+ = \frac{\bar{u}}{u_\tau} = \frac{1}{\kappa} \ln(y^+ E), \quad \text{for } y^+ \geq y_{tr}^+, \quad (33)$$

with $u_\tau = \sqrt{\tau_w/\rho}$ denoting the resultant friction velocity, which can be derived implicitly from Eq. (33) for given velocity and wall distance. Further, κ denotes the *von Kármán constant*, E a roughness parameter and y_{tr}^+ a transition parameter, described later. This law should be applied to a point adjacent to the wall, whose y^+ value is approximately in the range of $30 < y^+ < 150$. These values result from Figure 2.1, presented in [125]. For $y^+ \ll 30$, it can be seen that a deviation from realistic flow will occur, if the universal logarithmical wall function is extrapolated into the laminar boundary region.

2 Physical phenomena of single-phase flow

For the viscous laminar sublayer ($y^+ < 5$) the velocity distribution close to the wall is given as:

$$u^+ = y^+, \text{ for } y^+ < y_{tr}^+. \quad (34)$$

This profile is shown in Figure 2.1 as **curve 1**. For such flows *Low Reynolds* number models were developed, which are based on the physics of the laminar boundary sublayer.

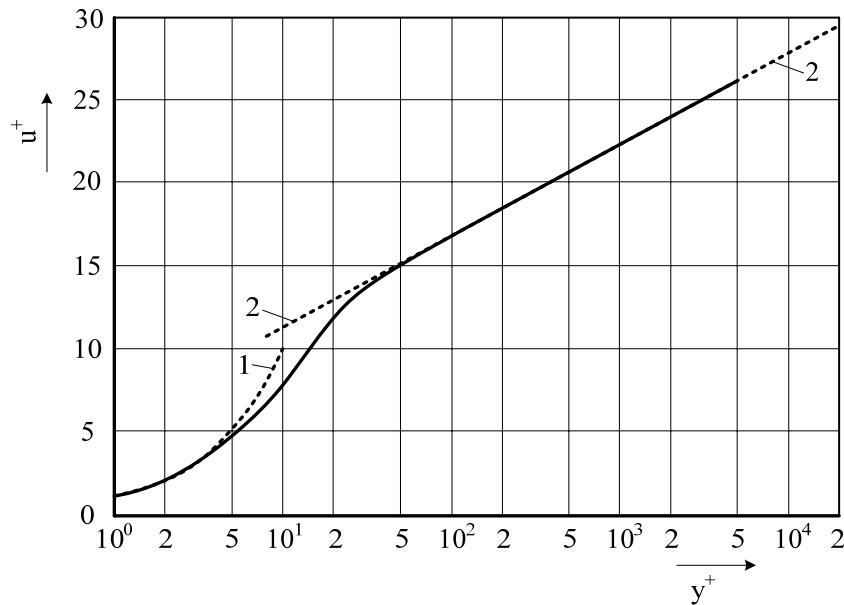


Figure 2.1 Universal velocity function with logarithmic abscissa scale [120]

In STAR-CD there is no extra formulation for the transition region or buffer zone introduced by *von Karman* for y^+ values in range of approximately $5 < y^+ < 30$. The transition between application of Eqs. (33) and (34) is achieved by introducing y_{tr}^+ , the intersection point of **curves 1** and **2** (Figure 2.1). It is dependent on the chosen values for the von Kármán constant κ and roughness parameter E , which are obtained in literature from various experiments and have some deviation (e.g. *Nikuradse* [114] derived for smooth pipes $\kappa=0.4$ and $E=9.025$). For smooth walls, applied in performed calculations STAR-CD uses $\kappa^{STAR} = 0.419$ and $E^{STAR} = 9.0$. Normally κ varies by about 10% for different shapes of surface (concave, convex). The constant κ^{STAR} used by STAR-CD is some average value to be applied for all shapes. Other default coefficients of the $k-\varepsilon$ model used in performed calculations are presented in Table 2.1.

Table 2.1 Default coefficients of the single-phase standard $k-\varepsilon$ turbulence model

C_{μ}^{STAR}	$C_{\varepsilon 1}^{STAR}$	$C_{\varepsilon 2}^{STAR}$	$Pr_k^{t,STAR}$	$Pr_{\varepsilon}^{t,STAR}$	$Pr_h^{t,STAR}$
0.09	1.44	1.92	1.0	1.219	0.9

Based on the *universal wall function* for the velocity profile the shear stress is derived. By similarity considerations, heat transfer coefficients and boundary conditions for turbulence are deduced.

2.4 Numerical treatment

2.4.1 General approach

The process of numerical simulation of any fluid flow can be divided into three levels: generation of the grid, discretization of the governing equations to get a set of algebraic equations and the solution of this set. Details of numerical treatment can be found in [140]. Here, the general ideas of finite volume method, discretization scheme and solution algorithm are illustrated by single-phase flow.

After the laws governing the fluid flow, heat transfer and other related processes have been expressed in terms of partial differential equations and constitutive relations and inlet and boundary conditions have been provided, a closed system of equations with unknown velocity vectors and pressure is achieved. After spatial and temporal discretization into control volumes (finite volume elements) an algebraic system of equations is obtained, which can be solved numerically.

2.4.2 Mathematical formulation and discretization methods

The mathematical model, presented in the previous chapter, consists of a set of conservation equations for mass, momentum and energy. All governing equations have a similar structure and can be written in a general form consisting of four types of terms: time dependent, convection, diffusion and source. For any conserved variable ϕ a general conservation equation for CV in differential form with Cartesian tensor notation results in:

$$\underbrace{\frac{\partial}{\partial t}(\rho\phi)}_{\text{Time dependent term}} + \underbrace{\frac{\partial}{\partial x_j}(\rho u_j \phi)}_{\text{Convection term}} = \underbrace{\frac{\partial}{\partial x_j}(\Gamma_\phi \frac{\partial \phi}{\partial x_j})}_{\text{Diffusion term}} + \underbrace{s_\phi}_{\text{Source term}}, \quad (35)$$

with s_ϕ a source term of conserved variable ϕ and Γ_ϕ the diffusion coefficient.

The values for conserved variable and diffusion coefficient for conservation equations are summarized in Table 2.2.

Table 2.2 Terms of the general conservation equation

Equation	ϕ	Γ_ϕ		s_ϕ
		Laminar flow	Turbulent flow	
Mass (Eq. (13))	1	0	0	s^m
Momentum (Eq. (14))	u_i	μ	$\mu + \mu^t$	s_i^{mom} e.g. body forces, external forces
Energy (Eq. (16))	h	$\frac{\lambda}{c_p^d}$	$\frac{\lambda}{c_p^d} + \frac{\mu^t}{Pr_h^t}$	s^h

2 Physical phenomena of single-phase flow

For the discretization process the integral form of the general conservation equation is used, which can be achieved by integration of Eq. (35) over any volume Ω :

$$\int_{\Omega} \left(\frac{\partial}{\partial t} (\rho\phi) + \frac{\partial}{\partial x_j} (\rho u_j \phi - \Gamma_{\phi} \frac{\partial \phi}{\partial x_j}) \right) d\Omega = \int_{\Omega} s_{\phi} d\Omega. \quad (36)$$

By applying the *Gauss's divergence theorem* to convection and diffusion terms, the volume integral over the volume of CV can be replaced by a surface integral over the area enclosing the volume S . The general conservation equation in a form adapted for numerical treatment is:

$$\int_{\Omega} \left(\frac{\partial}{\partial t} (\rho\phi) \right) d\Omega + \int_S \left(\rho u_j \phi - \Gamma_{\phi} \frac{\partial \phi}{\partial x_j} \right) \cdot n_j dS = \int_{\Omega} s_{\phi} d\Omega. \quad (37)$$

Eq. (37) expresses the balance of each conserved variable ϕ , controlled by the volumetric accumulation terms (time dependent and source) and the fluxes (convective and diffusive) of the conserved properties through the corresponding faces.

The **finite volume method** is applied to all transport equations yielding in a set of algebraic expressions. The solution domain is subdivided into a finite number of small non-overlapping control volumes (CVs). This subdivision into a grid (mesh) is carried out using software tools provided by CFD software. The computational nodes, where the solution is stored, are defined in the center of the CV. Then the transport equation (Eq. (37)) is evaluated for each CV. The global balance is inherently fulfilled by simultaneously solving equations for all CVs. Algebraic equations for every CV are achieved from each conservation equation by approximation of surface and volume integrals.

- approximation of the surface integral

The net flux through the whole surface of CV, S is the sum of integrals over the faces of the CV:

$$\int_S f dS = \sum_{cf=1}^k \int_{S_{cf}} f dS, \quad (38)$$

with f the convective or diffusive component of the flux vector directed normal to the face of the CV, cf the index of the cell face and k the number of such faces.

The surface integral for each face of CV can be approximated in 2 levels (see [46]).

1. Approximation of the integral in terms of the variable values at one or more locations on the cell face: e.g. using the simplest second-order approximation, *midpoint rule* the surface integral can be replaced by the mean value of the integrand over the face multiplied by the cell face area. This mean value is approximated by the functional value in the center of the cell face.

2. Approximation of cell face values in terms of the values in the center of the CV (node): e.g. first-order **upwind difference scheme (UDS)**, using *forward* or *backward*-difference approximation, depending on the flow direction or **central difference scheme (CDS)** and assuming a linear profile between neighboring nodes. Both are described in detail in the paragraph “spatial discretization”.
- approximation of the volume integral

Using the simplest approximation of second-order, the volume integral can be replaced by the mean value of the integrand q , with approximated position in the center of the CV (node) multiplied by the volume of the CV:

$$\int_{\Omega} q d\Omega = \bar{q} \cdot \Omega \approx q_{node} \cdot \Omega . \quad (39)$$

Higher order approximations require values of q in more locations than only the center, which can be achieved by interpolation of the center values e.g. using upwind scheme or shape functions [46].

Spatial discretization:

The first step of the spatial discretization, the subdivision of the computed domain in a mesh of CV, was already presented. For illustrating the idea of the spatial discretization method, approximating the cell face values in terms of the values in the center of the CV (nodes), the example of the convective term discretization for the east cell face “e” of the Cartesian grid (see Figure 2.2) is chosen.

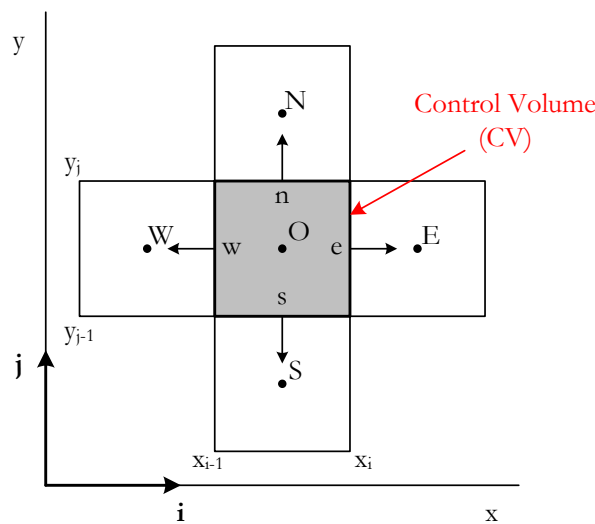


Figure 2.2 Typical slab, characterizing the CV for 2-D type-grid in Cartesian notation

The expression of the convective flux in terms of any conserved variable ϕ for compressible flow would be approximated at the cell face “e” as product of the mass flux through this cell face and the mean value of the variable ϕ at the cell face:

2 Physical phenomena of single-phase flow

$$\int_{S_e} (\rho u_j \phi) \cdot n_j dS \approx \dot{m}_e \cdot \phi_e, \quad (40)$$

with $\phi = 1$ for the continuity equation:

$$\dot{m}_e = \int_{S_e} (\rho u_j) \cdot n_j dS = -(\rho u)_e S_e, \quad (41)$$

with \dot{m}_e the mass flux through the cell face obtained by using the midpoint rule in the center of the cell face. If the velocity and fluid properties are constant over the cell face, Eq. (41) is exact on any grid.

Applying the first-order **upwind difference scheme (UDS)** for the spatial discretization, depending on the flow direction, *forward difference scheme (FDS)* or *backward difference scheme (BDS)* is used [46]. The conserved variable ϕ at cell face center “e” can be approximated with UDS in terms of neighboring nodes as:

$$\phi_e = \begin{cases} \phi_O, & \text{for } \dot{m}_e \geq 0 \quad - \text{BDS} \\ \phi_E, & \text{for } \dot{m}_e < 0 \quad - \text{FDS} \end{cases}. \quad (42)$$

This scheme was used in all performed calculations.

Another often used approximation method is the second-order **central difference scheme (CDS)**. It results in the linear interpolation between the nearest nodes:

$$\phi_e = (1 - f_e) \phi_O + f_e \phi_E, \quad (43)$$

with linear interpolation factor f_e , accounting for the distance between nodes and defined as:

$$f_e = \frac{x_e - x_O}{x_E - x_O}. \quad (44)$$

The gradient approximation needed for discretization of the diffusion flux applying CDS results in:

$$\left(\frac{\partial \phi}{\partial x} \right)_e = \frac{\phi_E - \phi_O}{x_E - x_O}. \quad (45)$$

Both methods reveal some disadvantages: UDS leads to numerical diffusion and CDS is not absolutely stable. Therefore various high-order schemes involving more nodes in the approximation process and countering stability problems were developed [46].

Temporal discretization:

Finite volume equations are applied over a discrete time step ∂t between two time levels n and $n+1$. For temporal discretization in the performed calculations a *fully implicit scheme* is used. The time dependent fluxes over this time step at the center of the CV (node) are obtained from the new time-level values of the variables at this node by solving an equation system:

$$\left(\frac{\partial(\rho\phi)}{\partial t}\right)_{node} = \frac{(\rho\phi)_{node}^{n+1} - (\rho\phi)_{node}^n}{\delta t} = f(\phi^{n+1})_{node}. \quad (46)$$

For steady state calculations relatively large time steps can be chosen for implicit methods.

The *explicit method* uses the old time-level values of the variables for the time dependent fluxes, no additional equation system is necessary:

$$\left(\frac{\partial(\rho\phi)}{\partial t}\right)_{node} = \frac{(\rho\phi)_{node}^{n+1} - (\rho\phi)_{node}^n}{\delta t} = f(\phi^n)_{node}. \quad (47)$$

For the explicit method the time step is limited by the *Courant criteria* (high variations can lead to numerical instabilities) [46].

Example:

In order to give a short and simple illustration for the numerical treatment of the transport equations, a heat conduction problem without flow, taking place in a quiescent single-phase fluid or in a solid will be considered. The heat conduction equation in Cartesian tensor notation is given by:

$$\underbrace{\rho \cdot c_p \frac{\partial T}{\partial t}}_{\text{Time dependent term}} = \underbrace{\frac{\partial}{\partial x_j} \left(\lambda \frac{\partial T}{\partial x_j} \right)}_{\text{Diffusion term}} + \underbrace{s^h}_{\text{Source term}}. \quad (48)$$

For steady state problems the heat conduction equation simplifies to:

$$-\frac{\partial}{\partial x_j} \left(\lambda \frac{\partial T}{\partial x_j} \right) = s^h. \quad (49)$$

The heat conduction equation in domain V in two- or three- space dimensions has to be complemented by boundary conditions. Here, it is assumed that the temperature is given on the boundary of V , *Dirichlet boundary condition*: $T = T_b$ on ∂V .

Integration over the control volume (CV) Ω and applying *Gauss's divergence theorem* to the diffusion term results in:

$$-\int_S \lambda \frac{\partial T}{\partial x_j} \cdot n_j dS = \int_{\Omega} s^h d\Omega. \quad (50)$$

The interpretation of the diffusion term yields the total heat flow \dot{Q} over the surrounding closed surface S of the CV:

$$\dot{Q} = -\int_S \lambda \frac{\partial T}{\partial x_j} \cdot n_j dS. \quad (51)$$

Assuming a two-dimensional grid (Figure 2.2), representing a slab of a thickness Δz and absence of heat fluxes in z direction, the whole heat conduction can be evaluated from the sum

2 Physical phenomena of single-phase flow

of the heat fluxes over each cell face of the CV (index cf represents the cell faces):

$$\dot{Q} = \sum_{\forall cf} \dot{Q}_{cf} = - \sum_{\forall cf} \int_{S_{cf}} \lambda \frac{\partial T}{\partial x_j} \cdot n_j dS. \quad (52)$$

Let us consider the heat transport from O to E through the east cell face “e”. Using the midpoint rule for approximation of the surface integral and a central difference scheme for the approximation of the gradient needed for the evaluation of the diffusive flux Eq. (52) becomes:

$$\dot{Q}_e = - \int_{S_e} \lambda \frac{\partial T}{\partial x_j} \cdot n_j dS \approx - \left(\lambda \frac{\partial T}{\partial x} n \right)_e \cdot S_e = - \lambda_e \frac{(T_E - T_O)}{d_e} \cdot S_e, \quad (53)$$

$$d_e = (x_E - x_O) \quad - \text{distance between center of the CV } O \text{ and the eastern cell } E, \text{ with } x \text{ coordinate of the cell center}, \quad (54)$$

$$\dot{Q}_e = -a_e (T_E - T_O) \quad - \text{with coefficient } a_e = \frac{\lambda_e \cdot S_e}{d_e} = f(\text{Material, Geometry}), \quad (55)$$

- with cell face area $S_e = (y_j - y_{j-1}) \cdot \Delta z$,

- with y coordinate of the cell face center.

Applying the same approximation to other CV faces the expression for the whole heat flow, Eq. (52), becomes:

$$\dot{Q} = -a_e (T_E - T_O) - a_n (T_N - T_O) + a_w (T_W - T_O) + a_s (T_S - T_O). \quad (56)$$

Assuming the whole heat flux evaluated for the CV with center node O the algebraic equation in terms of central and neighboring nodes can be achieved:

$$\dot{Q} = T_O \sum_{\forall nbn} a_{nbn} - \sum_{\forall nbn} a_{nbn} T_{nbn}, \quad (57)$$

where index nbn represents the neighboring nodes to CV node O .

In case of varying properties and cell sizes, an equivalent ratio of cell distance d and thermal conductivity λ_{eq} can be derived from the following expression by harmonic averaging:

$$\left(\frac{d}{\lambda_{eq}} \right)_e = \frac{x_e - x_O}{\lambda_O} + \frac{x_E - x_e}{\lambda_E}. \quad (58)$$

The source term also has to be discretised. Due to Eq. (39), the volume integral of the source term will be approximated as:

$$\int_{\Omega} s^h d\Omega = s_O^h \cdot \Omega. \quad (59)$$

It has to be pointed out that for the cells adjacent to the boundaries of the computational domain an additional discretization may be needed to apply the boundary conditions. For the simple case of the defined boundary temperature, the known temperature at the boundary cell face is substituted for T_{nbn} on the left hand side of Eq. (60) and this known term is brought to the right hand side of the equation.

By the described discretization of the heat conduction equation, an algebraic equation:

$$T_O \sum_{\forall nbn} a_{nbn} - \sum_{\forall nbn} a_{nbn} T_{nbn} = s_O^h \cdot \Omega, \quad (60)$$

is obtained for each CV of the computation domain. The resulting system of algebraic equations can be arranged in a matrix structure: $\mathbf{A} = \{a_{ij}\}$ consisting of the coefficients a_{nbn} and $\sum_{\forall nbn} a_{nbn}$, on the main diagonal, $\bar{\Phi} = \{T_i\}$ denotes the vector of the neighboring temperatures at the cell centers and \bar{S} contains known terms and boundary conditions. For a structured mesh this will result in a matrix with a band structure.

In the same way the whole system of coupled algebraic equations for all conserved variables corresponding to the CV over the whole solution domain can be expressed in compact form by:

$$\mathbf{A}\bar{\Phi} = \bar{S}, \quad (61)$$

with $\bar{\Phi}$ being a vector of unknown variables, \mathbf{A} being the coefficient matrix (which depends on $\bar{\Phi}$ for non-linear problems) and \bar{S} being the vector of source terms.

2.4.3 Initial and boundary conditions

To complete the set of algebraic equations previously obtained the initial and boundary conditions have to be implemented. Initial conditions are values of variables at the starting time $t = t_0$ and the boundary conditions specifying the values of the variables at the flow boundaries for $t \geq t_0$.

In the performed calculations the solution domain is bounded by following boundary types:

- Inlet On the inlet plane the distributions of all dependent variables and coefficients have to be defined (e.g. velocity vector or temperature).
- Outlet This boundary condition type (specific for STAR-CD) is equivalent to a pressure boundary at the outlet but suppresses reverse flow. This may introduce non-physical results in case of reverse flow, but the results are correct, if the final solution shows only outward directed flow.
- Wall boundary It is specified that all velocity components are zero at an impermeable wall at rest (No Slip):

$$u_i = u_w = 0. \quad (62)$$

For scalar variables ϕ (e.g. temperature) two main types of conditions are classified:

- Dirichlet conditions - the value of the variable is specified a priori along the boundary:

$$\phi_w = \phi_{given}; \quad (63)$$

2 Physical phenomena of single-phase flow

- *Neumann conditions* - the flux of the variable through the boundary surface is given:

$$\dot{q}_{\phi, w} = \dot{q}_{\phi, given} . \quad (64)$$

(For a unique solution, besides the *Neumann* conditions, at least on one point on the boundary a *Dirichlet* condition has to be given.) The variable ϕ can be determined implicitly from the given flux.

Standard settings for the wall roughness ($E = 9.0$, smooth wall) are set on the surfaces of the rods.

For laminar layers the velocity distribution is linearly approximated between the velocity value at the wall and the cell center next to the wall.

The wall treatment of the turbulent layer, already presented in Chapter 1.3, depends on the type of the sublayer:

- *Laminar (viscous) sublayer* - same linear treatment as for laminar layer (Eq. (34)),
- *Turbulent sublayer* - logarithmic wall law region (Eq. (33)).
- *Symmetry plane* By definition no fluid can go through the *symmetry plane*. Hence the component of velocity normal to the *symmetry plane* is equal zero:

$$u_i n_i = 0 , \quad (65)$$

implying zero scalar fluxes through the *symmetry plane*. In addition, the gradient of all dependent variables ϕ normal to the *symmetry plane* area is equal to zero:

$$\frac{\partial \phi}{\partial x_i} n_i = 0 . \quad (66)$$

For symmetrical flows the application of *symmetry planes* allows a reduced size of the solution domain. In the sub-channel application for the swirl flow the *symmetry plane* is set at the gaps between the rods (Figure 5.2).

- *Cyclic boundary* This type of boundary refers to a pair of mesh surfaces of identical size and shape, at which the flow repeats periodically. Such boundary condition allows reducing the size of the solution domain considerably. For instance for modeling the sub-channel under swirl conditions, it is sufficient to model a quarter of the sub-channel. Geometrically this element is symmetrical, but the symmetry is broken by the rotational symmetrical inlet conditions.

The cyclic conditions are applied to the planes intersecting in the center of the sub-channel having the same area for the solution domain (Figure 5.2). The incorporation of the boundary conditions (cyclic behavior of velocity and mass flux) for the sub-channel

quarter requires the introduction of virtual cells adjacent to the planes with applied cyclic boundaries. The values of the velocity vector components and the mass fluxes are equated respectively at the virtual nodes of the cells.

2.4.4 Solution method

After initial and boundary conditions are applied and fluid properties are defined, the whole system of algebraic equations has to be solved. It can be done iteratively e.g. with the SIMPLE-algorithm, which was used for all performed calculations and is described in detail in [46]. The idea of this algorithm is presented for the solution of the algebraic finite-volume coupled pressure and momentum equations resulting from discretization of the governing equations. In the single-phase calculation without heating there are three momentum equations and the continuity equation, this means four equations and four variables, so that the set of equations can be solved. The solution procedure is not straight forward because the three momentum equations contain the velocities and pressure as dependent variables and the continuity equation contains only the set of velocities. If the pressure field is known, the velocities can be solved from the momentum equations. Based on this idea *Spalding* in 1976 developed the SIMPLE-algorithm for the solution of the coupled equations of pressure and velocities [140].

The idea of this algorithm is to

1. Guess the pressure field p .
2. Solve the momentum equations using this field, thus obtaining velocities that satisfy momentum, but not necessarily continuity.
3. Evaluate continuity errors (residuals) for each cell.
4. Solve a pressure-correction equation to reduce the mass residuals. The coefficients are $\frac{du_i}{dp}$ and the sources are the continuity errors.
5. Adjust the pressure to obtain linearized velocity corrections that satisfy continuity residuals, but not necessary momentum (Similar to the *method of Newton-Raphson* [105]).
6. Go back to step 2, and repeat the iteration with the new pressure field. Repeat until continuity and momentum errors are acceptably small.

The advantage of this method is that the coefficient matrix of the pressure correction equation is the same as for the pressure equation.

3. Physical phenomena of two-phase flow

3.1 Definition

Multi-phase flows are very widespread in natural environment and two-phase flows are the simplest and the most common type of such flows. The examples for two-phase flow can be found not only in nature e.g. rainy or snowy wind, but also in different fields of the industry e.g. nuclear or chemical engineering or just in our everyday life e.g. boiling water or drinking champagne. The first systematic study related to fluid dynamic problems of two-phase flow was published in 1958 by *Teletov* [146], followed by *Mamaev et al.* [103] and *Wallis* [162], which concentrated on steady state flow in pipes. From that time more scientists chose this field of work, recognizing its importance for today's and tomorrow's human development [78].

Multi-phase flows consist of one or more continuous phases, which may be gaseous or liquid, and one (in case of two-phase flow) or more dispersed phases in the form of gas bubbles, liquid droplets or solid particles (in this thesis the dispersed phase always has the form of gas bubbles). The motion of both phases is influenced by each other through phase interaction and inter-phase effects such as inter-phase mass, heat and energy transfer. The strength of such interactions depends on various factors e.g. the dispersed particle's size, density, number, velocity and the temperature difference between phases.

In laminar flow the motion is deterministic i.e. each element released from a point is following a smooth unique trajectory. In the case of turbulent carrier flow, individually introduced elements have their own, random path due to their interaction with the fluctuating turbulent velocity field and may interact with each other (i.e. collision, coalescence and break up).

In water-steam systems, mass transfer occurs between the phases and induces an inter-phase heat transfer, which may also arise due to the inter-phase temperature differences. As a consequence the dispersed particles are changing their size. Thus, even if the initial size distribution is uniform (mono-dispersed), these effects will produce a variable-sized (poly-dispersed) population.

Changing the particle size can also be caused by fluid-dynamic forces acting on it i.e. a particle break up into smaller elements. On the other hand, the opposite effect can be achieved through

inter-element collision processes i.e. a size increase due to coalescence or agglomeration. In addition, if dispersed elements strike the wall, phenomena such as bouncing or shattering can occur, depending on the impact conditions [135], [136] and [138].

In CFD codes two methods of numerical treatment of two-phase flows are possible:

- **Homogenous two-phase model:** The velocities of both phases are described with only one velocity field (one set of equations is solved). This model allows a proper modeling of e.g. free-surface flows with phases separated by a well-defined interface, as done in the *Volume of fluid (VOF)* method.
- **Two-velocity field modeling:** This is a more general method because the phases are treated with separate velocity and enthalpy fields (two sets of equations are solved).

In the numerical modeling of two-phase flows two main possibilities of modeling the two-velocity fields approach are applied in the CFD codes [70]:

- **Euler-Lagrange Method:** In dispersed flows, single bubbles or particles can be tracked by using detailed physical phenomena for the interaction between dispersed phase and continuous phase. If the number of particles/bubbles is small and the feedback to the continuous phase is negligible, the computation time is small. But for a high number of particles distributed over the whole computational domain with feedback to the continuous phase, the computing time increases significantly, especially for stochastic particle tracking.
- **Euler-Euler Method:** A more general formulation is used by this technique. Here the interactions between both phases are volume averaged for all interactions within a control volume. This technique fits very well in the finite volume method since volume-averaged equations are considered here, too. This numerical method depends only on the number of control volumes and the computational effort is almost independent of the number of particles/bubbles.

For boiling problems the *Euler-Euler* method is normally the preferred one and is chosen for the presented two-phase CFD simulations carried out in terms of this work.

The following sections present two-phase flow modeling with the *Euler-Euler* technique, used in the performed calculations with STAR-CD, based on the code's methodology [136], lecture notes of Lo [98] and the publication of *Ustinenko* [161] with added details for each used formulation from other literature sources. The numerical treatment: grid generation, discretization and solution algorithm is essentially the same as already described in the previous chapter for single-phase flow and therefore it would not be described here.

3.2 Governing equations

The conservation equations for two-phase flow are solved for each phase, leading to two equations of mass conservation, six equations of momentum conservation and two energy equations. In those equations the part of the flow domain occupied by each phase is given by its volume fraction α , defined for the continuous c and dispersed phase d as:

$$\alpha_c = \frac{V_c}{V_d + V_c} \text{ and } \alpha_d = \frac{V_d}{V_d + V_c}, \text{ respectively.} \quad (67)$$

Each phase has its own velocity, temperature and physical properties. The pressure in a control volume is assumed to be the same for each phase, which is a good approximation as long as surface tension related phenomena have a minor impact on the flow.

Table 3.1 presents these equations in a differential coordinate-free form, written in generic form of phase k^1 ($k = c$ for continuous phase and $k = d$ for dispersed phase).

Table 3.1 Conservation equations for Eulerian two-phase model for turbulent flow

Continuity	$\frac{\partial}{\partial t}(\alpha_k \rho_k) + \nabla \cdot (\alpha_k \rho_k \vec{u}_k) = S_k^m$	(68)
Momentum	$\frac{\partial}{\partial t}(\alpha_k \rho_k \vec{u}_k) + \nabla \cdot (\alpha_k \rho_k \vec{u}_k \vec{u}_k) - \nabla \cdot [\alpha_k (\tau_k^l + \tau_k^t)] = -\alpha_k \nabla p + \alpha_k \rho_k \vec{g} + \vec{M}_k$	(69)
Energy	$\frac{\partial}{\partial t}(\alpha_k \rho_k h_k) + \nabla \cdot (\alpha_k \rho_k \vec{u}_k h_k) - \nabla \cdot \left(\alpha_k \lambda_k \nabla T_k + \frac{\mu_k^t}{Pr_h^t} \nabla h_k \right) = -\alpha_k \frac{Dp}{Dt} + \alpha_k (\tau_k^l + \tau_k^t) : \nabla \vec{u}_k + S_k^h$	(70)
Volume Fraction (additional equation)	$\sum_{k=c}^d \alpha_k = 1$	(71)

The two-phase model based on these conservation equations requires constitutive equations to achieve the closure, which are presented next.

3.3 Inter-phase momentum transfer

The inter-phase transfer of the momentum \vec{M}_k indicates the rate of the momentum transfer between phases per unit volume at the interface, which is expressed as a superposition of the terms representing different physical mechanisms (interfacial forces) and satisfies Newton's third law:

$$\vec{M}_d = -\vec{M}_c \quad (72)$$

¹ The *Einstein* summation convention is not applied for phase subscript k .

Interfacial forces included in STAR-CD are presented in the following Eq. (73) from left to right: drag, turbulent drag, lift, virtual mass, wall lubrication and momentum source associated with momentum transfer due to interfacial mass transfer (bulk boiling/condensation and wall boiling), respectively.

$$\vec{M}_k = \vec{F}_k^D + \vec{F}_k^T + \vec{F}_k^L + \vec{F}_k^{VM} + \vec{F}_k^W + \vec{S}_k^{mom} \quad (73)$$

In the following sub-sections these forces are described in detail.

3.3.1 Drag force

The drag force represents the viscous effects slowing down or accelerating a particle of the dispersed phase (gas bubble, liquid droplet or solid particle) in the fluid. The mean drag force acting on a single particle, \vec{D}_d , is modeled due to *Ishii and Mishima* [71] as:

$$\vec{D}_d = \frac{1}{2} C_D \rho_c |\vec{u}_r| \vec{u}_r \cdot A_d, \quad (74)$$

where C_D is the drag coefficient taking into account the character of the flow around the particle, $\vec{u}_r = (\vec{u}_c - \vec{u}_d)$ is the relative velocity between the two phases and A_d is the projected area of the particle in the direction of the flow.

Assuming that the particle has a spherical form with diameter d , its projected area results in:

$$A_d = \frac{\pi d^2}{4}. \quad (75)$$

In multi-particle systems the number of particles per unit volume n_d can be obtained as:

$$n_d = \frac{\alpha_d}{V_d} = \frac{6\alpha_d}{\pi d^3}, \quad (76)$$

with the volume of a spherical particle $V_d = (\pi d^3)/6$.

Hence the total drag force per unit volume \vec{F}_d^D , defined as the product of the force acting on a single particle and the number of the particles per unit volume, results in:

$$\vec{F}_d^D = n_d \vec{D}_d = \frac{3}{4} C_D \frac{\alpha_d \rho_c}{d} |\vec{u}_r| \cdot \vec{u}_r. \quad (77)$$

Experimental observations show that the drag force is influenced by many factors: particle Re-number, based on the absolute value of the slip velocity; particle size, type of the particle, impurities of dispersed and continuous phase, particle deformation and concentration and others. That is why drag forces and drag coefficients are very context dependent. An overview of formulations later needed for numerical simulations is presented below.

3 Physical phenomena of two-phase flow

For regions of high particle concentration a modified *Stokes' Law* is applied ([20], [133] and [170]):

$$\bar{F}_d^D = \frac{3}{4} C_D \frac{\alpha_d \rho_c |\vec{u}_r|}{d_b} \vec{u}_r \cdot (\alpha_c)^a \quad (78)$$

- *bubble particle*: $a = 4$ is used to model the bubble swarm rising effect, according to *Mersmann* [107]. It was observed that swarm bubbles tend to rise slightly faster than isolated bubbles; the apparent drag is therefore smaller.

Drag coefficient for general spherical particles:

For estimation of the drag force by Eqs. (77) and (78) the drag coefficient is needed. The following approach is generally suitable for spherical solid particles, liquid droplets and small-diameter bubbles [136]. The drag coefficient is achieved in terms of the particle *Reynolds* number Re_d , defined as:

$$Re_d = \frac{\rho_c |\vec{u}_r| d_b}{\mu_c} \quad (79)$$

Dependent on the value of Re_d different formulations for the drag coefficient have to be used:

- For low particle Re-number the force on a single particle depends linearly on the velocity difference (*Stokes' law regime* [143]).

$$C_D = \frac{24}{Re_d} \quad Re_d \rightarrow 0 \quad (80)$$

- For the *viscous regime* (the force depends non-linearly on the velocity difference) one of the most popular correlations for the drag on a rigid sphere in a steady motion is the *Schiller and Naumann* correlation [139]. According to *Clift et al.* [27] this correlation has an uncertainty of $\pm 4\%$.

$$C_D = \frac{24}{Re_d} (1 + 0.15 Re_d^{0.687}) \quad 0 < Re_d \leq 1000 \quad (81)$$

- For *Newton's law regime* Newton proposed the law equivalent to $C_D = 0.5$. On the other hand *Clift et al.* [27] pointed out that values of C_D vary by $\pm 13\%$ about the constant value $C_D = 0.445$. The constant value applied in STAR-CD can be found in Table 3.3.

$$C_D = const \quad Re_d > 1000 \quad (82)$$

For bubbly flow special correlations for obtaining the drag coefficient can be found in literature. The correlations vary depending on the quality of the liquid. In STAR-CD a correlation for the C_D of pure water is implemented. Other correlations for bubbly flow e.g. in slightly or highly contaminated water can be found in *Tomiyama et al.* [152], [153] and *Grace et al.* [52].

Drag coefficient for bubbles in pure water:

This correlation is based on the empirical correlation of *Wang* [163], derived by fitting measurements taken for a single bubble rising in pure water and may be used to obtain more realistic values for the bubble drag coefficient, accounting its possible deformation and departing from the spherical shape:

$$C_D = \exp[a + b \ln Re_d + c(\ln Re_d)^2], \quad (83)$$

where the coefficients a , b and c are presented in Table 3.2.

Table 3.2 Drag coefficients for single rising bubble in water [136]

Re_d	a	b	c
$Re_d \leq 1$	$\ln 24$	-1	0
$1 < Re_d \leq 450$	2.699467	-0.33581596	-0.07135617
$450 < Re_d \leq 4000$	-51.77171	13.1670725	-0.8235592
$Re_d > 4000$	$\ln(8/3)$	0	0

Clift et al. [27] and *Kolev* [79] give a detailed overview of many other existing correlations for drag force and drag force coefficients for various Re-numbers, types of particles and their form. They can be implemented in STAR-CD by means of user subroutines if needed.

Drag formulation in STAR-CD:

Drag formulations proposed by STAR-CD are noted by the drag parameter $C_{D,par}^{STAR}$ or can be defined in a user subroutine (drag.f). The models used in this work are summarized in Table 3.3.

Table 3.3 Drag formulation in STAR-CD

Drag parameter $C_{D,par}^{STAR}$	Drag force	Drag coefficient	Included formulations
1	Eq. (77)	user-specified constant value, with default $C_D^{STAR} = 0.44$	
2	Eq. (77)	Eq. (83)	
3	Eq. (77)	Eqs. (81) and (82)	
$C_{D,par}^{STAR} = 3$ user subroutine (drag.f)	i.e. high bubble loading Eq. (78) $a = 4$	Eqs. (80) and (83)	Variable diameter Eq. (122) [86] (optionally)

3.3.2 Turbulent drag (dispersion) force

Gosman and Ioannides [57] presented an averaged form of the interface momentum transfer term \vec{M}_k . It includes an additional drag term \vec{F}_d^T , based on the standard drag force modeled by

3 Physical phenomena of two-phase flow

Eq. (77) and accounts for fluctuations due to interaction between the dispersed phase and the surrounding turbulent eddies. This term was called turbulent drag or turbulent dispersion term and has the following form in STAR-CD:

$$\vec{F}_d^T = - \underbrace{\frac{3 C_D \alpha_d \rho_c |\vec{u}_r| \vec{u}_r}{4 d_b}}_{\text{drag force}} \cdot \frac{\mu_c^t}{\rho_c \alpha_d \alpha_c \text{Pr}_\alpha^t} \cdot \nabla \alpha_d, \quad (84)$$

where μ_c^t is the continuous phase turbulent viscosity and Pr_α^t is the turbulent *Prandtl* number for volume fraction, both described in Sub-section 3.4.1.

3.3.3 Lift force

In non-uniform continuous-phase flow a lift force is acting on the particles perpendicular to the rotation and relative velocity vector. The classical lift force was formulated for transverse migration of spherical bubbles in steady flow, due to the shear lift by *Žun* [174], *Drew* [38] and *Auton* [10] in terms of the cross product of the vorticity of the continuous phase and the slip velocity between phases. This formulation for lift force per unit volume results in:

$$\vec{F}_d^L = C_L \alpha_d \rho_c [\vec{u}_r \times (\nabla \times \vec{u}_c)], \quad (85)$$

where C_L is the lift coefficient, accounting for the net circulation of the liquid around an ellipsoidal bubble. For the flow around a single sphere *Drew* [38] and *Auton et al.* [11] derived analytically $C_L = 0.5$, using a simple shear model. Since the calculation was based on a weakly sheared inviscid flow (particle having an infinite *Reynolds* number), wake effects were not taken into account. For viscous flow the lift coefficient for a single bubble becomes smaller.

At this point it should be mentioned that, due to a large number of influencing factors, there is no model till now, which is able to describe in general the lateral motion of the bubbles accurately enough. This has its origin in the complex interaction of the various lateral forces. Various values for the lift coefficient C_L in Eq. (85) were used in computer code implementations of the two-fluid model as a fitting coefficient and a short overview of used values is presented next.

Žun [174] reported for small single air bubbles suspended in a tap water stream in a square duct a lift coefficient $C_L = 0.3$. *Lopez de Bertodano et al.* [102] recommended values between $C_L = 0.02$ and $C_L = 0.1$ to match different sets of experimental data for bubbly flows in vertical ducts. *Lahey et al.* [88] summarized several studies of bubbly flow done by RPI and ECL and found $C_L = 0.1$ and $C_L = 0.25$ for small bubbles (*Hill et al.* ([59], [60])). *Wang et al.* [164] correlated the lift coefficient C_L with a number of experiments for fully developed air-water circular flows in terms of local flow parameters e.g. volume fraction, bubble *Reynolds* number

and achieved values in the range of $C_L = 0.01$ and $C_L = 0.1$.

Later, *Moraga et al.* [111] and *Rusche* [123] pointed out that the lift coefficient has to become negative to fit some experimental data e.g. fully developed bubbly flow in a vertical pipe with sudden expansion [17] or some injection conditions by modeling of developing flow in a vertical pipe [56]. Hence it can be seen, that the optimum value of the lift coefficient may change drastically from one flow condition to the other.

On the one hand, the lift force in co-current bubbly flows is found to act perpendicular to the main flow in the direction to the lower liquid velocity, i.e. to the wall for the undeformed bubbles in a pipe flow [83]. On the other hand, if the bubbles are distorted, they may experience a lift force acting oppositely, towards higher liquid velocities, i.e. for the pipe flow - to the center of the pipe.

Various experiments for water-air flow in vertical tubes prove this effect e.g. [83]. At atmospheric pressure and room temperature the direction change takes place at a bubble diameter of about 5 - 6 mm (*Liu* [95] and [96]). The change of the sign of the lift force is supposed to be related to the increased deformation of the bubbles (the distorting effect in a shear flow), growing with the bubble size [124].

Due to aforementioned considerations a more complex correlation for the lift force, depending on the bubble diameter, proposed by *Tomiya et al.* [151] was applied with small modifications by *Ohnuki* and *Akimoto* for flow in a large vertical pipe [115]. According to this correlation, lift force is defined in terms of *Reynolds* Re_d and *Eötvös* $Eö_d$ numbers of particle and the lift coefficient C_L is defined as a sum of shear-induced C_{LF} and wake-induced C_{WK} lift coefficients:

$$C_L = C_{LF} + C_{WK}, \quad (86)$$

where the shear-induced lift coefficient is found to be a function of the *Reynolds* number:

$$C_{LF} = 0.288 \cdot \tanh(0.121 \cdot Re_d) \quad (87)$$

and the wake-induced lift coefficient depends on the *Eötvös* number:

$$C_{WK} = \begin{cases} 0, & Eö_d < 4; \\ -0.096Eö_d + 0.384, & 4 < Eö_d < 10; \\ -0.576, & Eö_d > 10; \end{cases} \quad (88)$$

with the particle *Eötvös* number, defined by using the bubble diameter as the characteristic length:

$$Eö_d = \frac{g_o(\rho_c - \rho_d)d_b^2}{\sigma}, \text{ where } \sigma \text{ is the surface tension.} \quad (89)$$

3 Physical phenomena of two-phase flow

In STAR-CD the standard lift force is defined by Eq. (85) with lift coefficient, which can be defined by the user and is set to $C_L^{STAR} = 0.25$ by default (only positive values are allowed in the graphical user interface) or can be defined in user subroutine e.g. according to Eq. (86).

3.3.4 Virtual mass force

The virtual mass force accounts for the additional resistance experienced by a bubble undergoing acceleration and is expressed by *Drew* [39] and *Drew and Lahey* [40] for a general case as:

$$\bar{F}_d^{VM} = C_{VM} \alpha_d \rho_c \left(\frac{D^c \bar{u}_c}{Dt} - \frac{D^d \bar{u}_d}{Dt} \right), \quad (90)$$

where D^k / Dt is the material derivative for phase k and C_{VM} is the virtual mass coefficient.

For a nearly inviscid quiescent fluid around an isolated sphere this force is equal to one half of the mass of the fluid displaced by the particle, times the acceleration of the center of the mass of the sphere, which means $C_{VM} = 0.5$.

In general, the value of C_{VM} is dependent on the shape and the particle concentration. *Houghton's* data [63] as mentioned in [40] give values in the range from $C_{VM} = 0.1$ to $C_{VM} = 0.5$ for various particles in accelerating flows. If the hydrodynamic interaction between the particles is significant then C_{VM} becomes a function of α_d [39].

In STAR-CD C_{VM} can be defined by the user and is set to $C_{VM}^{STAR} = 0.5$ by default.

3.3.5 Wall lubrication force

The flow field around a particle is modified in the vicinity of a wall. This gives rise to a viscous lubrication force, which tends to push the particles away from the wall. Assuming bubbles have a spherical form, this force was modeled by *Antal et al.* [9] for low void laminar flow as:

$$\bar{F}_d^W = -\frac{\alpha_d \rho_c \bar{u}_r^2}{d_b} \max \left[C_{w1} + C_{w2} \frac{d_b}{y_w}, 0 \right] \bar{n}_w, \quad (91)$$

where y_w is the distance to the nearest wall and n_w is the unit normal pointing away from the wall.

Often used values of the coefficients are $C_{w1} = -0.01$ and $C_{w2} = 0.05$ for a sphere. This means the force only exists in a region less than 5 bubble diameters from the wall [68]. *Antal et al.* [9] proposed the following coefficients: $C_{w1} = 2(-0.104 + 0.06 \bar{u}_r)$ and $C_{w2} = 0.147$.

Tomiyama et al. [151] proposed the wall coefficient to be a function of the *Eötvös* number to apply the formulation above to spherical and distorted bubbles.

The wall lubrication force is not a standard implementation in STAR-CD, but it can be supplied via user subroutines. For validation cases presented in Chapter 4.1 and carried out by CD-adapco the following coefficients were used: $C_{w1}^{STAR} = -0.06$ and $C_{w2}^{STAR} = 0.147$. In the validations carried out in this work (Chapters 4.2 and 4.3) the above mentioned set of coefficients for a sphere from [68] is applied: $C_{w1}^{STAR} = -0.01$ and $C_{w2}^{STAR} = 0.05$.

Despite the large efforts on modeling lateral forces, the prediction of the radial void fraction distribution for pipe flow is still a challenge due to many coupled effects of various phenomena, such as shear, wake phenomena and deformation on the lift force as well as the turbulence of the continuous phase and wall lubrication force.

3.4 Turbulence

3.4.1 Turbulence equations

The idea of turbulence modeling in general and the *High Reynolds number k-ε turbulence model* in detail has been already presented in Chapter 2.3 for single-phase application. The additional formulations needed for two-phase turbulence-modeling are presented in this chapter.

Flow turbulence in both phases is also based on the *High Reynolds number k-ε model* [91], resulting in additional transport equations for k and ε . These equations are modified for multiphase application and solved for the continuous phase. The turbulence of the dispersed phase is correlated using semi-empirical models. The modification of the equations is done by additional terms, which incorporate the effects of the dispersed phase on the turbulence field.

In Table 3.4 the modified k - ε equations solved for the continuous phase are presented using the turbulence production term $G = \mu_c [\nabla \bar{u}_c + (\nabla \bar{u}_c)^T] : \nabla \bar{u}_c$.

Table 3.4 Modified two-phase flow k - ε turbulence model

Kinetic energy of turbulence, k	$\frac{\partial}{\partial t} \alpha_c \rho_c k_c + \nabla(\alpha_c \rho_c \bar{u}_c k_c) = \nabla \left(\frac{\alpha_c (\mu_c + \mu_c^t)}{\text{Pr}_k^t} \nabla k_c \right) + \alpha_c (G - \rho_c \varepsilon_c) + S_{k2}$	(92)
Dissipation rate of turbulence, ε	$\frac{\partial}{\partial t} \alpha_c \rho_c \varepsilon_c + \nabla(\alpha_c \rho_c \bar{u}_c \varepsilon_c) = \nabla \left(\frac{\alpha_c (\mu_c + \mu_c^t)}{\text{Pr}_\varepsilon^t} \nabla \varepsilon_c \right) + \alpha_c (C_{\varepsilon 1} G - C_{\varepsilon 2} \rho_c \varepsilon_c) + S_{\varepsilon 2}$	(93)

The additional source terms, representing two-phase interactions for k and ε equations are:

$$S_{k2} = -A_D^* \underbrace{\frac{\mu_c^t}{\rho_c \alpha_c \alpha_d \text{Pr}_\alpha^t}}_{\text{turbulent drag force}} \bar{u}_r \cdot \nabla \alpha_d + 2A_D^* (C_t - 1) k_c \quad (94)$$

3 Physical phenomena of two-phase flow

and

$$S_{\varepsilon_2} = 2A_D^*(C_t - 1)\varepsilon_c, \text{ respectively,} \quad (95)$$

$$\text{with } A_D^* = \frac{3}{4} \frac{\alpha_d \rho_c C_D}{d_b} |\bar{u}_r|. \quad (96)$$

The relation of the dispersed phase turbulence to that of the continuous phase is presented through a turbulence response coefficient C_t , which is defined as the ratio of the r.m.s. of the dispersed phase velocity fluctuations to those of the continuous phase:

$$C_t = \frac{u'_d}{u'_c}. \quad (97)$$

The turbulent stress τ_k^t used in momentum and energy equations (Eqs. (69) and (70)) is modeled for the continuous phase in the same way as for single-phase flow (Eq. (21)) using turbulent viscosity (defined in Eq. (25)), resulting for the continuous phase in:

$$\mu_c^t = C_\mu \rho_c \frac{k_c^2}{\varepsilon_c}. \quad (98)$$

The dispersed-phase turbulent viscosity μ_d^t is correlated to the continuous-phase turbulent viscosity μ_c^t via the response coefficient C_t , such that

$$\mu_d^t = \frac{\rho_d}{\rho_c} C_t^2 \mu_c^t. \quad (99)$$

Eq. (99) is obtained, taking into account the kinetic energy of turbulence for the dispersed phase, correlated to the continuous phase according to the definition of k in Eq. (26) and C_t in Eq. (97) as:

$$k_d = C_t^2 k_c. \quad (100)$$

It results in the following correlation for the dispersed turbulent stress:

$$\tau_d^t = \frac{\rho_d}{\rho_c} C_t^2 \tau_c^t. \quad (101)$$

Most coefficients used in STAR-CD for single-phase flow can be used in two-phase turbulence modeling. The turbulent *Prandtl* number for volume fraction is set to unity $\text{Pr}_\alpha^{t,STAR} = 1$.

The modeling of the wall stress boundary condition assumes homogeneous wall contact. Standard wall functions already described for single-phase flow are applied within each phase and the wall contact area is assumed to be proportional to the local volume fraction [137].

3.4.2 Response coefficient C_t

For obtaining the additional terms in the k - ε transport equations, solved for the continuous phase due to turbulence of the disperse phase, the response coefficient C_t has to be evaluated.

Rusche [124] reported that the results of measurements of *Larue de Tournemme* [90] and *Garnier et al.* [49] showed that C_t for turbulent gas-liquid flows with both high and low void fractions is strongly dependent on the void fraction only below the limit value of the void fraction of circa 6 %. For the void fraction over this limit both phases fluctuate in unison and the response coefficient C_t has a constant value of one. Based on [90], the correlation for C_t as a function of void fraction was proposed by *Rusche* [123], which yields to:

$$C_t(\alpha_d) = 1 + (C_t^* - 1) \exp(-f(\alpha_d)), \quad (102)$$

with function $f(\alpha_d)$ defined as:

$$f(\alpha_d) = 1.80 \cdot 10^2 \alpha_d - 4.71 \cdot 10^3 \alpha_d^2 + 4.26 \cdot 10^4 \alpha_d^3, \quad (103)$$

where C_t^* is the value of C_t with $\alpha_d \rightarrow 0$. According to the model proposed by *Issa* [72] with validations performed by *Hill* and co-workers in [59] and [60], it can be obtained as:

$$C_t^* = \frac{3 + \beta}{1 + \beta + 2\rho_d / \rho_c}, \text{ where coefficient } \beta \text{ is defined as:} \quad (104)$$

$$\beta = \frac{2A_D l_e^2}{\alpha_d \mu_c \text{Re}^t}, \quad (105)$$

with Re^t denoting the turbulent *Reynolds* number based on the eddy length scale l_{ch}^t , also called characteristic turbulent length, and the r.m.s. of velocity fluctuations of the continuous phase u'_c , defined as:

$$\text{Re}^t = \frac{\rho_c u'_c l_{ch}^t}{\mu_c}, \quad (106)$$

where l_{ch}^t and u'_c of the continuous phase can be obtained in terms of k and ε as:

$$l_{ch}^t = C_\mu \frac{k_c^{3/2}}{\varepsilon_c} \text{ and} \quad (107)$$

$$u'_c = \sqrt{\frac{2}{3} k_c}. \quad (108)$$

In STAR-CD the used formulation of the response coefficient C_t is chosen by the turbulence parameter $C_{t,par}^{STAR}$, using values of 1 or 2:

- $C_{t,par}^{STAR} = 1$ no dependency on void fraction, $C_t = 1$,
- $C_{t,par}^{STAR} = 2$ dependent on void fraction, using Eq. (102).

3.5 Heat and mass transfer

3.5.1 Flow and heat transfer regimes

The model for heat and mass transfer presented here was first developed for sub-cooled boiling applications. Figure 3.1 presents a simplified sketch of the main flow and heat transfer regimes with axial temperatures and radial void profiles for the flow boiling in a vertical channel, showing the *dry out* phenomena at CHF conditions (dry out of the water film on the cladding surface, resulting in a steep increase of the wall temperature due to decreased heat transfer), which will be introduced in detail in Section 4.3.1.

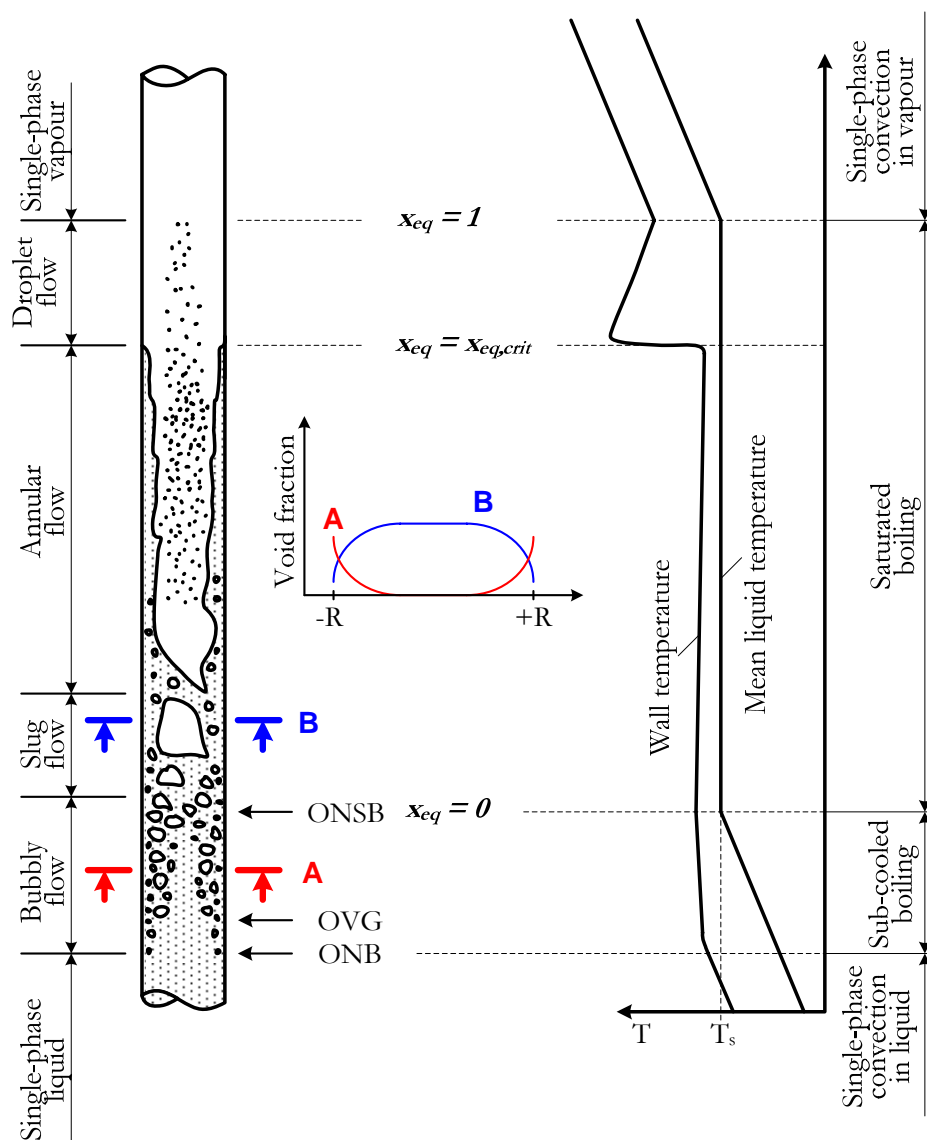


Figure 3.1 Flow and heat transfer regimes, axial temperatures and void profiles during flow boiling in a vertical pipe or channel

In a vertical channel with uniformly heated walls and sub-cooled liquid at the entrance, the heat is transferred to the sub-cooled liquid in terms of single-phase forced convection. This mechanism takes place as long as the wall superheat is less than the required one for the

nucleation of bubbles on cavities present on the wall surface. Such wall superheat is dependent on the size of the cavity and on the flow conditions.

If the wall superheat is high enough, then bubbles are formed, though the bulk liquid temperature (averaged over the cross section) is still sub-cooled. Such a position in axial direction, where the first bubbles occur is identified as **Onset of Nucleate Boiling (ONB)** or **Inception of Boiling (IB)** and the heat transfer regime downstream of this position is called *sub-cooled boiling*. The wall temperature in this region is nearly constant, at a few Kelvin above the saturation temperature.

Downstream of the point of ONB at a smaller degree of liquid sub-cooling, the void fraction starts to increase. This position is denoted as the point of **Onset of Vapor Generation (OVG)** and downstream of this point the void fraction grows rapidly. Figure 3.2 illustrates this effect, showing the axial void fraction distribution for the sub-cooled boiling region.

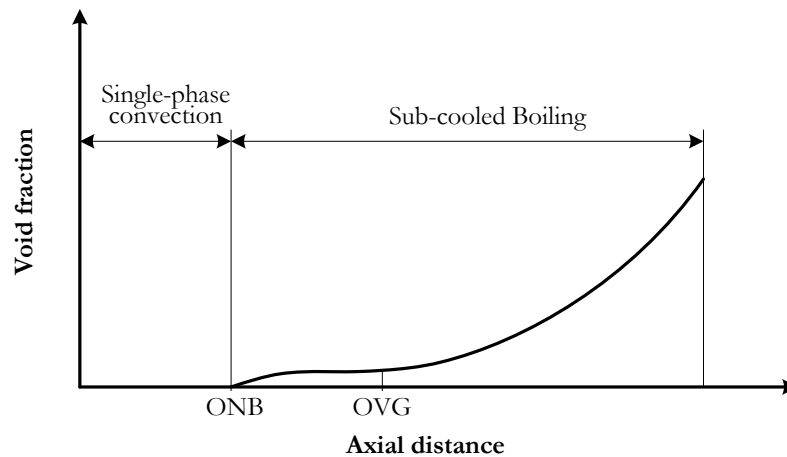


Figure 3.2 Axial void fraction distribution in a vertical pipe or channel

Bubbles grow and at a certain bubble diameter detach from the wall and move into the sub-cooled liquid, where some of them will be condensed, enhancing heat transfer to the liquid [98].

Further downstream, the position where the bulk liquid temperature reaches saturation, is identified as **Onset of Nucleate Significant Boiling (ONSB)** and the heat transfer regime downstream of this position as *saturated boiling* regime [126], characterized through heat transfer mainly due to bubbles formation and only with a little contribution due to single-phase convection; in the whole region of saturated boiling, bubbles (vapor blankets) are densely covering the wall surface.

At present, CD-adapco is further developing this model by applying an inter-phase surface topology map ([147], [148] and [161]), which allows the flow regime to change from bubbly to drop (mist) flow, depending on the local flow conditions e.g. volume fraction. These new

3 Physical phenomena of two-phase flow

developments are included in the so called extended boiling framework, a code version for BWR applications [137]. Compared to the model used in the calculations for the present work, which considers only the bubbly flow regime, the extended framework describes in addition the droplet flow and other regions that can be calculated as a transition between these two base regions. Furthermore, a first simplified model for a thin liquid wall film of constant thickness, treated as a separate flow regime, is also under development. In this model a film heat transfer coefficient is defined, which is based on the law of the wall, as proposed by *Whalley* [167], and on the *Reynolds* analogy for the film [137].

In this thesis the described model is applied to PWR sub-channel conditions. The steady state regimes found in PWRs are single-phase liquid flow with convective forced heat transfer to liquid or bubbly flow with sub-cooled boiling regime. At the last spacer span of some hot channels, defined later in Chapter 5.1, the saturated boiling heat transfer regime can also occur. According to *March* [104] referenced in *Garnier et al.* [50] a PWR core has a maximum local void fraction of 0.35 and the flow is finely dispersed. These results were obtained for refrigerant R12 as working fluid and by scaling the experimental inlet conditions to PWR working conditions, using the scaling law of *Ahmad* [2].

3.5.2 Interphase heat transfer (Boiling model)

Interphase heat transfer:

There are two mechanisms of interfacial heat transfer between two phases \dot{Q} : heat transfer due to temperature difference between the two phases \dot{Q}^i and heat transfer due to mass transfer between the two phases by evaporation/condensation \dot{Q}^{mass} :

$$\dot{Q} = \dot{Q}^i + \dot{Q}^{mass} . \quad (109)$$

Both terms are presented later in Sub-section 3.5.4 as the sources for energy conservation equations (Eqs. (151) and (152)).

Boiling model:

The model for inter-phase heat transfer due to the temperature difference and due to the inter-phase mass transfer is obtained by considering the heat transfer from the gas and the liquid to the gas/liquid interface, which is assumed to be at saturation temperature (T_s) as shown in Figure 3.3. This model describes both types of inter-phase mass transfer (evaporation and condensation).

The corresponding mass transfer between the phases is calculated from the net heat transfer to the interface. This model appears as the *boiling model* in literature [98].

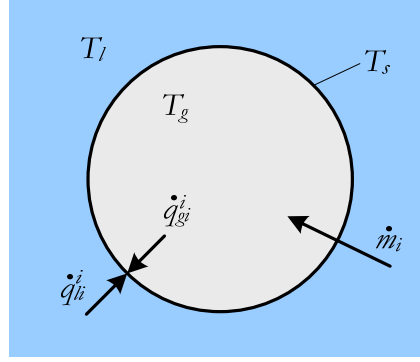


Figure 3.3 Heat and mass transfer between liquid and vapor bubble

The heat transfer rate from the liquid to the bubble interface across an *interfacial area* per unit volume A_i due to the temperature difference is estimated as:

$$\dot{q}_{li}^i = h_{li}^i A_i (T_l - T_s), \quad (110)$$

with h_{li}^i the heat transfer coefficient of the liquid side per unit of the interface area.

This coefficient can be obtained in terms of the *Nusselt* number:

$$h_{li}^i = \frac{\lambda_l Nu_{li}}{d_b}, \quad (111)$$

where λ_l is the thermal conductivity of the liquid and d_b is a typical length scale.

For a particle in a moving incompressible *Newtonian fluid* the *Nusselt* number is a function of the particle *Reynolds* number and the liquid phase *Prandtl* number:

$$Re_d = \frac{\rho_l |\vec{u}_r| d_b}{\mu_l} \quad \text{and} \quad (112)$$

$$Pr_l = \mu_l \cdot c_{p_l} / \lambda_l. \quad (113)$$

A widely used correlation is that of *Ranz and Marshall* [121] for flow around a sphere, derived originally for evaporating a droplet in forced convection:

$$Nu_{li} = 2 + 0.6 Re_d^{0.5} Pr_l^{0.3}, \quad \text{with } 0 \leq Re_d \leq 200. \quad (114)$$

In STAR-CD the *Nusselt* number may be:

- set to user-specified, constant value;
- calculated via the *Ranz and Marshall* correlation in a user subroutine (see Eq. (114)).

Taking into account the interfacial area for a single bubble $S_b = \pi d_b^2$, the total interfacial area per volume A_i can be obtained from S_b and the number of bubbles in the volume n_b , as defined in Eq. (76) as function of the void fraction α_d :

$$A_i = S_b n_b = \left(\pi d_b^2 \right) \left(\frac{6 \alpha_d}{\pi d_b^3} \right) = \frac{6 \alpha_d}{d_b}, \quad (115)$$

with d_b , specified later in this Sub-section as *bubble bulk diameter*.

3 Physical phenomena of two-phase flow

The heat transfer rate from the gas to the bubble interface across an interfacial area per unit volume A_i due to the temperature difference can be achieved in a similar way:

$$\dot{q}_{gi}^i = h_{gi}^i A_i (T_g - T_s). \quad (116)$$

Assuming the interface is at saturation temperature (T_s) the vapor temperature results also in T_s and due to Eq. (116) the heat transfer rate from gas to interface tends to zero:

$$T_g = T_i \text{ and } \dot{q}_{gi}^i = 0. \quad (117)$$

The heat transfer coefficient was heuristically proposed in STAR-CD to be equal to:

$$h_{gi}^i = 10 \frac{W}{m^2 K}. \quad (118)$$

The inter-phase mass transfer rate per unit volume can be obtained from the heat transferred to the interface, calculated using Eqs. (116) and (117) and assuming all the heat to be used in mass transfer (i.e. evaporation/condensation):

$$\dot{m}_i = \frac{\dot{q}_{li}^i + \dot{q}_{gi}^i}{h_{fg}}, \text{ where } h_{fg} \text{ is the latent heat.} \quad (119)$$

The contribution to the local inter-phase mass transfer rate per unit volume due to evaporation or condensation from liquid to gas phase and reverse can be obtained as following [137]:

$$\begin{cases} \dot{m}_{lg} = \max(m_i, 0) \\ \dot{m}_{gl} = \max(-m_i, 0) \end{cases} \quad (120)$$

According to Eqs. (117) and (119) the mass transfer rate between the two phases in Eq. (120) depends on the heat transfer rate, the latent heat and thus only on the liquid temperature. If the liquid is sub-cooled, then heat is removed from the interface and bulk condensation from gas to liquid phase occurs. When the liquid is superheated, the heat is added to the interface and bulk evaporation from the liquid to the gas occurs. In the near wall cells the inter-phase mass transfer rate is extended by an additional term due to wall evaporation heat, which is described in the next chapter.

Bubble bulk diameter:

According to Eq. (115) the interfacial area is a function of the the bubble bulk diameter, which has to be provided as an input parameter either from a suitable model or from experiment.

Different experiments show a spectrum of bubble diameters in the bulk of the flow moving with different velocities, which could be gathered in groups or classes. The bubble size can change due to coalescence and break up, evaporation and condensation, sub-cooling and pressure.

Lo [97] implemented the population balance approach based on the MUSIG (MUltiple-Size-Group) model to take into account coalescence and break up in adiabatic flows. *Yeoh* and *Tu*

([157] and [173]) extended it to account for wall nucleation and condensation for low pressure, using 15 classes of bubble bulk diameters. For each class a separate mass conservation equation is solved, i.e. individual interfacial area, *Reynolds* number, heat transfer coefficient and inter-phase mass transfer. Velocity and enthalpy fields are supposed to be the same and the closure formulations for momentum and energy conservation equations are obtained using the *Sauter mean diameter* calculated from the bubble size distribution as an approximation. It has to be noted that the solution of this additional set of equations is very time-consuming.

In this work either a constant bubble bulk diameter representing the whole size distribution, or a bubble bulk diameter as a function of the local liquid sub-cooling is used. This approximation is used for all equations and terms.

Kurul and *Podowski* [86] proposed to define the local bubble diameter using linear interpolation between the later described diameter of bubbles detaching from the wall (e.g. *Unal* [160] formulation, taken for high sub-cooling) and the largest stable diameter against break up at low sub-cooling (suggested by *Thomas* [149], based on dimensional analyses). The resultant expression for the bubble bulk diameter d_b from [86]:

$$d_b = d_1 - d_0^* \cdot \Delta T_{sub}, \quad (121)$$

with the liquid sub-cooling² defined as: $\Delta T_{sub} = T_s - T_l$ and coefficients: $d_1 = 0.0014$ m and $d_0^* = 0.0001$ m/K. Later in [87] a new value for the coefficient $d_1 = 0.0015$ m was proposed.

Examining these formulations it can be seen that the bulk diameter becomes negative at liquid sub-cooling of more than 14 K and 15 K, depending on the used value for d_1 .

Anglart and *Nylund* [5] used the formulation for the d_b from [87], applying a cut-off value to the function at two points of sub-cooling (high sub-cooling ΔT_0 and low sub-cooling ΔT_1):

$$d_b = \begin{cases} d_0 & \text{for } \Delta T_{sub} \geq \Delta T_0 \\ \frac{d_1(\Delta T_{sub} - \Delta T_0) + d_0(\Delta T_1 - \Delta T_{sub})}{\Delta T_1 - \Delta T_0} & \text{for } \Delta T_0 \geq \Delta T_{sub} \geq \Delta T_1, \\ d_1 & \text{for } \Delta T_{sub} \leq \Delta T_1 \end{cases} \quad (122)$$

with the following coefficients:

$$\begin{cases} d_0 = 0.0001 \text{ m} & \text{for } \Delta T_0 = 13.5 \text{ K} \\ d_1 = 0.0015 \text{ m} & \text{for } \Delta T_1 = 0 \text{ K} \end{cases} \quad (123)$$

They modeled the bubbly flow in a vertical annulus with heated inner tube (single-rod model) at $p = 45$ bar, $G = 1160$ kg/(m²s), $\dot{q}'' = 1080$ kW/m² and $\Delta T_{sub} = 43$ K and 19 K.

² In the case of superheating ΔT_{sub} becomes negative. The term sub-cooling will be used here for both phenomena.

3 Physical phenomena of two-phase flow

The radial void distribution at an altitude of 3.465 m calculated with variable bubble diameter taken from Eq. (122) for inlet high sub-cooling of 43 K was compared with the results of the calculation with different, but constant bubble bulk diameters ($d_b = 0.0005$ m, $d_b = 0.001$ m and $d_b = 0.0015$ m) and experimental data. The results achieved with variable diameter showed very good agreement with experimental data.

For the case with low inlet sub-cooling the difference between calculated and measured void profile was quite large. Especially the void fraction near the cold wall calculated with the model using variable bubble diameter was strongly overpredicted. In this case the measured local values of void fractions at the outlet were higher than 40 % over the whole tube diameter. Authors pointed out this case with such a high void fraction to exceed the limits of applicability of the used model.

In the literature also other coefficients can be found, depending on the application field. For the numerical simulation of sub-cooled boiling water flow in a vertical annulus with a heated inner tube at system pressure of 1 - 2 bars, the upper limit d_1 was varied in the range of 0.002 m to 0.008 m and the best agreement with experiments for the void fraction distribution was achieved with $d_1 = 0.005$ m [93]. This case was also used for validation of the STAR-CD code in [161], with best results applying $d_0 = 0.0001$ m and $d_1 = 0.004$ m.

For typical applications from nuclear technology *Krepper* [82] used following coefficients:

$$\begin{cases} d_0 = 0.00015 \text{ m} & \text{for } \Delta T_0 = 13.5 \text{ K} \\ d_1 = 0.002 \text{ m} & \text{for } \Delta T_1 = -5 \text{ K} \end{cases} \quad (124)$$

These diameters are obtained from Eq. (121) with $d_l = 0.0015$ m by setting ΔT_{sub} equal ΔT_0 and ΔT_1 , respectively. In STAR-CD according to [98] and [147] the coefficient set from Eq. (124) was used with Eq. (122). *Lo* also pointed out that the coefficients are problem dependent. It has to be noted, that [98] and [147] contain a misprint of sign concerning Eq. (122), but a correct formulation is implemented in the user subroutines, provided by STAR-CD.

In the current version of STAR-CD (version 3.27) using the *Extended boiling framework* [137] the same formulation is used, but the value of d_0 became smaller leading to the coefficients:

$$\begin{cases} d_0 = 0.0001 \text{ m} & \text{for } \Delta T_0 = 13.5 \text{ K} \\ d_1 = 0.002 \text{ m} & \text{for } \Delta T_1 = -5 \text{ K} \end{cases} \quad (125)$$

As an illustration the bubble bulk diameter as a function of local liquid sub-cooling calculated with the mentioned formulations is presented in Figure 3.4.

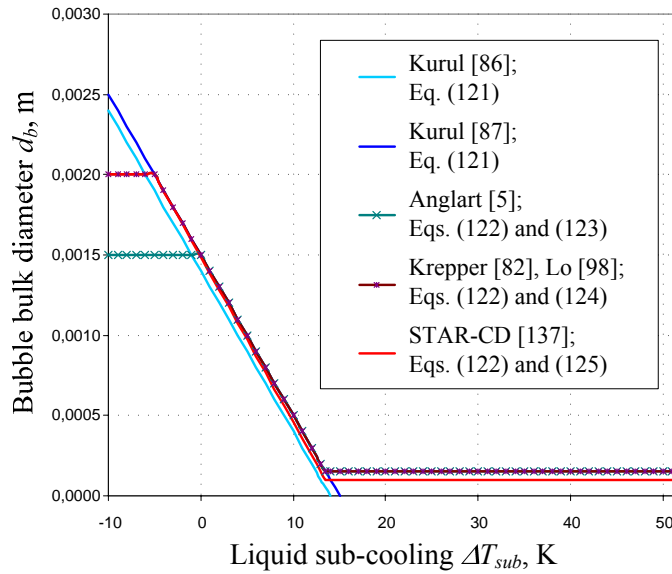


Figure 3.4 Variable bubble bulk diameter as a function of the liquid sub-cooling

3.5.3 Wall heat transfer model (Heat partitioning model)

Phases may also exchange heat with their surroundings depending on the applied boundary conditions. In this chapter, the wall heat partitioning model describes the heat transfer from the heated wall to the coolant, with a defined total heat flux at the heated wall. According to the mechanistic wall heat partitioning model proposed by *Kurul* and *Podowski* [86] the heat flux from the whole wall downstream the ONB can be split into three components: single-phase convection \dot{q}_c'' , evaporation heat for steam generation \dot{q}_e'' , and the heat flux due to quenching at the nucleation sites \dot{q}_q'' . These three mechanisms are shown in Figure 3.5 and the whole wall heat flux can be written as:

$$\dot{q}_w'' = \dot{q}_c'' + \dot{q}_e'' + \dot{q}_q'' \tag{126}$$

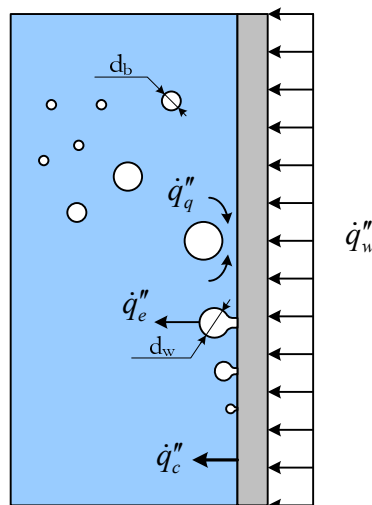


Figure 3.5 Heat partitioning model (schematic)

3 Physical phenomena of two-phase flow

Area of influence:

It is known that evaporation starts from nucleation sites at the heated surface. The heated surface is divided into two areas of influence with different mechanisms of heat transfer: a *boiling area of influence* A_e (fraction of surface area influenced by nucleation sites with evaporative and quenching heat transfer) and a *non-boiling area of influence* A_c (the remaining fraction of wall area not influenced by nucleation site and therefore with single-phase forced convective heat transfer). Assuming the existence of only two areas and no overlapping of the areas of the neighboring bubbles the fraction of the non-boiling area of influence A_c can be calculated complementary to the boiling area of influence A_e as follows:

$$A_c = 1 - A_e. \quad (127)$$

In accordance with *Del Valle and Kenning* [36] the boiling area A_e , is F_A times a fraction of the wall surface covered by the maximum bubble projected areas. This fraction is calculated from the active nucleation site density n'' and the maximum bubble diameter at the wall (in our case the bubble departure diameter d_w is assumed to be the same for all sites).

$$A_e = F_A \frac{\pi d_w^2}{4} n'', \quad (128)$$

with F_A so-called boiling model constant, described later in this Sub-section.

Nucleation density, bubble departure diameter and boiling model constant:

The first parameter for obtaining the boiling area is the *nucleation site density*, n'' (i.e., number of nucleation sites per area on the surface of a substrate). In different correlations it is mainly a function of wall heat flux or wall superheat and no significant effect of flow velocity or sub-cooling was applied. In addition, *Basu et al.* [13] and *Hibiki and Ishii* [58] pointed out the influence of the contact angle. *Kocamustafaogullari and Ishii* [76] proposed an effective wall superheat that allows using the correlation for both pool boiling and forced convection applications. *Sultan and Judd* [144], *Cornwell and Brown* [32] discussed the influence of the material and finishing of the wall, respectively.

Kurul and Podowski [86] obtained the active nucleation site density n'' , using correlated data of *Lemmert and Chawla* [94], which describes the nucleation site density as a function of wall superheat by the following relationship:

$$n'' = (m \Delta T_{sup})^p, \quad (129)$$

where $\Delta T_{sup} = T_w - T_s$ is the wall superheat, and the corresponding constants are $m = 210$ and $p = 1.805$. This formulation is applied in STAR-CD [98] with varied value for $m^{STAR} = 185$.

In Figure 3.6 data of *Lemmert and Chawla* [94] for a copper pipe of about 25 mm diameter with refrigerant R11 at a pressure of about 1 - 2 bar flowing normal to the pipe (cylinder) surface with low velocity and data for parallel flow with the same conditions to a copper flat plate is compared to the formulations used in [86] and [98].

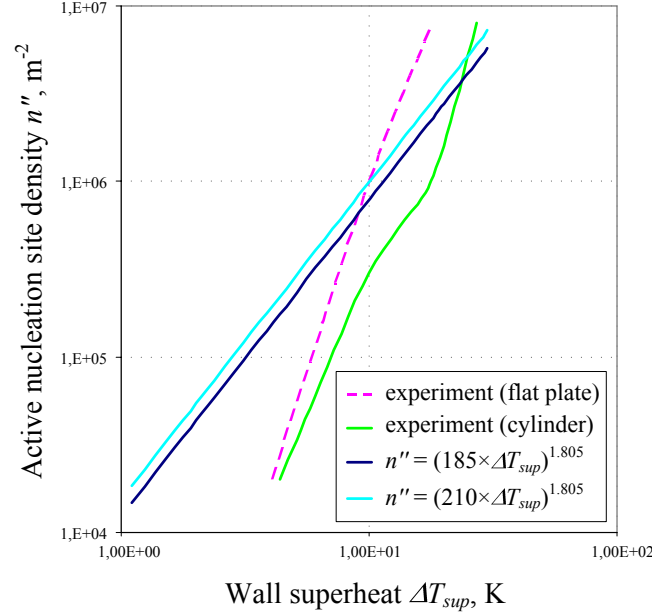


Figure 3.6 Nucleation site density as function of the wall superheat

It was pointed out by the authors [94] that the presented functions for the nucleation site density are computed indirectly from the measured value of the heat transfer coefficient. The irregularities of the green curve for the cylinder are not explained by the authors. It can be assumed that the experimental accuracy is limited.

The next parameter that needs to be predicted to obtain the boiling area is the *bubble departure diameter* d_w . According to *Cole* [28], in the initial stage of the bubble growth very small vapor bubbles coalesce on the heating surface to form patches of vapor. Once formed patches of vapor grow as single bubbles, eventually detach from the surface and then rise through the surrounding liquid.

This detaching diameter of the bubble at the moment of breakaway from the wall surface is called *bubble departure diameter* and is specified by an empirical correlation as function of the liquid sub-cooling $\Delta T_{sub} = T_s - T_l$, using experimental data of *Tolubinsky* and *Kostanchuk* [150]:

$$d_w = d_s \exp\left[-\frac{\Delta T_{sub}}{\Delta T_0}\right], \quad (130)$$

where bubble departure diameter at saturation $d_s = 0.0014$ m and $\Delta T_0 = 45$ K are model constants.

3 Physical phenomena of two-phase flow

The correlation of experimental data is derived from atmospheric pressure for liquid sub-cooling between 5 K and 60 K and is presented in Figure 3.7. The authors point out that the departure diameter is a heat flux independent value, but is expected to be a function of pressure. This pressure dependency is later shown in Appendix B.

In the validation analyses of STAR-CD at system pressure ranging from 20 bar to 70 bar, a smaller model constant $d_s^{STAR} = 0.0006$ m is used [147]. Since no further explanation for changing the value for this coefficient is given in [147], it is assumed that this was done in order to take heuristically into account the pressure dependence of d_s .

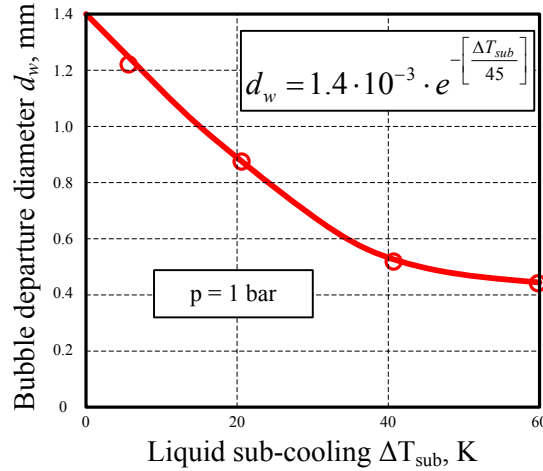


Figure 3.7 Dependence of bubble departure diameter upon the local liquid sub-cooling at system pressure of 1 bar (adopted from [150])

The last parameter for obtaining the boiling area is F_A , the *boiling model constant*, determining the ratio of the boiling area of influence to the maximum bubble projected area. Conventionally F_A is expected to be about 4 for pool boiling [36]. This means that the diameter of influence of the boiling area is 2 times larger than the bubble departure diameter. If the overlapping of the neighboring bubbles is taken into account F_A becomes smaller. Values of $F_A = 2$ and $F_A = 1$ produced satisfactory results in validation exercises [137] and [147].

Convective heating:

The convective heat flux from the wall surface to the liquid is modeled in a similar way as for the single phase turbulent flow over the non-boiling influence area A_c

$$\dot{q}_c'' = h_c A_c (T_{wall} - T_l), \quad (131)$$

with h_c the convective heat transfer coefficient, based on the conventional wall functions of the standard *High Reynolds number k-ε model* for single-phase flow evaluated as:

$$h_c = \frac{\bar{c}_p \rho u_\tau}{Pr_h^t (u^+ + P)}, \text{ where } P \text{ is the sublayer resistance factor given by [136] as:} \quad (132)$$

$$P \equiv 9.24 \left[\left(\frac{\text{Pr}_h}{\text{Pr}_h'} \right)^{0.75} - 1 \right] \left[1 + 0.28 \exp \left(\frac{-0.007 \text{Pr}_h}{\text{Pr}_h'} \right) \right]. \quad (133)$$

Velocities u^+ and u_τ are already presented by Eq. (33).

Evaporation heating:

Over the area covered by nucleation sites, the bubbles carry away the evaporation heat flux. The evaporation heat transfer rate at the wall is proportional to the nucleation sites density, the bubble departure diameter and *bubble departure frequency* f , and results in:

$$\dot{q}_e'' = \rho_g \left(\frac{\pi d_w^3}{6} \right) f n'' h_{fg}. \quad (134)$$

The bubble departure frequency used to calculate the evaporation heat is obtained from Cole [28] or Ceumern-Lindenstjerna [23], based on Deissler's analyses [35], assuming that the bubbles detach from the surface and coalesce, if the critical heat flux occurs. Under these conditions the bubble departure frequency can be obtained in terms of the bubble departure diameter and u_b (the rate at which the bubbles rise away from the surface) as:

$$f = \frac{u_b}{d_w}. \quad (135)$$

Solving the balance of buoyancy and drag force for freely rising bubbles for the bubble velocity, results in:

$$u_b = \sqrt{\frac{4 g (\rho_l - \rho_g) d_w}{3 C_D \rho_l}}. \quad (136)$$

Assumption that a drag coefficient $C_D = 1$ leads to following resulting expression for f :

$$f = \sqrt{\frac{4 g (\rho_l - \rho_g)}{3 d_w \rho_l}}. \quad (137)$$

This formulation for bubble departure frequency assumes that the bubble departure is immediately followed by the activation of the next bubble.

In addition to Eq. (134), the evaporation heat flux can be also written in terms of the temperature difference between wall and boiling interface and the heat transfer coefficient multiplied by the boiling area of influence as:

$$\dot{q}_e'' = h_e A_e (T_w - T_s) = h_e^* (T_w - T_s). \quad (138)$$

Using Eqs. (134) and (138) the heat transfer coefficient for evaporation h_e can be obtained as:

$$h_e = \rho_g \left(\frac{\pi d_w^3}{6} \right) f n'' h_{fg} / (A_e (T_w - T_s)). \quad (139)$$

3 Physical phenomena of two-phase flow

It has to be noted that the heat transfer coefficients in STAR-CD have already taken into account the areas of influence e.g. for evaporation h_e^* .

Assuming that the whole evaporation heat is used to create bubbles, the inter-phase mass transfer rate from liquid to gas due to wall boiling per area of the wall surface can be obtained in STAR-CD from the evaporation heat flux:

$$\dot{m}_{lg} = \frac{\dot{q}_e''}{h_{fg}}. \quad (140)$$

To achieve the whole liquid-gas inter-phase mass transfer term per unit volume, the term due to the wall boiling has to be added to the already evaluated term due to evaporation/condensation by Eq. (120). Here the term due to the wall boiling is obtained by multiplying the right hand side of Eq. (140) with the contact area of the cell with the wall surface. For the discretized equations the flux has to be additionally related to the cell volume.

Quenching:

The bubbles are created at the nucleation sites and when they depart from the wall, the space they have occupied is replaced by cooler water coming in contact with the wall and using a part of the wall heat flux for its heating. This heating is called quenching heat transfer. *Mikic* and *Rohsenow* [109] for pool-boiling and later *Del Valle* and *Kenning* [36] for sub-cooled flow boiling at high heat flux, modeled this heat transfer as a transient heat conduction to a semi-infinite body (the liquid here) with a step change in temperature $T_{wall} - T_l$ at the surface:

$$\dot{q}_q'' = h_q A_e (T_{wall} - T_l), \text{ with quenching heat transfer coefficient:} \quad (141)$$

$$h_q = 2f \sqrt{\frac{t_{wt} \lambda_l \rho_l c_{pl}}{\pi}}, \quad (142)$$

where λ_l , ρ_l and c_{pl} denote thermal conductivity, density and specific heat of liquid, respectively, and t_{wt} is the *waiting time* (bubble or preliminary period or hysteresis time) between the bubble departure and the activation of the next bubble.

The behavior of the bubble at the single nucleation site is presented schematically in Figure 3.8, showing the bubble departure diameter.

In experimental studies, *Tolubinsky* and *Kostanchuk* [150] found that at different sub-cooling at constant pressure the following expression is approximately constant:

$$\frac{t_{wt} + t_{ct}}{t_{ct}} \approx const, \quad (143)$$

with t_{ct} the *contact time* of the bubble with the heated wall and $t_{cycle} = t_{wt} + t_{ct}$ the *full cycle period*.

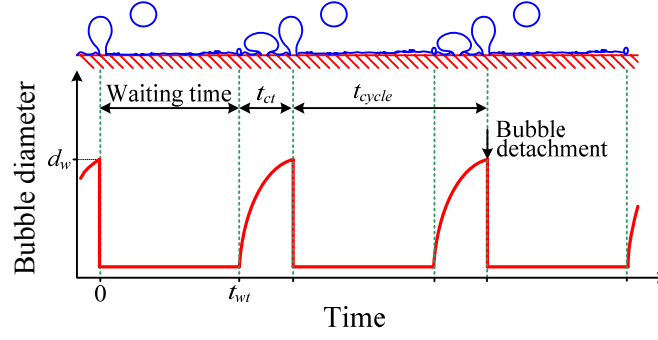


Figure 3.8 Behavior at a single nucleation site

Assuming that the constant in Eq. (143) at atmospheric pressure is in a range from 4 to 5 and the frequency f is reciprocally proportional to a full cycle period t_{cycle}

$$f = \frac{1}{t_{wt} + t_{ct}}, \quad (144)$$

the following expression can be obtained:

$$4 < \frac{1}{f \cdot t_{ct}} < 5. \quad (145)$$

Waiting time results then approximately in:

$$t_{wt} \approx \frac{0.8}{f}. \quad (146)$$

This formulation leads to a new frequency for obtaining the quenching heat transfer coefficient equal 80 % of the frequency calculated without accounting for the waiting time used in the formulation for the heat transfer coefficient for evaporation Eq. (139).

The pressure dependence of the waiting time was pointed out by *Tolubinsky* and *Kostanchuk* [150], but is not taken into account in the two-phase model of STAR-CD.

Wall temperature:

Depending on the boundary conditions applied at the wall (see Chapter 2.4) three options are possible: adiabatic $\dot{q}_w = 0$, fixed temperature and $t_w = const$ and fixed heat-flux boundaries (Wall temperature t_w is specified iteratively).

3.5.4 Sources for conservation equations

Mass source due to bulk boiling or condensation and wall boiling for mass conservation equation for the liquid is obtained via the following way [137]:

$$S_l^{mass} = -\dot{m}_{lg} + \dot{m}_{gl}. \quad (147)$$

Mass source for gas phase can be calculated complimentary to S_l^{mass} as follows:

$$S_g^{mass} = -S_l^{mass}. \quad (148)$$

3 Physical phenomena of two-phase flow

The momentum source due to bulk boiling or condensation and wall boiling for momentum conservation equation, including the term describing the interfacial transfer of the momentum yields for liquid phase in:

$$\bar{S}_l^{mom} = -\dot{m}_{lg}\bar{u}_l + \dot{m}_{gl}\bar{u}_g. \quad (149)$$

The gas momentum source can be obtained as:

$$\bar{S}_g^{mom} = -\bar{S}_l^{mom}. \quad (150)$$

Heat source for liquid and gas energy equations is obtained in terms of heat source due to bulk evaporation or condensation (temperature difference between fluid and interface) and additional heat sources due to bulk and wall boiling mass transfer, respectively as:

$$S_l^h = \underbrace{-\dot{q}_{li}^i}_{\text{due to temperature difference}} - \underbrace{(\dot{m}_{lg} - \dot{m}_{gl}) \cdot h_l(t_s)}_{\text{due to mass transfer}}, \quad (151)$$

$$S_g^h = -\dot{q}_{gi}^i + (\dot{m}_{lg} - \dot{m}_{gl}) \cdot h_g(t_s), \quad (152)$$

with $h_l(t_s)$ and $h_g(t_s)$ specific enthalpy at t_s for liquid and gas phase, respectively. Heat and mass transfer due to the wall boiling was presented in detail in the previous Sub-section.

3.6 Two-phase physical properties of fluids

3.6.1 General assumptions

The main application field of this work is flow under PWR conditions, hence for the performed calculations the system pressure of a PWR (~160 bar) is chosen. The fluid for this pressure is assumed to be incompressible for both phases.

For STAR-CD calculations two-phase properties for both the liquid and the gas phase have to be specified by the user. The saturation temperature and the latent heat of phase change are specified as constants for system pressure. *Krepper* [82] already showed for pressures in the order of a few MPa that the impact of the pressure difference over the core height on the saturation temperature dT_s/dz is negligible. Therefore, the assumption of constant saturation temperature of the entire fluid domain holds well for applications at higher pressures.

Two-phase properties in STAR-CD with two-phase modeling are currently defined as constant. Therefore, a suitable approximation for the values, which depends on the region of application, has to be found. The heat transfer regimes treated in this work are sub-cooled or saturated boiling, whereas fluid temperatures extend between high sub-cooling and slightly above the saturation temperature. These rather wide ranges of conditions explain the need for parameter sets describing both the sub-cooling and the boiling sufficiently accurately.

Inlet parameter for the gas-phase: No gas superheating is allowed in current modeling, because the interface of a bubble is at saturation. Hence, the gas phase is assumed to be at saturation and the inlet parameters for the gas phase are taken from the water-steam table at saturation conditions.

Inlet parameter for the liquid-phase: For the liquid phase some parameters are taken from the saturation conditions and some from the inlet sub-cooled conditions depending on the parameter purpose. The liquid molecular laminar viscosity and the thermal conductivity are specified at the inlet temperature. These values are assumed to be important for the evaluation of the wall friction at the entrance region with high sub-cooling. The density in contrast is taken at the saturation, because of its importance for the boiling process.

3.6.2 Evaluation of the specific heat

The relation between specific enthalpy and temperature in STAR-CD is obtained in terms of mean specific heat. Figure 3.9 presents the differential values of specific heat taken from a water-steam table for various pressures: atmospheric conditions and reactor conditions for BWR and PWR.

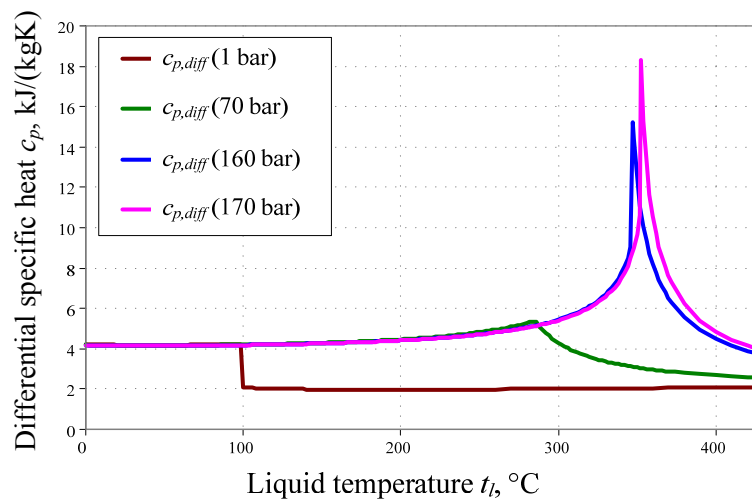


Figure 3.9 Differential specific heat dependent on the local liquid temperature at various pressures

Additionally plotted is the curve for a system pressure of 170 bar. This system pressure was estimated by a scaling process of the *Garnier* experiment, which was carried out with the refrigerant R12 as a working medium. The scaling procedure of R12 experimental inlet parameters to water is described in detail in Sub-section 4.2.1.

The corresponding values of specific enthalpy are shown in Figure 3.10

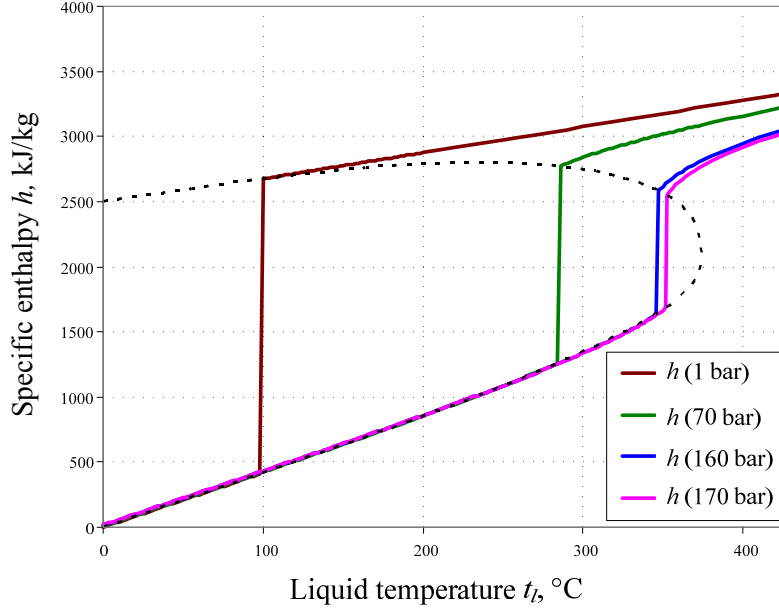


Figure 3.10 Specific enthalpy dependent on the local liquid temperature at various pressures

For atmospheric pressure it can be seen that values of differential specific heat can be replaced by constant values for both liquid and gas phase almost without error. With increasing pressure the gradient of the specific heat becomes higher with increasing temperature and using a constant value would result in deviations. Currently there is a restriction of using constant values in STAR-CD. Therefore, an approximation method has to be chosen, that evaluates specific heat with the smallest possible error.

The basic physical definition of specific heat at $p = \text{const}$ according to [141] can be written as:

$$c_p(T, p) = \left(\frac{dh}{dT} \right)_p. \quad (153)$$

By integration of Eq. (153) in a temperature interval between T_2 and T_1 and at constant system pressure p_0 the difference of specific enthalpy can be obtained in terms of specific heat, as:

$$h(T_2, p_0) - h(T_1, p_0) = \int_{T_1}^{T_2} c_p(T, p_0) dT. \quad (154)$$

In [141] the mean specific heat at $p = \text{const}$ is defined for the temperature interval $[T_1, T_2]$ as:

$$\int_{T_1}^{T_2} c_p dT = \bar{c}_{pT_1}^{T_2} \cdot (T_2 - T_1) \quad \text{or} \quad (155)$$

$$\bar{c}_{pT_1}^{T_2} = \frac{1}{T_2 - T_1} \int_{T_1}^{T_2} c_p dT. \quad (156)$$

Using the relation given by Eq. (156) to determine the mean specific heat, the reference-point of the enthalpy scale has to be specified, i.e., all the enthalpy calculations have to be related to a

certain reference temperature. This reference temperature is assumed here to be at $t_0 = 0^\circ\text{C}$ and is taken as a lower bound of the integration interval T_1 , because, as it was shown in Figure 3.9, water-steam table provides differential values for c_p for positive temperatures in $^\circ\text{C}$ and with the reference temperature $t_0 = 0^\circ\text{C}$, where the specific enthalpy is near zero (Figure 3.10). Additionally, Celsius temperatures are used in most nuclear engineering applications.

According to the zero-point of the enthalpy scale at the reference temperature $t_0 = 0^\circ\text{C}$, Eqs. (154) and (156) for any temperature t in degrees Celsius can be written as:

$$h(t) = h(0^\circ\text{C}) + \int_0^t c_p(t) dt = 0 + \bar{c}_{p0}^t \cdot t = \bar{c}_{p0}^t \cdot t \quad \text{and} \quad (157)$$

$$\bar{c}_{p0}^t = \frac{1}{t} \int_0^t c_p(t) dt. \quad (158)$$

For any temperature in degrees Celsius t_1 and t_2 Eq. (154) yields:

$$h(t_2) - h(t_1) = \int_{t_1}^{t_2} c_p(t) dt = \int_0^{t_2} c_p(t) dt - \int_0^{t_1} c_p(t) dt = \bar{c}_{p0}^{t_2} t_2 - \bar{c}_{p0}^{t_1} t_1. \quad (159)$$

As it was mentioned before the latent heat of phase change is specified at saturation temperature and constant pressure. Therefore, for a correct energy balance of the boiling process at $t = t_s$ the mean specific heat for liquid and gas is proposed to be specified for the temperature interval $[t_0, t_s]$ with $t_0 = 0^\circ\text{C}$. Hence, Eq. (157) at saturation temperature results in:

$$h(t_s) = h(0^\circ\text{C}) + \int_0^{t_s} c_p(t) dt = 0 + \bar{c}_{p0}^{t_s} \cdot t_s = \bar{c}_{p0}^{t_s} \cdot t_s. \quad (160)$$

The mean specific heat defined for the temperature interval $[t_0, t_s]$ with $t_0 = 0^\circ\text{C}$ can be obtained from Eq. (160) as:

$$\bar{c}_{p0}^{t_s} = \frac{h(t_s)}{t_s} \quad (161)$$

for liquid and gas Eq. (161) results in the following relations, respectively:

$$\bar{c}_{p0l}^{t_s} = \frac{h_l(t_s)}{t_s} \quad \text{and} \quad (162)$$

$$\bar{c}_{p0g}^{t_s} = \frac{h_g(t_s)}{t_s}. \quad (163)$$

First approximation method:

Mean specific heat at saturation temperature with reference temperature $t_0 = 0^\circ\text{C}$

The reference enthalpy $h(t_0) = 0$ is chosen at the reference temperature $t_0 = 0^\circ\text{C}$. The mean specific heat defined for the temperature interval $[t_0, t_s]$ and achieved from Eq. (161) is taken as

3 Physical phenomena of two-phase flow

an approximation of any mean specific heat obtained for the interval $[t_0, t]$ for $t_{inlet} \leq t \leq t_s$:

$$h(t) = h(t_o = 0^\circ C) + \int_0^t c_p(t) dt = 0 + \bar{c}_{p0}^t \cdot t \approx \bar{c}_{p0}^{t_s} t, \quad (164)$$

i.e. the mean specific heat is chosen at saturation conditions and applied as an approximation for the whole temperature range of the modeled case.

This formulation offers a proper description of latent heat and even for high sub-cooling the error of estimated enthalpy is still reasonable. This method is proposed in this work and is applied in the performed calculations.

Second approximation method:

Differential specific heat at saturation temperature with reference temperature $t_0 = 0^\circ C$

Another approximation method is the application of the differential specific heat at saturation, taken from the water-steam table as a constant value for the whole region of application.

$$h(t) = h(t_o = 0^\circ C) + \int_0^t c_p(t) dt = 0 + \bar{c}_{p0}^t \cdot t \approx c_p(t = t_s) \cdot t. \quad (165)$$

This method has an advantage in the region near saturation, but leads to large discrepancies by applying it to regions of high sub-cooling. It was chosen by STAR-CD in the two-phase tutorials and can also be found in other applications: e.g. *Krepper* pointed out the use of constant properties to reduce the calculating time. For the c_p he also used the differential values at saturation as constants for the whole temperature range from sub-cooling to saturation.

For a better understanding of the approximations the results are compared at chosen conditions with the differential values from the water-steam table.

Comparison of the described approximations:

For comparison the system pressure of 170 bar was chosen. This system pressure is obtained, when the *Garnier* experiment, which used refrigerant R12, is scaled to water as working fluid. The scaling procedure is shown later in Section 4.2.1. This pressure condition is near PWR conditions (topic of this thesis) and due to Figure 3.9 and Figure 3.10, the specific heat and enthalpy, respectively, have similar temperature dependency at 160 and 170 bar. Therefore the conclusions that are made for 170 bar are also applicable to PWR conditions.

The resulting values for specific heat from application of the first (blue curve) and second (green curve) approximation method were compared with the differential values for specific heat (red curve), taken from water-steam table, and presented in Figure 3.11 as a function of the local liquid temperature.

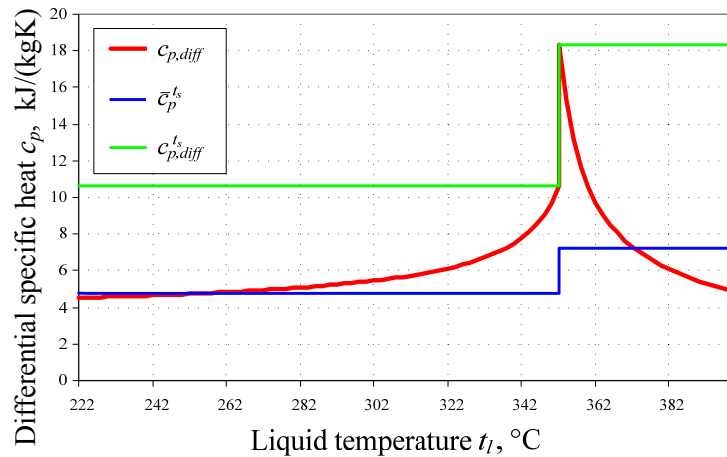


Figure 3.11 Specific heat dependent on the local liquid temperature at 170 bar

The dependency is shown from the inlet temperature of the case with the inlet sub-cooling of 130 K. Observing the curves for the liquid phase i.e. for temperatures below saturation temperature $t_s(p = 170 \text{ bar}) = 352 \text{ }^\circ\text{C}$, it can be seen, that using the differential values at saturation for the whole range of temperature is advantageous in the region near saturation, but with increasing liquid sub-cooling the discrepancy is growing as well. Oppositely, the higher the liquid sub-cooling the better are the approximations of the first method. This method, using the mean value at the saturation temperature for the whole range of the temperature, shows very good agreement with the differential values from water-steam table in the large range of sub-cooling temperatures and is proved to be the better choice for applications of sub-cooled boiling under PWR conditions.

Figure 3.12 presents the resulting specific enthalpy as a function of the liquid temperature for both approximation methods compared to the differential data achieved from water-steam table.

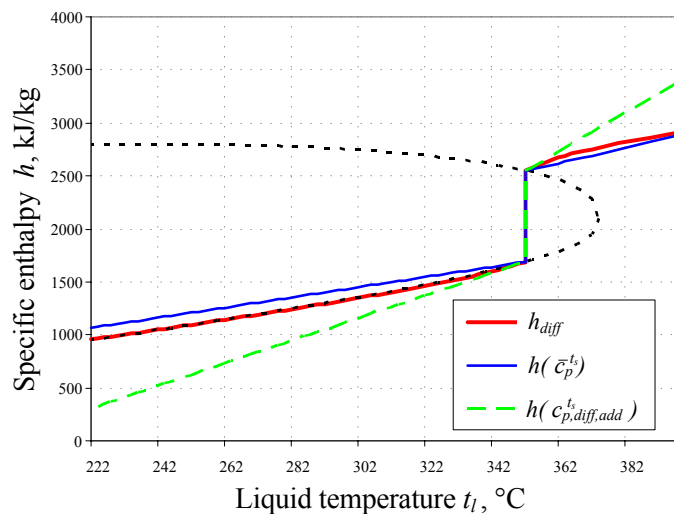


Figure 3.12 Specific enthalpy dependent on the local liquid temperature at 170 bar

3 Physical phenomena of two-phase flow

The results of the second approximation (green curve) are obtained by taking into account that the exact latent heat from the water-steam table is described for the boiling model independently of the approximation method and that the curve achieved from Eq. (165) can be shifted parallel using additive constants for both gas and liquid phase. Applying such a parallel shift is possible, because in STAR-CD the enthalpy transport equation computes the enthalpy up to an additive constant, i.e. only enthalpy differences need to be represented accurately, not their absolute values.

Additionally an example showing the error in the evaluation of enthalpy by these two approximation methods for two liquid temperatures is outlined in Appendix A. In the region near saturation with sub-cooling of 10 K the second method of the evaluation of the enthalpy provides errors that are 2 times smaller than the first one. The higher the liquid sub-cooling the better are the approximations of the first method. At the inlet of the model the first method has an estimation error about six times smaller than the second one.

Even if the second method shows good agreement with the differential values from the water-steam table in the region near saturation, it leads to large discrepancies moving away from this region for both liquid and gas phase. The first method in contrast approximates the values of the specific heat for high pressures sufficiently accurate for both phases in the whole range of the occurring liquid temperatures and would be applied for all presented calculations under conditions ~ PWR.

Considering the approximation of the liquid-phase enthalpy by the first approximation method, a further improvement was proposed.

Improvement for the first approximation method: **Mean specific heat at saturation with reference temperature $t_0 = t_{inlet}$**

Considering constant two-phase properties, a possible improvement of the obtained values of the enthalpy by terms of the mean specific heat can be achieved by using the inlet temperature $t_0 = t_{inlet}$ instead of $t_0 = 0^\circ\text{C}$ as a reference. Then Eqs. (154), (161) and (164) yield:

$$h(t_s) - h(t_{inlet}) = \int_{t_{inlet}}^{t_s} c_p(T) dT = \bar{c}_{p,t_{inlet}}^{t_s} (t_s - t_{inlet}), \quad (166)$$

$$\bar{c}_{p,t_{inlet}}^{t_s} = \frac{h(t_s) - h(t_{inlet})}{(t_s - t_{inlet})}, \text{ and} \quad (167)$$

$$h(t) = h(t_{inlet}) + \int_{t_{inlet}}^t c_p(t) dt = h(t_{inlet}) + \bar{c}_{p,t_{inlet}}^{t_s} (t - t_{inlet}). \quad (168)$$

In Figure 3.13 and Figure 3.14 the resulting specific heat and enthalpy for a system pressure of

170 bar and an inlet liquid temperature of 222 °C are presented and are compared to the results of the first approximation and to the differential values from water-steam table.

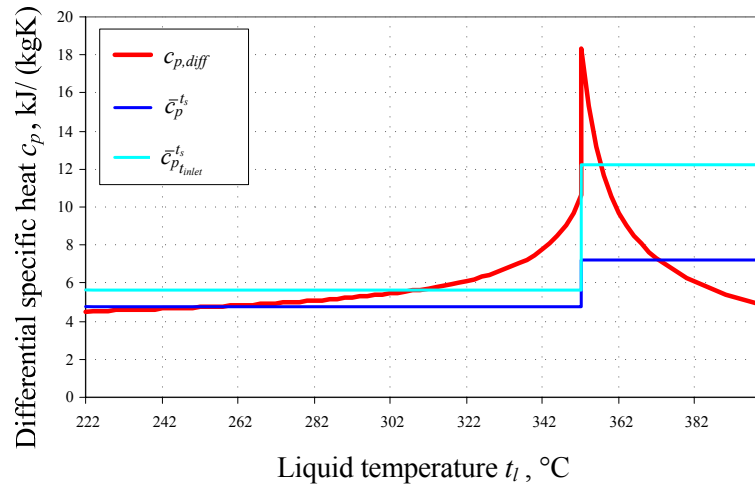


Figure 3.13 Specific heat dependent on the local liquid temperature at 170 bar. Improved variant

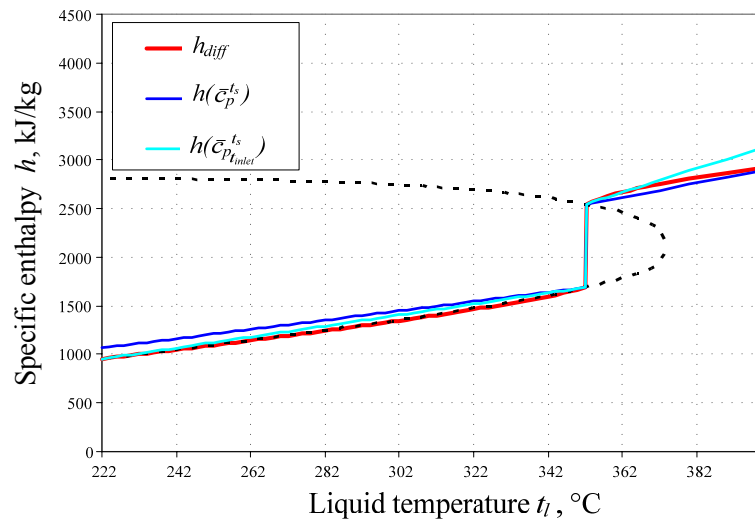


Figure 3.14 Specific enthalpy dependent on the local liquid temperature at 170 bar. Improved variant

It results in the correct description of the enthalpy for two points: at saturation and at the inlet temperature. However the reference enthalpy has to be adjusted for every run and the values at the gas side achieve a larger discrepancy with increasing liquid superheating. For the cases where liquid temperature does not strongly exceed the saturation value such a method would be very advantageous.

Future improvement:

For single-phase applications STAR-CD offers two possibilities:

- Input of explicit temperature function of the form $T(h)$. Temperature is obtained directly from enthalpy;

3 Physical phenomena of two-phase flow

- Implicit temperature functions of the form $h(T)$ with internal conversion to temperature when needed, by direct or iterative means as appropriate.

It is a current field of work to make these formulations also applicable for two-phase flows, which would be the accurate way to define enthalpy. Increased computational time should be acceptable with respect to the enhanced accuracy of the simulations.

3.6.3 Inlet temperature

As it was already mentioned the specific enthalpy is evaluated in STAR-CD from temperature and specific heat. A relation between temperature and enthalpy cannot be set. The methods to define specific heat were discussed in the previous sub-section. At the inlet, the temperature has to be set by the user. For the gas phase the saturation temperature is defined and for the liquid phase the inlet temperature has to be obtained.

Due to the constant values used for the specific heat two different methods describing the liquid temperature at the inlet can be used (if the specific heat is not described for the inlet condition):

- Exact value for temperature at the inlet, leading to deviation of the inlet specific enthalpy;
- Exact value for specific enthalpy at inlet, leading to deviation of the inlet temperature.

These methods are presented by means of the same example as already shown for the illustration of the approximation methods for the specific heat.

In the *Garnier et al.* [50] experiment with refrigerant R12 as a working medium, the inlet liquid temperature of the R12 was given [47]. From this temperature the corresponding value of specific heat was evaluated with help of the R12-table: $h_{inlet} = f(t_{inlet}, p_0)$ and the resulting value for the equilibrium quality at the inlet was calculated from Eq. (173), shown in Section 4.2.1. The inlet specific enthalpy for water as a working fluid was obtained assuming the same equilibrium quality at the inlet as for R12.

Now the inlet temperature can be obtained from the water-steam table as the corresponding value to this specific enthalpy. Then we get the exact value for the temperature at the inlet, leading to exact values for sub-cooling, but because of using constant values for specific heat, there are deviations of the specific enthalpy close to saturation (blue dot 1 in Figure 3.15). In the presented example, the inlet enthalpy calculated by the code from the mean value of the specific heat at saturation, applied for the whole range of the temperature, would be higher than the enthalpy obtained from the water-steam table. That means higher equilibrium quality at the inlet and results in overestimation of the void fractions in the model.

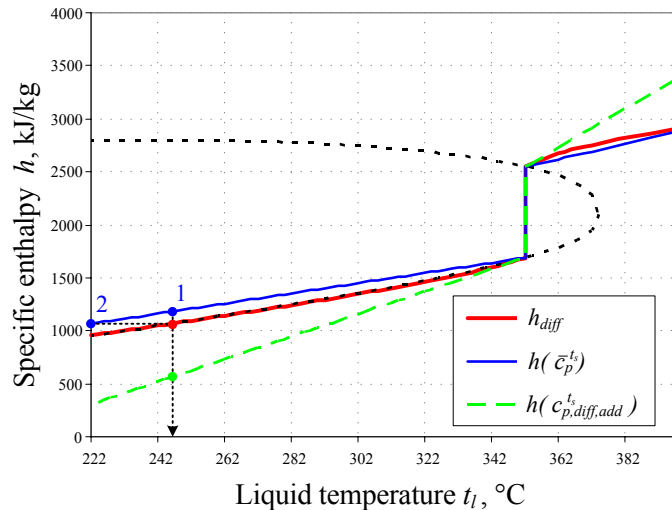


Figure 3.15 Specific enthalpy dependent on the local liquid temperature at 170 bar

If the specific enthalpy at the inlet is taken from a water-steam table to get the exact energy balance, the calculated inlet temperature assuming the mean value of the specific heat at saturation taken for the whole range of the temperature becomes 25 K lower, leading to significant overestimation of inlet sub-cooling (blue dot **2** in Figure 3.15). The correct heat balance is achieved, but the deviating sub-cooling temperature plays an important role in various formulations for boiling and wall heat partitioning.

Depending on the conditions, one of these two methods (dot **1** or **2**) is chosen in the performed calculations. On the one hand, for high sub-cooled cases always having negative equilibrium quality, exact values for the specific enthalpy are chosen e.g. in Chapter 4.2 for the validation of *Garnier* experiments. On the other hand, for validation of critical heat flux experiments in Chapter 4.3 the exact temperature values at the inlet are taken as the correct liquid sub-cooling or superheating is assumed to be of a higher importance for such cases. It also has to be noted that near saturation the enthalpy error becomes much smaller. For sub-channel analyses both phases are set to saturation, so that the problem of inlet values vanishes.

Application of the improved suggestion for the first approximation method (Figure 3.13) also solves this problem as both values for inlet temperature and inlet specific enthalpy are consistent by such an approximation.

Prescribing exact values of the inlet temperature together with a constant differential value of specific heat at saturation for the whole range of temperatures as it is done by some authors leads to correct sub-cooling at the inlet but a large deviation in the enthalpy difference, leading to much smaller void fractions in the model. Therefore, such a method is not advised to be used here.

3.7 Alternative formulation (Enhanced heat partitioning model)

The described modeling of the heat partitioning at the wall in Sub-section 3.5.3 is formulated for the liquid as a continuous phase and for the gas phase as a dispersed one. This model assumes that no gas has direct contact with the wall. The wall area is divided into two areas: the boiling area of influence, with evaporation of the liquid, and the remaining area, where convective heat transfer to the liquid (single-phase) and quenching occur.

In the latest version of STAR-CD with extended *Eulerian two-phase flow* modeling (version 3.27), especially developed for BWRs, the inter-phase surface topology map is applied, due to various flow regimes occurring in such types of reactors [137]. Depending on the local void fraction, bubbly or mist flow or transition flow (linear interpolation between these two flows) are assumed to occur. Due to such flow regimes, the formulation of the wall heat partitioning model is modified to:

$$\dot{q}_w'' = (1 - \theta) \cdot (\dot{q}_l'' + \dot{q}_i'') + \theta \cdot \dot{q}_g'', \quad (169)$$

with a transition variable θ , controlling the distribution of the wall heat flux \dot{q}_w'' (transition from wall heat transferred on the one side to the gas phase and to the liquid phase and the boiling interface on the other side). The liquid single-phase convective term and the quenching term are joined in one common liquid term, as they together describe the overall heat flux from the wall to the liquid: $\dot{q}_l'' = \dot{q}_c'' + \dot{q}_q''$. The heat flux transferred to the boiling interface for vapor creation is the evaporation heat $\dot{q}_i'' = \dot{q}_e''$.

In our applications no flow regime map was applied as the application field of this work is related to PWR conditions, where single-phase and bubbly flows occur under non-CHF conditions. Furthermore, in one validation case, which will be presented later in Chapter 4.3, STAR-CD was applied to PWR conditions with critical heat flux. For this purpose the model of Eq. (169) was applied together with standard two-phase modeling, which describes bubbly flow and was presented in Chapter 3.

In the standard model parameters of the heat partitioning model no bubbles directly contacting the wall surface were considered and therefore no steam superheating was implemented. Though the energy conservation equation is solved for the gas phase, vapor is assumed to be at saturation temperature everywhere and no heat flux from the wall can be transferred directly to the gas phase, i.e. $\dot{q}_g'' = 0$. Such a situation can be achieved with $\theta = 0$ with the new model extended by Eq. (169).

In this case Eq. (169) becomes identical to Eq. (126), i.e. the heat partitioning model proposed by *Kurul* and *Podowski* [86].

In the formulation proposed in this work a few bubbles or in the case of CHF a bubble swarm, which will be discussed in detail in Chapter 4.3, are assumed to accumulate on the wall surface. On the one hand such bubbles would get that fraction of the whole heat flux, that depends on its area of influence (fraction of surface area influenced/occupied by accumulated bubbles) corresponding to θ . This heat flux to the gas phase causes gas superheating resulting usually in a steep gradient of the wall temperature and a reduced heat transfer coefficient from the wall to the gas. This effect could not be modeled without a formulation like Eq. (169) and even at high wall heat fluxes the wall temperature would remain rather close to saturation temperature using previous approaches. On the other hand the area of influence of the liquid and boiling interface together is obtained as $1 - \theta$. The schematic of this model is shown in Figure 3.16.

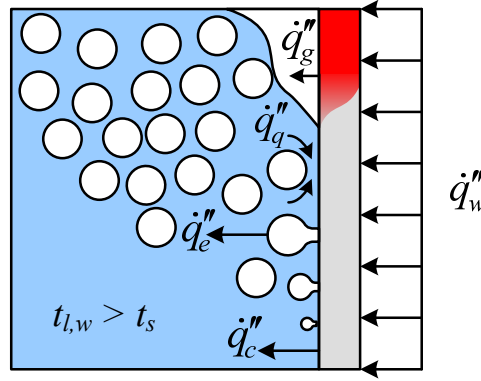


Figure 3.16 Enhanced heat partitioning model (schematic). Cell near the wall with $\alpha_g > 0.5$

One more open question is the specification of the transition variable θ . The proposed hypothesis allows gas superheating from the moment when the cell temperature of the liquid near the wall equals saturation $t_{l,w} = t_s$. The amount of wall heat transferred to the gas phase should be a function of local void fraction:

$$\theta = \max\left(\frac{\alpha_g - \alpha_1}{\alpha_2 - \alpha_1}; 0\right), \quad (170)$$

where the breakpoints have been set as $\alpha_1 = 0.5$ and $\alpha_2 = 1$. Choosing such breakpoints means that there is no gas superheating until the void near the wall is higher than the heuristic value of $\alpha_g = 0.5$ on the one hand ($\theta = 0$). On the other hand, if the void fraction reaches $\alpha_g = 1$ naturally the entire heat is assumed to be transferred into the gas phase, with the transition variable $\theta = 1$, and a wall area with the heat transfer mechanisms of liquid conduction;

3 Physical phenomena of two-phase flow

quenching and evaporative heat do not occur. For intermediate volume fractions $\alpha_1 < \alpha_g < \alpha_2$ in the interval between these two values the variable θ is linearly interpolated.

For the cases with high-subcooling and low heat flux there is almost no difference to the old modeling, because the liquid temperature reaches saturation only in a few cells and the volume fraction in such cells is usually not very high. That is why applying this new modeling to the *Garnier* validation cases, presented in Chapter 4.2, brought no relevant difference and therefore is not shown.

This model was validated for a coarse mesh and for a pipe heated with stepwise increased heat flux for two characteristic cases, presented in Sub-section 4.3.3.2. Both cases showed that the wall temperature is increasing significantly at the high heat flux, compared to the standard modeling, which shows almost constant wall temperature at high heat fluxes. For one case it was even possible to get a quite strong increase of the wall temperature resulting in almost correct prediction of the DNB-phenomena, though the quantitative values of wall temperature are still too small.

However, the model can be seen as a first step to achieve a correct prediction of CHF. It should be improved in the future to find a more general model for various inlet conditions.

Additional detailed physical modeling of the CHF phenomena is needed. The existing physical CHF models (bubble agglomeration and layer evaporation) should be studied and further developed for implementation into a CFD code to get a more realistical description of the CHF.

4. Validation

4.1 Validation basis of STAR-CD two-phase modeling

4.1.1 Overview

Verification of the two-phase STAR-CD model was a joint project of ANL, Sarov Lab, VNIIEF and CD-adapco sponsored by DoE (IPP). No new experiments were carried out for validation goals, but as it was pointed out by *Ustinenko et al.* [161] an extensive literature review on experiments designed for the study of two-phase flow and phase-change phenomena has been conducted. 24 papers, which can be used for the validation of the base code and of the extended boiling framework (CFD-BWR code), described in the previous chapter, were chosen. The experiments were divided in 6 groups, depending on the involved two-phase phenomena.

A - Adiabatic flow with non-heated walls of steam-water and air-water mixture experiments, for the validation of interfacial drag and wall friction models;

B - Surface Boiling experiments, for the validation of models for boiling, inter-phase heat and mass transfer, interfacial heat transfer, interfacial drag during boiling, boiling crisis;

C - Steam Condensation experiments for the validation of inter-phase heat and mass transfer models and interfacial drag models;

D - Dispersed flow of water droplets in steam experiments, for the validation of models for inter-phase heat and mass transfer, droplet deposition on heated surfaces, and wall heat transfer;

I - Integral tests in which several two-phase flow regimes occur and which can be used to validate the flow regime map and the interaction between multiple phenomenological models;

M - Model of two-phase flow tests in bundles of uniformly and non-uniformly heated fuel rods, which can be used for the benchmarking of models and the code under conditions representative for BWR operating conditions.

Multiple experiments from this list have already been validated with the present two-phase STAR-CD model and the results of several experiments were presented in [147], [148] and [161]. Such results of STAR-CD calculations as axial positions of the onset of nucleate boiling, axial temperature profile, axial and radial void distribution were compared with experiments.

4 Validation

Good agreement was obtained for a large number of cases. Table 4.1 shows an overview of the presented cases, including: number of the experiment and the group it represents from the six mentioned above; a short description of the experiment with the name of the author and the input data; published two-phase parameters and version of STAR-CD used for numerical simulation; compared data for experiment and calculation and, if available, the way of its measurement; discussion of this comparison.

Table 4.1 Overview of experiments for validation of the boiling model of STAR-CD

N°	Group	Star CD Version	Experimental data	Star-CD Two-phase parameter	Compared data/ measurements method	Results and Discussion
1	A	3.27	<p><u>Author:</u> <i>Wang et al.</i> [164] The water-air bubbly mixture flow in pipe, obtained in the mixture tee. Pipe: $d = 57.15$ mm, $L =$ not given, $p = 1$ bar, $\dot{q}'' = 0$ MW/m², $t_l = 20^\circ\text{C}$; <u>Experiment #1:</u> parameter of mixture at inlet: $u_{l,inlet} = 0.43$ m/s, $u_{g,inlet} = 0.1$ m/s, $\alpha_{g,inlet} = 0.132$</p>	<p>Input data is taken mainly from <i>Troshko</i> and <i>Hassan</i> [156]: $L = 10$ m, $d_b = 2.8$ mm; Lift force: $C_L = 0.25, -0.025$, $C_L = f(E\ddot{o})$ [154]; Wall lubrication force: $C_{wl} = -0.06$, $C_{w2} = 0.147$</p>	<p>Radial profiles of void fraction and liquid velocity</p>	<p>The best agreement was achieved for the case with $C_L \sim 0$. <i>Eötvös</i> number formulation [154], dependent on $d_b = 2.8$ mm, is also in satisfactory agreement with the experimental data, including near wall peak. It is noted that in the air-water flow under normal conditions the lift force given by [154] changes its sign at $d_b = 5$ mm. Standard formulation shows a too small near wall peak. There is an improvement in the radial liquid velocity profile in the center and near the wall region [148].</p>
2	A	3.27	<p><u>Author:</u> <i>Liu</i> [95] The water-air bubbly mixture flow in pipe, obtained in the mixture tee. Pipe: $d = 57.2$ mm, $L =$ not given, $p = 1$ bar, $\dot{q}'' = 0$ MW/m², $t_l = 20^\circ\text{C}$; <u>Experiment #8:</u> parameter of mixture at inlet: $u_{l,inlet} = 1.0$ m/s, $u_{g,inlet} = 0.1$ m/s, $\alpha_{g,inlet} = 0.106$</p>	<p>The same as in N°1</p>	<p>Radial profiles of void fraction and liquid velocity</p>	<p>The best agreement is achieved for the case with <i>Eötvös</i> number formulation [154]. The case with close to zero coefficient $C_L = -0.025$ is also in satisfactory agreement with the experimental data. Standard formulation $C_L = 0.25$ shows about 40 % higher void fraction at the wall. An improvement in the liquid velocity radial distribution profile is shown; except in the region near the wall, where the standard formulation has better agreement with measured data [148].</p>

3	A	3.27	<p><u>Author:</u> <i>Serizawa et al.</i> [134] The water-air bubbly flow in pipe, obtained in the mixture tee.</p> <p>Pipe: $d = 60$ mm, $L = 2.15$ m, $p = 1$ bar, $\dot{q}'' = 0$ MW/m², $t_l = 20$ °C;</p> <p><u>Experiment #2:</u> parameter of mixture at inlet: $u_{l,inlet} = 1.03$ m/s, $u_{g,inlet} = 0.151$ m/s, $\alpha_{g,inlet} = 0.102$</p>	The same as in N°1 $d_b = 4$ mm	Radial profiles of void fraction and liquid velocity	The best agreement is achieved for the case with $C_L \sim 0$. <i>Eötvös</i> number formulation [154], dependent on $d_b = 4$ mm is also in satisfactory agreement with the experimental data. It is noted that in the water-air flow under normal conditions the lift force given by [154] changes its sign at $d_b = 5$ mm. There is also some improvement in the liquid and air velocity radial distributions compared to standard formulation. Liquid and air are slightly too fast in the center and too slow at the region near the wall [161].
4	B	3.26	<p><u>Author:</u> <i>Bartolomei</i> and <i>Chanturiya</i> [14] Upward water flow with boiling in a heated pipe.</p> <p>Pipe: $d = 15.4$ mm and 24 mm, $L = 2$ m, $p = 14 - 45$ bar, $\dot{q}'' = 0.4 - 0.8$ MW/m² $\Delta T_{sub} = 160 - 20$ K;</p> <p><u>Simulated case:</u> $d = 15.4$ mm, $L = 2$ m, $p = 45$ bar , $\dot{q}'' = 0.57$ MW/m², $G = 900$ kg/(m²·s), $\Delta T_{sub} = 60$ K</p>	Inlet data: $u_{l,inlet} = 1.03$ m/s, $u_{g,inlet} = u_{l,inlet}$ $\alpha_{g,inlet} = 0.0001$ $d_b = \text{const}$; Lift force: $C_L = 0.25$; Wall lubrication force: no	Axial distributions of the wall temperature (Thermocouples), bulk liquid temperature (Thermocouples) and void fraction profiles (Gamma-ray densitometry: source Tm-170, detector FEU-37A)	Wall temperature was compared with experiments and correlations: <i>Dittus-Boelter</i> [89] for single-phase entrance region and <i>Thom</i> [89] for two-phase region. Very good agreement was achieved for all presented curves [147].

5	B	3.26	<p><u>Author:</u> <i>Tarasova et al.</i> [145] Surface boiling water flow in vertical pipe with heated walls: $d = 8.25$ mm, $L = 0.5$ m; Each series was carried out for constant p; \dot{q}'', G and ΔT_{sub} are variable; series finishing condition: $t_l \sim t_s$ (at outlet) <u>Simulated case:</u> $p = 24.5$ bar, $\dot{q}'' = 0.625$ MW/m², $G = 2000$ kg/(m²·s)</p>	Turbulence; Turbulent dispersion force; Virtual mass: $C_{VM} = 0.5$; Drag force: $C_{D, par} = 2$; Lift force: $C_L = 0.25$; Wall lubrication force: no; $d_b = 1$ mm	Pressure drop along the boiling length (DT-150 differential manometer filled with bromoform)	Overall, rather good agreement between numerical and experimental data was obtained. The effect of increasing pressure drop for heated wall case compared with adiabatic flow was obtained numerically [161].
6	B	3.26	<p><u>Author:</u> <i>Lee et al.</i> [93], <i>Tu and Yeoh</i> [157] and [173]; Upward sub-cooled boiling water flow in a vertical (concentric) annulus: $D_{i1} = 19$ mm (heated), $D_{i2} = 37.5$ mm, $L = 2.376$ m, heated section of the inner pipe: $L_h = 1.67$ m, $p = 1 - 2$ bar, $\dot{q}'' = 0.1148 - 0.3204$ MW/m², $G = 474 - 1061$ kg/(m²·s), $\Delta T_{sub} = 21.3 - 11.5$ K; <u>Experiment</u>(#C3 [157], #C1 [173]): $p = 1.42$ bar, $\dot{q}'' = 0.1523$ MW/m², $G = 474$ kg/(m²·s), $T_{sub} = 13.4$ K $d_b = [2.4, 4.6]$ mm, radial distribution from [173]</p>	Buoyancy; No-slip for water; Slip for vapor; Turbulence; Turbulent dispersion force; Virtual mass: $C_{VM} = 0.5$; Drag force: $C_{D, par} = 2$; Lift force: $C_L = 0.25, -0.025, -0.25, -0.5$; $C_L = f(E\ddot{o})$ [154]; Wall lubrication force: $C_{w1} = -0.06$, $C_{w2} = 0.147$ $d_b = f(T_{sub})$ Kurul [85]	At elevation of 1.61 m from the inlet: radial void distribution (Two-conductivity probe, with error ± 3 %) and radial velocity distribution (Pitot tube, with error ± 3.3 %)	Results of the standard model and as a function of the <i>Eötvös</i> number are not presented. The best agreement with experiments for radial void fraction profile show the calculation with $C_L = -0.5$. Radial profiles achieved with lift force using the <i>Eötvös</i> number formulation are similar to the case with a close to zero lift force. The reason is maybe the large value of d_b of about 5 mm, taking place in experiment (Lift force given by [154] depends on <i>Eötvös</i> number and changes its direction when bubble size exceeds a critical value of $d_b = 5$ mm). Good agreement for liquid velocity profile for the best case, but vapor is too fast in the center and too slow at the wall [161].

7a	B+C	3.26	<p><u>Author:</u> Avdeev and Pekhterev [12]; Bartolomei et al. [16] Upward flow of water with boiling in a heated lower section of the pipe followed by flow with condensation of the steam in an adiabatic higher section of the pipe.</p> <p>Pipe: $d = 12.03$ mm, $L = 1.4$ m, heated lower section: $L_h = 1.67$ m, $p = 68.9$ bar;</p> <p><u>Experiment #2</u> $\dot{q}'' = 1.2$ MW/m², $G = 1500$ kg/(m²·s), $\Delta T_{sub} = 63$ K;</p> <p><u>Experiment #5</u> $\dot{q}'' = 0.8$ MW/m², $G = 1000$ kg/(m²·s), $\Delta T_{sub} = 55$ K</p>	$d_b = f(T_{sub})$ Kurul [85]	Axial void fraction distribution	Reasonably good agreement, although the discrepancy in some sections is up to circa 30 %. Vaporization and condensation models should be improved, because there are both over- and under-prediction of the void fraction [147].
7b	B+C	3.27	Same as 7a	$d_b = f(T_{sub})$ Kurul [85]	Axial void fraction distribution	Compared to 7a the results show more discrepancy for the condensation region. It is strange that radial void distributions stay equal. It is not clear from papers what the difference is between 7a and 7b in modeling [161].

8a	C	3.26	<p><u>Author:</u> <i>Bartolomei and Gorburov</i> [15] Upward flow of a water-steam mixture, created in a mixing chamber attached to the bottom of the pipe, in an adiabatic pipe involving steam condensation.</p> <p>Pipe: $d = 32$ mm, $L = 2$ m;</p> <p><u>Experiment #5-a:</u> $p = 20$ bar, $\dot{q}'' = 0$ MW/m², $G = 250$ kg/(m²·s), mixing chamber: $\Delta T_{sub} = 15$ K, $\alpha_{g,inlet} = 0.25$;</p> <p><u>Experiment #7-b:</u> $p = 30$ bar, $\dot{q}'' = 0$ MW/m², $G = 420$ kg/(m²·s), mixing chamber: $\Delta T_{sub} = 35$ K, $\alpha_{g,inlet} = 0.4$</p>	$Nu = 1$ $d_b = 1.3$ mm (according to holes in the mixing chamber), Wall lubrication force: no Lift force: $C_L = 0.25$	Axial void distribution (Gamma-ray densitometry: source Tm-170, detector FEU-24 (photo-electric multiplier))	Good agreement between numerical and experimental results has been achieved. Discrepancy is observed only at low void fractions (not enough condensation). Possible way to improve: void-fraction dependent bubble diameter during condensation below a specified threshold void fraction [147]. That is, changing the bubble size instead of changing the number of bubbles (as is done in the standard condensation model). Results of this improvement are presented in experiment 8b [161].
8b	C	3.26	Same as N°8a	$Nu = 2$ $d_b = 2.3$ mm $d_b = f(\alpha_g)$	Axial void distribution	The case with constant diameter has the same problem as 8a. For the case with variable diameter very good agreement for the whole length. Low void fraction region now has excellent agreement and in high void region small discrepancy up to circa 10 % [161].

9	D	3.27.063	<p><u>Author:</u> Koizumi <i>et al.</i> [77] Upward steam-water dispersed flow. Steam-water mixture was fed into the measuring channel and there was no film on the heated rods. Film can develop on lower parts of the rods due to droplet deposition from the flow. <u>Test section:</u> Single rod in a channel (annulus: coaxial rod in a circular pipe): $D_{i2} = 20$ mm, $L = 2$ m; 25 rods bundle in a square cross-section channel <u>Simulated case:</u> $p = 30$ bar, $\dot{q}'' = 0.346 - 0.493$ MW/m², mixture data: $G = 310$ kg/(m²·s), $T_{mix} = 507$ K, $\alpha_{g,inlet} = 0.012$</p>	Standard STAR-CD models for turbulent dispersion force; Virtual mass: $C_{VM} = 0.5$; Lift force: $C_L = 0.25$; Wall lubrication force: no; Numerical modeling of liquid film: no	Axial distribution of the wall temperature	The temperature of the heated rod in simulations starts to rise in the lowest point with heating (the annulus inlet). The coordinate of this point is assumed to be equal to the dry-out point in the experiment. For $\dot{q}'' < 0.367$ MW/m ² temperature is over-predicted and in the other case under-predicted [161].
10	M	3.27.063	<p>2x2 sub-channel model under BWR conditions [101] (bare rods without spacer): $L = 4.09$ m, heated upper section: $L_h = 3.8$ m, $d = 12.27$ mm, $pt = 16.2$ mm, $p = 72$ bar, $\dot{q}'' = 0.537$ MW/m², $\Delta T_{sub} = 10$ K</p>	Steady state, without flow regime map	Averaged void fraction at exit was obtained analytically for slip ration $S = 0$ and $S = 1.2$	Derivation about 3 % [101]

11	M	3.27.063	<p><i>BFBT model-NUPEC benchmark</i> [112]: 60 electrically heated pins of typical BWR dimensions organized in 8x8 array with 7 square spacer grids with perimeter vanes, water channel displacing the 4 rods at the center of the assembly, fuel channel; heat flux is supplied by pin power map, full length model without spacer grid.</p> <p>outlet pressure: $p = 72 \text{ bar}$,</p> <p>pin bundle inlet velocity: $u_{inlet} = 2.33 \text{ m/s}$,</p> <p>inlet enthalpy: $h_{inlet} = 50.22 \text{ kJ/kg}$</p> <p>Simulated cases:</p> <ul style="list-style-type: none"> • low quality $x = 0.05$, • medium quality $x = 0.12$, • high quality $x = 0.25$ 	<p>Steady state, without flow regime map;</p> <p>Computational model without spacer details (dimples, springs and vanes)</p>	<p>Sub-channel averaged void fraction at outlet</p>	<p>Good agreement, average deviation of 8 %. Large deviations in region near water channel [101] (max. 108 %)</p>
----	---	----------	--	--	---	---

4 Validation

4.1.2 Discussion and conclusions

The boiling model available in the *Eulerian* two-phase flow model in STAR-CD provides: (1) models for calculating inter-phase heat and mass transfer to simulate evaporation and condensation, (2) a wall heat partitioning model to compute the wall heat transfer according to three mechanisms: convection, evaporation and quenching.

The validity and accuracy of these models were checked in a detailed validation series **A**, **B** and **C**. A first test-case for series **D**, is briefly documented in Table 4.1.

Radial distribution (void and velocity): Radial distribution profiles of void fraction and velocity were validated only at atmospheric conditions (*1 bar*) for upward adiabatic water-air flows in pipes with a diameter of ~ 60 mm (cases N°1 - 3). Also close to atmospheric conditions the radial void and velocity profiles were analyzed for water-steam flows in an annulus with outer diameter 37.5 mm and heated inner pipe of 19 mm (case N°6). Different values of lift force are needed for wall boiling and adiabatic flow to get good agreement with experimental data. Close agreement, including the void peak near the heated wall, was achieved for adiabatic flow and for surface boiling with lift coefficients: $C_L \sim 0$ and $C_L = -0.5$, respectively.

Using the *Eötvös* number formulation for the lift force depending on the bubble diameter in the bulk, shows results similar to the ones achieved by a lift force close to zero. This effect is caused by the large size of the bubbles in both measured and computed system. If the bubble size exceeds a critical value, the lift force changes its sign. Therefore, the values of the lift force for a diameter close to the critical value are close to zero. The critical value depends on the system pressure. For atmospheric conditions of the validated cases the critical diameter is about 5 mm and for high pressures decreases to a value of 2 mm. Additionally, the wall lubrication force was applied. Both *Eötvös* number formulation and wall lubrication force together allowed to get good agreement for cases with water-air flow in a pipe, but due to the critical diameter also with a lift force equal to zero good agreement can be achieved. For the chosen case with heated walls such kind of modeling was not successful. Therefore, enhanced modeling of the lateral forces is needed to describe various test cases with a unique parameter set.

In almost all other validation cases the standard lift coefficient of $C_L = 0.25$ has been used and no wall lubrication force was applied.

Axial distribution (temperature, pressure and void): Axial distributions of the wall and bulk liquid temperature, as well as the pressure, in upward flow in heated pipes with a diameter of 15.4 and 8.25 mm and pressure of 45 and 24 *bar*, respectively, show very good agreement with experimental data (cases N°4 and 5). Axial void fraction distributions for upward flow in heated

pipes of diameter 12.03 mm at 70 bar showed qualitatively good agreement for the heated and non-heated region (case N°7). Quantitatively, the discrepancy in different sections is up to ~ 30 %. The evaporation and condensation model has to be improved to handle a wider range of flow situations with the same two-phase parameters of the CFD model. The condensation experiment at 20 and 30 bar in upward flow in a pipe with a diameter of 32 mm provided good agreement for the region of high void fraction and after applying a void dependent diameter formulation the region of low void fraction also achieved an excellent agreement (case N°8). Overall, good agreement was obtained for boiling and condensation processes.

Although the boiling model needs some improvement for condensation, evaporation and radial forces the general conclusion of the validation cases is that the boiling model in STAR-CD can be used to model the boiling two-phase flows in fuel assemblies. To prove this conclusion the validation series of group **M** were carried out. Averaged void fraction at the outlet was compared with the analytical value for a 2x2 sub-channel geometry under BWR conditions and showed a small deviation of about 3 % (case N°10). Later, the boiling model was applied to model complete BWR fuel assemblies at 72 bar. Geometrical details of the spacers were not included in the computational model. Comparisons of the computed void against available data of a NUPEC benchmark [112] have shown that axial profiles of void averaged across the channel cross-section agree reasonably well with the measured data (case N°11). However, the distribution of void close to the water channel requires further improvement and more information on the heat transfer from the channel.

Also the first validation of group **D** analyzing the steam-water flow in an annulus at 30 bar was carried out for various heat fluxes applied at the wall. The axial temperature of the rod surface was compared with experimental data. For all computed cases the temperature was either under- or overpredicted. The numerical modeling of the liquid film should improve the future results. Previous computations assumed bubbly flow (group **A**, **B** and **C**) or mist flow (group **D**) existing everywhere in the computational domain. A second generation of the boiling model is now under development, which uses a local topology variable to allow the following flow regimes: a) a bubbly flow regime with spherical vapor bubbles in a continuous liquid, b) a droplet or mist regime with spherical liquid droplets flowing in a continuous vapor field, and c) a transition regime which combines the features of the two previous flow regimes in various proportions. The local topology is determined in this model using a simple local topology map based on the local void fraction. In the future also more detailed maps can be introduced. At the moment the topology map only demonstrates its potential. Within the mist flow region, a liquid

film model is applied to the computational cells adjacent to the walls. The validations of group I are subject of current development and therefore not considered here.

4.2 Radial void fraction distribution in a vertical pipe flow

4.2.1 Description of experiment with R12. Scaling for water-steam application

As it was already discussed in the previous chapter, validation of axial void distribution for boiling water in a vertical pipe with heated walls [147] showed good agreement with experiments carried out at a system pressure of 45 and 69 bar. The presented validations of the radial void distributions in vertical pipes were carried out only for air-water bubbly flow in pipes with adiabatic walls and under atmospheric pressure [148].

CFD applications presented in this thesis are conducted under PWR operating conditions, i.e. a system pressure of 160 bar and water-steam flow in a reactor sub-channel with heated rods. Experiments containing radial distributions of void fraction at high pressure conditions for heated pipes with water-steam flow were needed to validate the CFD two-phase modeling of lateral inter-phase forces.

For such a validation experimental results of sub-cooled boiling heat transfer of refrigerant R12 (CCl_2F_2 /Freon 12) in a vertical tube with upflow conducted by *Garnier et al.* [50] were chosen, because the experimental conditions can be scaled to equivalent PWR operating conditions quite well in spite of some uncertainties. The chosen experiments have the additional benefit of including both bulk and wall boiling processes, compared to other available experiments with measured radial void distribution and conducted without wall heating.

Garnier et al. [50] provided detailed results for radial volume fraction distribution for different inlet sub-cooling, measured at the end of the heated length by means of a two-sensor optical probe. The test section is presented in Figure 4.1. The heated tube is 3.5 m long and has an inner diameter of 19.2 mm. The flow is assumed to be axis-symmetric. The accuracy of the measurement of volume fraction is assumed to be about $\pm 1\%$. For each measured curve the individual values for inlet pressure, mass and heat flux were converted into CFD boundary conditions and fluid properties (e.g. Table 4.2) under PWR operating conditions.

In the first step of validation work, data of the experimental fluid (R12) was scaled to water conditions at high pressure, as the topic of this work is analyses under PWR conditions. Such technique of fluid modeling was often applied in the past to study the thermal and hydraulic behavior of a given system by means of an easy to handle model fluid rather than by the working one [2]. The reason, why the R12 experiments were scaled to water conditions lies in

the fact that the boiling model of STAR-CD contains several semi-empirical correlations derived from water experiments. An application of these correlations to R12 is not straightforward and reliability of computations for R12 using those correlations directly would remain questionable.

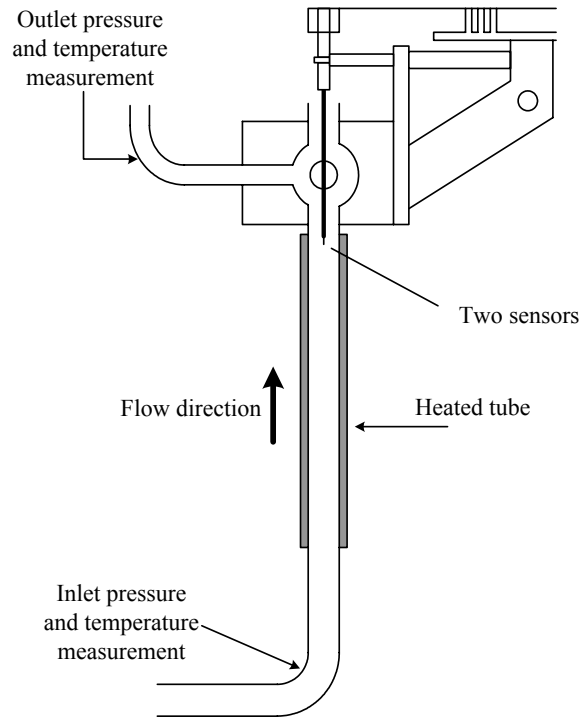


Figure 4.1 DEBORA experiment adapted from Garnier *et al.* [50]

Aim of the validation is to provide quantitative insight into the application of the two-phase CFD model to PWR conditions, having sub-cooled water as a working medium. Moreover, a successful validation of CFD with an adapted model correlation for R12 would not prove automatically that it could be successfully applied to water conditions.

However, the scaling process of the fluid data has its uncertainty and the best variant would be a validation using high pressure water-steam experiments. Such experiments were not found in literature, but R12 measurements are very common because of its lower latent heat of vaporization and pressure compared to scaled water data, which lead to simpler and cheaper experiments.

Experimental results of Garnier *et al.* [50], which have been chosen for this validation, cover the applied wall heat flux in the range from a tenth of the critical heat flux (CHF) to almost the occurrence of the CHF. The definition of the CHF is presented in Section 4.3.1.

Ahmad [2] listed thirteen relevant dimensional quantities resulting from fluid-to-fluid scaling theory, where most of them are classical characteristic numbers with their known fundamental

4 Validation

importance for characterizing a flow system (see Appendix A). *Cheng* pointed out that even if geometric scaling and the effect of surface properties are neglected, there still exist more than ten independent dimensionless numbers describing the boiling crisis under forced flow conditions ([24], [25]). It is obviously impossible to achieve a complete similarity using different fluids because of the limiting degree of freedom available for experimentation. During the CHF experiments four thermal-hydraulic parameters can normally be adjusted: pressure, mass flux, steam quality and heat flux.

The following pragmatic approach for the scaling of pressure, steam quality and heat flux assumes they should obey the following set of equations for identical geometry $D_{R12} = D_{water}$:

- Same vapor/liquid density ratio to scale the corresponding pressure p :

$$\left(\frac{\rho_l}{\rho_g} \right)_{R12} / \left(\frac{\rho_l}{\rho_g} \right)_{water} = 1, \quad (171)$$

- Same equilibrium inlet quality to determine the equivalent inlet temperature t_{inlet} :

$$\left(x_{eq}^{inlet} \right)_{R12} / \left(x_{eq}^{inlet} \right)_{water} = 1, \quad (172)$$

with equilibrium inlet quality defined as:

$$x_{eq}^{inlet} \triangleq \frac{h_l(t_{inlet}) - h_l(t_s)}{h_{fg}}, \quad (173)$$

- Same Boiling number to calculate the corresponding heat flux \dot{q}'' :

$$\left(\frac{\dot{q}''}{G \cdot r} \right)_{R12} / \left(\frac{\dot{q}''}{G \cdot r} \right)_{water} = 1, \quad (174)$$

Ahmad [2], *Cheng* and *Müller* [25] modeled critical heat flux with $\dot{q}'' = \dot{q}''_{crit}$.

Based on CHF test data obtained in seven different fluids, *Groeneveld et al.* [54] pointed out that the same Weber number is a reliable parameter to determine the corresponding mass flux G , instead of the mass flux ratio:

$$\left(\frac{G^2 D}{\rho_l \sigma} \right)_{R12} / \left(\frac{G^2 D}{\rho_l \sigma} \right)_{water} = 1. \quad (175)$$

Garnier et al. [50] used these four similarity criteria (Eqs. (171)-(175)) to find equivalent conditions scaling water to R12 for an identical geometry. Additionally, in the work of *du Bousquet* [41], which was referenced by *Garnier* and is related to nuclear engineering, the mass flux is obtained from an empirical correlation. Nevertheless, the authors pointed out that the *Weber* number scaling is consistent with results achieved from correlations. The same scaling numbers were later used by *Francois* and *Garnier* [48].

To consider the hydrodynamic of flow in CHF, *Ahmad* [2] derived the dimensionless number ψ_σ , using dimensional analyses in relation to the phenomenology of two phase flow:

$$\psi_\sigma = \underbrace{\left(\frac{GD}{\mu_l}\right)}_{\text{Reynolds number}} \cdot \underbrace{\left(\frac{\mu_l^2}{\rho_l \sigma D}\right)^{2/3}}_{\text{Weber-Reynolds number}} \cdot \underbrace{\left(\frac{\mu_g}{\mu_l}\right)^{1/5}}_{\text{viscosity ratio}} \quad (176)$$

and also wrote ψ_σ in the form of classical numbers by rearranging the above definition:

$$\psi_\sigma = \underbrace{\left(\frac{G^2 D}{\sigma \rho_l}\right)^{2/3}}_{\text{Weber number}} \cdot \underbrace{\left(\frac{GD}{\mu_l}\right)^{-2/15}}_{\text{Reynolds number of liquid}} \cdot \underbrace{\left(\frac{GD}{\mu_g}\right)^{-1/5}}_{\text{Reynolds number of gas}} \quad (177)$$

The ratio of the *Ahmad* number can be written as:

$$\psi_{\sigma,R12} / \psi_{\sigma,water} = 1. \quad (178)$$

The values of the exponents in Eq. (177) were obtained from experimental data of R12 and water at density ratio $(\rho_l / \rho_g) \cong 20$ and in a simple pipe geometry. But the author pointed out that this number is expected to be applicable to different types of fluids, density ratios, and geometries.

Eq. (177) was successfully applied and assessed to CHF by *Cheng and Müller* [25] in circular tubes and in wide square rod bundles.

In the same work for practical applications *Ahmad* [2] proposed to replace the *Weber-Reynolds* number in Eq. (176) by the *Barnett* number, because surface tension data for Freon compounds were not available or had a considerable scatter depending on sources (*E.I. DuPont*, [42]).

This proposal results in a number called the *CHF Ahmad* number for simplicity reasons:

$$\psi_{CHF} = \left(\frac{GD}{\mu_l}\right) \cdot \underbrace{\left(\sqrt{\frac{\gamma}{\rho_l D}} \frac{\mu_l}{D}\right)^{2/3}}_{\text{Barnett number}} \cdot \left(\frac{\mu_l}{\mu_g}\right)^{1/8}, \quad (179)$$

with

$$\gamma = \left| \frac{d(\rho_l / \rho_g)}{dp} \right| \text{ at saturation.} \quad (180)$$

The values of exponents were estimated once again. This new formulation of the *Ahmad* number, *CHF Ahmad* number was used by *Katsaounis* [74] and *VDI-Waermeatlas* [158] instead of the *Weber* number to obtain the mass flux ratio:

$$\psi_{CHF,R12} / \psi_{CHF,water} = 1. \quad (181)$$

4 Validation

It has to be noted, that the choice of the scaling laws (presented in greater detail in Appendix B), depending on their importance to CHF behavior and leading to its reduction from thirteen to four scaling numbers is of course a simplification violating the remaining scaling numbers. That is why the author called his model distorted, but supposed it is based on the most relevant parameters, measured during CHF experiments, i.e. CHF is assumed to depend only weakly on the remaining parameters.

However, such a scaling procedure neglects some other important parameters for two-phase phenomena, e.g. neglecting bubble-wall interaction has an important impact on bubble formation. The bubble bulk diameter is a required parameter to obtain the interfacial area and it does not appear in any of the used numbers (variable D = tube diameter). Bubble diameters estimated by means of dimensional analyses can be found in the literature. The diameter of the largest bubble which is stable against breakup in turbulent flow is defined by *Thomas* [149], assuming the *Weber* number for the bubble exceeding a critical value, based on *Kolmogorov-Hinzes'* ([81], [61]) prediction, as:

$$d_{\max} = \underbrace{\left(\frac{\sigma}{\rho_l} \right)^{3/5}}_{\text{Bubble Weber number}} \cdot \varepsilon^{-2/5} \quad (182)$$

and can be compared for both fluids, water and R12.

Assuming the same turbulence dissipation rate, the diameter of the largest water bubble at scaled conditions is five times larger than the diameter of the largest R12 bubble. This means that the critical bubble *Weber* number is the same if the maximum diameter of the bubble in water is five times larger. *Garnier et al.* [50] presented some measured radial distributions of the bubble diameter at the pipe outlet for sub-cooled boiling. The diameter of the bubbles is in the range from 0.1 mm to 0.5 mm. This data was obtained for different inlet and boundary conditions as the available radial void fraction distribution data. But the flow regime is supposed to be similar. The approximation for the values of the bubble diameter of water under scaled conditions at the outlet results in a range between 0.5 mm and 2.5 mm.

The variable bubble bulk diameters proposed in Sub-section 3.5.2 for nuclear applications in Eq. (124) can vary depending on different local liquid sub-cooling from 0.1 mm to 2 mm. It is assumed that the CFD results would match the measured results (radial void fraction profiles) better using larger diameters in the two-phase model proposed in Eq. (122), because of the scaling process.

The reason why scaling of the bubble diameter in the bulk is so important is that the interfacial area is reciprocally proportional to this diameter. Hence, the condensation mass flow rate in the bulk flow is influenced by the bubble diameter, resulting finally in the local (radial) void fraction dependent on the local bubble bulk diameter.

Application of the similarity criteria leads to the R12-Water equivalent conditions of Table 4.2. The ratios of the *Ahmad* number with both definitions were calculated for control. In the presented validation study the mass flux was calculated from the equivalence of *Weber* numbers, Eq. (175).

Table 4.2 R12 operating conditions and corresponding water flow characteristics

Parameters	Equation number	Unit	R12	Water
Pressure		bar	30	171.39
Mass flux		kg/m ² s	1025	1294
Heat flux		kW/m ²	66	923
Equilibrium inlet quality	Eq. (171)	-	[-0.84; -0.65]	[-0.84; -0.65]
Equilibrium exit quality	Eq. (172)	-	[-0.23; -0.03]	[-0.23; -0.03]
Vapor/liquid density ratio	Eq. (173)	-	4.6360	4.6360
Boiling number ratio	Eq. (174)	-	1	1
Weber number ratio	Eq. (175)	-	1	1
Ahmad number ratio	Eq. (178)	-	1.08	0.92
CHF Ahmad number ratio	Eq. (181)	-	1.05	0.95

4.2.2 Numerical method

4.2.2.1 CFD Model: geometry, inlet and boundary conditions

Detailed information about geometry and design of the experiment was achieved from the extensive work of *Garnier et al.* [50]. In this work inter alia, it was shown that the two-phase flow in a circular pipe is approximately axisymmetric. This symmetrical result justifies carrying out the numerical computations in an axisymmetrical domain. Applying *symmetry* boundary conditions to the azimuthal direction of the slice, the pipe model is reduced to a sector with an angle of $\Theta = 5^\circ$, radius $R = 9.6$ mm and heated length $L_h = 3.5$ m in a cylindrical coordinate system as presented in Figure 4.2.

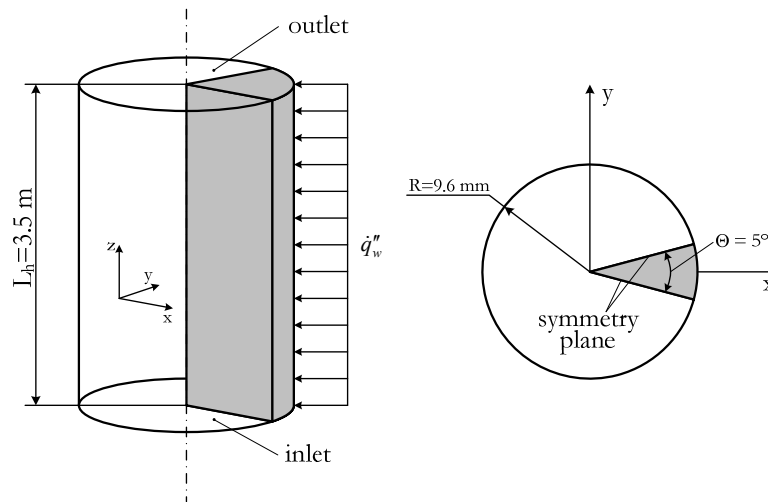


Figure 4.2 View of the pipe and its cross-section and boundary conditions

A uniform liquid flow was provided at the inlet area and the type *outlet* boundary conditions as the exit boundary. *Garnier et al.* [50] pointed out that the wall heat flux during experiment was almost constant, which is why a uniform heat flux can be applied to the *wall* boundary. The wall roughness is not taken into account.

Hexahedra are commonly known to give good numerical stability in the calculations. A first set of CFD calculations was carried out in cylindrical coordinates for a coarse mesh with 1x25x1750 hexahedral cells in azimuthal, radial and axial directions, respectively. Figure 4.3 shows a section of the CFD-model with the computational mesh.

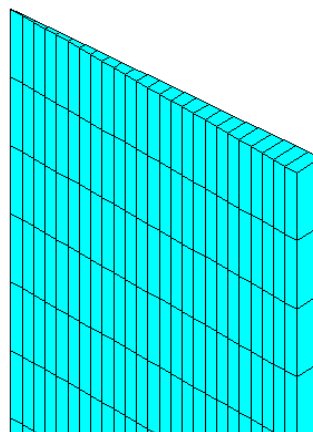


Figure 4.3 CFD model of the heated pipe. Computational mesh

The presented measurements of the void fraction at the outlet were carried out for 50 positions in radial direction. Therefore, the mesh shown in Figure 4.3 was refined later in radial direction to get 50 cells and additionally it was refined in axial direction (1x50x3500). The results were compared, showing that the results in the bulk are almost not changing with the refinement, but in the region near the wall the evaluated variables were different (increase of the void fraction at the wall). The fine mesh was chosen for the final calculations.

The calculations were performed at PWR operating conditions achieved after scaling of the inlet data of the measured fluid R12, taken from the paper of *Francois* and *Garnier* [48]. The scaling procedure from R12 experiment inlet data to water-steam CFD calculation inlet data was already described in Section 4.2.1.

In [48], for each analyzed case with various void fraction distributions at the outlet for different sub-cooling the average system pressure and mass flux were given, but the corresponding uniform heat flux was missing for a few cases. These missing parameters, as well as individual measurements of the inlet system pressure, mass flux and sub-cooling, uniform heat flux and outlet equilibrium quality corresponding to each void fraction profile at each case were obtained via private communication with *Francois* [47]. The inlet data for an example case is presented in Table 4.2.

The inlet vapor volume fraction was taken as a very small value of 10^{-4} , as zero values are not allowed by the code. The physical inlet conditions e.g. density, heat conductivity, viscosity, specific heat, temperature, were chosen as described in Section 3.6.

4.2.2.2 Numerical analyses

This study used the commercial CFD code, STAR-CD version 3.27, to solve the coupled system of governing equations with constitutive equations and closure models for two-phase turbulent flow in a heated pipe. The calculations are carried out as steady state. The numerical treatment, with the used discretization schemes, for convection and diffusion terms (UDS) and the solution algorithm for velocity-pressure coupling (SIMPLE), was presented in Chapter 2.4. The linearized difference equations for the pressure-correction, volume fraction and enthalpy were solved by the algebraic multi-grid method (AMG) as preconditioner [136]. The iterative calculation was continued until the residuals of all governing equations (except the dissipation of the liquid turbulent kinetic energy) were less than 10^{-4} or 10^{-5} .

By parameter variation the impact of the interfacial lift force, lubrication force, turbulent dispersion force, mean bubble diameter, bubble departure diameter, nucleation site density and frequency on the closure models was analyzed. These parameters are known to have a large influence on the phase distribution in a boiling two-phase bubbly sub-cooled flow [68].

The best agreement was found, when the lift force \vec{F}_k^L and lubrication force \vec{F}_k^W (modeled by Eqs. (85) and (86), respectively) were assumed to cancel each other out. Then the remaining forces are the turbulent dispersion \vec{F}_k^T , drag force, set by user subroutine *udrag.f* (see Table 3.3) and the virtual mass with the standard coefficient $C_{VM}^{STAR} = 0.5$. It has to be noted that the bubble

4 Validation

bulk diameter as well as the response coefficient in the two-phase $k-\varepsilon$ turbulence modeling for the first studies is assumed to be constant ($d_b = 1$ mm and $C_t = 1$, respectively). Later, the variable bubble diameter defined by Eq. (122) is used with different parameters and the response coefficient is applied as function of the local void fraction defined by Eq. (102). The bubble departure diameter is modeled by Eq. (130). At saturation temperature for the liquid it results in $d_s = 0.6$ mm. All other parameters are described in detail in Chapter 3.

4.2.3 Results and discussion

4.2.3.1 Model with coarse mesh

The calculated radial void distributions in the heated pipe are compared with the measured ones. The measurements were performed at the outlet for different sub-cooling of the inlet fluid, as shown in Figure 4.1. Lift and lubrication forces were varied for two cases with high and low inlet sub-cooling to achieve the best agreement in the region near the wall.

The best agreement was achieved for balanced lift and wall lubrication forces.

After that, all other curves were also calculated with this assumption. For illustration, a calculated 2-D void fraction distribution for outlet quality $x_{eq} = -0.0835$ is presented in Figure 4.4 (note that the axial length scale is compressed for a clearer view).

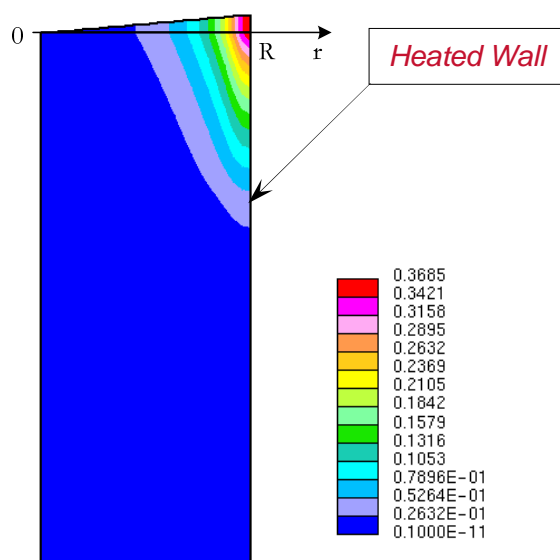


Figure 4.4 2-D void fraction distribution for $x_{eq} = -0.0835$ (STAR-CD calculation, coarse mesh)

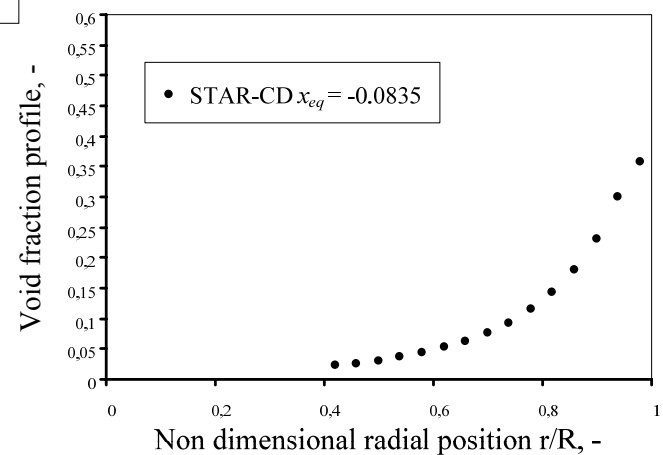


Figure 4.5 Radial void fraction distribution for $x_{eq} = -0.0835$ at the outlet (STAR-CD calculation, coarse mesh)

It can be seen that the *Onset of Nucleate Boiling* occurs in the second half of the model length and that even at the outlet the bubbles are almost fully condensed in the center region of the pipe. This is also shown in the Figure 4.5, presenting the radial distribution of the void fraction at the outlet.

The calculated radial distributions of the local void fraction at the outlet are compared to the measured values for six different inlet sub-cooling conditions. Figure 4.6 shows the corresponding radial void distribution curve for each measured value of equilibrium quality at the outlet: filled and empty squares represent computational result and experiment, respectively.

Qualitatively, the shapes of the curves are in quite good agreement. For experimental results with bubble accumulations at the rod surface with a void fraction less than 30 % (first four curves), very good quantitative agreement is achieved in the near wall region. This indicates that the bubble physics is still applicable. For lower sub-cooling the calculated values significantly overestimate the void fraction at the wall, but the agreement in the center of the pipe is better.

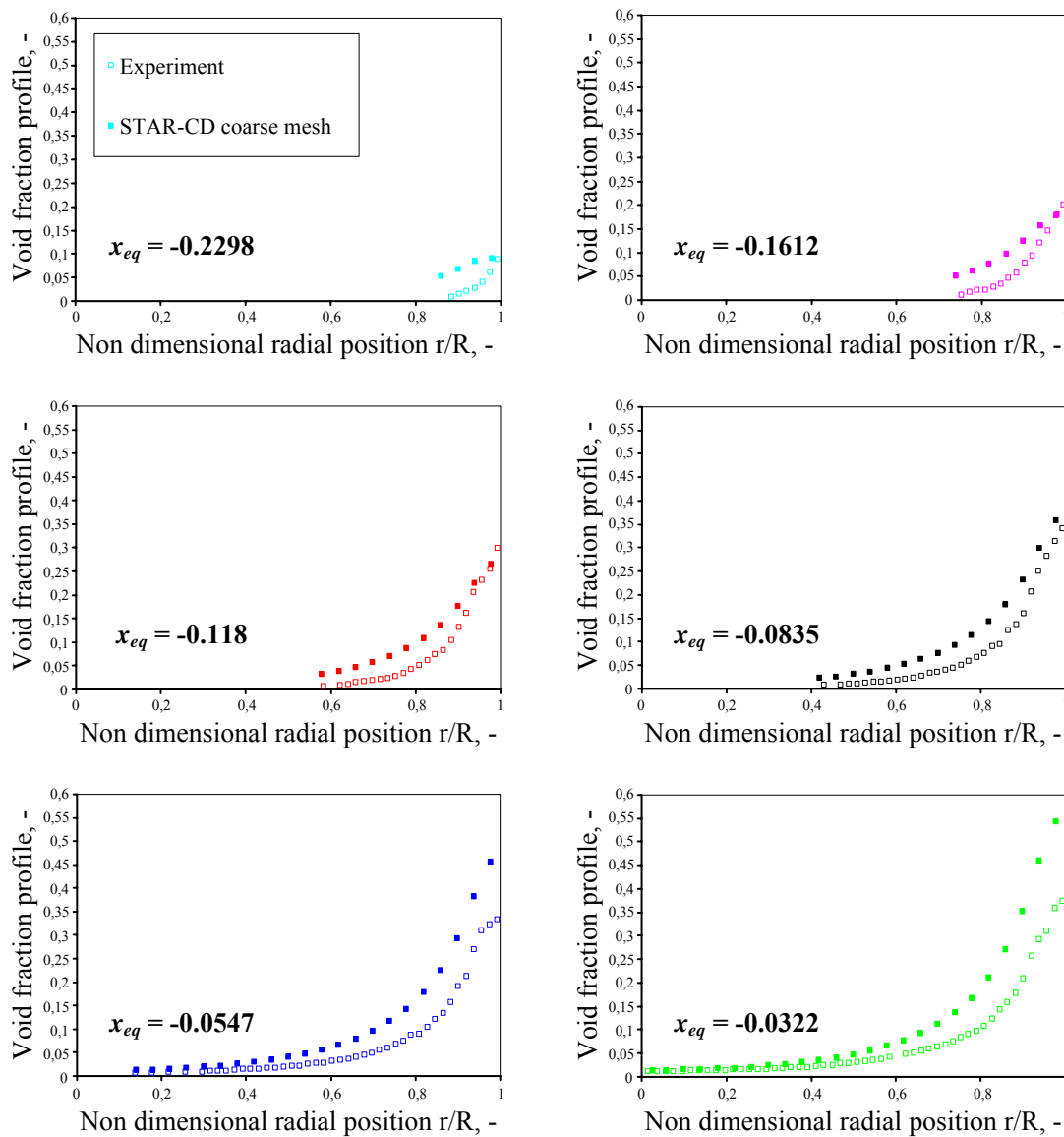


Figure 4.6 Radial void fraction distribution at the outlet for various x_{eq} at the outlet. Measured data of Garnier (empty squares) compared to results of the STAR-CD calculations with coarse mesh and $d_b = 1$ mm (filled squares)

4 Validation

As a next step the refinement of the computational mesh was carried out to exclude numerical deviations caused by too coarse mesh size.

4.2.3.2 Model with fine mesh

In the second set of simulations, the mesh was refined so that the number of radial nodes in the computational mesh is equal to the number of measured points: in the experiment 50 points along the radius were considered. Two-phase parameters as interfacial forces (lift force coefficient, drag force formulation and coefficient), turbulence (turbulence response coefficient) and boiling parameters (nucleation density, boiling model constant, bubble departure diameter) were varied for the chosen case with outlet quality $x_{eq} = -0.118$ (intermediate sub-cooling with respect to considered cases). The detailed results of these parameter variations can be found in Appendix B.

The main conclusion of this parameter study is that considering the constant bubble diameter the best agreement in the bulk can be achieved by applying the standard two-phase parameter set, which was proposed by STAR-CD in two-phase tutorials and partly described in the presented validations [147], [148] and [161]. The main difference to these validations is that the best results were achieved assuming the compensation of the wall lubrication and lift forces in the whole flow domain. Variations of all other parameters take this assumption into account.

Almost all parameters except the bubble departure diameter have not shown a large influence on the radial void distribution. The value of the departure diameter at the wall at saturation temperature was proposed by CD-adapco to be set to 0.6 mm. This value was found to be important for the radial void profile and proved to be the most suitable for the chosen validation cases. Figure 4.7 shows, for each measured value of equilibrium quality at outlet, the corresponding radial void distribution curve: filled and empty squares present computational result and experiment, respectively. The violet triangles represent the coarse mesh. The evaluations assume a constant bubble bulk diameter of 1 mm.

The refinement shows almost no changes with regard to the calculated local void fraction in the bulk flow for all cases. Therefore, the influence of the numerics on the results in this region is assumed to be negligible. For the region near the wall the refinement leads to higher voids at the wall. If these values at the wall are compared to the measured ones it can be seen that the refinement leads to an improved agreement with the measured data at the wall for the first three cases. For the other three cases the refined results overestimate void at the wall more than the coarse ones.

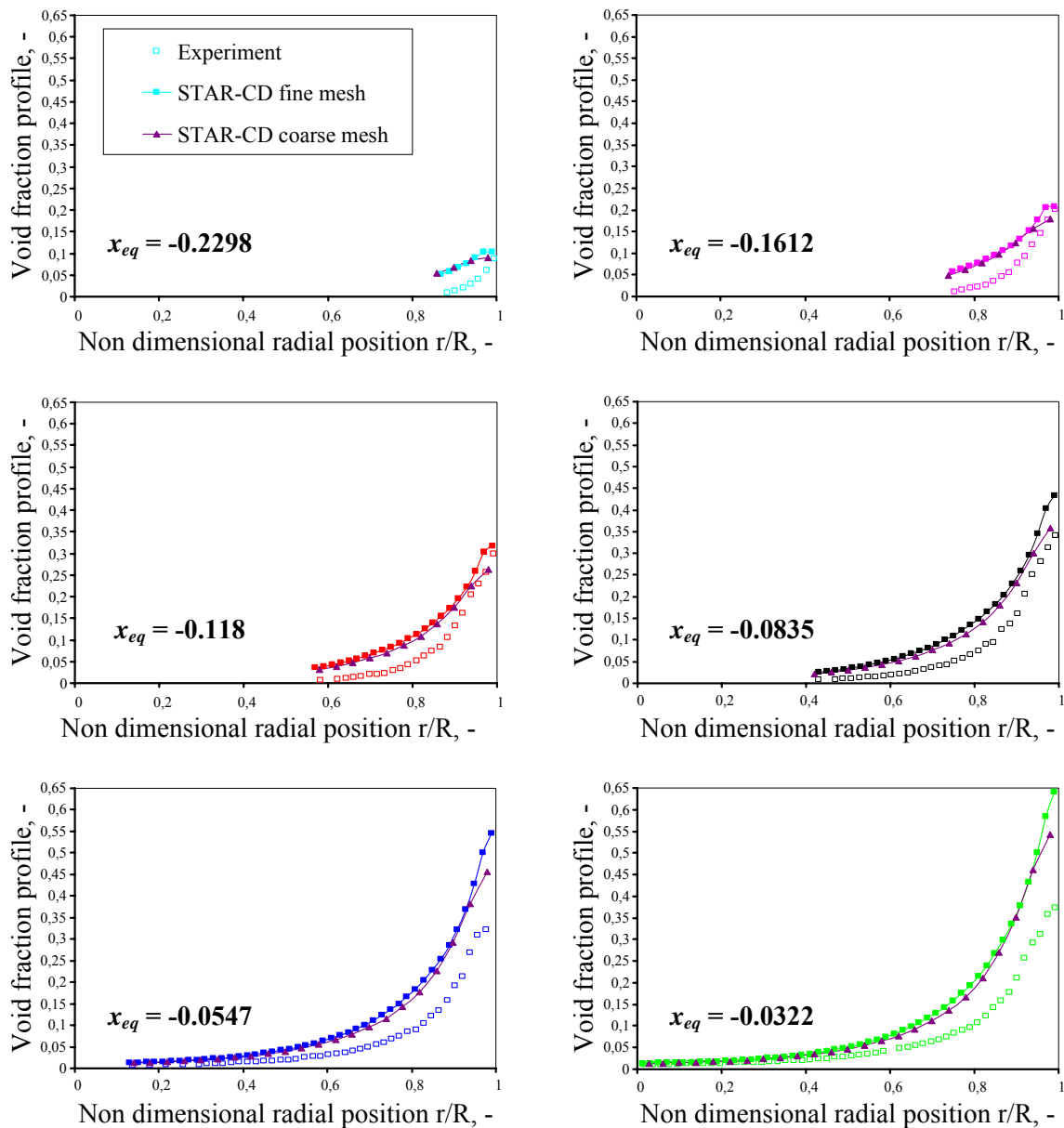


Figure 4.7 Radial void fraction distribution for various x_{eq} at the outlet. Measured data of *Garnier* (empty squares) compared to results of the STAR-CD calculations (filled squares) with fine mesh and with coarse mesh (violet filled triangles). With constant $d_b = 1$ mm

Generally it can be concluded, that the mesh refinement did not significantly improve the agreement of calculated and experimental results. Furthermore, there is almost no difference in the radial void profile resulting from coarse or fine mesh, except for the cells adjacent to the wall. The calculated evaporation at the wall seems to be mesh dependent with the tendency of higher void fraction for the refined mesh.

Looking at the bulk region (for $r/R > 0.4$), an overestimation of the void fraction is observed generally. Because the void fraction at the wall is in reasonable agreement with the experimental data (in the first four cases), it is concluded that in these cases condensation is underestimated. The condensation rate is strongly dependent on the interfacial area, which was

4 Validation

derived from the simple approach of a model with a constant bubble diameter in the whole flow domain (Eq. (115)).

It seems that the interfacial area is underestimated. As an improvement a variable bubble diameter following [86] and [98] (resulting in a higher interfacial area) was applied.

4.2.3.3 Variable bubble bulk diameter

Kurul and Podowski [86] described the bubble diameter in the bulk as a function of the local liquid sub-cooling. It was presumed that the bubble size grows with increasing local liquid temperature and is linearly interpolated between two values of diameter at high and low sub-cooling, described with Eq. (121). Based on this idea, Eq. (122) was used e.g. in [98] for nuclear applications, where the bubble diameter is calculated by linear interpolation between $d_0 = 0.15$ mm at liquid sub-cooling of $\Delta T_0 = 13.5$ K and $d_1 = 2$ mm at liquid sub-cooling of $\Delta T_1 = -5$ K. In the current version [137] the value of the bubble bulk diameter at high sub-cooling was changed to $d_0 = 0.1$ mm. The applied set of coefficients was presented in Eq. (125).

Comparing the void distribution achieved from this modeling with the result of the simulation with a constant diameter of 1 mm and with the experimental results for the chosen case with outlet quality $x_{eq} = -0.118$ presented in Figure 4.8, significant underestimation of the void fraction is observed in the whole calculation domain. This could indicate too high condensation and overestimation of the interfacial area.

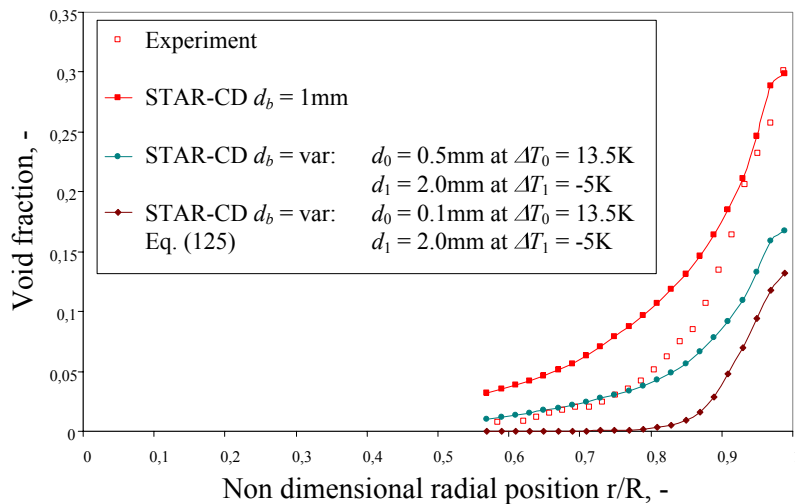


Figure 4.8 Radial void fraction distribution for $x_{eq} = -0.118$ at the outlet for various d_b

Next, the diameter at high liquid local sub-cooling was increased to better fit this region. This becomes necessary because of the scaling process of the experimental R12 data described in Section 4.2.1. The diameter at high sub-cooling was assumed to be 5 times larger than the measured bubble size for R12 of 0.1 mm, leading to a diameter of 0.5 mm. Using the same

formulation for variable diameter, with the bubble diameter of the high sub-cooling increased from 0.1 mm to 0.5 mm, allowed to describe the bulk region much better, as it can be seen in Figure 4.8. The void fraction at the wall region is too small because the condensation might be too high here, but in the bulk region the void prediction is better.

In order to fit the profile, the bubble diameter has to be optimized. Taking into account the scaling procedure between water and R12 and the particular operation conditions, all four parameters d_0 , d_1 , ΔT_0 and ΔT_1 were considered.

Eq. (183) shows the parameters leading to the best agreement with the experimental data for the void fraction distribution of the chosen case (see Figure 4.9):

$$\begin{cases} d_0 = 0.0003 \text{ m} & \text{for } \Delta T_0 = 26 \text{ K} \\ d_1 = 0.0025 \text{ m} & \text{for } \Delta T_1 = 22 \text{ K} \end{cases} \quad (183)$$

The illustration of the Eq. (183) is shown in Figure 4.12.

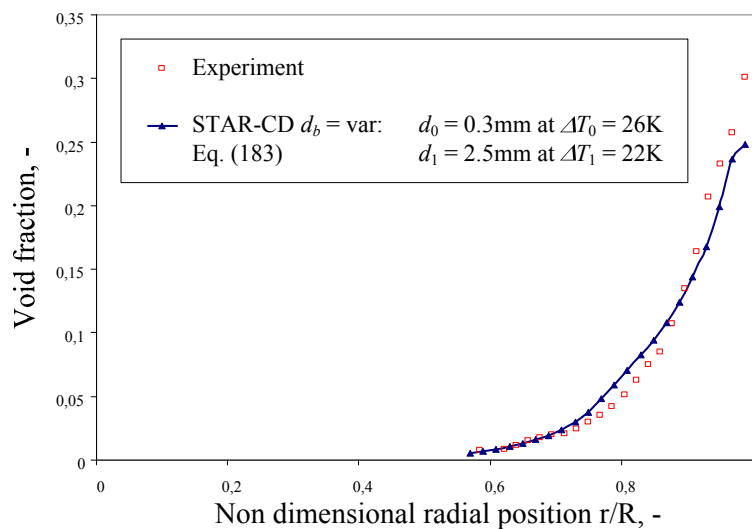


Figure 4.9 Radial void fraction distribution for $x_{eq} = -0.118$ at the outlet for the parameters fitting best the experiment values

Further, the optimized parameter set for the variable bubble diameter model was applied to a second case with outlet quality $x_{eq} = -0.1612$ (higher inlet sub-cooling). The void profile resulting from these optimized parameters was compared to the experimental data, to the profiles resulting from constant bulk diameter and to the profiles resulting from parameters for a variable diameter applied in [137]. Figure 4.10 shows a significant improvement and excellent agreement with the experiments for optimized model parameters in the whole cross-section, i.e. both bulk and wall region at the outlet.

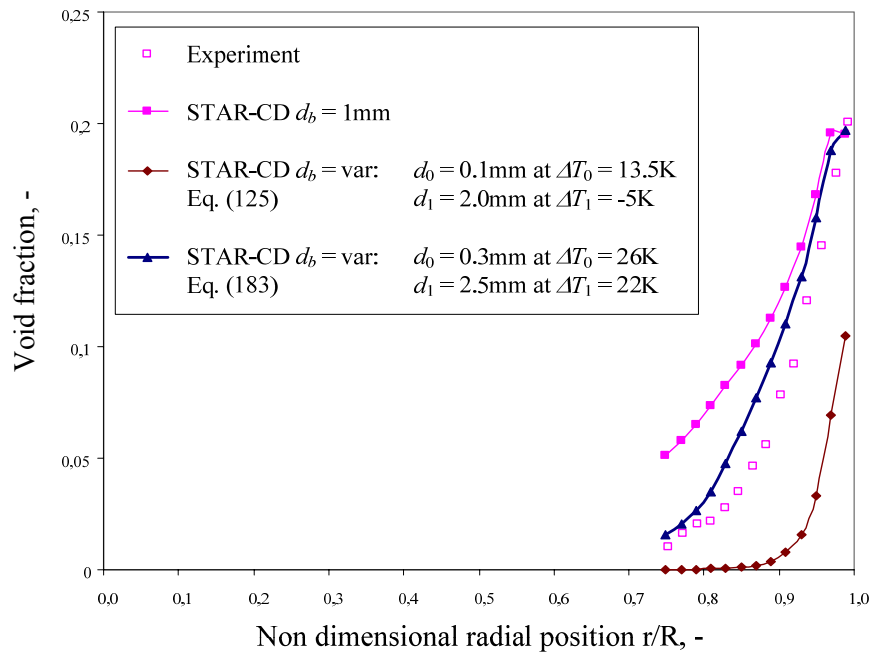


Figure 4.10 Radial void fraction distribution for $x_{eq} = -0.1612$ at the outlet for various bubble diameters

The diameter model according to Eq. (183) describes the local void distribution at sub-cooled boiling very well. To examine this formulation in the region near saturated boiling, the case with $x_{eq} = -0.0322$ is chosen. Comparing the void distribution achieved from the proposed modeling with the result of the simulation with constant diameter of 1 mm and with the experimental data, presented in Figure 4.11, shows a too high void fraction, caused by a too low condensation rate in the whole flow domain.

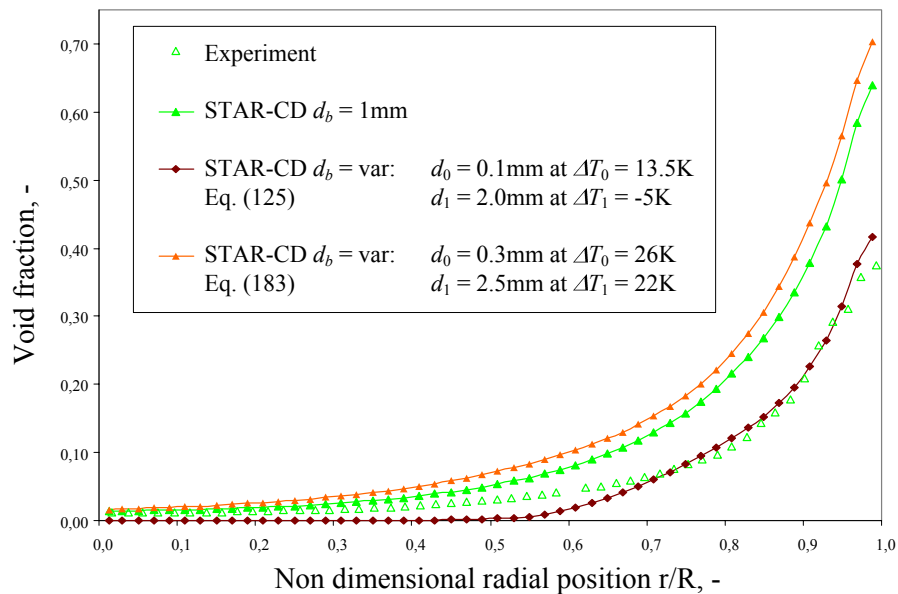


Figure 4.11 Radial void fraction distribution for $x_{eq} = -0.0322$ at the outlet for various bubble diameters

In contrast to the cases with higher sub-cooling the common formulation for variable diameter presented in Eq. (125) shows excellent agreement with experimental data for the case with high quality. Only in the bulk region the condensation is slightly overestimated.

To get the perfect fit for this flow conditions, Eq. (122) was used with new parameters. Bubble diameters d_0 and d_1 were calculated from Eq. (121), the first formulation of the *Kurul* and *Podowski* [86], at $\Delta T_{sub} = \Delta T_0 = 10$ K for high sub-cooling and at saturation $\Delta T_{sub} = \Delta T_1 = 0$ K at low sub-cooling, respectively. As it is well illustrated in Figure 4.12 the function for the bubble diameter remains the same but the cut-off limits are changed. The resulting coefficients are following:

$$\begin{cases} d_0 = 0.0004 \text{ m} & \text{for } \Delta T_0 = 10 \text{ K} \\ d_1 = 0.0014 \text{ m} & \text{for } \Delta T_1 = 0 \text{ K} \end{cases} \quad (184)$$

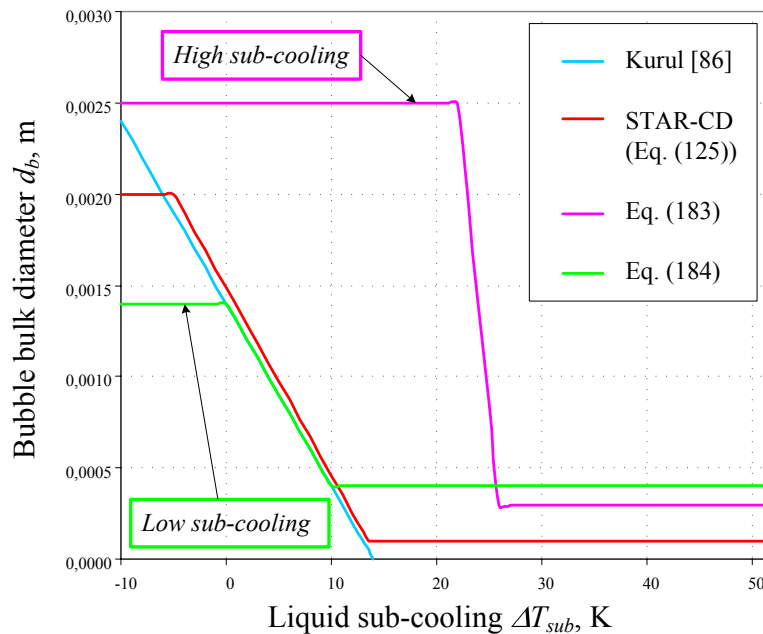


Figure 4.12 Variable bubble bulk diameter as a function of the liquid sub-cooling. New coefficients for various regimes of sub-cooling

Figure 4.13 presents the computed void distribution, which agrees very well with the experimental data. It seems that the formulation of *Kurul* and *Podowski* [86] was evaluated for such cases beginning with sub-cooled boiling and extending close to saturation boiling, which is typical for PWR conditions. For the high sub-cooling regions this formulation significantly underestimates the void fraction.

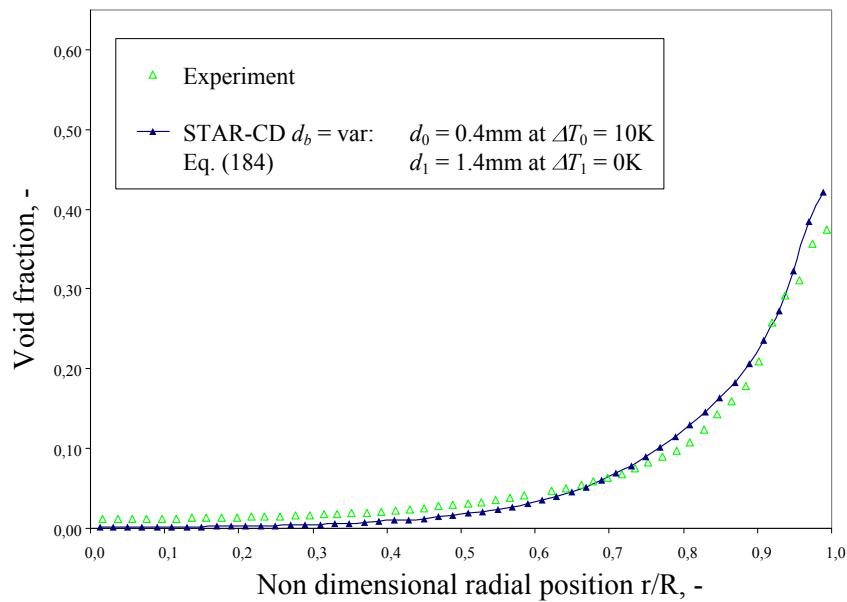


Figure 4.13 Radial void fraction distribution for $x_{eq} = -0.0322$ at the outlet. Best agreement with experimental values

The proposed parameters in this thesis by Eq. (183) are good for high sub-cooling, but with increasing equilibrium quality at the outlet it begins to overestimate the void fraction.

The results indicate that it might not be sufficient to look only for a correlation between bulk bubble diameter and the local sub-cooling. An extended development of the additional transport equation for the bulk bubble diameter and interfacial area, like the MUSIG model of *Lo* [97] or the *Ishii* and *Mishima* modeling [71] would be a more general approach.

4.2.4 Conclusions

The numerical model describing simple bubble physics (e.g. no coalescence or break up) is valid for void fractions up to 20 - 30 %. For these void fractions the validation of the *Garnier* experiment showed that the two-phase STAR-CD model considering the bubbly flow regime achieves good agreement for radial void distributions. A constant bubble diameter in the bulk was applied in these CFD calculations. Variation of two-phase parameters showed that the standard set is applicable for the considered cases. The lift and lubrication forces are assumed to be balanced to get the best agreement with the experimental data. While the calculated values of the local voids at the wall were in very good agreement, the bulk values were overpredicted. Application of a variable diameter as a function of the liquid sub-cooling and fitted coefficients made the agreement excellent for the cases with various maximum local void fractions up to circa 40 %.

Depending on the sub-cooling different models for the variable bubble diameter in the bulk have to be chosen:

For *high sub-cooling* the formulation of the variable diameter with cut-off points at higher sub-coolings and with larger diameters compared to standard parameters of this model should be used. Such parameter set is presented in Eq. (183) resulting in void fraction profiles similar to the measured ones in the whole calculated domain. For such high sub-cooled cases the standard coefficients lead to too small diameters (in high sub-cooled regions), as the linear increase of the bubble diameter almost does not occur with cut-off points chosen in that way. This leads to too high condensation and finally to a strong under-estimation of the void fraction.

For *low sub-cooling* with near saturation flow conditions at the outlet, standard coefficients can be used. For the validated case such coefficients provide very good agreement with the measured data, only the bulk region could be slightly improved by adjusting the diameter formulation to reduce the condensation in the bulk. This was reached by a new parameter set with larger diameters in the bulk region for smaller sub-coolings, which was presented in Eq. (184). For the following calculations of the sub-channel under PWR conditions the standard coefficients for the formulations of the variable bubble diameter are used if the outlet conditions are near saturation or slightly superheated.

However, using R12 data for validation of the two-phase water-steam model is an approximation. In the validations performed here, the geometry is a simple pipe and the heat flux is near non-CHF PWR conditions. The main field of interest of the nuclear industry is the use of CHF experiments carried out with R12 instead of water experiments for bundle geometry, applying reliable scaling theory. Already a lot of work has been done in this direction, but with conflicting conclusions. *Katsaounis* [74] showed the *Ahmad* scaling laws to be valid for 3x3 and 5x5 bare rod bundle in PWR geometry at mass flow rates higher than 1000 kg/(m²s) and for the same bundle with spacer grids. On the other hand *Chen et al.* [26] compared CHF data for R12 and water for 4x4 bundle experiment scaled by various fluid-to-fluid models, e.g. *Ahmad* and *Groeneveld*, and found out all models overpredicting the CHF data for water and the spacer grid effect to be different.

In summary, the current approach is promising, but more work has to be done before a reliable industrial applicability can be achieved. The large amount of available experiments carried out with refrigerants can be used in the future for a better understanding of the two-phase flow phenomena e.g. CHF.

4.3 Critical heat flux considerations based on pipe flow

4.3.1 Theoretical background and motivation

During thermal-hydraulic design analyses of the light-water reactor fuel assemblies the compliance with the following three criteria have to be satisfied [116]:

- Unrestricted reusability of the fuel assemblies,
- Exclude nuclear fuel melting to avoid excessive fission gas release and fuel relocation,
- Cladding temperature shall not exceed material dependent critical values to avoid excessive corrosion or melting. This can be assured by sufficient cooling of fuel rods and avoiding critical boiling conditions i.e. CHF at both reactor operation and transient conditions.

If some improvement of the CHF performance of light-water fuel assemblies is achieved, it can be used to increase the safety margins, to enlarge the radial and axial peaking or to enhance the reactor power. The latter two would lead to a better economic efficiency of the nuclear plant.

Reaching the critical heat flux leads to a rapid decrease of the heat transfer from fuel rod cladding to the coolant. Depending on the flow conditions (pressure, mass flux and enthalpy) two different mechanisms are possible:

- Dry out: This is typical for BWRs at high equilibrium qualities and is schematically presented in Figure 4.14. Close to CHF conditions the fuel rod is cooled by a water film on the cladding surface, while steam flows in the center of the sub-channel with higher velocity. Reaching CHF leads to a dry out of the water film on the cladding surface. This results in a rise of the cladding temperature due to decreased heat transfer.
- Departure from nucleate boiling (DNB): If during nucleate boiling the heat flux reaches the critical value where vapor bubbles are generated faster than they are detached or condensed, a vapor film is formed on the cladding surface. Due to its thermal insulation the heat transfer is strongly decreased and the cladding temperature increases rapidly. For such a situation, DNB is schematically presented in Figure 4.15 and is typical for PWR conditions studied in this work.

According to the present knowledge there is no physical model available that describes these two effects for the full range of flow conditions for light-water reactors accurately enough to predict the critical heat flux. Therefore correlations based on experimental results at various conditions are developed for design and licensing purposes. Furthermore, for any design change that may influence CHF performance new test series are necessary to prove that the existing correlation is applicable; or to be the base for the development of a new correlation.

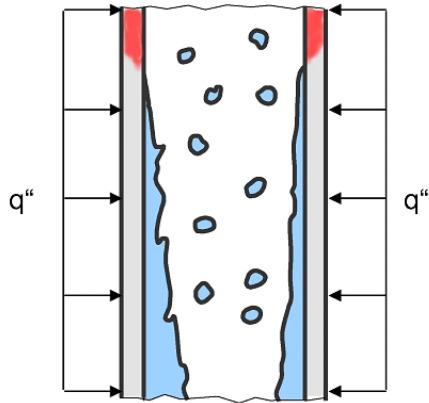


Figure 4.14 Dry out

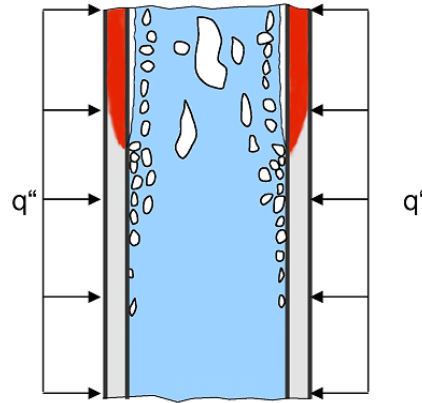


Figure 4.15 Departure from nucleate boiling (Burn out)

CFD may provide new possibilities in this field. A multitude of designs can be modeled and calculated in a relatively short time. Only the most promising design variants would undergo the expensive experimental CHF tests. Such goal can be achieved only with a realistic two-phase flow modeling of the CHF phenomena. Even if the critical heat flux still can not be predicted with sufficient accuracy by CFD codes, some two-phase parameters (criteria) possibly could be found to support optimization work.

The first step in this direction is to assess the potential of the recent STAR-CD version in two-phase modeling and to find possibilities for improvement. Within the framework of this study such analysis has been performed for DNB at physical conditions of PWR. Due to the similarity of the CHF phenomena in sub-channel and in pipe flow, the upward flow in a heated pipe system was chosen to simplify the numerical model. Critical values were achieved from the suitable empirical correlation of *Doroshchuk* for DNB in a vertical pipe flow, which is presented in following.

CHF formulation of *Doroshchuk*. Scope of validity:

As it was mentioned before the CHF correlations for light-water reactors are derived from series of measurements under varying conditions to obtain a mathematical form relating various parameters, such as local equilibrium quality, mass flow rate, pressure, geometrical parameters (type of the sub-channel hydraulic diameter, rod diameter, pitch, and distance from spacers), power distribution, etc. to CHF. The number of such correlations only for a simple geometry of the pipe flow is extremely high (~ 400) and almost every correlation is valid only for a narrow range of parameter values.

One such empirical correlation for a water-steam mixture was proposed by *Doroshchuk et al.* [34] for uniformly heated circular pipe flow at high pressures and mass fluxes, obtained from a large experimental data base also summarized as a look-up table. Later, *Drescher* and

4 Validation

Köhler [37] proved that this correlation represents DNB phenomena better than other known correlations and is consistent with ~ 3000 experimental data points [159]. Critical heat flux \dot{q}''_{crit} given in kW/m² is presented in this equation as a function of system pressure p , mass flux G , pipe cross-section averaged equilibrium quality at critical point x_{eq}^{crit} and a hydraulic pipe diameter D :

$$\dot{q}''_{crit} = 10^3 \left[10.3 - 17.5 \left(\frac{p}{p_{crit}} \right) + 8 \left(\frac{p}{p_{crit}} \right)^2 \right] \cdot \left(\frac{8 \cdot 10^{-3}}{D} \right)^{0.5} \left(\frac{G}{1000} \right)^{0.68} \left(\frac{p}{p_{crit}} \right)^{-1.2} x_{eq}^{crit}^{-0.3} \cdot e^{-1.5 x_{eq}^{crit}} \quad (185)$$

The area of validity for this equation is given in Table 4.3. The PWR conditions at which CHF tests are carried out are inside this area of validity.

Table 4.3 Dimensions and valid ranges of different parameters

Parameter	Symbol	Unit	Validity
Pressure	p	bar	[29; 200]
Mass flux	G	kg/(m ² s)	[500; 5000]
Inlet liquid sub-cooling	ΔT_{sub}^{inlet}	K	[0; 75]
Pipe diameter	D	m	[0.004; 0.025]

The error between the original experimental results and its approximation by Eq. (185) was given in [159]. The ratio of the calculated values of CHF to the measured ones shows a mean value of 0.99 and a r.m.s. deviation of 16 %. Maximum deviations occur near the limits of validity.

Eq. (185) was used in this work to evaluate the CHF in a pipe flow for chosen conditions. Afterwards, the achieved CHF values were compared with the experimental results to find the error for the cases considered in this work. The calculated relative error is less than 2 %.

CHF experiment. Boiling- or Nukijama-curve:

The relation between the heat flux transferred from the heating surface to the coolant and superheating of the wall surface is called *boiling-curve*. Figure 4.16 shows the experimental results of the boiling-curve for water at normal steady-state conditions for the case of pool boiling, also named after its inventor *Nukijama-curve*. In this experiment the system was heat flux controlled; the heat flux was changed stepwise.

Nucleate boiling begins only if there is a certain degree of wall superheating (point **A**). Point **B** shows the critical heat flux, the maximum heat flux for which stable nucleate boiling occurs.

If the heat flux is increased beyond point **B** there is a jump from point **B** to point **D** with a significant increase of the wall temperature (DNB) and the beginning of film boiling, such that the boiling curve branch (points **B-C-D**) can not be obtained. The described process of the step-wise increase of the heat flux follows the red arrows in Figure 4.16.³

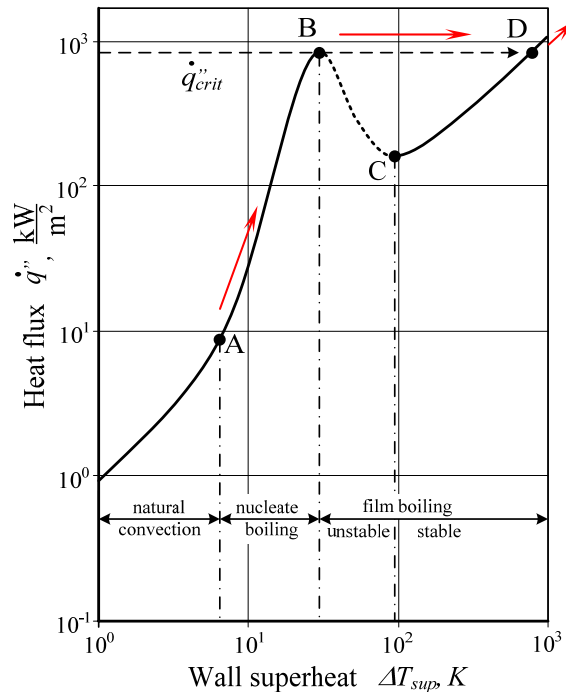


Figure 4.16 Nukijama-curve for pool boiling at 1 bar (adopted from [158])

Under forced convection conditions, the heat flux controlled measured boiling-curve follows a similar step-like temperature increase. A schematic example of such boiling-curve for the flow in a pipe at 100 bar is presented in Figure 4.17. Under high pressures and forced convection the boiling-curve exceeding the CHF is not so steep and the temperature increase can be not as high as for the pool boiling under normal conditions.

In case of the pipe geometry, the critical heat flux depends on the thermal hydraulic conditions (see also *Doroshchuk* formulation). Some differences due to the influence of the flow motion added to the buoyancy effects can be seen using the temperature controlled experiments. The experimental results for a system with stepwise changing wall temperature, presented in Figure 4.18 (effect of stored energy is neglected), show the influence of the mass flux on the boiling-curve under a pressure of 155 bar (~ PWR conditions). It can be seen, that the difference between heat fluxes in points **B**, **C** and **D** is relatively small and point **C** cannot be defined well.

³ Point **C** in Figure 4.16 corresponds to the minimum stable film boiling (MSFB) temperature, which can be achieved only by a decreasing power transient

4 Validation

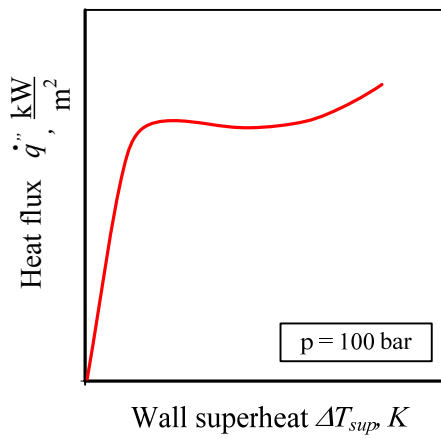


Figure 4.17 Schematic boiling-curve for flow boiling at 100 bar (adopted from [106])

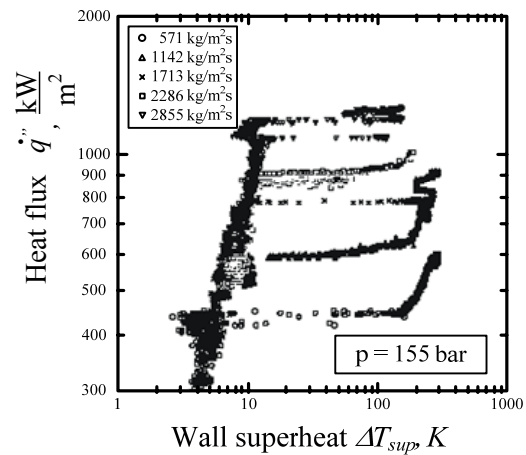


Figure 4.18 Measured boiling-curves for flow boiling in tube experiments at 155 bar (adopted from [65])

4.3.2 Numerical method

4.3.2.1 CFD Model: geometry, inlet and boundary conditions

The important challenge for nuclear applications is to prove the possibility of CFD codes to predict CHF for real rod bundle geometries. The comparison could be carried out based on the experimental results for 5x5 rod bundle experiments. For CFD two-phase calculations such a model needs a high number of cells for discretizing (e.g. to resolve the geometry of real spacers requires about 20 Million cells for just one spacer span) and is very time-consuming. Therefore, for the first study a pipe geometry with vertical inlet flow was chosen at PWR conditions and with the pipe diameter similar to the sub-channel hydraulic diameter.

In the calculated cases the critical heat flux should be applied. The wall temperature is expected to increase strongly for all performed cases at the critical point, where the critical equilibrium quality averaged over the pipe cross-section is reached. In the CHF experiments the heat flux is increased in small discrete steps and the wall temperature is measured. After the CHF is reached, the experiment is stopped to avoid damage of the rods.

For pipes the experiment is carried out in a similar way. It is supposed that the general conclusions that would be achieved for pipe flow in this thesis could be applied analogously to sub-channel flow.

Detailed information about geometry and design of the pipe experiment was not available. Assuming the flow in the pipe to be axisymmetric, the pipe model is reduced to a sector with an angle $\Theta = 5^\circ$ (see Figure 4.19) and *symmetry* boundary conditions are applied to the sides of the slice (see also Sub-section 4.2.2.1).

CFD calculations are first carried out for 1x20x2500 hexahedral cells in azimuthal, radial and axial directions, respectively.

The CFD-model with the computational mesh looks the same as shown in Figure 4.3.

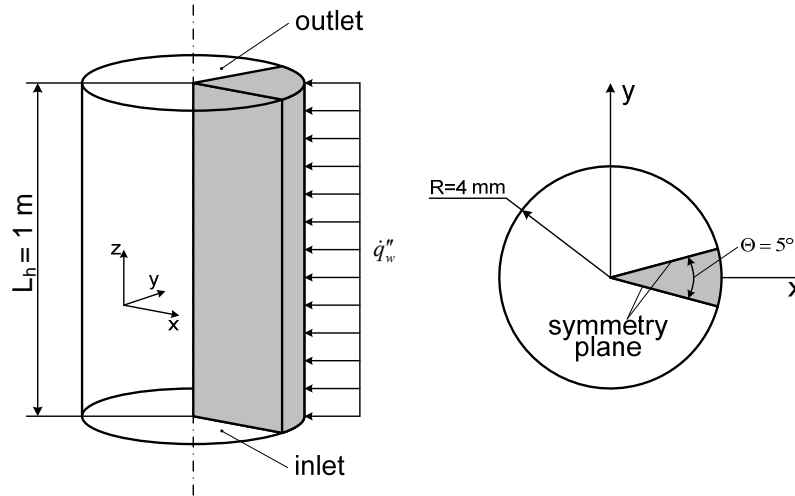


Figure 4.19 View of the pipe and its cross-section. Boundary conditions. Critical experiment

To cover the whole region of interest for the PWR CHF-experiments thirteen flow situations with various conditions presented in the Table 4.4 were chosen for the first calculations.

Table 4.4 Conditions for the pipe flow validation at critical heat flux conditions

Parameter	Symbol	Unit	Values
Pressure	p	bar	100, 125, 160
Mass flux	G	kg/(m ² s)	1500, 2000, 3000
Critical equilibrium quality averaged over the pipe cross-section at outlet	x_{eq}^{crit}	-	0.05, 0.1, 0.15

The ratio $(8 \cdot 10^{-3} / D)^{0.5}$ in Eq. (185) takes into account pipe diameters that are different from $D = 8$ mm. To avoid such geometrical approximation a pipe radius of $R = 4$ mm was chosen.

The wall surface was uniformly heated with a critical heat flux obtained from Eq. (185) with $\dot{q}_{crit}'' = f(p, G, x_{eq}^{crit}, D)$. The critical heat flux for the chosen thirteen points is in the range between 765 and 1950 kW/m².

The heated length $L_h = 1$ m is chosen after some trials assuming the single-phase flow at the inlet of the CFD model as under PWR conditions and CHF conditions occurring at the outlet of the model for all calculated points. The equilibrium quality at the inlet boundary was obtained from the following relation, derived in Appendix C:

$$x_{eq}^{inlet} = x_{eq}^{crit} - \frac{4 \cdot \dot{q}_{crit}''}{D \cdot G \cdot r} \cdot L_h \quad (186)$$

4 Validation

Figure 4.20 shows the dependency of the equilibrium quality averaged over the sub-channel at the inlet on the critical equilibrium quality averaged over the sub-channel and occurring at the outlet at 1 m for various pressures and mass fluxes.

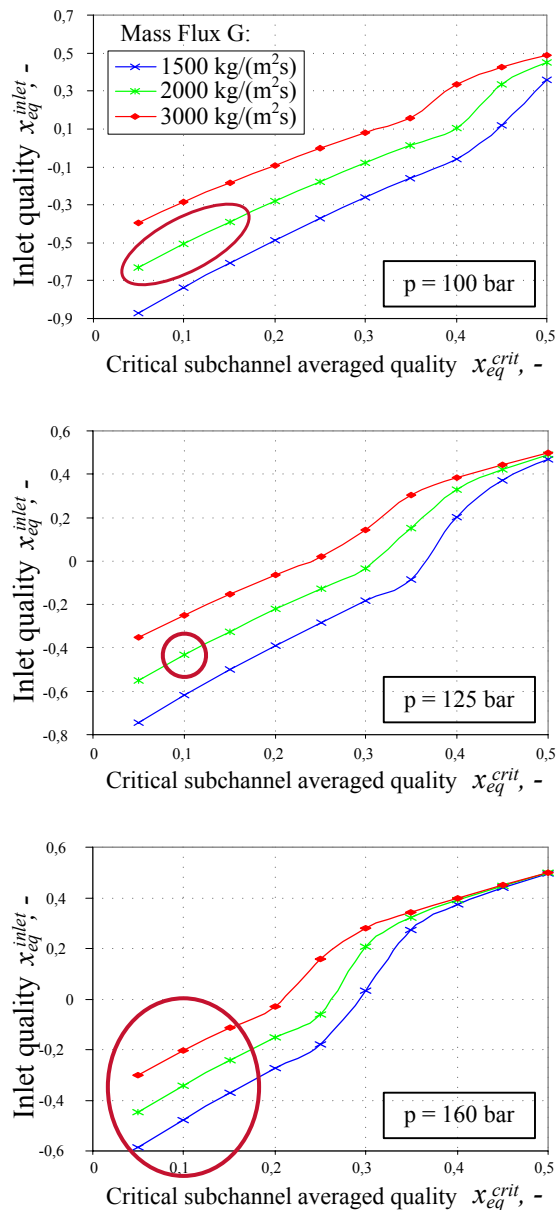


Figure 4.20 Equilibrium quality averaged over the sub-channel at the inlet dependent on the critical equilibrium quality averaged over the sub-channel at critical length $L_h = 1$ m for various pressures and mass fluxes

The chosen points are marked with red circles. It can be seen that the inlet qualities of all related points have negative values, if the model length is equal to 1 m.

The vertical velocity at the inlet is evaluated from the corresponding value for mass flux as:

$$u_{z,inlet}^l = G / \rho_l \quad (187)$$

The vapor volume fraction at the inlet is set to a very small value of 10^{-4} , because a value of zero is not allowed by the code's numerics. Other physical inlet conditions e.g. density, heat

conductivity, viscosity, specific heat, temperature, are chosen in a way described in the Section 3.6

4.3.2.2 Numerical analyses

For the steady state calculations presented in Sub-section 4.3.3.1 the STAR-CD version 3.26 was applied. In Sub-section 4.3.3.2 the STAR-CD version 3.27 was used, which takes into account possible gas-superheating for bubbles in contact with heated surfaces, discussed in detail in Section 3.7. The numerical parameters chosen were the same as in the Sub-section 4.2.2.2. The iterative calculations were carried out until the residuals of all governing equations were in the order of 10^{-5} (converged calculation).

Due to results of validation of the *Garnier* experiment (radial void distribution), presented in Section 4.2.3, applied inter-face forces are drag, virtual mass and turbulent dispersion force. Lift and lubrication force are assumed to be balanced. The bubble bulk diameter was taken as constant at 1 mm. The response coefficient C_l in two-phase $k-\varepsilon$ turbulence modeling was assumed to be equal to one. The bubble departure diameter is modeled by Eq. (130) and is for liquid at saturation temperature $d_s = 0.6$ mm. All other parameters were described in detail in Chapter 3.

Later, the variable bubble diameter defined by Eq. (122) was used with standard parameters proposed by STAR-CD and the response coefficient was applied as a function of the local void fraction defined by Eq. (102).

4.3.3 Results and discussion

4.3.3.1 Standard model and fine mesh

For some of the chosen 13 points the critical heat flux calculations diverged. Converged results have only been achieved for up to 70 % of critical heat flux. For these cases volume fraction at the region close to the wall was 100 % already.

As it was shown for the *Garnier* validations for the conditions near saturated boiling (Figure 4.11), the radial distributions of the void fraction, which were achieved applying variable bubble diameter of *Kurul* and *Podowski* [86] showed very good agreement with the experimental values.

Applying this formulation for the chosen 13 cases (x_{eq} at outlet is positive for all cases) smaller values of the bubble bulk diameter were calculated i.e. a higher interfacial area resulting in more condensation and smaller void fractions. This improves the convergence of the cases.

All cases converged for 75 % of the critical heat flux. Some of the cases converged for the CHF

4 Validation

conditions. As an example for such cases the numerical results for $p = 160$ bar, $G = 1500$ kg/(m²s) and $x_{crit}^{eq} = 0.05$ are presented. The critical heat flux for these conditions due to Eq. (185) is equal to $\dot{q}'' = 1778$ kW/m². This heat flux is applied in the presented case.

Figure 4.21 shows 2-D void fraction distribution (note: axial length scale is compressed). The maximum value of the void fraction is in the cell near the wall at the outlet. As it is shown in Figure 4.22 the outlet surface corresponds to $x_{crit}^{eq} = 0.05$ and shows correct energy balance.

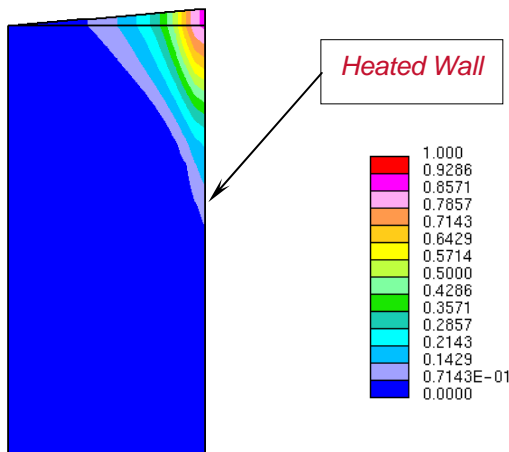


Figure 4.21 2-D void fraction distribution (STAR-CD): $p = 160$ bar, $G = 1500$ kg/(m²s), $x_{crit}^{eq} = 0.05$, $\dot{q}'' = 1778$ kW / m²

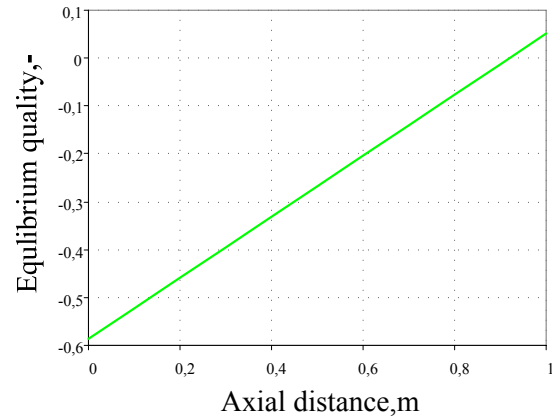


Figure 4.22 Axial distribution of the averaged equilibrium quality over the cross-section (STAR-CD)

The averaged void fraction over the pipe cross-section is plotted along the axial distance in Figure 4.23. The point of ONB can be found at an altitude of about 0.26 m. The point of OVG is at an altitude of about 0.5 m of the model.

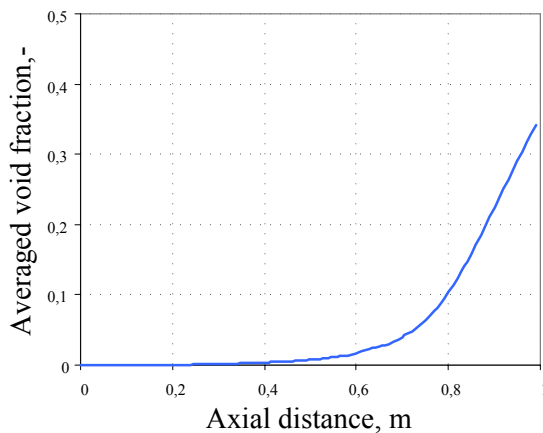


Figure 4.23 Axial distribution of the averaged void fraction over the cross-section (STAR-CD)

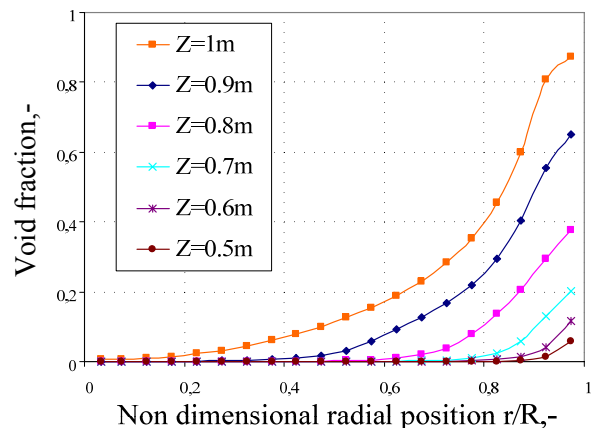


Figure 4.24 Radial void fraction distribution at different altitudes (STAR-CD)

Further downstream the void increases rapidly as shown from the radial void profiles in Figure 4.24. All curves show the void peak near the wall surface and the maximum of the void fraction 84 % near the outlet.

In Figure 4.25 the axial distribution of the wall temperature and the liquid temperature averaged over the pipe cross section are shown. The averaged liquid temperature stays below the saturation temperature of $t_s = 347.36^\circ\text{C}$, in the whole model resulting in sub-cooled boiling regime. Downstream of the Onset of Vapor Generation (at about 0.26 m) the heat transfer is improved by evaporation leading to a slight decrease of the wall temperature.

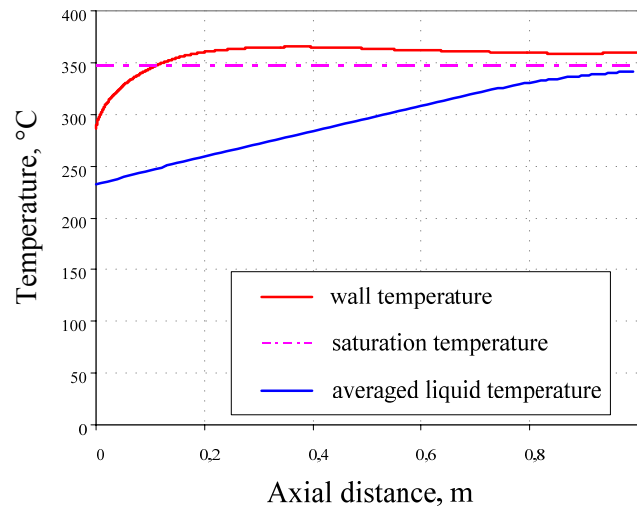


Figure 4.25 Axial distribution of averaged liquid and wall temperature over the cross section along the pipe length

The main conclusion of this study is the following: for cases where critical heat flux was applied at the wall, no significant increase of the wall temperature was observed at the critical length ($z_{crit} = 1$ m see Appendix C). In the situation when the limits of CFD two-phase modeling regarding CHF are reached, it is proposed to look for some other two-phase parameters that could show similar behavior for all cases at critical heat flux and could become a criterion for reaching such heat flux. Such a criterion could then be further applied to sub-channel geometries of various designs to make predictions regarding CHF performance.

As a hypothesis the void fraction at the outlet was proposed to be such a parameter. The comparison of the CFD calculation results for the same mesh with applied critical heat flux show that few cases achieve almost 100 % void fraction in the cell near the wall at the outlet where the critical point is expected, while other cases get values of 70 % - 85 % (see Figure 4.24). Other flow parameters e.g. velocity profiles were compared and also gave no similarity for all chosen cases.

Therefore, it was decided to try to improve the numerical model of the wall temperature at CHF conditions as the most important value for reaching CHF.

4 Validation

4.3.3.2 Modified heat partitioning model. Coarse mesh

A new formulation for the heat partitioning model takes into account possible gas-superheating for bubbles in contact with heated surfaces. This modification was included later in version 3.27 of STAR-CD. In contrast to the previous calculations, the energy equation in the current simulations had to be solved for the second phase. In the previous calculations the gas temperature was generally set to saturation at the interfacial area, resulting consequently in saturation conditions inside the bubbles. A detailed description of the model can be found in Section 3.7.

By applying this new model, a high increase of the wall temperature becomes possible. To prove this fact, two characteristic cases were chosen from Figure 4.20 for 160 bar: the first case with low mass flux and high void at the outlet and the second one with high mass flux and small void at the outlet. The applied heat flux is varied stepwise and the wall superheating is evaluated, simulating the heat flux controlled CHF experiment typical for nuclear field (see Section 4.3.1).

Thereby, *boiling curves* obtained for both chosen cases, shown in Figure 4.26 and Figure 4.27 respectively, display a steep increase of the wall temperature at high heat fluxes. This is considered to be a major advantage of the extended heat partitioning model over the previous model.

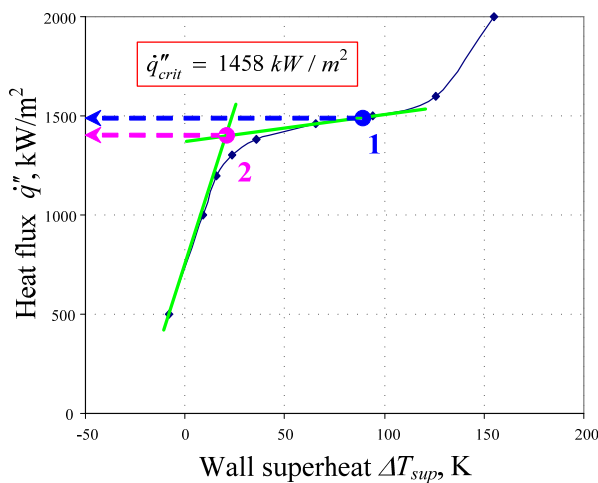


Figure 4.26 CHF experiment validation (STAR-CD): $p = 160$ bar,
 $G = 1500$ kg/(m²s), $x_{crit}^{eq} = 0.15$

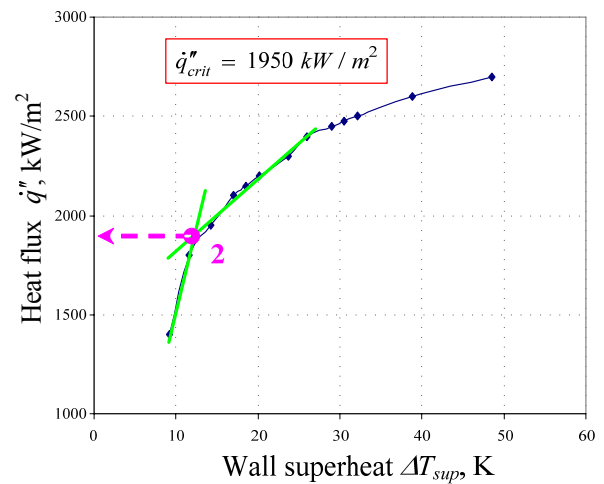


Figure 4.27 CHF experiment validation (STAR-CD): $p = 160$ bar,
 $G = 3000$ kg/(m²s), $x_{crit}^{eq} = 0.05$

It has to be noted that the cases with high heat flux were “semi-converged”, i.e. the monitored values at the outlet were not changing with additional iterations, although the residuals were still relatively large. Nevertheless, the shape of the first boiling curve (Figure 4.26) seems to be very similar to the measured curves at high pressure and forced convection conditions in Figure 4.18.

The form of the boiling-curve in Figure 4.27 could be explained by low void fractions near the wall region at the outlet and the gas-superheating for the bubbles in contact with heated surfaces that starts too early. In the cell near the wall (by such coarse meshes), the relatively high condensation to the sub-cooled flow in the bulk can cool down the super-heated bubbles. So, coarse meshes, especially near the wall could be a reason for the underprediction of the wall temperature.

As it has already been mentioned before, one of the most important tasks of modern two-phase CFD calculations is a reliable prediction of the CHF.

Taking the inflection point of the boiling curve performed by STAR-CD calculations as the criterion for the occurrence of CHF, an almost correct prediction of the CHF for DNB phenomena is possible for the first characteristic case presented in Figure 4.26. The calculated value by the *Doroshchuk* formulation (Eq. (185)) results in a critical value for the heat flux of 1458 kW/m^2 and the heat flux given by the inflection point (point 1 in Figure 4.26) is about 1500 kW/m^2 . Thus, the estimated relative error of CHF by such a method for this case is about 2%. Although the prediction is excellent, it has to be pointed out that quantitatively the achieved wall temperatures with a heat flux higher as the critical value are underestimated. For the second case (see Figure 4.27) the inflection point is absent.

To find another criterion that would fit both curves, it was tried to find a point, where the gradient of the wall temperature changes and to obtain the critical heat flux from there. Using such criteria (point 2) the estimated error is about 5% in Figure 4.26 and about 3% in Figure 4.27, for the first and second case, respectively. It is assumed that such a criterion can be used as a first approximation.

These first calculations were carried out using the CFD model with a coarse mesh to save computational time. As a next step, the mesh has to be refined and the convergence improved. Applying the enhanced heat partitioning model to the fine mesh to get more accurate results was not possible due to the divergence of the solution. However, the model can be seen as a first step to the proper prediction of CHF. It should be improved to find the general form for various inlet conditions with correct calculated values of the wall temperatures. It could be done by developing detailed physical models of the CHF phenomena e.g. an improved partitioning model by means of models taking into account a gas film and bubble sliding along the wall surface, as well as a transport equation for the bubbles, including coalescence and breakup etc.

5. Flow in sub-channels under swirl conditions

5.1 Introduction and motivation

The economic efficiency of a nuclear power plant can be increased by some improvement of CHF performance of light-water fuel assemblies e.g. by an improved spacer grid design. The primary function of the development of the spacer grid was to ensure the desired radial position of the rods, but it was shown in experiments that its design significantly influences heat transfer and in particular the occurrence of the CHF [8]. This explains the complex geometry of the spacer grid and the reason for intensive design work aimed at its optimization.

The work presented in this thesis is devoted to the mixing spacer grids, spacers with integrated swirl generating components e.g. vanes (Chapter 1). Besides generation of the swirl flow superposed on the vertical flow, such components induce mixing between adjacent sub-channels, leading to better heat transfer.

The power density distribution in the single sub-channel and in the whole core does not remain constant through the power cycle. As the purpose of thermal-hydraulic core design is to prevent fuel melting or film boiling at any point in the core under both *normal operation conditions (NOC)*, i.e. during normal operation and anticipated operational occurrences, and under *upset operating conditions (UOC)*, i.e. any transient conditions arising from faults of moderate frequency, the hot channel concept was developed and applied for various plants.

The average values for thermal loading on the reactor core (heat flux, enthalpy rise), which are of decisive importance in determining the main dimensions are taken to represent the *average* or *normal channel*. The *hot channel* is assumed to be subject to the greatest local power peaks occurring in the core and all the adverse effects resulting from manufacturing tolerances or from operating conditions deviating from normal. The flow conditions of such hot channel for PWR are modeled in the following chapters.

The improvements of any new design of the fuel assembly considering CHF performance can be verified only by very expensive CHF experiments. All existing CHF correlations included in sub-channel codes are valid for a specific type of geometry (FA-design). Application of CFD methods allows two-phase flow and heat transfer modeling independent from the geometry.

Chapter 4.3 showed the present capability of CFD to model the critical heat flux for pipe flow indicating the need for further model improvements (e.g. proper wall temperature increase at heat flux near CHF). However, the validations of the present two-phase CFD model against numerous experiments (Chapters 5.1 and 5.2) proved the good prediction of the flow distribution (flow velocity and void fraction). Hence, instead of using CFD for the direct determination of CHF in fuel assemblies the flow distributions will be used to derive criteria for FA-design optimization with respect to CHF performance. In the following chapter, possible optimization criteria are outlined and discussed for various sub-channel applications.

5.2 Simplified model with defined rotational inlet flow. Quarter of the sub-channel

5.2.1 CFD Model: geometry, inlet and boundary conditions

For the first study a simplified model of a single sub-channel under PWR conditions was chosen. This model covers the span between two spacers (450 mm); its dimensions are shown in Figure 5.1. As the study was aimed on gathering generic results, the sub-channel model includes no geometrical details e.g. spacer grid or springs and the mixing vanes were not explicitly modeled.

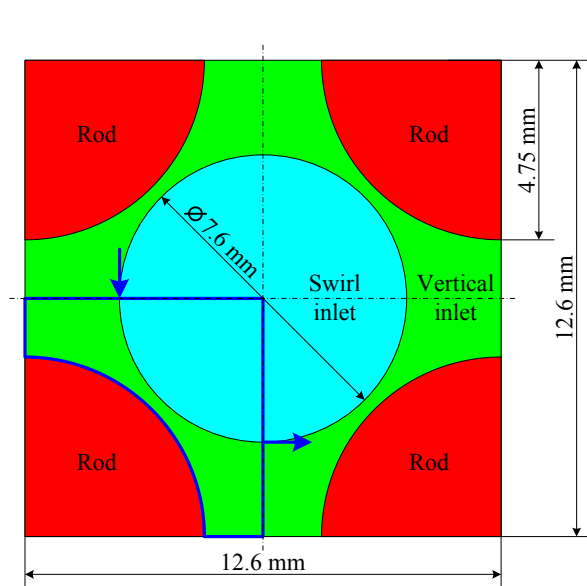


Figure 5.1 Dimensions of the simplified model with generic swirl at inlet

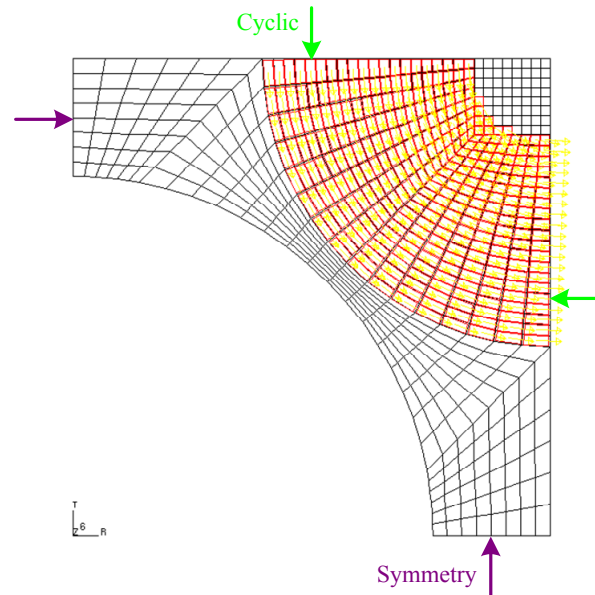


Figure 5.2 Computational mesh of the simplified model with generic swirl at inlet

The inlet flow is defined by a uniform axial velocity component over the whole inlet area and a superposed tangential velocity component in the circular area related to the vane position to create the swirl flow there. *Swirl Inlet* (cyan color) in Figure 5.1 is defined for the radial interval $0.001 \text{ m} \leq r \leq 0.0038 \text{ m}$. The *Vertical Inlet* area (green color) has only an axial component of

5 Flow in sub-channels under swirl conditions

velocity. The model provided a continuous axially propagating circular swirl. Rather than computing the intricate details of the flow induced by swirl promoters, only generic information on the decay of the swirl in a rod bundle was analyzed. Exit boundary conditions of the type *outlet* boundary were chosen. Within the sub-channel *cyclic* boundary conditions were applied (quarter of the whole sub-channel was modeled). At the gaps between the rods *symmetry* boundary conditions were used and for the cases with heated walls uniform heat flux was applied. As shown in Figure 5.2 a body fitted mesh with 608x400 hexahedral cells was used to map the geometry.

One of the important optimization parameters for the real spacer geometry is the “declination angle” φ of the used vanes, schematically presented in Figure 5.3. In the simplified CFD model the corresponding “declination angle” of vanes φ was determined as an angle between flow direction and axial component (see Figure 5.4). Thereby the horizontal flow component was varied.

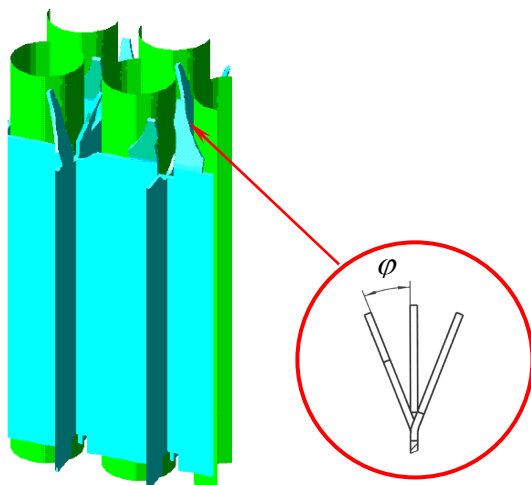


Figure 5.3 Spacer grid with split vanes without geometry details. Sketch of declination angle φ

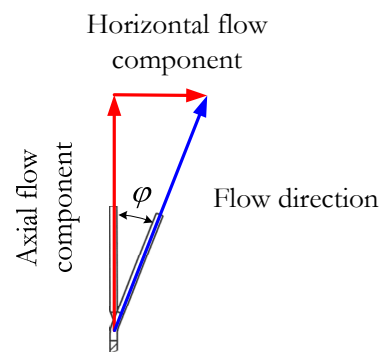


Figure 5.4 Determination of φ for the simplified model with generic vanes

For all following two-phase calculations, the hot channel of PWR reactors already defined in Chapter 5.1 was chosen and furthermore the span between the last spacer grid and the end of the active zone was modeled. For such conditions, saturated boiling is possible (in the performed cases both phases are injected at saturation) and it is assumed that the void fraction is uniform across the inlet and about 2 %. Such values were chosen according to the results of thermal-hydraulic sub-channel analyses performed with a sub-channel code Cobra. The uniform axial inlet velocity component was chosen as 5 m/s for both phases and the superposed horizontal velocity component was varied between 0 and 9 m/s. The applied wall heat flux is equal to 600 kW/m². The physical properties were chosen according to Section 3.6 at operating pressure of 160 bar.

5.2.2 Numerical analyses

In this chapter the STAR-CD version 3.27 was applied and steady state calculations were carried out. The numerical parameters chosen were the same as in the Sub-section 4.2.2.2. The iterative calculations were carried out until the residuals of all governing equations were in the order of 10^{-5} , which was considered as converged calculation. Applied inter-phase forces for two-phase analyses were drag, virtual mass, turbulent dispersion force and in some cases lift force with standard lift coefficient $C_l = 0.25$. The bubble bulk diameter was taken as constant at 0.1 mm or as the function of local liquid sub-cooling defined by Eq. (122) with standard parameters proposed by STAR-CD in Eq. (125). The response coefficient C_t in two-phase $k-\varepsilon$ turbulence modeling was applied as the function of the local void fraction modeled by Eq. (102).

For the two-phase flow cases without heated walls no wall heat partitioning and no interphase mass transfer were used. For heated cases other parameters were described in detail in Chapter 3. The bubble departure diameter was modeled by Eq. (130) and at saturation temperature $d_s = 0.6$ mm. In Sub-section 5.2.3.3 the enhanced heat partitioning model taking into account possible gas-superheating for bubbles in contact with heated surfaces is considered.

5.2.3 Results and discussion

5.2.3.1 Single-phase isothermal calculations

Axial decay of the swirl. Optimization criterion for declination angle of the vanes:

In [129] the CFD analyses were started with a single-phase isothermal analysis. As it was mentioned the experimental data indicate that swirl superposed to axial sub-channel flow improves the CHF performance. Therefore, swirl might be used as a relevant indicator for ranking the CHF performance.

Swirl decay along the sub-channel length for different values of horizontal component of the inlet velocity (a qualitative measure for the declination angle of swirl inducing vanes) was evaluated here with the present version of STAR-CD code 3.27. The most important area of a single span with respect to CHF is upstream the last spacer. Hence, the magnitude of horizontal velocity at the level 400 mm downstream the spacer (inlet in this model) was chosen as the characteristic of the intensity of the swirl and as a first criterion for the optimization of the “declination angle”.

Figure 5.5 shows a shallow maximum of the swirl as a function of the “declination angle” at the outlet at about 0.6 (scaled value). For angles in the area of practical interest presented in this figure, the pressure loss shows only small variation. This gives room for variations of other

5 Flow in sub-channels under swirl conditions

parameters with respect to CHF. The higher angles are not interesting as the pressure loss will increase significantly.

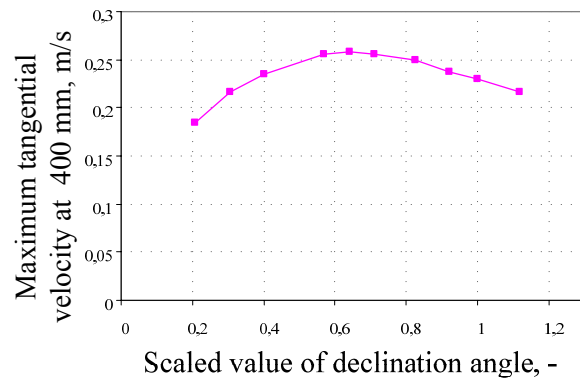


Figure 5.5 Maximum tangential velocity at 400 mm as a function of the inlet flow deflection. Single-phase calculation

Though this is not a two-phase CHF calculation, it shows the potential of CFD analyses to assess the impact of geometrical variations on flow parameters (e.g. swirl) influencing CHF performance. However, significant improvements can only be received from more detailed two-phase calculations.

5.2.3.2 Two-phase isothermal calculations

Void fraction and velocity distribution. “Bubble pocket”:

First two-phase calculations did not contain wall heating and were carried out for the same generic geometry, described in Section 5.2.1 (*Salnikova*, [130]). At the inlet 2 % void was injected uniformly. The lift, virtual mass and turbulent dispersion forces were taken into account. Figure 5.6 shows numerical results for the void distribution downstream the first spacer span (outlet).

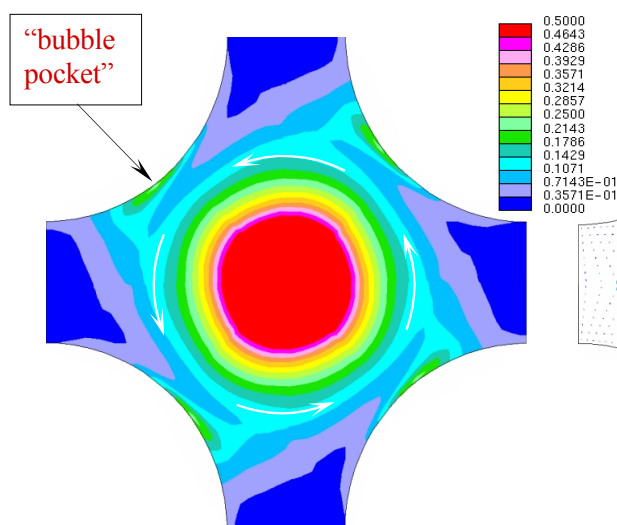


Figure 5.6 Void fraction distribution at the outlet

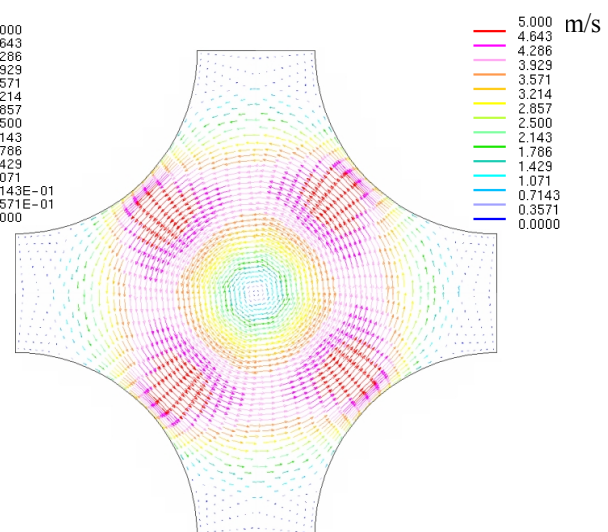


Figure 5.7 Liquid phase velocity distribution at the outlet

Four quarters of the generic model were assembled to reconstruct the sub-channel by exploiting symmetry.

The analyses demonstrate the development of void concentration under swirl in the center of the sub-channel. Domination of local centrifugal forces yields phase separation. Bubbles are collected in the center of the sub-channel. But the most interesting point is the accumulation of bubbles on the rod in the form of a “bubble pocket”.

Evaluation of the centrifugal forces:

For the purpose of better understanding the phenomena of phase separation, the centrifugal force F_C within each cell i was evaluated as follows:

$$F_{C_i} = \rho v_k v_k t_{i,j} t_j, \tag{188}$$

where t_j is a unit tangential vector of the velocity field and $t_{i,j}$ the curvature (i.e. the directional change of the unit tangential vector).

A detailed look at Figure 5.7 demonstrates local changing of the sign of curvature of the lateral flow component; resulting in a change of the sign of centrifugal force shown in Figure 5.8 and Figure 5.9.

On the lee side of the rod the inertia and centrifugal forces of the heavy fluid drive the bubbles towards the rod surface. This could be an indicator that at the position of “bubble pockets”, the heat transfer is decreased and DNB can occur.

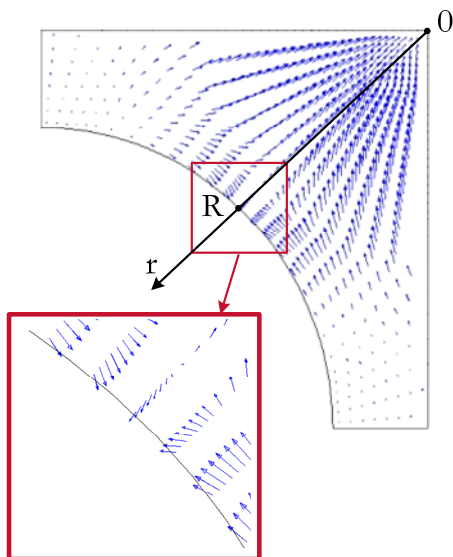


Figure 5.8 Centrifugal forces (acting on the bubble) at outlet

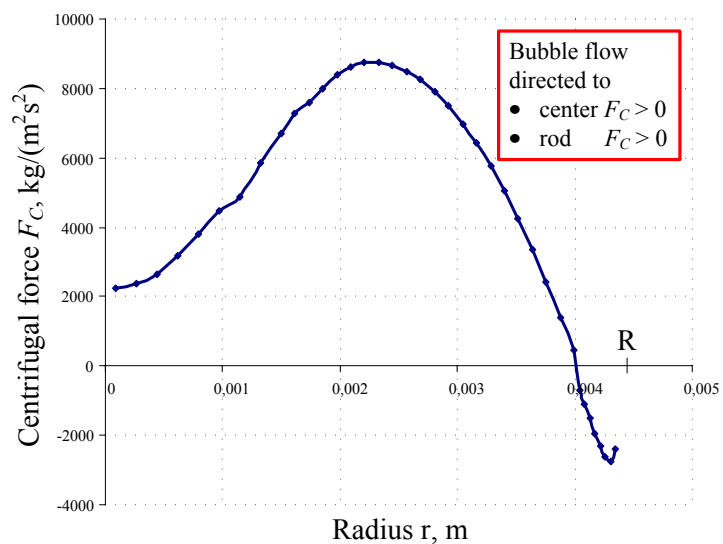


Figure 5.9 Radial distribution of centrifugal force at outlet normal to the rod surface

5 Flow in sub-channels under swirl conditions

Variation of inlet volume fraction:

Figure 5.10 demonstrates the dependency of the maximum void at the rod surface at the outlet on the inlet void. As can be seen on the corresponding table for higher inlet void fractions the sensitivity of the void fraction at the rod surface decreases. It has to be considered for high void fractions that a strong coalescence will occur, because at 80 % void fraction spherical bubbles would already be densely packed.

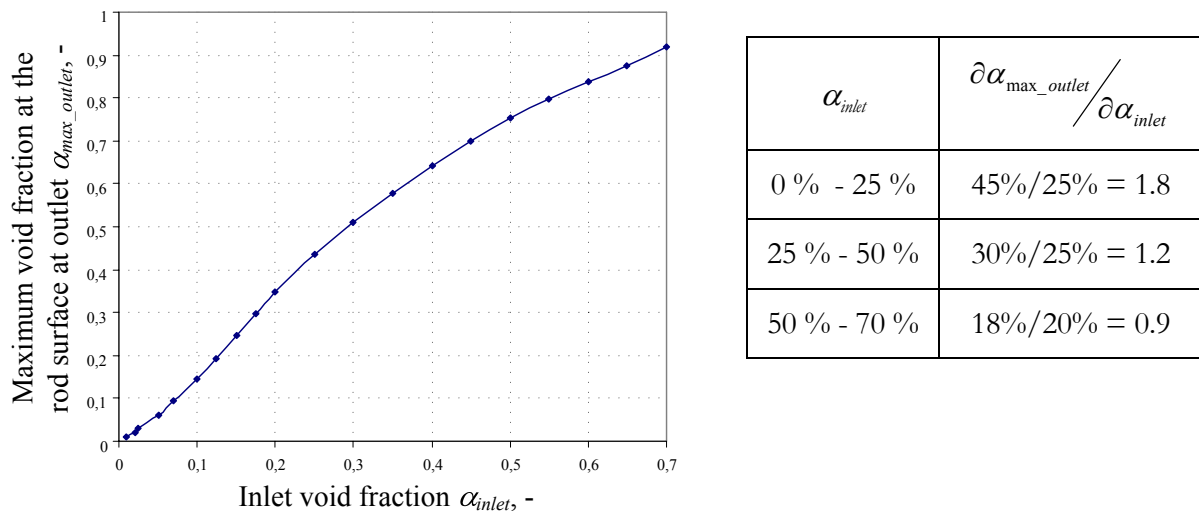


Figure 5.10 Sensitivity of the maximum void at the rod at outlet on the inlet void fraction

5.2.3.3 Two-phase non-isothermal calculations with heated rods

Optimization criteria for declination angle of the vanes:

Using the same simplified model, heat and mass transfer was included, i.e. condensation and evaporation were taken into account. The wall heat flux was fixed at the rod surface. The heat flux from the wall is divided in convective heat for the liquid, evaporation heat for generation of steam and quenching for heating of liquid in the nucleation sites, according to a wall heat partitioning model.

Calculations for different “declination angles” with constant bubble bulk diameter of 0.1 mm and STAR-CD version 3.24 were presented in [131]. A new criterion “maximum void fraction in the center of the sub-channel” was used to optimize vanes. Bubbles collected in the center of the sub-channel cannot influence the wall heat transfer and are an advantage in the design of fuel elements.

The first criterion “swirl”, derived for single-phase calculations, was found to have an obvious impact on the void distribution for the heated rods. By the swirl most void is accumulated in the sub-channel center and only a small “bubble pocket” can be generated, but without swirl the concentration of bubbles is almost homogeneously distributed over the rod surface with a higher

risk of early DNB [165]. For the area of interest, the value of the void fraction of the bubbles on the rod changes only slightly with the increased inlet swirl. Furthermore, there is a maximum of void in the center of the sub-channel as a function of the “declination angle”. The optimum was found to be almost coincident to the single-phase results.

The same calculations for various declination angles were carried out with the present STAR-CD version 3.27 and two-phase formulation presented in Chapter 3. According to the *Garnier* validations, the bubble bulk diameter is a very important two-phase parameter. For the flow conditions near saturated boiling (Figure 4.11), the radial distributions of the void fraction, which were achieved applying variable bubble diameter of *Kurul* and *Podowski* [86], showed very good agreement with the experimental values. Hence, in this study such variable diameter was applied for the liquid at saturation, resulting in values from 1.5 to 2 mm, depending on liquid superheating. The value of bubble departure diameter becomes higher than 0.6 mm due to saturation conditions at the inlet. The wall heat flux was fixed at the rod surface at 600 kW/m^2 . Inlet void fraction was set to 2 % and inlet uniform axial velocity was set equal to 5 m/s for both phases. Other inlet and boundary conditions as well as geometry were presented in Section 5.2.1.

Figure 5.11 and Figure 5.12 show the impact of the swirl on the 3-D void fraction distribution at the outlet of the model.

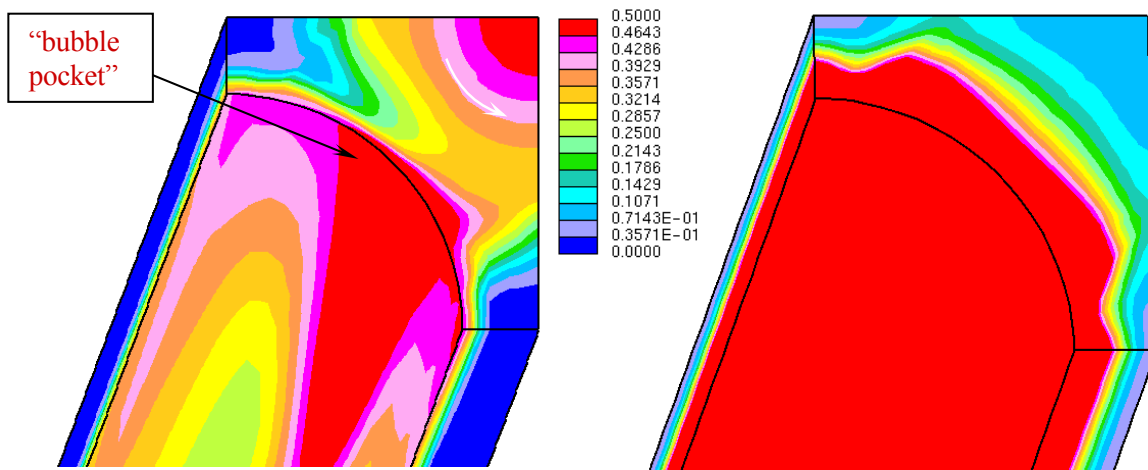


Figure 5.11 Void fraction distribution at outlet for case with inlet swirl

Figure 5.12 Void fraction distribution at outlet for case without swirl

The left figure is the result of the calculation with a horizontal velocity of 3 m/s directed anti-clockwise. Due to the centrifugal forces, a large portion of the bubbles is collected in the center of the sub-channel. The contour of the bubble condensation on the rod surface shown in Figure 5.12 shows some impact of the coarse meshing.

5 Flow in sub-channels under swirl conditions

The effect of the centrifugal force can also be clearly seen in the next figures, presenting the void fraction distribution at the plane normal to the rod surface for the same two cases: with and without swirl (Figure 5.13 and Figure 5.14, respectively).

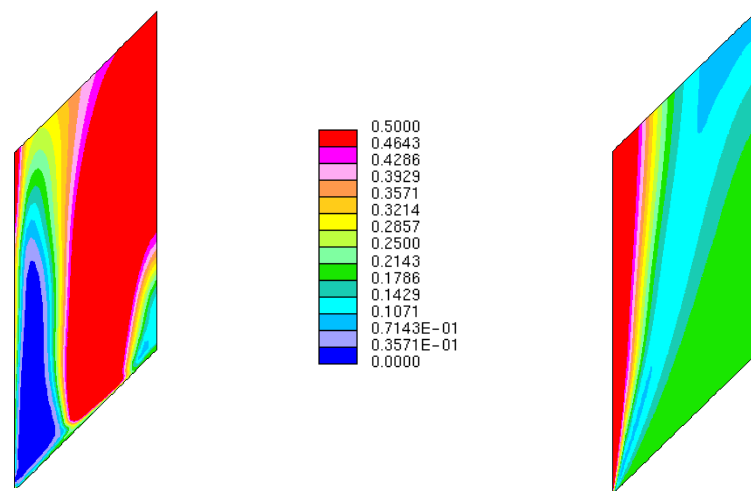


Figure 5.13 Void fraction distribution normal to rod surface. With swirl

Figure 5.14 Void fraction distribution normal to rod surface. Without swirl

The same calculation was carried out for different values of the declination angle. The value of the void fraction in the center of the sub-channel and the maximum value of the void on the rod surface at the outlet were evaluated and presented in the Figure 5.15.

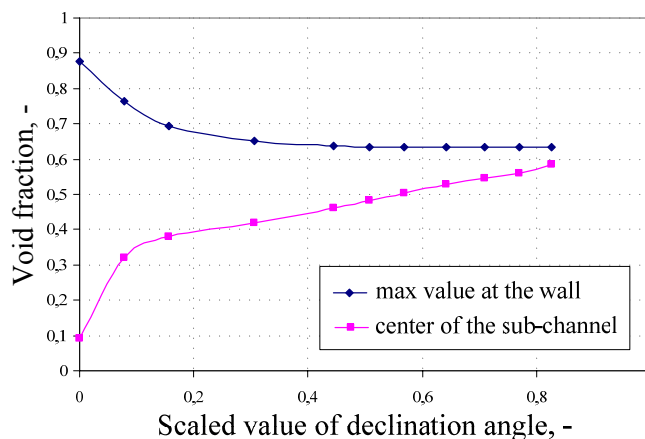


Figure 5.15 Void fraction at outlet for various horizontal velocities at inlet

The optimization goal can be formulated as the avoidance of “bubble pockets” on the rod surface and a maximum void fraction at the center of the sub-channel. Figure 5.15 shows that from some point (about 0.6 degree, scaled angle) further increasing of the inlet swirl does not result in a lower value of the maximum void fraction on the wall surfaces. This value remains almost constant due to the “bubble pocket” formed at the wall as shown in Figure 5.11. As the accumulation of bubbles in the center of the sub-channel is growing the “bubble pocket” would be only slightly thinner with higher swirl. For the same points the first optimization criterion

“swirl” upstream the last spacer grid, presented in Sub-section 5.2.3.1 for single-phase calculation, was evaluated for two-phase calculations with heated walls (Figure 5.16).

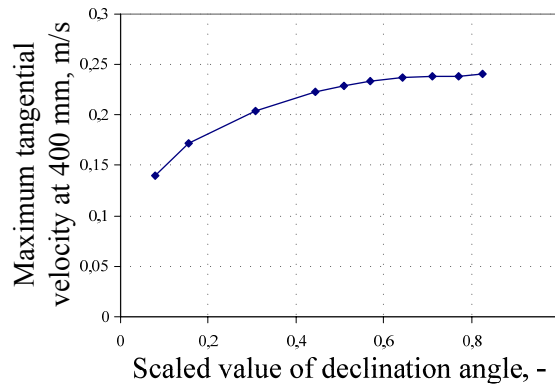


Figure 5.16 Maximum tangential velocity at 400 mm downstream the inlet for various horizontal velocities at inlet. Two-phase calculation

Quantitatively, due to the impact of the second phase (bubbles are slowing down the liquid velocity) the single-phase flow reaches smaller values of the swirl near the outlet compared to results of Figure 5.5. Qualitatively, the optimization result is similar, even though two-phase calculations show no maximum at 0.6 (scaled angle). In the two-phase calculation, over a scaled angle of 0.6 further increasing of the inlet swirl results in almost constant maximum value of the swirl near outlet. Hence this value can be taken as optimum. Both optimization criteria lead to the same optimum range of the declination angle near 0.6 (scaled angle).

Wall temperature as optimization criterion:

Additionally the wall temperature was evaluated to show the impact of the swirl. Figure 5.17 and Figure 5.18 show that even with the scale showing temperature difference of only circa 2 K the swirl leads to lower wall temperatures. As long as the heat flux is much smaller than the critical heat flux only small values of superheating at the wall are possible.

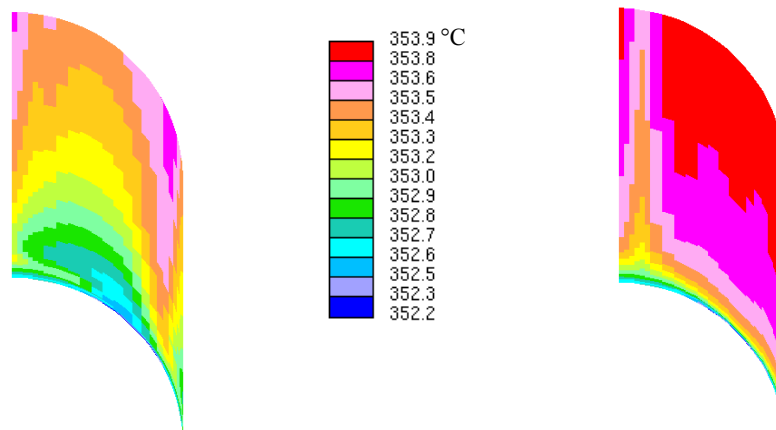


Figure 5.17 Wall temperature distribution. With swirl

Figure 5.18 Wall temperature distribution. Without swirl

5 Flow in sub-channels under swirl conditions

However, Figure 5.17 shows the temperature maximum at the position of the “bubble pocket” (Figure 5.11). This behavior will be valid also for higher heat fluxes. The bubbles pocket position and the maximum local surface temperature could be parameters to compare different designs with respect to CHF.

Evaluating the maximum wall temperature for various angles presented in Figure 5.19 shows a reduction of the wall temperature already at small values of the swirl at the inlet. At higher swirl the wall temperature remains almost constant. The saturation temperature is 347.36°C and the wall superheat is about 6 K.

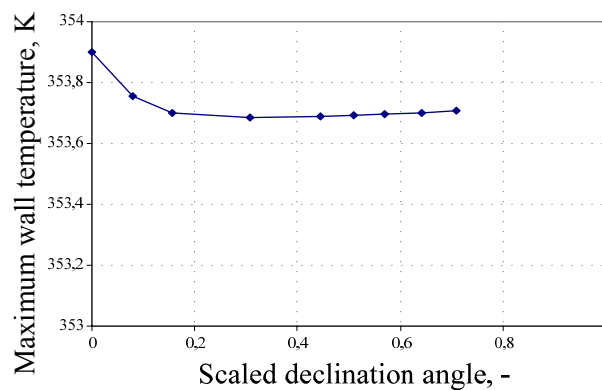


Figure 5.19 Maximum wall temperature for various horizontal velocities at inlet

For this small heat flux only a 3 % effect in superheating at the wall is observed. But it already would indicate that the maximum wall temperature is reduced by swirl. This effect is in accordance with the observation that CHF is improved by swirl. The temperature differences will be more pronounced, if reliable calculations close to CHF can be performed by CFD.

In the next step the enhanced heat partitioning model described in Section 3.7, which allows gas super-heating for bubbles in contact with heated surfaces, was used for the same cases as presented in Figure 5.17 and Figure 5.18. Computed wall temperature distribution is presented in Figure 5.20 and Figure 5.21, respectively.

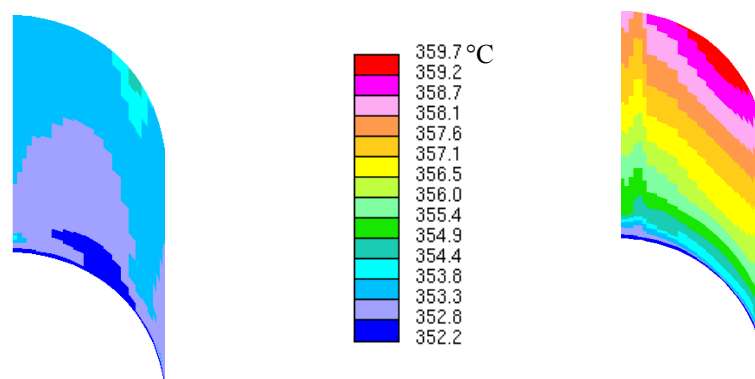


Figure 5.20 Wall temperature distribution. Enhanced heat partitioning model. With swirl

Figure 5.21 Wall temperature distribution. Enhanced heat partitioning model. Without swirl

Applying this model the maximum wall superheat without swirl reaches about 12 K compared to about 6.5 K calculated with a standard model. The temperature difference at the rod surface achieved with defined horizontal velocity at the inlet of 3 m/s was changed from 6 K to 7 K with the new modeling. This shows already more pronounced differences in temperature differences with and without swirl and therewith indicates an improvement of DNB for sub-channel flows under swirl conditions.

5.3 Simplified vanes in the single sub-channel geometry

5.3.1 CFD Model: geometry, inlet and boundary conditions

In the next step, a single sub-channel model with 4 simplified mixing vanes, presented in Figure 5.22, was designed.

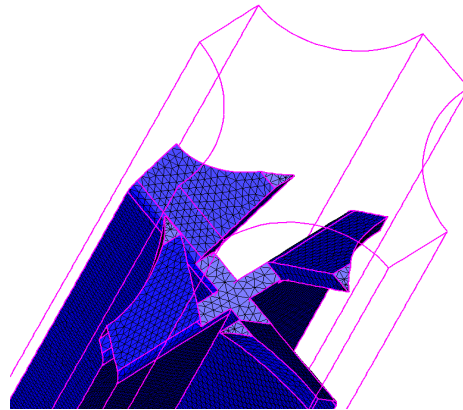


Figure 5.22 Four simplified mixing vanes

For the first calculations a coarse model with about $1.71 \cdot 10^5$ hexahedral cells and $3.5 \cdot 10^3$ tetrahedral cells was chosen and is shown in Figure 5.23. The model has a typical PWR sub-channel pressure of 160 bar and dimensions with a rod diameter of 9.5 mm and a pitch to diameter ratio of 1.32. The length of the model is 512 mm and consists of a short developing length, a spacer grid with mixing vanes, the span above the tip of the vanes and the next spacer grid of 470 mm. At the inlet a 2 % void is injected and an axial uniform velocity of 5 m/s is defined for both phases.

For the first study almost the same two-phase physical conditions and Euler-Euler modeling as for the generic model were applied. The only difference was the application of the lift force with the standard lift coefficient of 0.25 and the constant bubble bulk diameter of 0.1 mm.

Exit boundary condition, the type *outlet* boundary were chosen. At the gaps between the rods *symmetry* boundary conditions (Figure 5.23) were used and a uniform heat flux of 600 kW/m^2 was applied at the rod surface.

The modeling of the spacer grid and the vanes is simplified compared to the real geometry.

5 Flow in sub-channels under swirl conditions

The spacer model with four vanes induces a flow pattern, which is similar to the simplified model with defined inlet swirl. The flow under these swirl conditions was studied to give generic information on the void distribution.

For the following studies a refined model was designed. A mesh with $7.5 \cdot 10^5$ hexahedral and a few hundreds tetrahedral cells was used to map the geometry (see Figure 5.24). The model has the same dimensions, inlet and boundary conditions as the model with the coarse mesh.

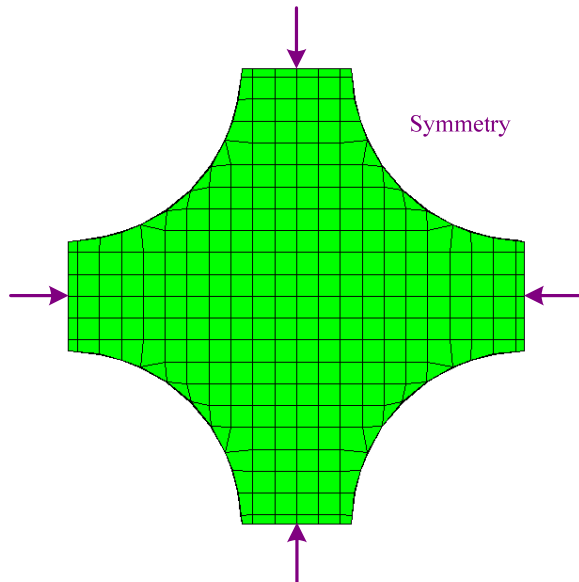


Figure 5.23 Coarse computational mesh of the simplified model with mixing vanes (4 vanes)

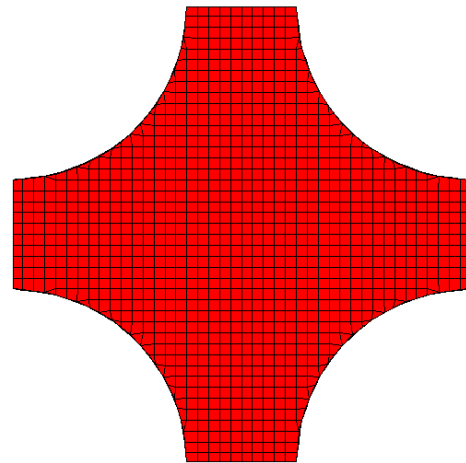


Figure 5.24 Fine computational mesh of the simplified model with mixing vanes (4 vanes)

5.3.2 Numerical results and discussion. Coarse model

Velocity and void fraction distribution:

Figure 5.25 and Figure 5.26 show the velocity distribution for the first and the second phase, respectively. It can be seen that the second phase is slightly faster than the first one and that the tangential velocity in the region of the vanes is in a range between 1 and 5 m/s.

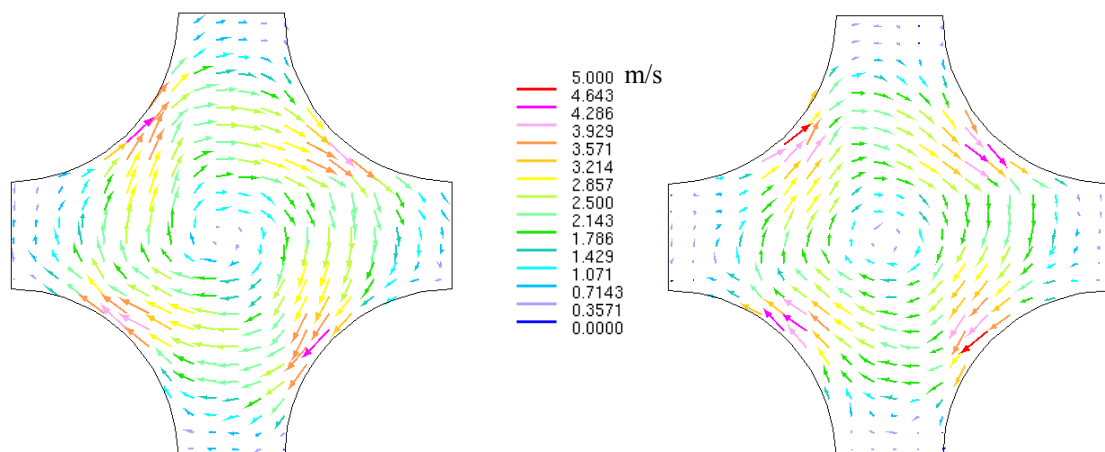


Figure 5.25 First phase distribution directly downstream the tip of the vanes. Coarse model

Figure 5.26 Second phase distribution directly downstream the tip of the vanes. Coarse model

By comparing Figure 5.25 and Figure 5.27 the swirl decay can be seen. The maximum value of the tangential velocity changes its value by a factor of 25 over the span from tip of the vanes to the outlet.

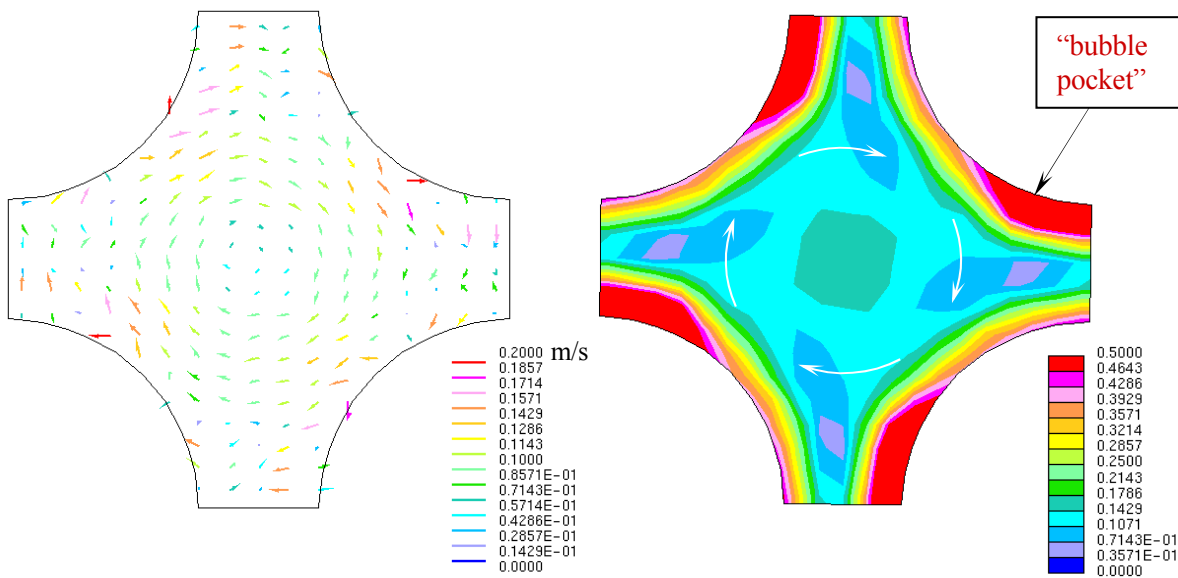


Figure 5.27 First phase distribution at outlet. Coarse model

Figure 5.28 Void fraction distribution at outlet. Coarse model

In Figure 5.28 the void distribution at the outlet shows a similar “bubble pocket” as it was already found in the non-isothermal calculation with the simplified geometry in the Sub-section 5.2.3.3. The effect seems to be enlarged due to the application of the lift force, which always acts in the direction toward the wall modeled by Eq. (85).

Next, the impact of the vanes on the flow was tested for the model with the coarse mesh.

Impact of the swirl on the radial void distribution:

For the same physical, initial and boundary conditions the impact of the fuel assembly components (in this case vanes) on the two-phase flow with heated rods is shown in the following two figures. The radial void fraction distribution normal to the rod surface (on a traverse with 45° in Figure 5.23) is evaluated at various axial distances downstream the inlet for the already presented case with simplified mixing vanes and for a case without vanes. In the case without swirl in Figure 5.30 bubbles accumulate on the rod surface. The void fraction increases near the wall along the heated sub-channel length. In the case with vanes the swirl exerts centrifugal forces on the steam water mixture. Most of the bubbles accumulate on the axis of the sub-channel forming a bubble core. By local change of curvature a phase separation occurs close to the rods forming a “bubble pocket”. Close to the vanes the bubble concentration on the axis is dominant, whereas, further downstream the void fraction of the “bubble pocket” becomes more relevant.

5 Flow in sub-channels under swirl conditions

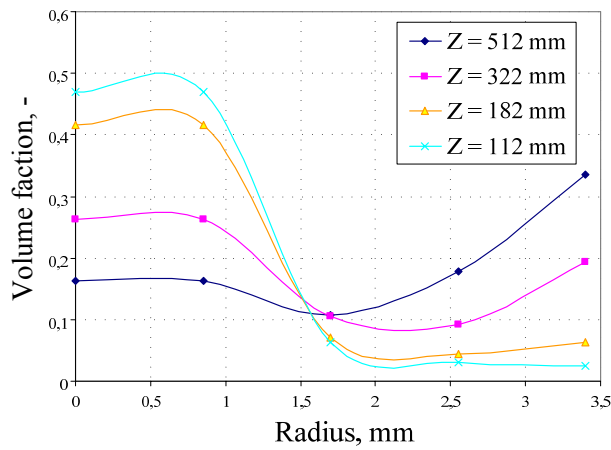


Figure 5.29 Radial void fraction distribution. Model with mixing vanes

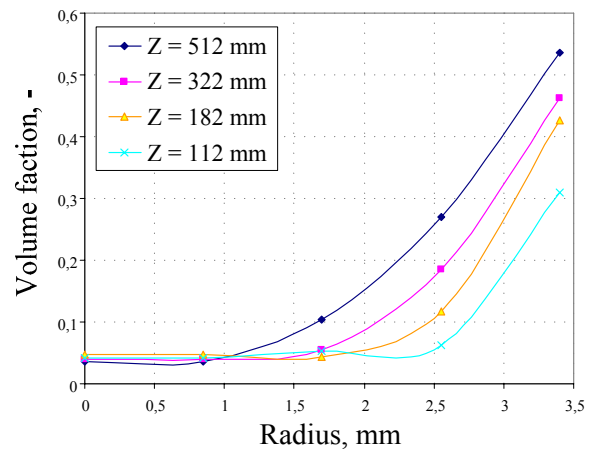


Figure 5.30 Radial void fraction distribution. Model without vanes

However, the conclusion of this study can, to some degree, be similar to the calculation for the simplified geometry, that higher swirl leads to an increase of the heat transfer. But in two-phase mixtures the flow separation under swirl has to be taken into account. The accumulation of bubbles in the center will be positive for the heat transfer, but in the region of the “bubble pockets” the heat transfer is deteriorated, having maybe a negative impact on CHF performance. Next, the refinement of the computational mesh was carried out to study the impact of the mesh.

5.3.3 Numerical results and discussion. Fine mesh

Axial and radial void fraction distribution. Axial decay of the swirl:

The model has the same initial and boundary conditions as the CFD model with the coarse mesh. In Figure 5.31 the sub-channel averaged axial void fraction distribution along the heated sub-channel is presented for both fine and coarse mesh. This comparison shows that there is a mesh dependency in almost the whole computational domain. Hence, all further evaluations are carried out for the fine mesh.

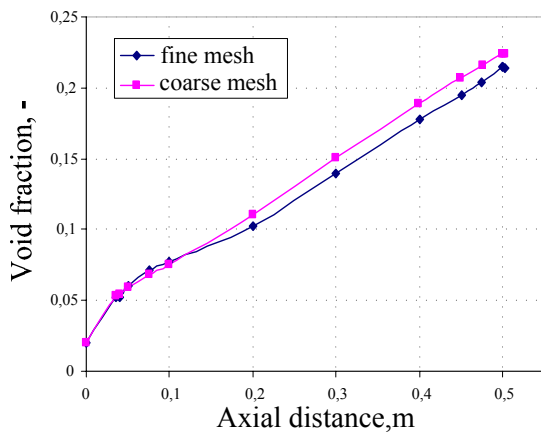


Figure 5.31 Axial void fraction distribution for model with fine and coarse mesh

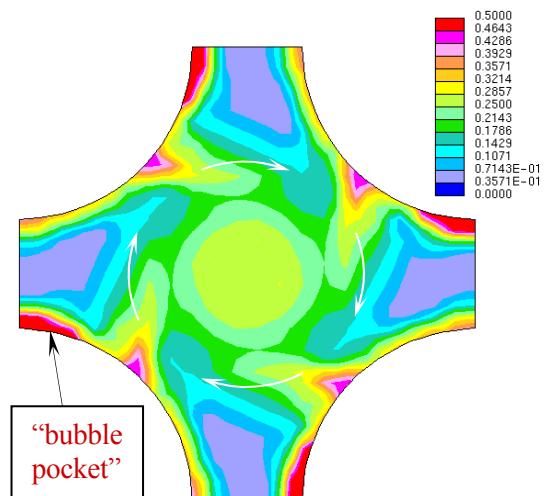


Figure 5.32 Void fraction distribution at the outlet. Fine mesh

Figure 5.11, Figure 5.28 and Figure 5.32 show similar void distributions with a “bubble pocket” always on the lee side of the rod. I. e. the generic model, the coarse model and the fine mesh model resolve the local bubble accumulation in a similar way. The fine mesh shows a thinner layer of bubbles at the rod than the results of the coarse mesh.

From the next two figures the phase separation due to centrifugal forces can be examined. In Figure 5.33 the axial distribution of the void fraction in the center of the sub-channel is shown. The value of the void fraction in the center is growing downstream the tip of the mixing vanes and then after a fast decrease it remains almost constant.

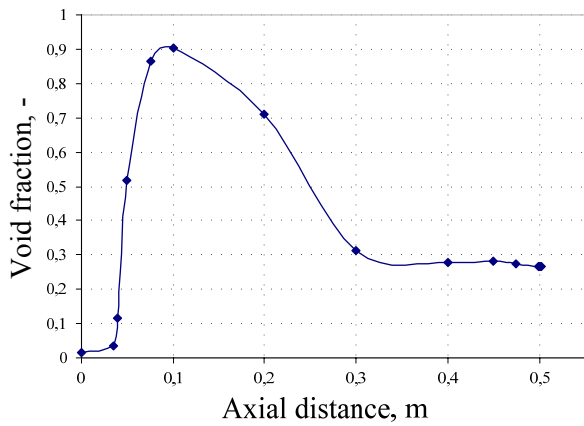


Figure 5.33 Axial distribution of the void fraction in the center of the sub-channel. Fine mesh

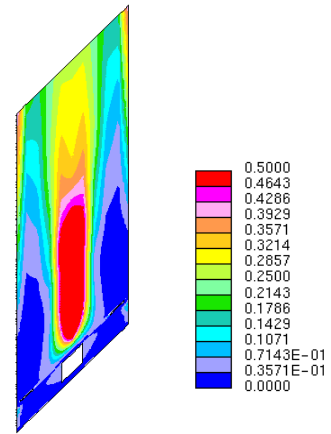


Figure 5.34 Void fraction distribution over the vertical slice. Fine mesh

Figure 5.34 shows the void fraction distribution over a vertical slice section through the centre of the sub-channel and 45° of the rod. The axial length scale is compressed. It can be seen that at first bubbles collect in the center of the sub-channel and further downstream distribute over the whole sub-channel due to the turbulent dispersion and decreasing of the swirl. The void fraction at the wall is generated by wall heating.

Axial decay of the swirl:

In Chapter 5.2 the maximum horizontal velocity was taken as the measure for the swirl over the horizontal section. For this case the value at 60 mm downstream the inlet (15 mm above the tip of the vanes) of 2.597 m/s can be evaluated from Figure 5.35.

For a more detailed evaluation of the swirl decay for the two-phase flow the mean curl velocity was calculated and performed as a function of the sub-channel altitude.

For each cell i of the thickness l with inside of the chosen control surface with perimeter U the mean curl-velocity is evaluated from the following equation:

$$\bar{v}_{perimeter} = \frac{\sum_{i=1}^N \left(\frac{\partial w_i^l}{\partial x_i} - \frac{\partial u_i^l}{\partial z_i} \right) \cdot (1 - \alpha_i) dV_i}{U \cdot l} \tag{189}$$

5 Flow in sub-channels under swirl conditions

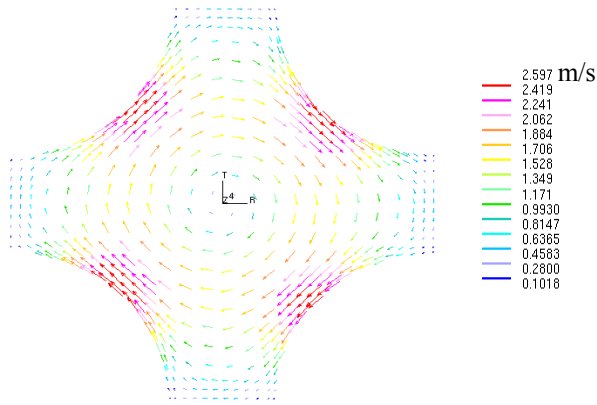


Figure 5.35 Horizontal velocity distribution at 60 mm downstream the inlet

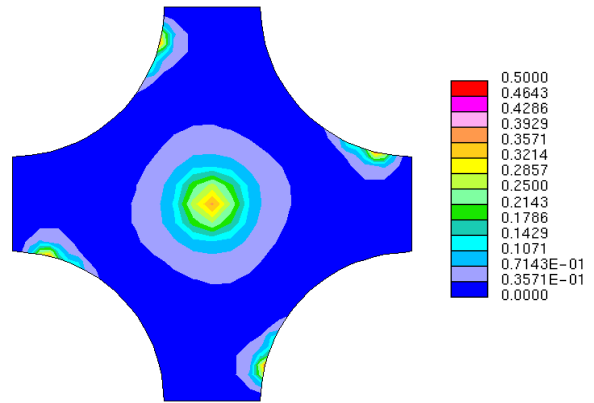


Figure 5.36 Void fraction distribution over the vertical slice at 60 mm downstream the inlet

The swirl intensity was derived from the curl of the liquid velocity field after multiplication with the volume fraction of the liquid over the first control surface with a perimeter $U_1 = 29$ mm (Figure 5.35, Figure 5.36 and Figure 5.37). The results are presented in Figure 5.38 and the chosen control area over which local values will be integrated is marked with a red color line.

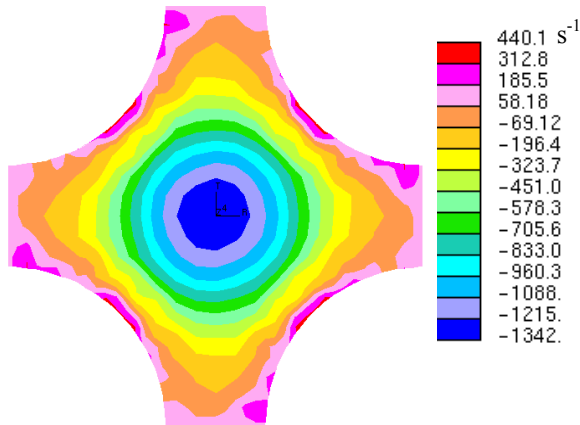


Figure 5.37 Curl distribution at 60 mm downstream the inlet

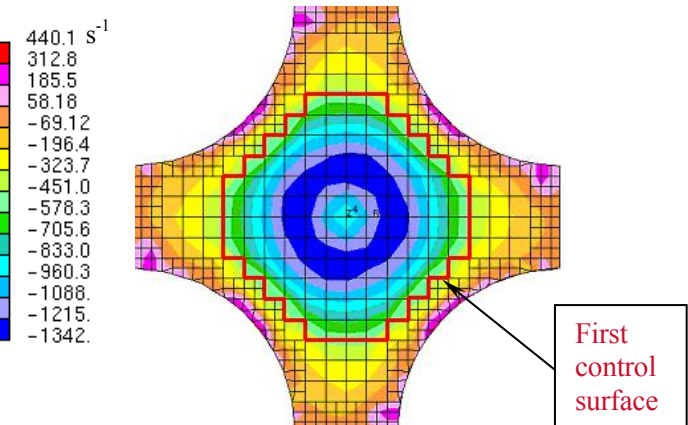


Figure 5.38 The distribution of (Curl * Volume fraction of liquid) at 60 mm downstream the inlet. $U_1 = 29$ mm

Figure 5.39 shows the decay of the swirl intensity with the length z of the sub-channel. The decay curve is almost reciprocally proportional to the length and loses about 90 % of its initial intensity after half of the spacer span.

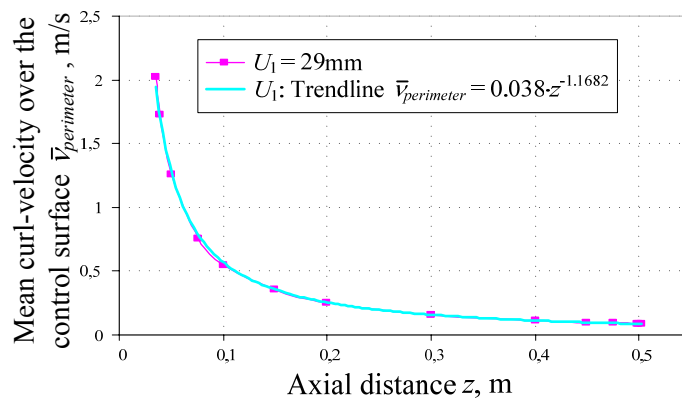


Figure 5.39 Axial decay of the swirl

To see the influence of the control area a second differently shaped area was chosen that has a perimeter $U_2 = 24$ mm. Figure 5.40 shows this control area and Figure 5.41 the comparison calculation of the curl-velocity as a function of the axial distance. The influence seems to be very small when looking at the whole distribution.

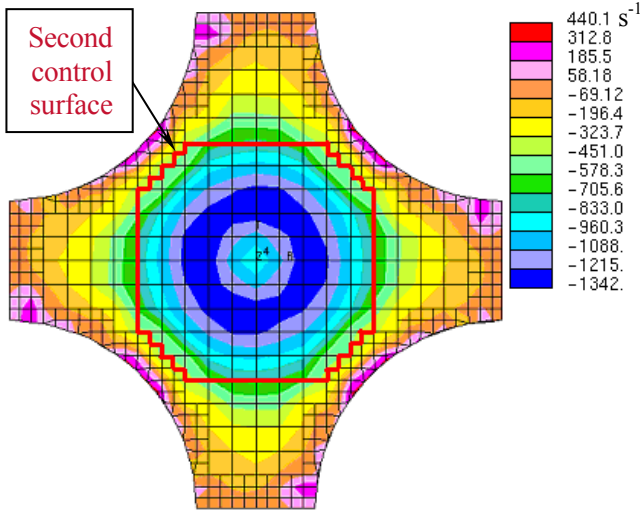


Figure 5.40 The distribution of (Curl * Volume fraction of liquid) at 60 mm downstream the inlet. $U_2 = 24$ mm

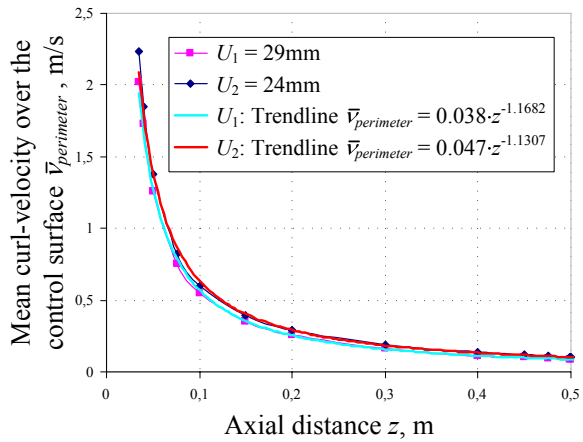


Figure 5.41 Axial decay of the swirl for two different control areas

Influence of the lift force and the bubble bulk diameter:

The influence of the lift force on the outlet void fraction distribution is presented in Figure 5.42. Due to the much higher impact of the centrifugal force on the sub-channel flow under swirl conditions compared to other lateral forces e.g. lift force, the void distribution of Figure 5.42 is qualitatively similar to Figure 5.32, presenting the void distribution for the calculation for the same two-phase parameters and geometry, but with and without applied lift force (standard lift coefficient of 0.25).

Quantitatively, the flow separation is higher for the case without lift force. More bubbles accumulate in the center of the sub-channel, but the values between the rods and the region of the sub-channel center show lower void. Near the wall surface the calculation without lift force achieves slightly higher values.

The influence of the bubble bulk diameter on the void fraction distribution at outlet can be observed comparing both figures Figure 5.42 and Figure 5.43. The formulation of variable diameter according to *Kurul* and *Podowski* [86] leads to a higher bubble diameter as the constant value of 0.1 mm used for the calculation presented in Figure 5.42. The range of diameters in the bulk domain varies from 1.5 to 2 mm. It results in a smaller interfacial area and higher local void fractions near the wall surface. In Figure 5.43 four regions with a very low

5 Flow in sub-channels under swirl conditions

void fraction are present. This phenomenon is due to the higher bubble diameter, which results in lower drag forces and higher slip velocities. Therefore, increased radial flow phase separation by dominating centrifugal forces occurs.

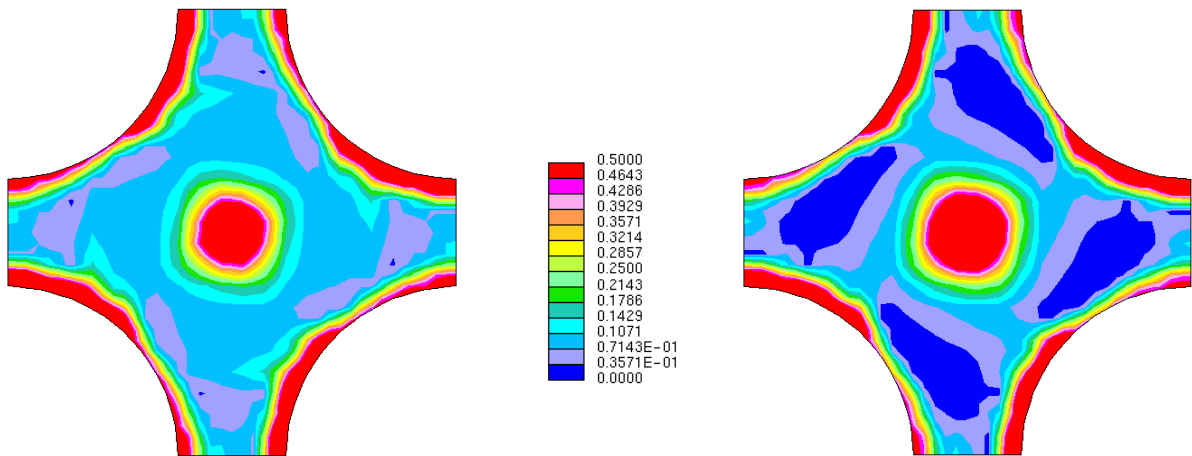


Figure 5.42 Radial void fraction distribution at the outlet. Without lift force

Figure 5.43 Radial void fraction distribution at the outlet. Without lift force. Variable diameter

5.4 Simplified swirl promoter in single channel geometry around the rod

5.4.1 CFD Model: geometry, inlet and boundary conditions

In both previous studies the swirl in sub-channel was defined on the inlet boundary of the simplified model in Chapter 5.2 or generated by mixing vanes in Chapter 5.3. But there are also other types of swirl generating components, e.g. swirl promoters generating a swirl flow around the rods. In this chapter only the basic structures of such promoters are taken into account and the resulting flow distribution is compared with the results of the model with simplified vanes.

Due to convergence problems different meshes were created. The most detailed and converged results were achieved using a model with a fine mesh of $1.3 \cdot 10^6$ hexahedral cells and $3 \cdot 10^3$ tetrahedral cells (for the region near wall and near to the spacer grid) to map the geometry of the model, presented in Figure 5.44. The model incorporates PWR sub-channel dimensions with a rod diameter of 9.5 mm and a pitch to diameter ratio of 1.4. The length of the model is 512 mm and consists of a short developing length, a spacer grid with swirl promoters and the span between the top of a spacer grid and the leading edge of the downstream spacer (or the end of the active zone) of ~ 450 mm.

Symmetry boundary conditions are applied to the planes intersecting in the center of the sub-channel (Figure 5.44). At the inlet 2 % steam is injected and uniform axial velocity of 5 m/s is defined for both phases. The rod surface uses an adiabatic *wall* as boundary condition and an

isothermal two-phase calculation is performed. At the exit boundary conditions of the type *outlet* are chosen.

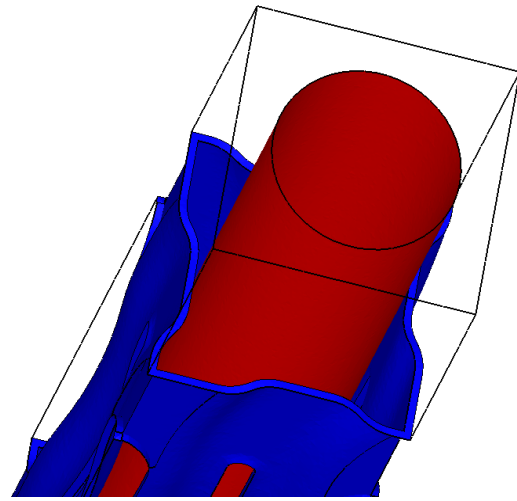
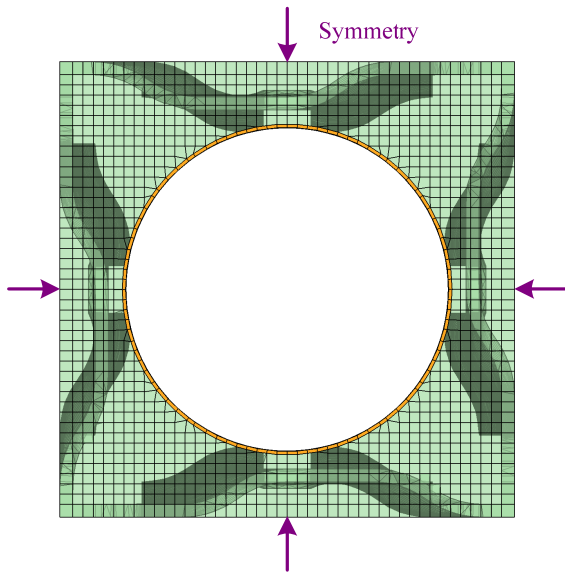


Figure 5.44 Computational mesh of the simplified model with swirl promoters

Figure 5.45 Spacer grid with swirl promoters and fuel rod

For this study almost the same two-phase physical conditions and Euler-Euler modeling as for the isothermal calculation with generic model was applied. The main difference is that the flow was modeled as laminar due to the divergence caused in case of turbulent flow. In this study a constant bubble diameter of 1 mm was chosen for the bulk flow region.

The model of the spacer grid is simplified compared to the real geometry because only generic flow properties under swirl conditions were studied. The simplified model is presented in Figure 5.45.

The results of this model are compared in the next sub-section with the results of the simplified model with mixing vanes presented in Chapter 5.3. The calculations were performed for the same conditions of the isothermal two-phase laminar flow with constant bubble bulk diameter of 1 mm.

5.4.2 Numerical results and discussion

The detailed comparison for both models is presented in Appendix D. The void fraction and the velocity distributions for both phases are presented there, comparing the simplified model with mixing vanes and the simplified model with swirl promoters integrated in the spacer grid generating the swirl in the sub-channel and around the rod, respectively. The distributions are evaluated across various axial sections from the section immediately downstream the tip of the vanes (or just below the top of the spacer grid with integrated swirl promoters) and to the outlet of the spacer span.

5 Flow in sub-channels under swirl conditions

The simplified model with mixing vanes for isothermal two-phase laminar flow shows similar behavior as the turbulent flow in the heated sub-channel presented in Chapter 5.3. The bubbles accumulate in the center of the sub-channel and in the form of a “bubble pocket” on the rod surface. Under the applied conditions the “bubble pocket” on the rod has a very small area, which is almost constant from the axial section 100 mm above the tip of the vanes onwards. The velocity distributions presented in Appendix D can explain the effects of the accumulation of bubbles by means of centrifugal forces. The void fraction distribution at altitude of 450 mm above the tip of the vanes (outlet) is presented in Figure 5.46.

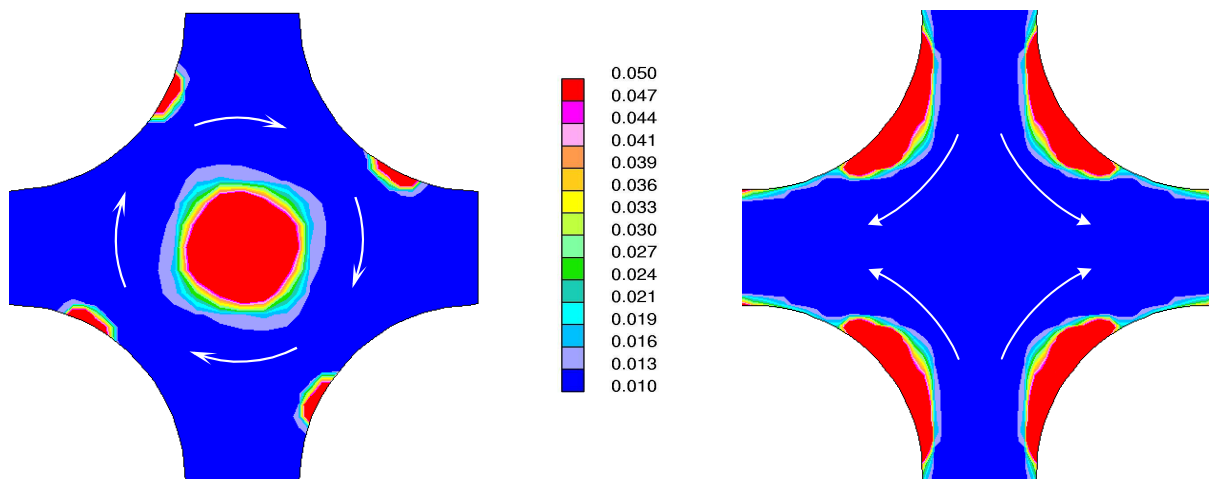


Figure 5.46 Void fraction distribution. Simplified model with mixing vanes at the outlet

Figure 5.47 Void fraction distribution. Simplified model with swirl promoters at the outlet

When the same conditions to the simplified model with the swirl promoters integrated in the spacer grid are applied, almost the whole area of the rod surface is covered with bubbles. For better comparison the geometry was rearranged to present results in the form of a sub-channel (Figure 5.47).

The rod surface covered with bubbles in front of the next spacer in Figure 5.47 is much higher than the one shown in Figure 5.46 and the maximum value of the void fraction is four times higher for the model with the swirl promoters integrated in the spacer grid (Appendix D).

The calculations were performed without heated walls and turbulence was not taken into account.

Nevertheless, the much higher accumulation of bubbles on the rod surfaces (caused by the swirl generated around the rods), as compared to the “bubble pocket” (achieved by the swirl in the sub-channel) can decrease the cladding-liquid heat transfer and result in a higher wall temperatures.

5.5 Simplified vanes in the 2x2 sub-channel geometry

5.5.1 CFD Model: geometry, inlet and boundary conditions

Combining high computational power with improved numerical methods allows a first isothermal two-phase calculation of a simplified spacer grid in a 2x2 sub-channel geometry at system pressure of PWR of 160 bar [132]. The computational mesh is about 2 million cells (Figure 5.48) and the mixing vanes have a two vane layout. The converged result has been achieved for inlet void of 2 % and 5 m/s inlet velocity for both phases. Compared to the previous sub-section in this case turbulence is taken into account.

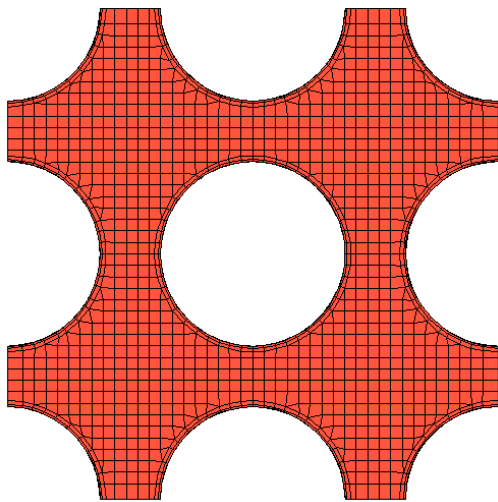


Figure 5.48 Coarse computational mesh of the simplified 2x2 sub-channel model with mixing vanes [132] (pairs of two-vanes)

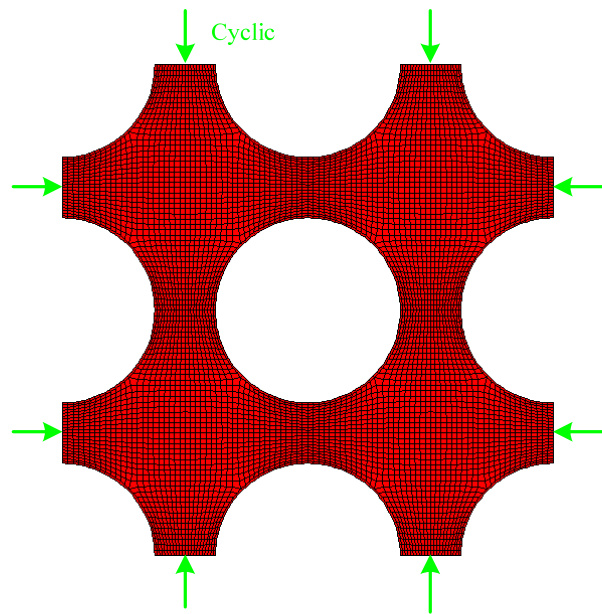


Figure 5.49 Fine computational mesh of the simplified 2x2 sub-channel model with mixing vanes (pairs of two-vanes)

Finally, a new computational mesh of a 2x2 sub-channel geometry with a slightly different spacer grid including mixing vanes (2 vane layout) has been created. The model has typical PWR sub-channel dimensions with a rod diameter of 9.5 mm and a pitch to diameter ratio of 1.32. The length of the model is 519 mm and consists of a short developing length, a spacer grid with mixing vanes and the span above the tip of the vanes to the next spacer grid of 488 mm. The vane pattern and the mesh are presented in Figure 5.50 and Figure 5.51, respectively. For simplification fuel rod supports and weld nuggets are not modeled. With this model a non-isothermal calculation using the boiling and wall heat partitioning model was conducted. Here a constant heat flux of 100 kW/m² is applied to the rods. The flow inlet conditions and the applied turbulence are the same as for the isothermal case.

A fine mesh of about $5.51 \cdot 10^6$ hexahedral and $7.2 \cdot 10^4$ tetrahedral cells presented in Figure 5.49 is used for non-isothermal calculations. All other two-phase parameters are left the same as in

5 Flow in sub-channels under swirl conditions

the previous calculations. For this model with a two vane layout the boundary conditions at the gaps between the rods are defined as *cyclic*, due to the cross flow between the sub-channels. It differs from the previous models with a four vane layout, where *symmetry* boundary conditions have been applied.

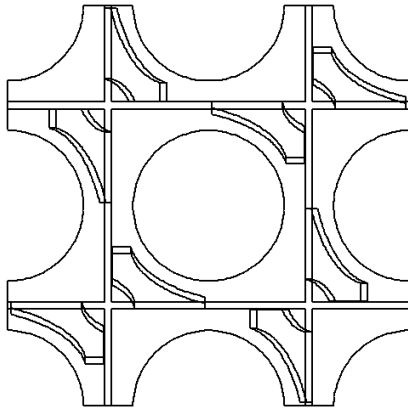


Figure 5.50 Vane pattern of the CFD model (View from Top of the grid, upstream the flow)

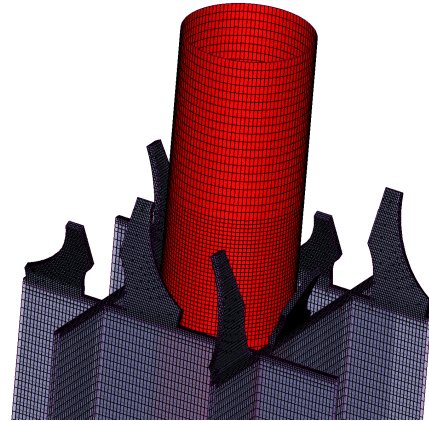


Figure 5.51 Mesh for the simplified mixing vanes with two vane layout

5.5.2 Numerical results and discussion

Radial velocity distribution:

Figure 5.52 presents the horizontal velocity distribution downstream the spacer grid with mixing vanes for the liquid phase. The axial altitude is measured from the tip of the vanes.

The dominant swirl can be found in the centers of the sub-channels, created by the mixing vanes at a few millimetres ($Z = 5$ mm) downstream the tip of the vanes. The direction of the swirl flow depends on the orientation of the corresponding pair of the vanes. Compared to the simulations of the single sub-channel with 4 mixing vanes the swirl is not circular anymore. Detailed examining of this swirl flow shows two vortices in the center of the sub-channel created on the vane tip. Additionally, there are also other smaller swirls in the gaps created by the vanes. Such secondary swirls are shown experimentally for the single phase flow in a sub-channel immediately after the mixing vanes (2 vane layout) and are explained in this special geometry by the base of the vane partly extending in the rod gap and inducing local swirl [28].

Further downstream the vanes the swirl flows in the gap disappear and two vortices in the sub-channel joining to one swirl flow. Such effect is also shown in the single-phase 5x5 rod bundle experiments [28]. The decay of this central swirl flow in each single sub-channel along the axial altitude can be seen, leading to very small values of the horizontal velocities before the next spacer grid. The swirl can be well-recognized up to the outlet.

Besides the swirl flow in each sub-channel already performed in previous calculations in single

sub-channel geometry a cross flow between the adjoining sub-channels and the impact of the mixing vanes plays a very important role in the 2x2 sub-channel geometry (Figure 5.52). This cross flow reduces the temperature differences in the adjoining sub-channels and contributes to an improved CHF performance of the fuel elements.

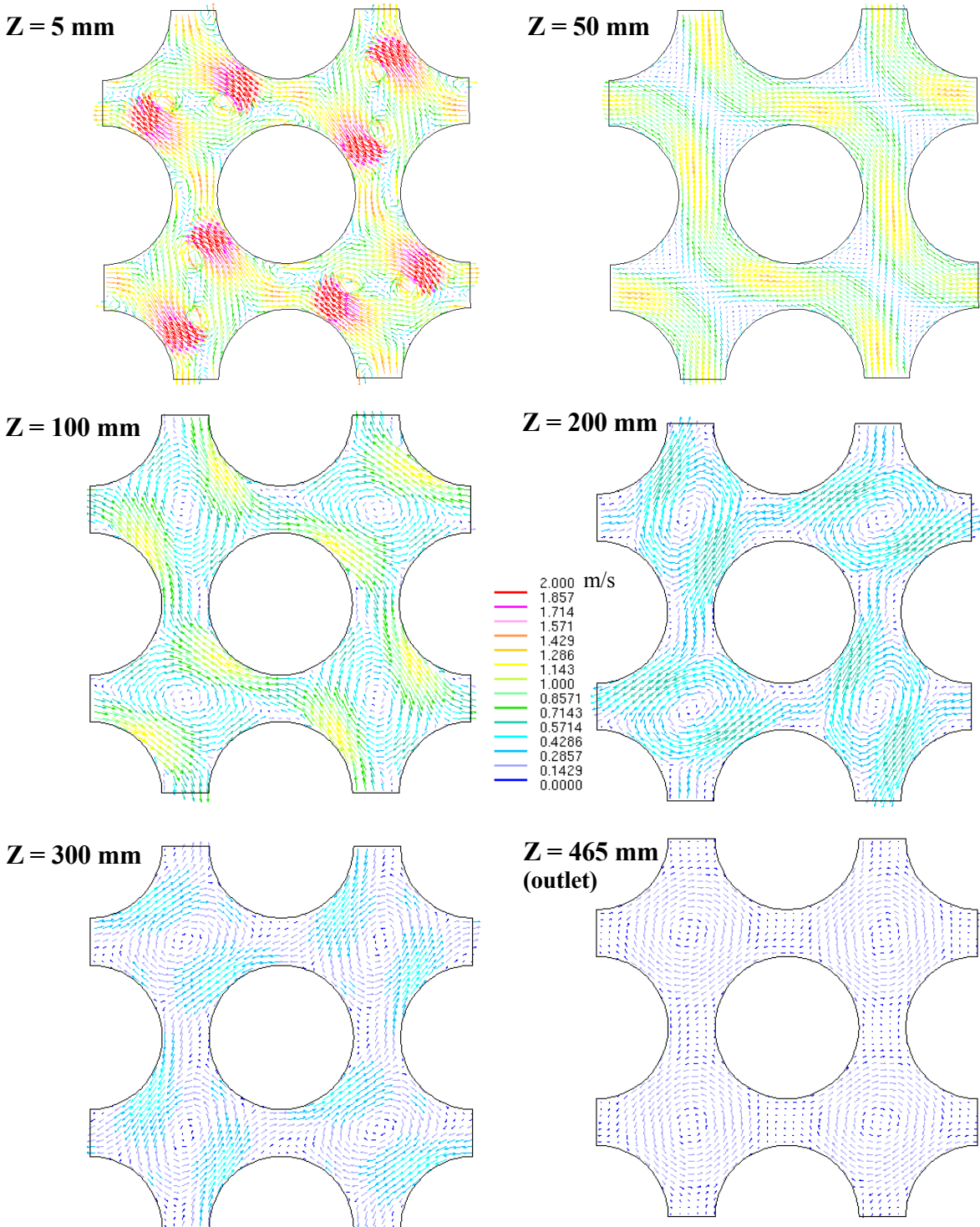


Figure 5.52 Horizontal velocity distribution of the liquid phase downstream the mixing vanes. Fine mesh

5 Flow in sub-channels under swirl conditions

Compared to the results of the isothermal calculation from [132] the main phenomena such as the swirl flow in the sub-channels and the cross flow between sub-channels look very similar.

Void fraction distribution:

Figure 5.53 presents the void fraction distribution calculated for the 2x2 sub-channel flow with heated rods immediately downstream the tip of the vanes. It shows one more example for the phase separation by centrifugal forces caused by the deflection of the vanes.

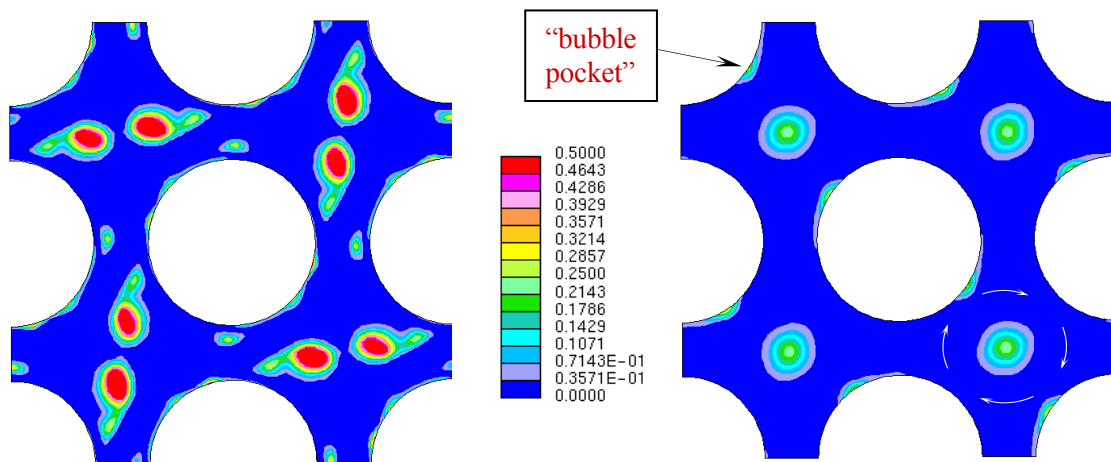


Figure 5.53 Void fraction distribution immediately downstream the tip of the vanes. Non-isothermal calculation

Figure 5.54 Void fraction distribution at the outlet. Non-isothermal calculation

The bubbles are accumulating at the tip of the vanes. Such accumulation is also shown in isothermal calculation presented in [132]. A similar effect has been achieved by recent two-phase calculation with another CFD code [110], where boiling Freon tests in a single heated tube with three-mixing blades are simulated. Although the steam is produced at the wall, passing through the mixing device most of the steam bubbles move to the center of the wakes induced by the blades and accumulation of the bubbles immediately downstream the tip of the blades is shown. Unfortunately such results are not validated due to missing measured data in the region near the mixing vanes.

In Figure 5.54 the void fraction distribution upstream the next spacer grid is presented. The calculated void distribution at outlet in 2x2 sub-channel geometry also has two areas of accumulation of bubbles as for the single sub-channel calculations. Due to the local centrifugal forces the bubbles are accumulating in the center of the sub-channels and additionally “bubble pockets” on the lee side of the rods can be seen. The accumulation of the bubbles in the sub-channel is slightly shifted from the center of the sub-channel. Each rod has two pockets, because of the 2 vane layout. In the previous calculations for the single sub-channel a 4 vane layout has been modeled and 4 “bubble pockets” were seen.

5.6 Conclusions

The calculations performed for a simplified sub-channel geometry with defined rotational flow at the inlet already show the potential of CFD analyses to assess the impact of geometrical variations on flow parameters influencing CHF performance. First, two-phase optimization studies of the declination angle of the vanes were carried out for this simplified geometry. As analyzed parameters swirl, pressure loss, accumulation of bubbles on the rods and in the center of the sub-channel (caused by local centrifugal force) as well as the wall temperature were chosen. The positive impact of the swirl was proven and an optimum for the declination angle was found. An extended heat partitioning model for the heat transfer at the heated surfaces was applied in the code. This new model allows superheating of gas bubbles in contact with heated surfaces. Application of this model to the simplified sub-channel geometry leads to a more pronounced improvement of DNB for sub-channel flows under swirl conditions.

For a more realistic description of the flow distribution in a single sub-channel, simplified swirl generating vanes of a four vane layout were modeled. Compared to the simplified sub-channel geometry with defined rotational flow at inlet this model showed similar swirl decay downstream the vanes and the impact of the swirl on the void fraction distribution. Flow separation due to the centrifugal forces leads to two regions of the accumulation of bubbles in the center of the sub-channel and on the lee side of the rod. With the refinement of the mesh qualitatively, the same physical phenomena was shown. But there is quantitatively an impact of the mesh on the void distribution; a thinner layer of bubbles at the walls was calculated. Therefore, for all further calculations the fine mesh was taken.

The evaluation method for the swirl was improved using the curl-velocity on an adapted control surface instead of the maximum horizontal velocity used in the previous optimization studies for simplified sub-channel geometry with defined rotational inlet flow. The axial decay of the swirl was calculated, showing that the swirl loses $\sim 90\%$ of its intensity after half of the span (The choice of the control surface showed a small influence.) Next, the centrifugal force was proved to have a very high impact on the flow distribution in the sub-channel under swirl conditions. Two-phase parameters (lift force or bubble bulk diameter) showed a small influence on the flow distribution in opposite to cases with the vertical flow in the pipes without swirl.

As an example for a swirl generating component without vanes a simplified swirl promoter integrated in the spacer grid and inducing swirl around the rod was modeled. The calculated void fraction distribution upstream the next spacer grid was compared to the distribution achieved with the previous simplified model with four mixing vanes, generating swirl in the

5 Flow in sub-channels under swirl conditions

sub-channel. The comparison was carried out for a non-isothermal case without taking into account the turbulence of the flow. Both models showed phase separation leading to the accumulation of the bubbles at the rod surface, but for the calculation with the mixing vanes the “bubble pockets” were much smaller. The impact of the turbulence and wall heating on the void fraction distribution are important factors for the sub-channel flow under swirl conditions and they should be modeled in the future work to get more realistic conclusions.

A significant step towards the two-phase CFD modeling in real geometries and under real flow conditions was taken in the concluding part of this work. Combining high computational power with improved numerical methods allowed isothermal two-phase calculation of a simplified spacer grid with mixing vanes of a two vane layout in a 2x2 sub-channel geometry and finally the first non-isothermal solution, taking the turbulence of the flow into account.

The velocity distribution of the liquid phase calculated immediately downstream the tip of the vanes shows a complicated form of the flow consisting mostly of the cross flow between the adjacent sub-channels and swirling flows: swirls on the tip of the vanes and small vortices in the gaps between the rods. Swirl flows lead to the accumulation of bubbles in their centers due to centrifugal forces. Further downstream, the swirls on the tip of the vanes join to one central swirl that decays with the axial distance. The axial decay of the cross flow between the adjacent sub-channels as well as vanishing of the small swirls are also shown in the velocity patterns. Such behavior of the flow is consistent with measurements carried out for the single-phase flow with the spacer grids of the same layout [28] and with the calculations carried out with another CFD code for boiling Freon flow under swirl conditions [110].

In the most interesting region for the possible occurrence of CHF before the next spacer grid the void fraction distribution for the 2x2 sub-channel geometry with mixing vanes of the two vane layout shows similar phenomena of phase separation due to the centrifugal force as in previous calculations of single sub-channel with mixing vanes of the four vanes layout. All differences are plausible and can be explained by the form of the vanes and the additional cross flow.

The two-phase non-isothermal model of the 2x2 sub-channel geometry proved the existence of two regions of the accumulation of bubbles. Due to the impact of the centrifugal force on the void distribution, bubbles primarily accumulating in the sub-channel center. Because of changing the sign of the streamlines in the vicinity of the rods, there are also “bubble pockets” generated on the rod surfaces (in all simulations independent of the model). It has a significant impact on the local heat transfer and could be a new CHF-indicator (more realistic than single-phase indicators).

6. Closure

6.1 Conclusions

One of the main long-term goals for the development of the thermal-hydraulic methods is to improve CHF prediction for flow boiling in real fuel assembly geometries and under real thermal-hydraulic conditions by CFD calculations. The reviewed literature dedicated to CFD applications in the nuclear field showed clearly the need of two-phase flow analyses for various sub-channel geometries under swirl conditions for PWR applications. This motivated the research work presented in this thesis. As working tool the CFD code STAR-CD was used to achieve a contribution towards this goal.

In the following, the main achievements of this work are summarized:

- The two-phase methodology used in STAR-CD was analyzed with respect to sub-channel application under high pressures. The origin and some limitations of the applied models were pointed out.
- Validation-work available from literature for the current two-phase STAR-CD version were summarized and reviewed. Contributions have been made towards improved modeling of flow boiling under PWR conditions using detailed CFD analyses of experimental data of radial void distributions in pipes.
- An enhanced mechanistic wall heat transfer partitioning model applied to CHF conditions showed improvement with respect to the realistic description of the CHF phenomena validated by CHF experiments.
- An important contribution was made towards the detailed modeling of boiling in fuel assembly geometry under swirl conditions and the definition of the possible two-phase indicators of CHF performance.

In this Section the most relevant conclusions of the performed work are reviewed, followed by suggestions for future work presented in Section 6.2. Both sections are arranged into two parts with the focus on the two-phase CFD modeling with its validations, and sub-channel applications under swirl PWR conditions, respectively.

Two-phase CFD model with its validations:

For illustration of CFD modeling first STAR-CD methodology for single-phase flow is outlined. Further, a detailed overview of changes and additional terms needed for two-phase modeling was provided. Equations used for the STAR-CD calculations with the *Euler-Euler* technique were discussed in detail based on literature sources.

In the present STAR-CD two-phase model the physical properties are defined as constant, so that suitable approximations of the values have to be found. In particular, the method chosen for the approximation of the specific heat by a constant value has a very noticeable influence on the calculated results e.g. void fraction. Disadvantages of the already known method applied by various authors for sub-cooled boiling at high pressures were shown. An improved method for such flow conditions was proposed and used in the calculations presented in this work.

Published papers and presentations related to validations for the current two-phase STAR-CD model for various geometries were reviewed. In those validations firstly, axial distributions of the temperature, pressure drop and void fraction as well as radial distribution of the velocity and void fraction at various flow conditions for simple geometries (pipe, annulus, mixing chamber) were compared with experimental data, showing good agreement. Finally, for a full-length 8x8 BWR rod bundle with spacer grids without swirl promoters the sub-channel averaged void fractions at outlet were pointed out to be very well predicted.

As the sub-channel analyses in this thesis were carried out under PWR conditions, the validations under high pressures were summarized; the axial and radial flow profiles were validated for air-water experiments. For water-steam flow, only axial flow profiles were successfully compared with experiments. Therefore, additional validations under high pressure conditions were required. For this purpose an experiment including detailed results for local void distribution in a heated vertical tube with Freon as a working medium and scaled to water-steam PWR conditions was chosen. The most important two-phase parameters were varied and two sets of parameters for the physical models were found showing good agreement for low and high void fractions, respectively. These physical models provide already a very good approximation to reality; however, they still should be improved in depth and detail.

An additional important topic within the framework of this study was to show the potential of two-phase CFD codes for modeling of CHF and to find ways for its improvement. The analysis has been performed for DNB at PWR conditions for upward directed vertical flow in a heated pipe system, since the computed results for critical heat flux can be compared with reliable results of existing correlations. In this work, critical values were obtained from the empirical

DNB correlation of *Doroshchuk* for comparison with CFD results. The generic model available at the time of this study did not show a typical temperature rise at CHF conditions. A modification in the wall heat partitioning model was proposed, which allows steam superheating for bubbles in contact with heated surfaces. The transition between the standard and modified wall heat partitioning model was defined heuristically. A method for obtaining the critical heat flux value was proposed and applied for two cases resulting in good prediction of the CHF values compared to the values from empirical correlation. Although such results were achieved only for pipes flow with a relative coarse mesh, they represent an important step towards the CHF prediction for pipes and, in the future, for sub-channel applications. The modified wall heat partitioning model has only an impact on the cells adjacent to the surface. Therefore, the application to non-pipe geometries should be permissible.

Sub-channel CFD analyses under swirl conditions:

A general method for deterministic CHF predictions for sub-channel geometry based on two-phase CFD analyses is not yet available. Therefore, assessments of CHF behavior based on relevant physical parameters are helpful to assess trends of CHF for different designs. Some parameters to indicate DNB were analyzed for various sub-channel geometries: swirl, cross flow, pressure loss and accumulations of bubbles on the rods. These analyses can be divided into three parts carried out under swirl conditions: single-phase calculation of the sub-channel flow, calculation of two-phase adiabatic flow and calculations of the two-phase non-adiabatic flow with heated rods. For the last part the superheating at the wall was analyzed as an important additional parameter.

A study of fluid flow in fuel assemblies requires a special focus on swirl conditions in sub-channels. For a better understanding of the impact of swirl, CFD analyses of sub-channel flow started with a generic swirl model with a defined rotational flow at the inlet. For a more realistic description of the flow in a single sub-channel, simplified vanes were modeled for swirl generation within the sub-channel. Additionally, the same single sub-channel geometry was analyzed with another type of swirl generating component inducing swirl around the rod. The geometric model was continuously further developed. Finally, a combination of high computational power with improved numerical methods allowed non-isothermal two-phase calculation for complex geometries such as realistic vanes in connected sub-channels.

Already the calculations performed for the simplified model with generic swirl defined at inlet allowed to assess the impact of the geometrical variation on the flow parameters assumed to influence the CHF performance. Two-phase optimization studies of the declination angle of

6 Closure

vanes were carried out. The application of an extended wall heat partitioning model for the heat transfer at the heated surfaces showed a more pronounced and distinguishable improvement of DNB for sub-channel flows under swirl conditions.

The performed two-phase calculations showed phase separation, mainly caused by centrifugal forces. Bubbles are collecting at the center of the sub-channel. In the vicinity of the rods, “bubble pockets” are generated on the lee side of the rod surfaces, due to a sign change of the curvature of the streamlines. This effect occurred in all analyzed geometries and could be a new indicator for CHF behavior. The prevention or minimization of such “bubble pockets” could be a new two-phase optimization criterion for FA-design.

The bubble accumulation at the rod surface was used to assess two different types of the swirl generating components in the single sub-channel geometry. Calculations showed locally a significantly different void distribution having an impact on the surface temperature of the rods. Because in these first calculations cross-flow between adjacent sub-channels, turbulence and wall heating have not been modeled, no general conclusion can be drawn yet, but some phenomena occurring in different geometrical designs can be qualitatively well explained.

A major step in the direction of the two-phase flow CFD simulations for real fuel assemblies was achieved with successful modeling of the non-isothermal flow in the 2x2 sub-channel geometry with mixing vanes. The results provide CHF relevant details for improved interpretation of the flow situation with respect to heat transfer that will significantly increase the reliability of engineering judgment.

6.2 Suggestions for future work

Two-phase CFD model with its validation:

- When increased computational power is available, variable material properties from water-steam tables should be used instead of constant values to enhance the quantitative accuracy of the simulations.
- In the future, the validation process for the two-phase models should be based on a unambiguous and consistent set of parameters applied to the whole range of validation cases without further tuning.
- Also further basic research should be performed to quantify the physical effects, especially with regard to three-dimensional numerical modeling from water as a carrier fluid with dispersed steam bubbles at the inlet straight through to steam as a carrier fluid

with dispersed water droplets at the outlet. The use of flow regime maps offers some promising potential for a more general modeling.

- The proposed enhanced heat partitioning model showed promising results with respect to CHF prediction. It should be further applied to various inlet conditions and also numerically improved. As a rigorous theoretical physical model without empirical correlations describing in detail the DNB phenomena does not yet exist, the development of reliable mechanistic models with wide applicability based on the theoretical approach but still using some empirical equations is recommended. In the future, this model should take into account bubbles sliding along the wall surface, transport equation for the bubbles including coalescence and breakup, etc.
- Reliable local measurements of void fraction, temperature and velocity for the steam-water flow at high pressures would aid future development of the CFD as a reliable two-phase tool for reactor applications.

Sub-channel CFD analyses under swirl conditions:

- The comparison of the different geometrical designs with respect to DNB should be further conducted for connected sub-channels with heated rods.
- For more accurate two-phase CFD simulations, it is required to include details of rod support structures in the future as they influence the approaching flow profile upstream the mixing vanes and are already modeled in detail in single-phase flow calculations. Such modeling is currently carried out but numerical methods needed to be improved for non-isothermal application to a model with such fine geometry details.
- Although the influence of the turbulence model has not been investigated within the scope of this work, it is an important point for the prediction of the flow distribution. More complex (e.g. *Reynolds-Stress* models higher-order turbulence models) should be applied in the future, as the $k-\varepsilon$ model is known to be less accurate in describing secondary flow effects in rod bundles. The measurement technology should be further developed to show the influence of the second-phase on the flow distribution and to validate velocity profiles for both phases at high pressures.
- With the goal to make conclusions with respect to the CHF performance of fuel assemblies, the geometry of the model should be further enlarged to 5x5 fuel rod models. Further developed two-phase modeling is needed for a better prediction of critical heat transfer conditions. For a first validation of the CHF modeling, pipe

6 Closure

experiments can be sufficient. Achieving these two goals, the validation of the existing CHF 5x5 rod bundle experiments would be possible.

- For more realistic conclusions on fuel assembly thermal-hydraulic behavior in the core of a reactor the feedback from neutron physics and axial and radial power profiles has to be taken into account. A current pilot project exists, carried out in cooperation between ANL, KAERI, Purdue University and CD-adapco, coupling two-phase flow with neutron physics and the structural analyses that might show the potential for a full reactor core computing [100]. This will require of course reliable coupling of physical models and massive computational power.

Appendix A

Error estimation of specific enthalpy for different approximation methods

The temperature and specific enthalpy in STAR-CD are related by specific heat. Due to a restriction in the current code only constant values for specific heat - for liquid and gas phase respectively can be chosen. Various approximation methods can be applied to evaluate these constants.

In Section 3.6 such methods were presented. In the first method, proposed in this work, a mean specific heat is chosen at saturation conditions and is applied as an approximation for the whole temperature range. The second method, proposed by STAR-CD in a tutorial or by *Krepper* for nuclear applications applies differential specific heats at saturation conditions for the whole temperature range.

To estimate the error of specific enthalpy evaluated with such approximation methods, one validation case of *Garnier* experiments from Chapter 4.2 was chosen and the estimated error was compared for different sub-cooling of the liquid, characterizing the region of the high sub-cooling of the liquid temperature and the region, where liquid temperature is near saturation, respectively:

- a) high sub-cooling region : $\Delta T_{sub}^{inlet} = 130.02 K$ ($t = t_{inlet} = 222.94^\circ\text{C}$),
- b) near saturation region: $\Delta T_{sub}^{inlet} = 10 K$ ($t = 342.96^\circ\text{C}$).

Input data of the validation case chosen for the error estimation is presented in Table A-1.

Table A-1 Inlet parameter for validation case $x_{eq} = -0.118$

	Water	Steam
Pressure	$p = 171.39 \text{ bar}$	
Saturation temperature	$t_s = 352.96 \text{ }^\circ\text{C}$	
Inlet temperature	$t_{inlet} = 222.94 \text{ }^\circ\text{C}$	$t_s = 352.96 \text{ }^\circ\text{C}$
Specific enthalpy at saturation	$h_l(t_s) = 1695.8 \text{ kJ/kg}$	$h_g(t_s) = 2542.4 \text{ kJ/kg}$
Latent heat	$h_{fg} = 846.6 \text{ kJ/(kgK)}$	

Appendix A

It has to be pointed that the latent heat is set by the user in the boiling subroutine and independent of the applied approximation method the boiling process is modeled with the exact latent heat for the corresponding pressure.

First approximation method: Mean specific heat defined for the temperature interval $[t_0, t_s]$ and applied for any temperature from interval $t_{inlet} \leq t \leq t_s$ with reference temperature $t_0 = 0^\circ\text{C}$

The temperature interval for error estimation is $t_{inlet} \leq t \leq t_s$. Eq. (159) with $t_2 = t_s$ and $t_1 = t$ yields:

$$h(t_s) - h(t) = \int_t^{t_s} c_p(t) dt = \int_0^{t_s} c_p(t) dt - \int_0^t c_p(t) dt = \bar{c}_{p0}^{t_s} t_s - \bar{c}_{p0}^t t. \quad (\text{A-1})$$

According to the approximation using mean specific heat obtained for the temperature interval $[t_0, t_s]$, applied for any temperature from interval $t_{inlet} \leq t \leq t_s$:

$$\bar{c}_{p0}^{t_s} = \bar{c}_{p0}^t = \frac{h(t_s)}{t_s}. \quad (\text{A-2})$$

Then Eq. (A-1) can be written in terms of sub-cooling:

$$h(t_s) - h(t) = \bar{c}_{p0}^{t_s} (t_s - t). \quad (\text{A-3})$$

Mean specific heat obtained for the temperature interval $[t_0, t_s]$ for both phases can be calculated from Eqs. (162) and (163) as following:

$$\bar{c}_{p0l}^{t_s} = \frac{h_l(t_s)}{t_s} = \frac{1695.8}{352.96} = 4.80451 \frac{\text{kJ}}{\text{kgK}}, \quad (\text{A-4})$$

$$\bar{c}_{p0g}^{t_s} = \frac{h_g(t_s)}{t_s} = \frac{2542.4}{352.96} = 7.20308 \frac{\text{kJ}}{\text{kgK}}. \quad (\text{A-5})$$

The relative error of specific enthalpy at liquid sub-cooling estimated in terms of mean specific heat obtained for the temperature interval $[t_0 = 0, t_s]$ is defined here as:

$$\delta_h^m(t) = \frac{\bar{c}_{p0}^{t_s} (t_s - t) - [h(t_s) - h(t)]}{h(t_s) - h(t)} \cdot 100\%, \text{ with } h(t) \text{ taken from the water-steam table.} \quad (\text{A-6})$$

This error is estimated for two different regions of sub-cooling:

High sub-cooling region: $\Delta T_{sub}^{inlet} = 130.02 \text{ K}$

Enthalpy obtained from water-steam table:

$$h_i(t_{inlet}) = 961.48 \frac{\text{kJ}}{\text{kg}}. \quad (\text{A-7})$$

The relative error of specific enthalpy from Eq. (A-6) for $t = t_{inlet} = 222.94^\circ\text{C}$ estimated by terms of mean specific heat defined for the temperature interval $[t_0 = 0, t_s]$ results in:

$$\delta_h^m(t = 222.94^\circ\text{C}) = 15.2\% . \quad (\text{A-8})$$

Near saturation region: $\Delta T_{sub}^{inlet} = 10 \text{ K}$

Enthalpy obtained from water-steam table:

$$h_l(t = 342.96^\circ\text{C}) = 1604.8 \frac{\text{kJ}}{\text{kg}} . \quad (\text{A-9})$$

The relative error of specific enthalpy from Eq. (A-6) for $t = 342.96^\circ\text{C}$ estimated by terms of mean specific heat defined for the temperature interval $[t_0 = 0, t_s]$ is equal:

$$\delta_h^m(t = 342.96^\circ\text{C}) = 47.2\% . \quad (\text{A-10})$$

Second approximation method: Differential specific heat at saturation applied for any temperature from interval $t_{inlet} \leq t \leq t_s$ with reference temperature $t_0 = 0^\circ\text{C}$

The temperature interval for error estimation is $t_{inlet} \leq t \leq t_s$. According to the approximation using differential specific heat at saturation applied to any temperature in the interval $t_{inlet} \leq t \leq t_s$:

$$\bar{c}_{p_0}^{t_s} = \bar{c}_{p_0}^t = c_p(t_s) . \quad (\text{A-11})$$

Then Eq. (A-1) can be written as:

$$h(t_s) - h(t) = c_p(t_s)(t_s - t) . \quad (\text{A-12})$$

Values of differential specific heat for both phases can be obtained from water-steam table:

$$c_{p_l}(t_s) = 11.049 \frac{\text{kJ}}{\text{kgK}} , \quad (\text{A-13})$$

$$c_{p_g}(t_s) = 18.845 \frac{\text{kJ}}{\text{kgK}} . \quad (\text{A-14})$$

The relative error of the specific enthalpy at liquid sub-cooling estimated in terms of the differential specific heat at saturation is defined here as:

$$\delta_h^d(t) = \frac{c_p(t_s)(t_s - t) - [h(t_s) - h(t)]}{h(t_s) - h(t)} \cdot 100\% . \quad (\text{A-15})$$

Appendix A

This error is estimated for two different regions of sub-cooling:

High sub-cooling region: $\Delta T_{sub}^{inlet} = 130.02 K$

The relative error of specific enthalpy from Eq. (A-15) for $t = t_{inlet} = 222.94^{\circ}C$ estimated by terms of differential specific heat at saturation yields in:

$$\delta_h^d(t = 222.94^{\circ}C) = 95.6\% . \quad (A-16)$$

Near saturation region: $\Delta T_{sub}^{inlet} = 10 K$

The relative error of specific enthalpy from Eq. (A-15) for $t = 342.96^{\circ}C$ estimated by terms of differential specific heat at saturation results in:

$$\delta_h^d(t = 342.96^{\circ}C) = 21.4\% . \quad (A-17)$$

It can be seen that for the case b (in the region near saturation with sub-cooling of 10 K) the second method of the evaluation of the enthalpy provides errors that are much smaller than the first one. With increased liquid sub-cooling the approximations of the second method becomes worse. The maximum error of estimation of the second method is achieved at the inlet of the model (case a). There it is about six times higher than the error of the first method.

Therefore, for the calculations of the sub-cooled boiling under PWR conditions the first approximation method is recommended for use.

Appendix B

Validations based on *Garnier* experiment

B.1 Scaling laws following *Ahmad*

Ahmad in [2] presented the distorted fluid-fluid critical heat flux model, proposed following set of the relevant π -terms derived from classical scaling theory:

$\pi_1 = \frac{\phi}{G\lambda_{lg}}$	(Boiling Number)	(B-1)
$\pi_2 = \frac{GD}{\mu_l}$	(<i>Reynolds</i> Number)	(B-2)
$\pi_3 = \frac{\mu_l^2}{\sigma D\rho_l}$	(<i>Weber-Reynolds</i> Number)	(B-3)
$\pi_4 = \frac{\mu_l}{\mu_g}$	(Liquid/Vapor Viscosity Ratio)	(B-4)
$\pi_5 = \frac{\Delta h}{r}$	(Sub-cooling Number)	(B-5)
$\pi_6 = \frac{\rho_l}{\rho_g}$	(Liquid/vapor density ratio)	(B-6)
$\pi_7 = \frac{L}{D}$	(Specifies geometric similarity)	(B-7)
$\pi_8 = \frac{g D^3 \rho_l}{\mu_l^2}$	(<i>Froude-Reynolds</i> Number)	(B-8)
$\pi_9 = \frac{c_{p,l}\mu_l}{\lambda_l}$	(Liquid <i>Prandtl</i> Number)	(B-9)
$\pi_{10} = \frac{c_{p,g}\mu_g}{\lambda_g}$	(Vapor <i>Prandtl</i> Number)	(B-10)
$\pi_{11} = \frac{\lambda_l}{\lambda_g}$	(Liquid/vapor thermal conductivity ratio)	(B-11)
$\pi_{12} = \sqrt{\frac{\gamma}{\rho_l}} \cdot \frac{\mu_l}{D}$	(<i>Barnett</i> Number)	(B-12)
$\pi_{13} = \frac{\beta c_{p,l}}{\gamma r}$, with $\beta = \left. \frac{\partial T}{\partial p} \right _{\text{at saturation}}$	(Saturation temperature Number)	(B-13)

B.2 Variation of parameters

For the following validation study the measured radial void fraction profile of the refrigerant R12 in a vertical tube with upflow conducted by *Garnier et al.* [50] is chosen. The measured outlet equilibrium quality for the chosen case is $x_{eq} = -0.118$. The inlet data of the experimental fluid is scaled to water conditions using the scaling laws presented in Section 4.2.1 and then used for corresponding CFD calculations. The used numerical method is presented in Section 4.2.2. The bubble diameter in the bulk in all following calculations is set to constant value of 1 mm.

Lift force:

Leaving all other two-phase parameters constant, the lift force modeled by Eq. (85) is varied. It has to be noted, that during this study the wall lubrication force is not taken into account. Radial void fraction distributions achieved without lift force, with a small lift coefficient $C_L = 0.05$ and with a standard lift coefficient $C_L = 0.25$ were compared with the measured results.

Figure B-1 shows that the best agreement with the experimental data for constant bubble diameter in the bulk can be achieved if lift force is near zero. The region near the wall is matched perfectly, but in the whole bulk region with existing bubbles the void fraction is overpredicted. Though the bulk region (almost till $r/R < 0.9$) can be modeled much better with the standard lift coefficient, the void fraction at the wall is increasing rapidly to unrealistic high values. This study indicates that the compensation of the lift and lubrication forces can be advantageous for the considered cases. All other calculations take into account this assumption.

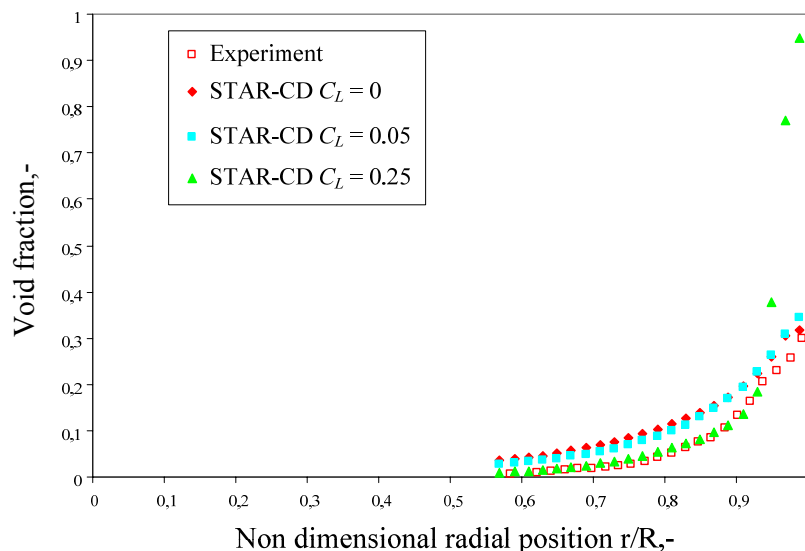
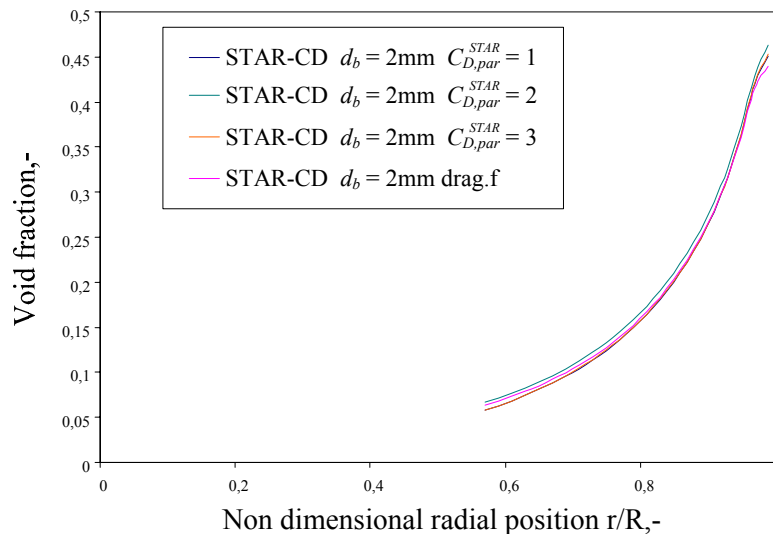


Figure B-1 Radial void fraction distribution for $x_{eq} = -0.118$ at the outlet. Measured data (*Garnier et al.* [50]) compared to results of STAR-CD calculations for various values of C_L

Drag force and drag coefficient:

For calculations with a bubble diameter in the bulk $d_b = 1$ mm, which is applied in all other cases with constant diameter, it was not possible to achieve convergence for all types of drag modeling. Therefore, the sensitivity of the results on the formulation for drag force and drag coefficient is investigated based on the calculations made for constant $d_b = 2$ mm.

The models corresponding to the values of $C_{D,par}^{STAR}$ have been summarized already in Table 3.3. The comparisons show that there is no big difference in the radial void distribution for various formulations (see Figure B-2).



**Figure B-2 Radial void fraction distribution for $x_{eq} = -0.118$ at the outlet.
Results of STAR-CD calculations for various drag formulations**

In all following calculations considered a constant bubble diameter in the bulk the user subroutine drag.f with standard drag force formulation and factor taking into account particle accumulations presented in Eq. (78) is applied. Further, the chosen model for the drag coefficient takes into account bubbles with non-spherical shape, based on empirical correlation of Wang [163] (Eq. (83)).

In the later calculations a variable bubble diameter in the bulk flow is used to improve the two-phase modeling with respect to the radial void fraction distribution. For these cases variable diameter is also implemented in the user drag subroutine.

Turbulence response coefficient:

The turbulence response coefficient C_t is defined in Eq. (92). To test the influence of this coefficient on the radial void distribution two formulations are compared. The first one, noted with parameter $C_{t,par}^{STAR} = 1$, assumes no dependency on the void fraction and sets the response coefficient equal unity. The velocity fluctuations of the dispersed and continuous phase are

Appendix B

assumed to be equal applying this formulation. The second formulation is void-dependent and proposed by *Rusche* [124] for applications with high values of the void fraction (Eq. (102)). This formulation is noted by parameter $C_{t,par}^{STAR} = 2$. In both calculations all other two-phase parameters are equal and the applied bubble bulk diameter is set to $d_b = 1$ mm.

Figure B-3 shows small influence, but for void-dependent formulation the values of void fraction are lightly closer to the experimental values in both wall and bulk regions. This formulation is chosen for all other calculations.

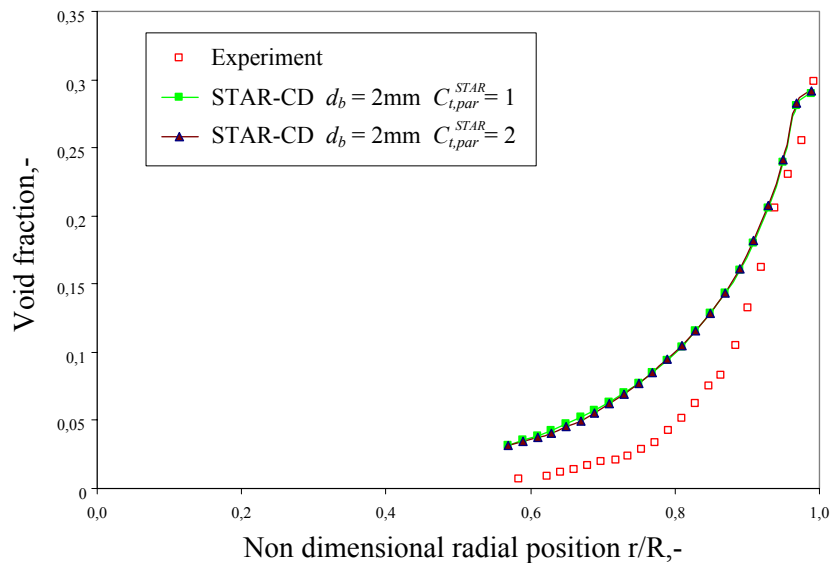


Figure B-3 Radial void fraction distribution for $x_{eq} = -0.118$ at the outlet. Measured data (*Garnier et al.* [50]) compared to results of STAR-CD calculations for various formulations of C_t

Nucleation density:

The nucleation density is modeled by Eq. (129). Values of the model constant m are found to be $m = 185$ in STAR-CD applications e.g. [98] and $m = 210$ in CFX applications e.g. [68]. The used value for the second model constant, power p is the same in both cases $p = 1.805$. First, these two variants are calculated and the void fraction distribution at outlet is compared to the experimental results of the *Garnier* in Figure B-4. It can be seen that with CFX value $m = 210$ the value of the void fraction distribution has a perfect agreement with the experimental data at the outlet direct near the wall, but in the whole bulk region the calculated values are overestimating the experiments stronger than results of modeling with STAR-CD value $m = 185$.

Eq. (129) was pointed out by *Kurul and Podowski* [86] to be obtained using correlated data of *Lemmert and Chawla* [94]. Figure B-5 illustrates this experimental data [94] for parallel flow with refrigerant R11 at atmospheric pressure flowing with low velocity normal to the surface of a heated flat plate.

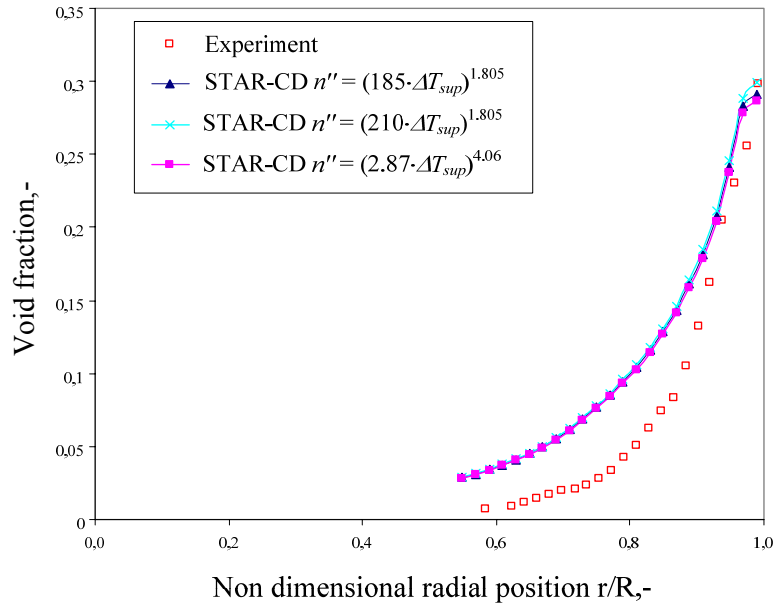


Figure B-4 Radial void fraction distribution for $x_{eq} = -0.118$ at the outlet. Measured data (Garnier et al. [50]) compared to results of STAR-CD calculations for various modeling of n''

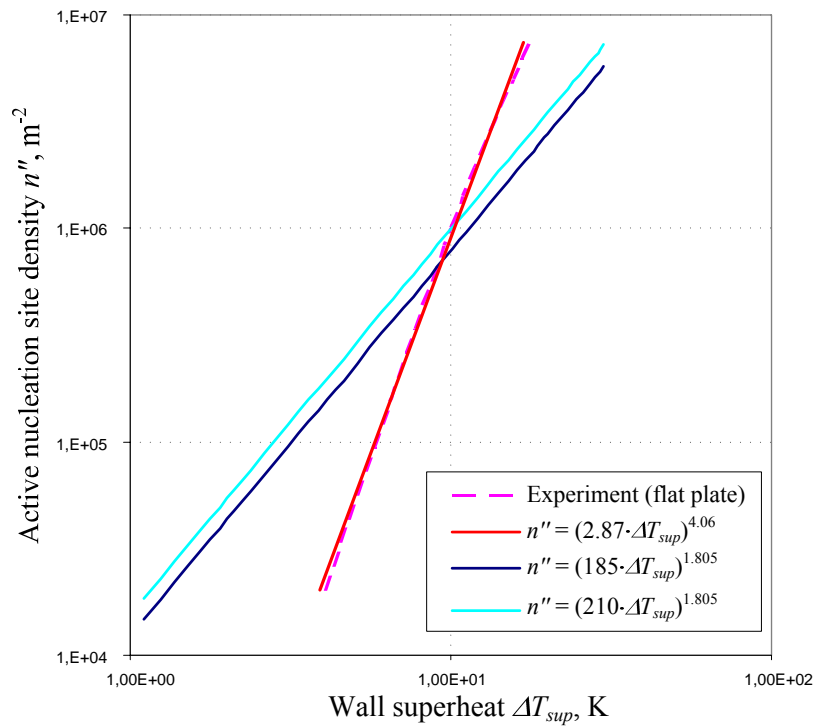


Figure B-5 Nucleation site density as a function of wall superheat. Various formulations compared to the experimental value from [94]

This data was correlated leading to constants $m = 2.876$ and $p = 4.06$. The void fractions at outlet achieved with this fit are also presented in Figure B-4 and are practically similar to the ones calculated with the STAR-CD standard formulation.

The reason why the results are so similar is that different formulations yield changing of the wall temperature. Therefore similar values of the nucleation density (difference is less than 2 %)

Appendix B

are achieved. For the following calculations the standard formulation used by STAR-CD with $m = 185$ and $p = 1.805$ is chosen.

Bubble departure diameter:

Following the influence of the formulation for the departure diameter d_w modeled with Eq. (130) as function of liquid sub-cooling is tested, based on experimental data of *Tolubinsky* and *Kostanchuk* [150] at atmospheric pressure of 1 bar. The value of the bubble departure diameter at liquid temperature at saturation d_s is varied between the measured value at 1 bar [150] of 1.4 mm, value used in [147] of 0.6 mm and new value of 0.28 mm, proposed here.

The last value is estimated by examining the measured dependency of the bubble departure diameter on the pressure at constant sub-cooling of 20 K from 1 to 10 bar, presented in Figure B-6. This curve shows that with an increase of the pressure until a pressure value of 8 bar the bubble departure diameter is decreasing and then almost does not change its value.

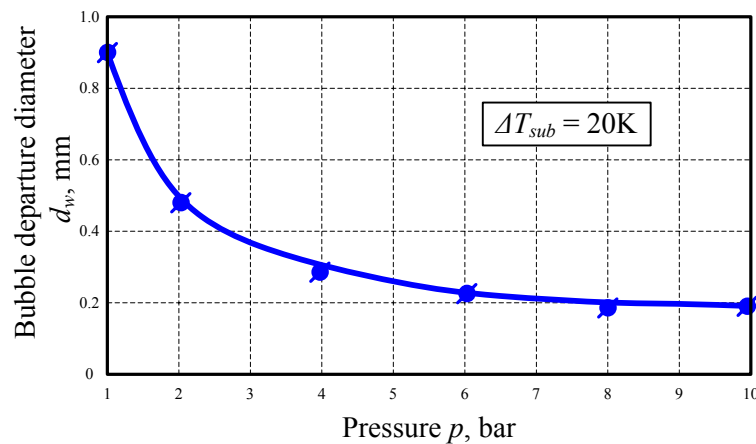


Figure B-6 Dependence of the bubble departure diameter on the system pressure at sub-cooling of 20 K (adopted from [150])

It can be proposed that the bubble departure diameter for flow conditions with liquid temperature at saturation with $\Delta T_{sub} = 0$ K at system pressure of 160 - 170 bar is about 20 % of the diameter at saturation at 1 bar: $d_s(p = 170 \text{ bar}) \approx d_s(p = 1 \text{ bar}) \cdot 0.2$. Then the value of the bubble departure diameter at saturation liquid temperature becomes $d_s(p = 170 \text{ bar}) \approx 0.28$ mm, due to value $d_s(p = 1 \text{ bar}) = 1.4$ mm, which can be obtained from measured data (Figure 3.7).

Comparison with experimental data points showed that the model using $d_s = 1.4$ mm (value achieved from experimental data of *Tolubinsky* and *Kostanchuk* [150] at 1 bar and used as a standard value in different CFD programs inter alia STAR-CD version 3.26) is as expected due to pressure dependency overestimating the void fraction at the wall (see Figure B-7). The real value has to be smaller. The model using $d_s = 0.28$ mm proposed here underestimates the void fraction at the wall. As the consequence of pressure dependency the value $d_s = 0.6$ mm used in

[147] (new standard value for STAR-CD version 3.27) has the best agreement with experimental results. It seems to be more practicable for higher pressures and is chosen for all following calculations.

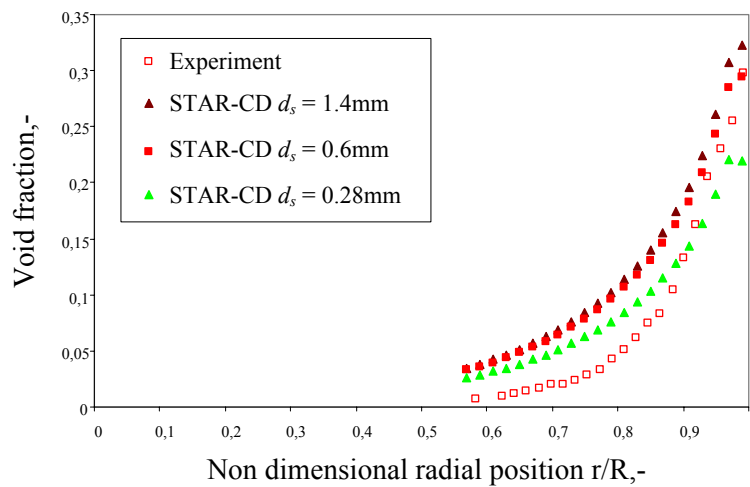


Figure B-7 Radial void fraction distribution for $x_{eq} = -0.118$ at the outlet. Measured data (Garnier *et al.* [50]) compared to results of STAR-CD calculations for various values of d_s

Boiling model constant:

The area of boiling is modeled by Eq. (122) and is used for evaluation of the heat parts in wall heat partitioning model. Boiling model constant F_A used in this formulation is determining the ratio of the boiling area of influence to the maximum bubble projected area. F_A is found to be equal 4 for pool boiling in [36] and to show good agreement with experiments describing forced convection boiling as well, being equal 1 in [137]. The sensitivity of the results to a change of this coefficient is presented in Figure B-8. The smaller value of $F_A = 1$ is assumed to take into account the overlapping of the neighboring bubbles and is used for all next calculations.

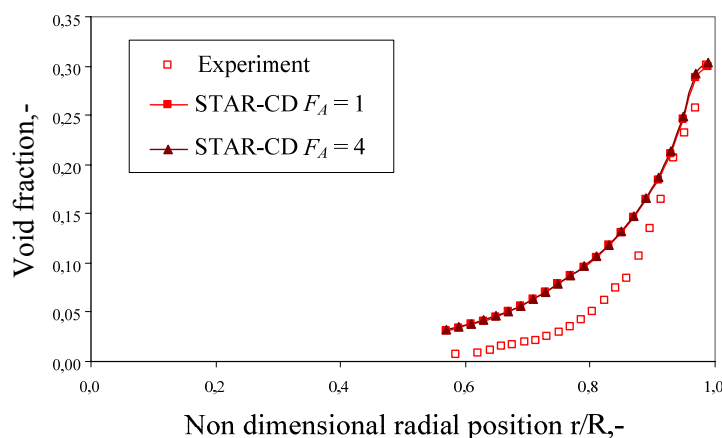


Figure B-8 Radial void fraction distribution for $x_{eq} = -0.118$ at the outlet. Measured data (Garnier *et al.* [50]) compared to results of STAR-CD calculations for various values of F_A

Appendix C

Validation of pipe flow critical experiment

C.1 Evaluation of the inlet equilibrium quality

Definition of equilibrium quality:

$$x_{eq} = \frac{h - h(t_s)}{h_{fg}} . \quad (C-1)$$

For inlet equilibrium quality:

$$x_{eq}^{inlet} = \frac{h(t_{inlet}) - h(t_s)}{h_{fg}} ; h(t_{inlet}) = h(t_s) + x_{eq}^{inlet} \cdot h_{fg} . \quad (C-2)$$

For any local equilibrium quality:

$$x_{eq}^l = \frac{h(t_l) - h(t_s)}{h_{fg}} ; h(t_l) = h(t_s) + x_{eq}^l \cdot h_{fg} . \quad (C-3)$$

The balance for a heated channel yields:

$$\frac{dh}{dz} = \frac{\dot{q}'}{\dot{m}} , \text{ where } \dot{q}' \text{ is linear heat generation rate.} \quad (C-4)$$

Enthalpy difference can be written:

$$dh = \frac{\dot{q}'}{\dot{m}} dz . \quad (C-5)$$

Integration from inlet to local point along vertical axis z with $z=0$ at inlet leads to:

$$\int_{h(t_{inlet})}^{h(t_l)} dh = \int_0^z \frac{\dot{q}'}{\dot{m}} dz . \quad (C-6)$$

Then specific enthalpy difference between inlet and local point can be obtained as:

$$h(t_l) - h(t_{inlet}) = \frac{\dot{q}'}{\dot{m}} \cdot z . \quad (C-7)$$

Using Eqs. (C-2) and (C-3) this equation can be written in terms of equilibrium qualities:

$$h(t_l) - h(t_{inlet}) = h(t_s) + x_{eq}^l \cdot h_{fg} - h(t_s) - x_{eq}^{inlet} \cdot h_{fg} = h_{fg} (x_{eq}^l - x_{eq}^{inlet}) = \frac{\dot{q}'}{\dot{m}} \cdot z . \quad (C-8)$$

The difference between inlet and local equilibrium qualities yields to:

$$x_{eq}^{inlet} - x_{eq}^l = -\frac{\dot{q}'}{\dot{m} \cdot h_{fg}} \cdot Z. \quad (C-9)$$

In CHF correlation wall heat flux \dot{q}'' is used. The heat transfer can be defines in terms of both heat flux and linear heat generation rate:

$$\dot{Q} = \dot{q}'' \cdot \pi \cdot D \cdot z = \dot{q}' \cdot Z. \quad (C-10)$$

Then the linear heat generation rate can be obtained from heat flux:

$$\dot{q}' = \dot{q}'' \cdot \pi \cdot D. \quad (C-11)$$

Using Eq. (C-9) the inlet equilibrium quality can be calculated from:

$$x_{eq}^{inlet} = x_{eq}^l - \frac{\dot{q}'' \cdot \pi \cdot D}{\dot{m} \cdot h_{fg}} \cdot Z. \quad (C-12)$$

In the CHF correlation the given value is inlet mass flux instead of mass flow:

$$\dot{m} = \frac{\pi \cdot D^2}{4} G. \quad (C-13)$$

Then the inlet equilibrium quality obtained in terms of mass flux and local equilibrium quality:

$$x_{eq}^{inlet} = x_{eq}^l - \frac{4 \cdot \dot{q}''}{D \cdot G \cdot h_{fg}} \cdot Z. \quad (C-14)$$

For critical parameter the inlet equilibrium quality is equal:

$$x_{eq}^{inlet} = x_{eq}^{crit} - \frac{4 \cdot \dot{q}''_{crit}}{D \cdot G \cdot h_{fg}} \cdot Z_{crit}. \quad (C-15)$$

Appendix D

Flow in sub-channels under isothermal swirl conditions

D.1 Comparison of the flow distribution for two simplified models with swirl in the sub-channel and around the rods

Laminar two-phase flow distributions in a non-heated sub-channel with an inlet velocity of 5 m/s and the injected void fraction $\alpha_g^{inlet} = 0.02$ are compared for simplified models with two different types of swirl generation. The first model is described in Chapter 5.2. This is the sub-channel model with mixing vanes, generating the swirl in the center of the sub-channel. The second model is presented in Chapter 5.3 and is a sub-channel model with the swirl promoters integrated in the straps of the spacer grid, generating the swirl around the rod. Depending on the mechanism of the swirl generating, further in the text these models referred to as the “sub-channel centered swirl” model and the “rod centered swirl” model, respectively.

In the following figures the distributions of the void fraction and of the liquid and gas velocities are presented, compared for “sub-channel centered swirl” and “rod centered swirl” simplified models. The distributions are evaluated across various axial sections. The altitude of the chosen section is labeled with the variable Z and the axial distance from the tip of the vanes is given in mm for the “sub-channel centered swirl” model and from the top of the spacer grid for the “rod centered swirl” model. In all figures of Appendix D the scale of the presented void fraction distribution is cut off at 5 % for a clear visualization of the bubble concentration near the rod surface with exception of Figure D-9 and Figure D-10.

Figure D-1 and Figure D-2 show the flow distributions at a few millimeters ($Z = -6$ mm) upstream the tip of the vanes (or the top of the spacer grid “rod centered swirl” model). For the “sub-channel centered swirl” model an accumulation of bubbles at the rear side of the vanes due to the redirection of the axial flow at this position can be observed. At the same altitude for the “rod centered swirl” model bubbles are accumulating at the rod and between the swirl

promoters and the spacer grid.

Another detailed comparison is carried out at 100 mm above the tip of the vanes (or the top of the spacer grid for “rod centered swirl” model) and is presented in Figure D-3 and Figure D-4. The void fraction distribution for the “sub-channel centered swirl” model shows the same two accumulation regions: in the center of the sub-channel and the “bubble pocket” on the lee side of the rod as for the turbulent flow presented before. The local changing of the sign of the curvature of the lateral flow component results in the change of the sign of the centrifugal force. The inertia and the centrifugal force of the heavy fluid drives the bubbles towards the rod surface on its lee side. The maximum values of the flow component calculated by the “rod centered swirl” model have a similar magnitude to that ones calculated by the “sub-channel centered swirl” model, but they can be found on the symmetry planes between the rods. For the “rod centered swirl” model the bubble accumulation can be found in this region. Additionally, there is a small “bubble pocket” on the wall accounting to the same phenomena caused by the local centrifugal forces in the flow under swirl conditions as in the “rod centered swirl” model.

Figure D-5 to Figure D-10 show the void fraction distribution for both models at axial sections from the tip of the vanes (or the top of the spacer grid) to the outlet. Just above the vanes both models show an accumulation of bubbles on the tip of the vanes (the top of the spacer grid with integrated swirl promoters), due to local centrifugal forces. Further downstream the distribution of the void fraction for the “rod centered swirl” model is rearranging as seen in Figure D-6.

Beginning with the axial section 200 mm above the tip of the vanes (or the top of the spacer grid) and till the outlet of the model observation of a similar type for all presented figures can be made. For the described flow conditions the “sub-channel centered swirl” model provides an accumulation of bubbles in two regions: in the center of the sub-channel and a small “bubble pocket” on the rod surface. Under the same conditions applied to the “rod centered swirl” model almost the whole area of the rod surface is covered with bubbles (void fraction > 5 %). Here, the previously mentioned distribution of the axial flow component is vanishing. Therefore, a more homogeneous swirl flow directs the bubbles off the symmetry planes toward the rod surfaces.

In the two last figures Figure D-9 and Figure D-10 the color scale is cut off not at $\alpha_g = 0.05$ as in all previous (void fraction) figures, but by $\alpha_g = 0.8$. Such view allows showing the maximum values of the void fraction at the rod surface for both “sub-channel centered” and “rod centered swirl” model. The value for the “rod centered swirl” model at the rod surface is

Appendix D

four times higher than for the “sub-channel” one. Higher accumulation of bubbles on the rod surface close to the end of the span just upstream the next spacer might indicate a deterioration of the heat transfer coefficient in the real geometry.

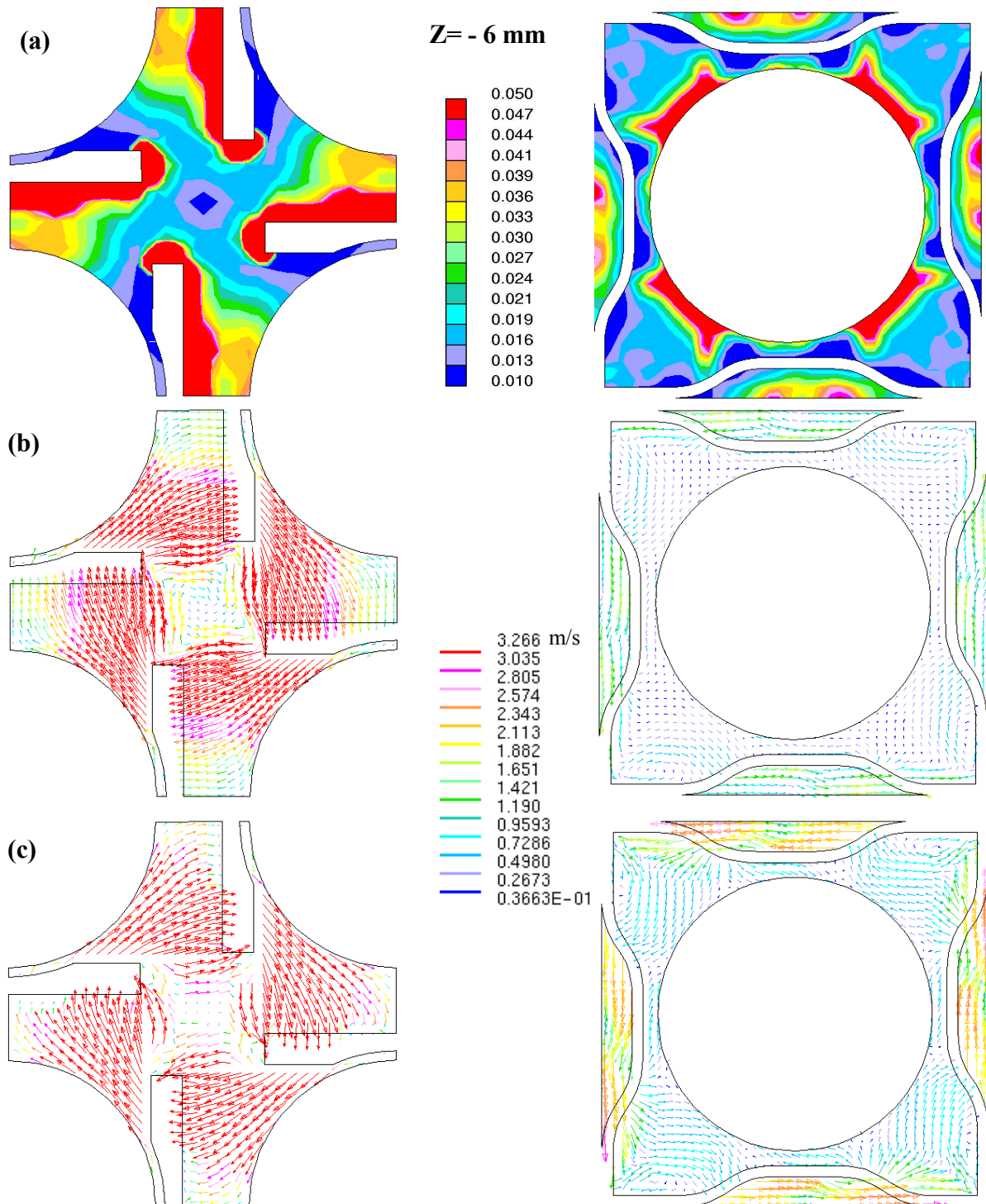


Figure D-1 Simplified model with *mixing vanes* at axial distance ($Z = - 6 \text{ mm}$) from tip of the vanes

Figure D-2 Simplified model with *swirl promoters* integrated in the spacer grid at axial distance ($Z = - 6 \text{ mm}$) from the top of the spacer

(a) - void fraction distribution, (b) - liquid phase velocity distribution, (c) - gas phase velocity distribution

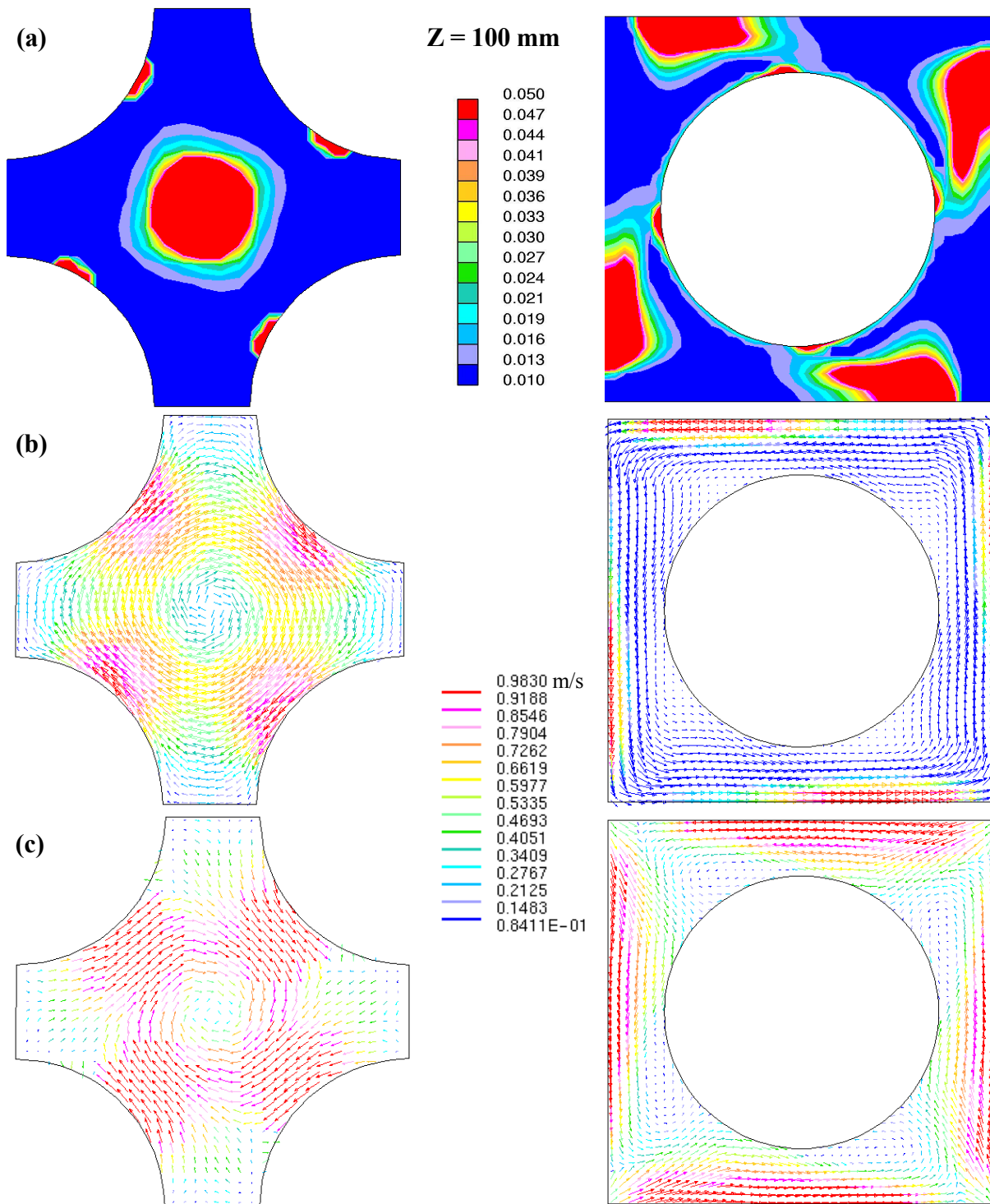


Figure D-3 Simplified model with *mixing vanes* at axial distance ($Z = 100 \text{ mm}$) from the tip of the vanes

Figure D-4 Simplified model with *swirl promoters* integrated in the spacer grid at axial distance ($Z = 100 \text{ mm}$) from the top of the spacer

(a) - void fraction distribution , (b) - liquid phase velocity distribution,
(c) - gas phase velocity distribution

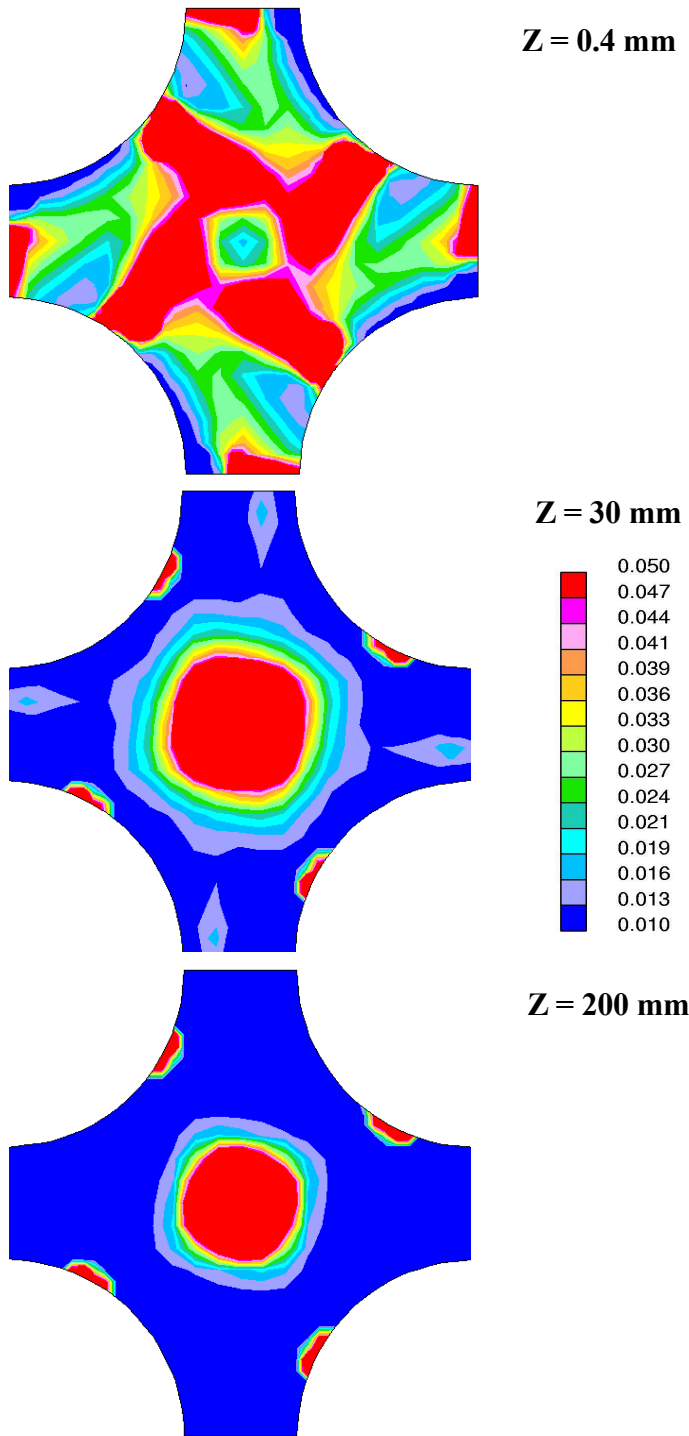


Figure D-5 Void fraction distribution. Simplified model with *mixing vanes* at various axial distances from the tip of the vanes ($Z = 0.4, 30$ and 200 mm)

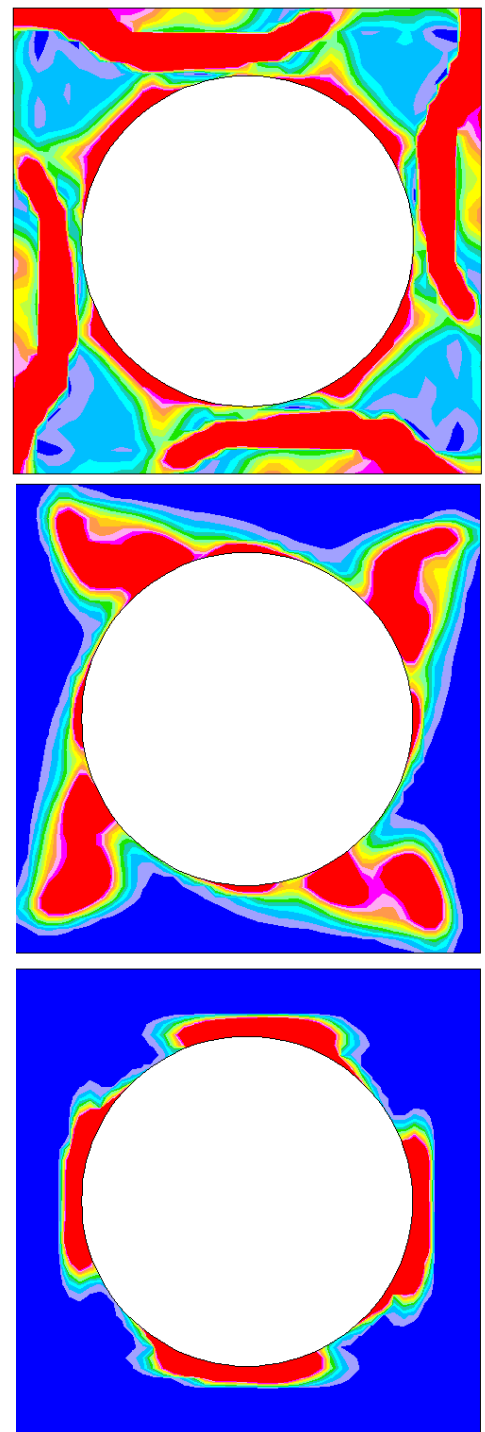


Figure D-6 Void fraction distribution. Simplified model with *swirl promoters* integrated in the spacer grid at various axial distances from the top of the spacer ($Z = 0.4, 30$ and 200 mm)

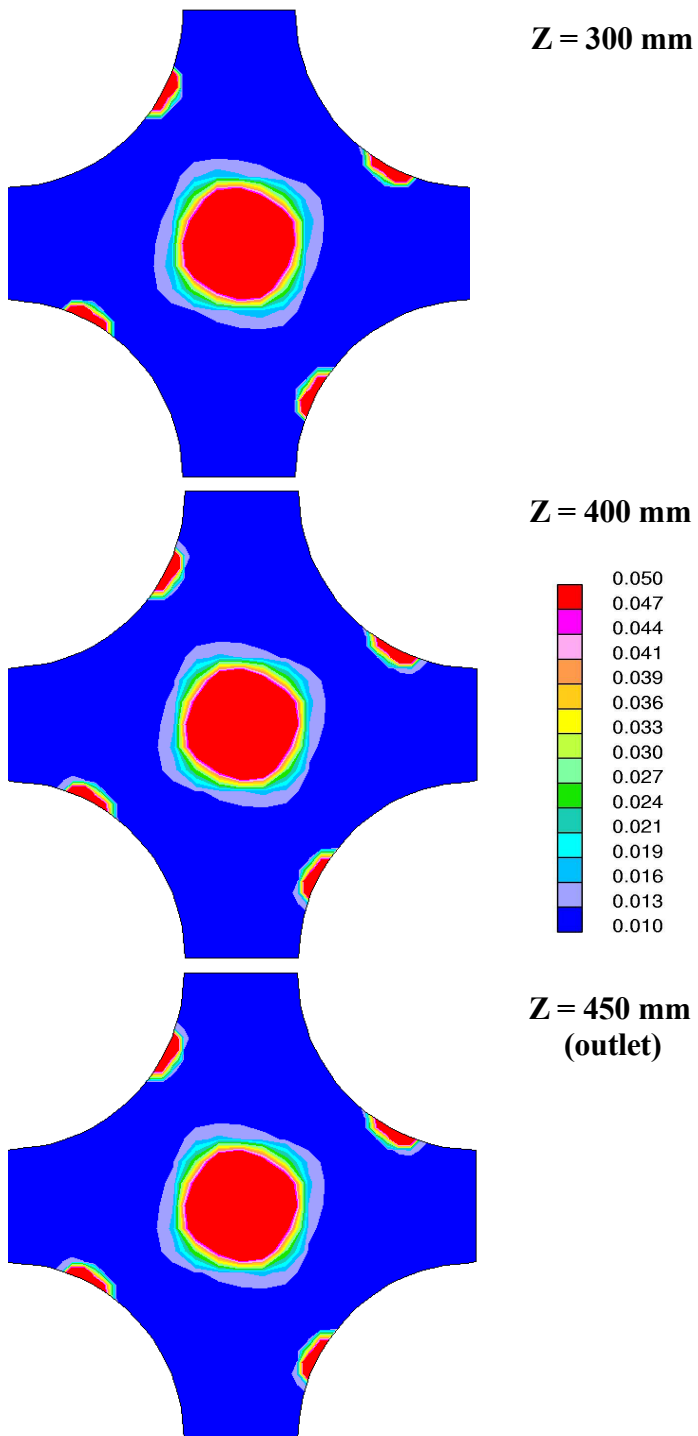


Figure D-7 Void fraction distribution.
Simplified model with *mixing vanes*
at various axial distances
from the tip of the vanes
($Z = 300, 400$ and 450 mm)

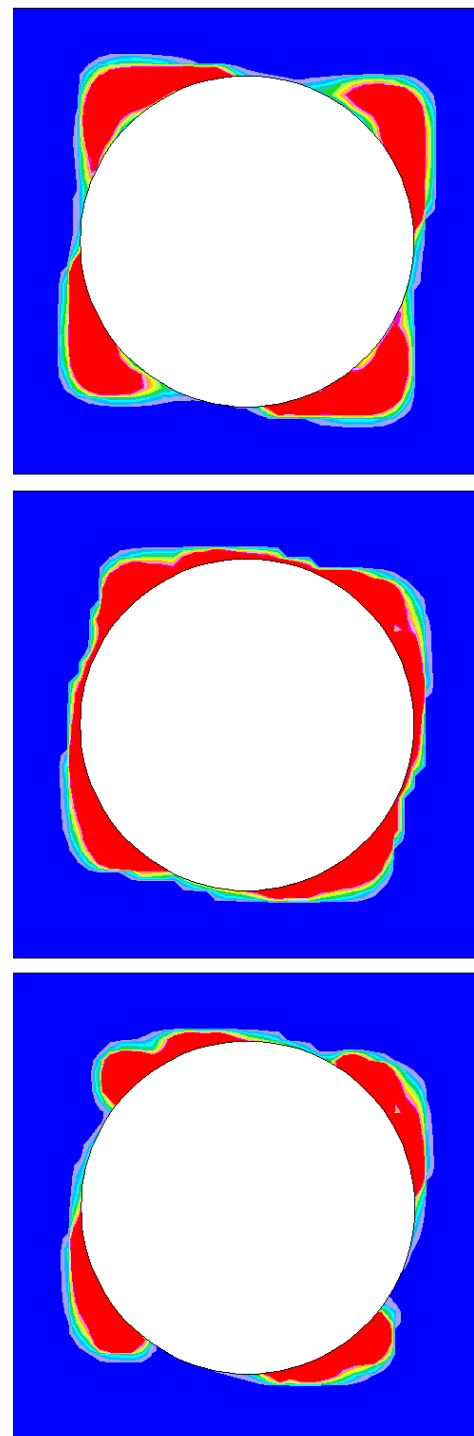


Figure D-8 Void fraction distribution.
Simplified model with *swirl promoters*
integrated in the spacer grid at various
axial distances from the top of the spacer
($Z = 300, 400$ and 450 mm)

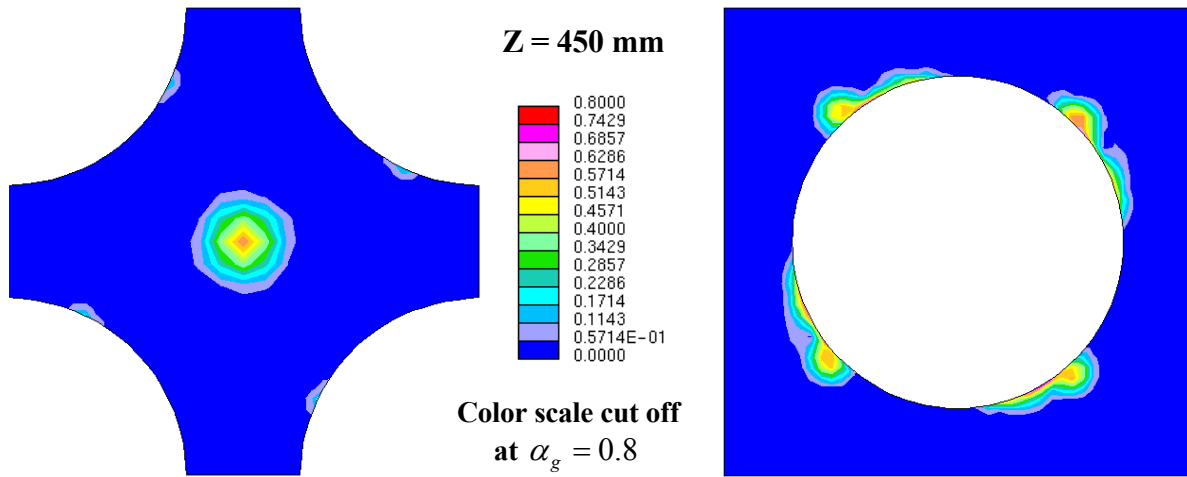


Figure D-9 Void fraction distribution.
Simplified model with *mixing vanes*
at the *outlet*
(*Z = 450 mm* above the tip of the vanes)

Figure D-10 Void fraction distribution.
Simplified model with *swirl promoters*
integrated in the spacer grid at the *outlet*
(*Z = 450 mm* from the top of the spacer)

Bibliography

- [1] Ajabegovic A., et al., “A new mechanistic model of critical heat flux in forced-convection subcooled boiling”, Proc. NURETH-8, pp. 973-980, Kyoto, Japan, 1997.
- [2] Ahmad S., “Fluid to Fluid Modelling of Critical Heat Flux: A Compensated Distortion Model”, Int. J. Heat Mass Transfer, Vol. 16, No. 2, pp. 641-662, 1973.
- [3] Anglart H., “Modelling of vapour generation at wall in sub-cooled boiling two-phase flow”, 1st international CFDS users conference, Oxford, UK, pp. 183-207, 1993.
- [4] Anglart H., “CFD predictions in LWR fuel assemblies”, Proc. CFX Int. Users Conference, Friedrichshafen, Germany, 1999.
- [5] Anglart H., Nylund O., “CFD application to prediction of void distribution in two-phase bubbly flows in rod bundles”, Nucl. Eng. Des., Vol. 163, pp. 81-98, 1996.
- [6] Anglart H., et al., “An analyses of multidimensional void distribution in two-phase flows”, Proc. 6th Int. Topical Meeting on Nuclear Reactor, pp. 139-153, 1993.
- [7] Anglart H., et al., “CFD prediction of flow and phase distribution in fuel assemblies with spacers”, Proc. NURETH-7, New York, 1995; Nucl. Eng. Des., Vol. 177, pp. 215-228, 1997.
- [8] Anglart H., et al., “Thermal-hydraulic design of nuclear fuel assemblies – current needs and challenges”, Proc. of Workshop on Modeling and Measurements of Two-phase Flows and Heat Transfer in Nuclear Fuel Assemblies, KTH, Stockholm, Sweden, 2006.
- [9] Antal S., et al., “Analysis of phase distribution in fully developed laminar bubbly two-phase flow”, Int. J. Multiphase Flow, Vol. 7, pp. 635-652, 1991.
- [10] Auton T., “The dynamics of bubbles, drops and particles in motion in liquids”, Ph.D. dissertation, University of Cambridge, UK, 1983.
- [11] Auton T., et al., “The force exerted on a body in inviscid unsteady non-uniform rotational flow”, J. Fluid Mech., Vol. 197, pp. 241-257, 1988.
- [12] Avdeev A., Pekhterev V., “Vapour condensation in non-equilibrium bubbly flows”, High Temp., Vol. 24, No. 6, p. 1125, 1986.

Bibliography

- [13] Basu N., et al., "Onset of nucleate boiling and active nucleation site density during subcooled flow boiling", *J. Heat Transfer*, Vol. 124, pp. 717-728, 2002.
- [14] Bartolemei G., Chanturiya V., "Experimental study of true void fraction when boiling subcooled water in vertical tubes", *Therm. Eng.*, Vol. 2, pp.123-128, 1967.
- [15] Bartolemei G., Gorburov V., "Experimental study of vapour phase condensation in liquid subcooled below saturation temperature", *Therm. Eng.*, No. 12, pp. 79-83, 1969.
- [16] Bartolemei G., et al., "Void fraction of the diabot flow in tubes by different heating laws", *Teplomassobmen - VI*, Vol. 5, Minsk, ITMO AN BSSR Press, pp. 38-43, 1980.
- [17] Bel Fdhila R., "Analyse expérimentale et modélisation d'un écoulement vertical à bulles un élargissement brusque", Ph.D. thesis, L'Institut National Polytechnique de Toulouse, Toulouse, France, 1991.
- [18] Bestion D., "The physical closure laws in the CATHARE code", *Nucl. Eng. Des.*, Vol. 124, pp. 229-245, 1990.
- [19] Boucker M., et al., "Towards the prediction of local thermal-hydraulics in real PWR core conditions using NEPTUNE_CFD software", *Workshop on Modeling and measurements of two-phase flows and heat transfer in nuclear fuel assemblies*, KTH, Sweden, 2006.
- [20] Bouillard L., et al., "Porosity distribution in a fluidised bed with an immersed obstacle", *AICHE*, 35, pp.908-922, 1989.
- [21] Boussinesq J., "Essai sur la théorie des eaux courantes", *Mémoires présentés par divers savants à l'Académie des Sciences*, Paris, Vol. 23, No. 1, p. 46, 1877.
- [22] Campbell R., et al., "Computational fluid dynamics prediction of the grid spacer thermal-hydraulic performance with comparison to experimental results", *Nuclear technology, Thermal hydraulics*, Vol. 149, pp.49-61, 2005.
- [23] Ceumern-Lindenstjerna W.-C., "Bubble Departure Diameter and Release Frequencies during Nucleate Pool Boiling of Water and Aqueous sodium chloride Solution", *Heat Transfer in Boiling*, edited by Hahne E. and Grigull U., Academic Press and Hemisphere, New York and Washington DC, Chapter 3, 1977.
- [24] Cheng X., "Experimental investigations on critical heat flux in 8 mm tubes and in 7-rod bundles", *Research Center Karlsruhe, KfK-Report 4884*, 1991.
- [25] Cheng X., Müller U., "Review on Critical Heat Flux in Water Cooled Reactors", *Research Center Karlsruhe, FZKA 6825*, 2003.
- [26] Chen J., et al., "Fluid to Fluid modeling of Critical Heat Flux in 4x4 Rod Bundles", *Nucl. Eng. Des.*, Vol. 232, pp. 47-55, 2004.

- [27] Clift R., et al., "Bubbles, Drops and Particles", Academic Press Inc (London), United Kingdom Edition, pp. 111-147, 1978.
- [28] Cole R., "A photographic study of pool boiling in the region of the critical heat flux", *AIChE J.*, Vol. 6, pp. 533-542, 1960.
- [29] Conner M., et al., "Lateral Flow Field Behavior Downstream of Mixing vanes In a Simulated Nuclear Fuel Rod Bundle", Proc. ICAPP-4, Pittsburgh, USA, pp. 1513-1519, 2004.
- [30] Crecy F., "The Effect of grid assembly mixing vanes on critical heat flux values and azimuthal location in fuel assemblies", *Nucl. Eng. Des.*, Vol. 149, p. 1, 1974.
- [31] Conner M., et al., "Heat transfer coefficient testing in nuclear fuel rod bundles with mixing vane grids", Water Fuel Performance Meeting, Kyoto, Japan, 2005.
- [32] Cornwell K., Brown R., "Boiling surface topology", Proc. 6th Int. Heat Transfer. Conf., Toronto, Canada, Vol. 1, pp. 157-161, 1978.
- [33] Cui X.-D., Kim K.-Y., "Three dimensional analyses of turbulent heat Transfer and Flow through Mixing vane in a subchannel of nuclear Reactor", *J. Nucl. Sci. Technol.*, Vol. 40, No. 10, pp. 719-724, 2003.
- [34] Doroshchuk V., et al., "Recommendations for calculating burnout in around tube with uniform heat release", *Teploenergetika*, Vol. 22, No. 12, pp. 66-70, 1975.
- [35] Deissler R., Columbia university heat transfer symposium, New York, 1954.
- [36] Del Valle M., Kenning D., "Sub-cooled flow boiling at high heat flux", *Int. J. Heat Mass Transfer*, Vol. 28, No. 10, pp. 1907-1920, 1985.
- [37] Drescher G., Köhler W., "Die Ermittlung kritischer Siedezustände im gesamten Dampfgehaltsbereich für innendurchströmte Rohre", *BWK* 33, Nr. 10, 1981.
- [38] Drew D., "Force on a small sphere in a slow viscous flow", *J. Fluid Mech.*, Vol. 88, No. 2, pp. 393-400, 1978.
- [39] Drew D., "The analyses of virtual mass effects in two-phase flow", Proc. OECD (NEA) CSNI, 2nd. Spec. Meet. Trans. Two-phase Flow, Paris, CSNI Report, No. 31, 1978.
- [40] Drew D., Lahey R., "Applications of general constitutive principles to the derivations of multidimensional two-phase flow equations", *Int. J. Multiphase Flow*, Vol. 5, pp. 243-264, 1979.
- [41] du Bousquet J., " Etudes thermohydrauliques en similitude Fréon", Rapport TT 124, 1974.
- [42] E.I. DuPont de Nemours & Co., "Surface tension of the Freon Compounds", Freon Technical Bulletin # D-27, 1967.

Bibliography

- [43] Falk F., Giacomelli A., “Rapport d’essais AGATE-Promoteur de mélange”, CEA Internal report DTP/SETEX/LTAC/93-191, 2003.
- [44] Falk F., Hugonnard A., “Rapport d’essais DEBORA-Promoteur de mélange, essais de BO et de topologie, campagnes 4800-4900-5000”, CEA Internal report DTP/SETEX/LTAC/92-158, 2002.
- [45] Feng Z-G., Michaelidis E., “Fluid dynamics of a sphere in an arbitrary electric field”, Proc. 4th Int. Conf. on Multiphase Flow, New Orleans, USA, 2001.
- [46] Ferziger J., Peric M., “Computational Methods for Fluid Dynamics” – 3rd rev. Edition, Berlin; Heidelberg; New-York: Springer, 2002.
- [47] Francois F., private communication (E-mail from 08.06.2006).
- [48] Francois F., Garnier, J., “Towards a new approach for predicting DNB, under non-uniform heat flux profile”, Proc. NURETH-11, 2005.
- [49] Garnier C., et al., “Measurements of local flow characteristics in buoyancy-driven bubbly flow at high void fraction”, in [45].
- [50] Garnier J., et al., “Local measurements on flow boiling of refrigerant 12 in a vertical tube”, Multiphase Sci. Technol., Vol. 13, pp. 1-111, 2001.
- [51] Glück M., “Ein Beitrag zur numerischen Simulation von Fluid-Struktur-Interaktionen-Grundlagenuntersuchungen und Anwendung auf Membrantragwerke“, D 29, Diss. Universität Erlangen-Nürnberg, Shaker Verlag, Aachen, 2003.
- [52] Grace J., et al., “Shapes and velocities of single drops and bubbles moving freely through immiscible liquids”, Trans. Inst. Chem. Eng., Vol. 54, pp.167-173, 1976.
- [53] Groeneveld D., et al., “1986 AECL-UO CHF look-up table”, Heat Transfer Eng., Vol. 7, p. 46, 1986.
- [54] Groeneveld D., et al., “CHF fluid-to-fluid modelling studies in three laboratories using different modelling fluids”, Proc. NURETH-5, pp. 531-540, 1992.
- [55] Groeneveld D., et al., “The 1995 look-up table for critical heat flux in tubes”, Nucl. Eng. Des., Vol. 163, p. 1, 1996.
- [56] Grossetete C., “Caraterisation experimentale et simulations de l’evolution d’un ecoulement diphasique a bulles ascendant dans un conduite verticale”, Collection de notes internes de la Direction des Études et Recherches, Electricité de France, 1995.
- [57] Gosman A., Ioannides S., “Aspects of computer simulation of liquid-fueled combustors”, AIAA J. of Energy, Vol. 7, No. 6, pp. 482-490, 1983.
- [58] Hibiki T., Ishii M., “Active nucleation site density in boiling systems”, Int. J. Heat Mass Transfer, Vol. 46, No. 14, pp. 2587-2601, 2003.

- [59] Hill D., “The computer simulation of dispersed two-phase flows”, Ph.D. thesis, Imperial College, University of London, UK, 1998.
- [60] Hill D., et al., “Numerical prediction of bubble dispersion in shear layers” 3rd Int. Symp. on Multiphase Flow and heat transfer, Xi’an, China, pp. 110-117, 1994.
- [61] Hinze J., “Fundamentals of the hydrodynamic mechanism of splitting in dispersion processes”, *AICHE J.*, Vol. 1, pp. 289-295, 1955.
- [62] Holloway M., et al., “The effect of support grid features on local, single-phase heat transfer measurements in rod bundles” , *J. Heat Transfer, Trans. ASME*, Vol. 126, pp. 43-53, 2004.
- [63] Houghton G., “Final report in subcontract (S-1101) for the investigation of the particle-fluid forces in accelerative flows (Letter to Ransome V. (EG&G) see [59]).
- [64] Hwang D., et al., “Development of a bundle correlation method and its application to predicting CHF in rod bundles”, *Nucl. Eng. Des.*, Vol. 139, p. 205, 1993.
- [65] Iguchi T., et al., “Experimental investigation of boiling curve in vicinity of CHF and rewetting conditions, Part 1: Boiling Curve, Experiments and Post-CHF Test Results”, *Proc. EXHFT-5, Thessaloniki, Greece*, 2001.
- [66] Ikeda K., et al., “Single-phase CFD applicability for estimation fluid hot-spot locations in a 5x5 fuel rod bundle”, *Nucl. Eng. Des.*, Vol. 236, pp. 1149-1154, 2006.
- [67] In W., “Numerical study of coolant mixing caused by the flow deflectors in a nuclear fuel bundle”, *Nucl. Technol.*, Vol. 134, pp. 187-195, 2001.
- [68] In W., et al., “CFD evaluation of the two-phase flow models for the subcooled boiling flow in a rod bundle”, *Proc. NURETH-11, Avignon, France*, 2005.
- [69] In W., et al., “CFD simulations of a flow mixing and heat transfer enhancement in an advanced LWR nuclear fuel assembly”, *Proc. Int. LWR Fuel Performance Meeting, San Francisco, USA*, 2007.
- [70] Installing and Introduction, AEA Technology plc., Website: <http://www.software.aeat.com/cfx>, Copyright, 1996-2002.
- [71] Ishii M., Mishima K., “Two-fluid model and hydrodynamic constitutive relations”, *Nucl. Eng. Des.*, Vol. 82, pp. 107-126, 1984.
- [72] Issa R., “A simple model for C_t ”, private communication, see [59], 1992.
- [73] Karoutas Z., et al., “3-D Flow analyses for Design of nuclear Fuel Spacer”, *Proc. NURETH-7, New York, USA*, 1995.
- [74] Katsaounis A., “Verification of Ahmad’s fluid-to-fluid scaling law by bundle experiments”, *Winter Annual Meeting of ASME, HDT*, Vol. 14, 1980.

Bibliography

- [75] Kim K.-Y., Seo J.-W., “Numerical optimization for the design of a spacer grid with mixing vanes in a pressurized water reactor fuel assembly”, Nucl. Technol., Thermal Hydraulics, Vol. 149, pp. 62-70, 2005.
- [76] Kocamustafaogullari G., Ishii M., “First established the foundation of the interfacial area transport equation and its closure relations”, Int. J. Heat Mass Transfer, Vol. 38, pp. 481-493, 1993.
- [77] Koizumi Y., et al., “Post-dryout heat transfer of high-pressure steam-water two-phase flow in single rod channel and multi rod bundle”, Nucl. Eng. Des., Vol. 99, pp.157-165, 1987.
- [78] Kolev N., “Multiphase flow dynamics”, Vol. 1 Fundamentals, Springer, Berlin, Heidelberg, 2002.
- [79] Kolev N., “Multiphase flow dynamics”, Vol. 2 Mechanical and thermal interactions, Springer, Berlin, Heidelberg, 2002.
- [80] Kolev N., “Multiphase flow dynamics”, Vol. 3 Turbulence, gas absorption and release, diesel fuel properties, 1st ed., Springer, Berlin, Heidelberg, New York, 2007.
- [81] Kolmogorov A., “The break up of droplets in a turbulent stream”, Dokl. Akad. Nauk SSSR, Vol. 66, pp. 825-828, 1949.
- [82] Krepper E., “CFD modelling of sub-cooled boiling”, Proc. NURETH-10, Seoul, Korea, 2003.
- [83] Krepper E., et al., “On the modelling of bubbly flow in vertical pipes”, Nucl. Eng. and Des., Vol. 235, pp. 597-611, 2005.
- [84] Krepper E., et al., “Modelling of subcooled boiling – concept, validation and application to fuel assembly design”, Nucl. Eng. Des., Vol. 237, pp. 716-731, 2007.
- [85] Kurul N., “Multidimensional effects in two-phase flow including phase change”, Ph.D. Thesis, Rensselaer Polytechnic Institute, 1991.
- [86] Kurul N., Podowski M., “Multidimensional effects in forced convection subcooled boiling”, Proc. 9th Int. Heat Transfer Conf., Jerusalem, Israel, pp. 21-26, 1990.
- [87] Kurul N., Podowski M., “On the modelling of multidimensional effects in boiling channels”, ANS Proc. National Heat Transfer Conf., Minnesota, USA, 2001.
- [88] Lahey R., et al., “Phase distribution phenomena in complex geometry conduits”, Nucl. Eng. Des, Vol. 122, pp.17-40, 1990.
- [89] Lahey R., et al., “The thermal-hydraulics of a boiling water nuclear reactor”, 2nd Edition, ANS, USA, 1993.

-
- [90] Larue de Tournemine A., et al., "Experimental study of the turbulence in bubbly flows at high void fractions" in [45].
- [91] Launder B., Spalding D., "The numerical computation of turbulent flows", *Comp. Meth. Appl. Mech. Eng.*, Vol. 3, pp. 269-289, 1974.
- [92] Lee M., "A critical heat flux approach for square rod bundles using the 1995 Groenefeld CHF table and bundle data of heat transfer research facility", *Nucl. Eng. Des.*, Vol. 197, pp. 357-374, 2000.
- [93] Lee T., et al., "Local flow characteristics of subcooled boiling flow of water in a vertical annulus", *Int. J. Multiphase Flow*, 2002, Vol. 28, pp.1351-1368, 2002.
- [94] Lemmert M., Chawla J., "Influence of Flow Velocity on Surface Boiling Heat Transfer Coefficient," *Heat Transfer in Boiling*, edited by Hahne E. and Grigull U., Academic Press and Hemisphere, New York and Washington DC, Chapter 11, pp. 237-247, 1977.
- [95] Liu T., "The role of bubble size on liquid phase turbulent structure in two-phase bubbly flow", *Proc. ICMF-98*, Lyon, France, CD ROM Publication, 1998.
- [96] Liu T., "Bubble size and entrance length effects on the void development in a vertical channel", *Int. J. Multiphase flow*, Vol. 19, pp. 99-113, 1993.
- [97] Lo S., "Application of the MUSIG model to bubbly flows", AEA Technology, AEAT-1096, 1996.
- [98] Lo S., "Modelling multiphase flow with an Eulerian approach", von Karman Institute Lecture Series, von Karman Institute, Belgium, 2005.
- [99] Lo S., "Modelling of industrial multiphase flow with STAR-CD", von Karman Institute Lecture Series, Presentation 20C, von Karman Institute, Belgium, 2005.
- [100] Lo S., "Progress in Modelling Advanced Light Water Reactors with STAR-CD", Workshop: Requirements and Capabilities for Thermal Hydraulic, CFD and Neutronic Analyses of Advanced LWR, Presentation ICONE-14, Miami, USA, 2006.
- [101] Lo S., "Modelling boiling in water reactor assemblies", CFD-workshop, Presentation ICONE-15, Japan, 2007.
- [102] Lopez de Bertodano M., et al., "Phase Distribution in Bubbly Two-Phase Flow in Vertical Ducts", *Int. J. Multiphase Flow*, Vol. 20, No. 5, pp. 805-818, 1994.
- [103] Mamaev W., et al., "Gidrodinamika gasogidkosnykh smesey w trubach", Moskva, 1969.
- [104] March P., "Caractérisation et modélisation de l'environnement thermohydraulique et chimique des gaines se combustible des réacteurs à eau sous pression en présence d'ébullition", Thèse de doctoral, Université de Provence Aix-Marseille I, 1999.

Bibliography

- [105] Marsal D., “Die numerische Lösung partieller Differentialgleichungen in Wissenschaft und Technik”, Bibliographisches Institut AG, Zürich, 1976.
- [106] Mayinger F., “Strömung und Wärmetübergang in Gas-Flüssigkeits-Gemischen”, Springer-Verlag, Wien, New York, 1982.
- [107] Mersmann A., “Design and scale-up of bubble and spray columns”, Ger. Chem. Eng., Vol. 1, pp. 1-11, 1978.
- [108] Migay V., Golubev L., “Friction and heat transfer in turbulent swirl flow with variable swirl generator in a pipe”, Heat transfer, Soviet Research, Vol. 2, No. 3, pp. 68-73, 1970.
- [109] Mikic B., Rohsenow B., “A new correlation of pool boiling data including the effect of heating surface characteristics”, J. Heat Transfer, Vol. 9, pp. 245-250, 1969.
- [110] Mimouni S., et al., “Modeling and computation of cavitation and boiling bubbly flows with the NEPTUNE_CFD code”, Int. Workshop CFD4NRS, Germany, 2006.
- [111] Moraga F., et al., “Lateral forces on spheres in turbulent uniform shear flow”, Int. J. Multiphase Flow, Vol. 25, pp. 1321-1372, 1999.
- [112] Neykov B., et al., “OECD-NEA/US-NRC/NUPEC BWR Full-Size Fine-Mesh Bundle Test (BFBT) Benchmark”, Volume I: Specifications, NEA No. 6212, NEA/NSC/DOC (2005)5, ISBN 92-64-01088-2, 2006.
- [113] Nylund O., et al., “Measurements of hydrodynamics characteristics, instability thresholds, and burn out limits for 6-rod clusters in natural and forced circulation”, FRIGG-1 Report, ASEA and AB Atomenergi, Sweden, 1967.
- [114] Nikuradse J., VDI-Forschungsheft Nr. 361, 1933.
- [115] Ohnuki A., Akimoto H., “Model development for bubble turbulent diffusion and bubble diameter in large vertical pipes”, J. Nucl. Sci. Technol., Vol. 38, No. 12, pp. 1074-1080, 2001.
- [116] Oldekop W., “Druckwasserreaktoren für Kernkraftwerke”, 2. Auflage, Verlag Karl Thiemig AG, München, Germany, 1979.
- [117] Patankar S., “Numerical heat transfer and fluid flow”, Hemisphere Publishing Corporation., USA, 1980.
- [118] Podowski M., “CFD simulations of critical heat flux in PWR Fuel assemblies”, Proc. ISSCA-4, pp. 15-26, Tokyo, 1997.
- [119] Prandtl L., “Bericht über Untersuchungen zur ausgebildeten Turbulenz”, ZAMM, Vol. 5, No. 2, pp.16-139, 1952.

-
- [120] Prandtl L., et al., “Führer durch die Strömungslehre”, 8. Auflage, Vieweg, Braunschweig, Germany, 1984.
- [121] Ranz W., Marshall W., “Evaporation from Drops. Part 1”, Chem. Eng. Prog., Vol. 48, No. 3, pp. 141-146, 1952.
- [122] Rao Y., et al., “Numerical simulation of two-phase boiling flows and prediction of DNB under PWR conditions with a multidimensional Two-Fluid model”, JAME, Series B, Vol. 43, No. 4, 2000.
- [123] Rusche H., “Modelling of interfacial forces at high phase fraction”, I. Lift, Project Report III-4, Brite/EuRam BE-4322, 2000.
- [124] Rusche H., “CFD of dispersed two-phase flows at high phase fractions”, Ph.D. Thesis, Imperial College of science, Technology and Medicine Department of Mechanical Engineering, 2002.
- [125] Rodi W., “Turbulence models and their applications in hydraulics - a state of the art review”, 2nd Edition, University of Karlsruhe, 1984.
- [126] Rohsenow W., “A method of correlating heat transfer data for surface boiling liquids”, Trans. ASME, Vol. 74, p. 969-976, 1952.
- [127] Rosal E., et al., “Rod bundle heat transfer test facility design description report”, PSU-ARL NRC-04-01, 2001.
- [128] Sadatomi M., et al., “Two-phase flow in vertical noncircular channels”, Int. J. Multiphase flow, Vol. 8, pp. 641-655, 1982.
- [129] Salnikova T., “Generic CFD analyses on basic models”, Bachelor Thesis, Hochschule Zittau/Görlitz (FH), Reg. Nr. FB M/B/02/02, 2002.
- [130] Salnikova T., “CFD analyses of two-phase flows under swirl conditions”, Diploma Thesis, Hochschule Zittau/Görlitz (FH), Reg. Nr. FB M/B/02/02, 2003.
- [131] Salnikova T., “3-D CFD analyses in sub-channels under swirl conditions”, Proc. Annual Meeting on Nucl. Technol., Nuremberg, Germany, 2005.
- [132] Salnikova T., “Progress in CFD analyses applied to subchannel conditions”, Proc. 15th Int. Conf. on Nucl. Eng., ICONE 15, Nagoya, Japan, 2007.
- [133] Samuelsberg A., Hjertager B., “Computational modelling of gas/particle flow in a riser”, AIChE, Vol. 42, pp. 1536-1546, 1996.
- [134] Serizawa A., et al., “Turbulent structure of air-water bubbly flow”, Int. J. Multiphase Flow, Parts I-III, Vol. 2, pp. 221-259, 1975.
- [135] STAR-CD Version 3.15 Methodology Manual, Chapter 13, CD-adapco, UK, 2001.

Bibliography

- [136] STAR-CD Version 3.20 Methodology Manual, Chapter 13, CD-adapco, UK, 2004.
- [137] STAR-CD Version 3.27 Extended boiling framework, Lo S., Splawki A., CD-adapco UK, 2006.
- [138] STAR-CD Version 4.00 Methodology Manual, Chapter 13, CD-adapco, 2006.
- [139] Schiller L., Naumann A., VDI Zeits., Vol. 77, pp. 318-320, 1933.
- [140] Spalding D., "A general purpose computer program for multi-dimensional one- and two-phase flow", Mathematics and Computers in Simulation XXIII, pp. 267-276, London, 1981.
- [141] Stephan K., Mayinger F., "Thermodynamik. Grundlagen und technische Anwendungen", 13. Auflage, Band 1, Einstoffsysteme, Springer, Berlin /Heidelberg 1986, p. 84, 1990.
- [142] Stokes G., "On the effect of the internal friction of fluids on the motion of pendulums", Trans. Camb. Phil. Soc., Vol. 8, 1845.
- [143] Stokes G., "Mathematical and Physical papers", Vol. 1, Cambridge University press, London, 1880.
- [144] Sultan M., Judd R., "Spatial Distribution of Active Sites and Bubble Flux Density", J. of Heat Transfer, Vol. 100, pp. 56-62, 1978.
- [145] Tarasova N., et al., "Local drag in surface-boiling water in pipes", High Temperature, Vol. 5, No. 1, pp. 130-136, 1967.
- [146] Teletov S., "On the problem of fluid dynamics of two-phase mixtures", Vol. 1 Hydrodynamic and energy equations, Bulletin of the Moscow University, No. 2, p. 15, 1958.
- [147] Tentner A., et al., "Computational Fluid Dynamics Modelling of Two-phase Flow in a Boiling Water Reactor Fuel Assembly", Proc. Int. Conf. on Mathematics and Computations, American Nuclear Society, France, 2005.
- [148] Tentner A., et al., "Advances in computational fluid dynamics modelling of two phase flow in a boiling water reactor fuel assembly", Proc. ICONE-14, USA, 2006.
- [149] Thomas R., "Bubble coalescence in turbulent flows", brief communication, Int. J. Multiphase Flow, Vol. 7, No. 6, pp. 709-717, 1981.
- [150] Tolubinsky V., Kostanchuk D., "Vapour bubbles growth rate and the heat transfer intensity at subcooled water boiling", Heat Transfer, Vol. 5, B 2.8, 1970.
- [151] Tomiyama A., et al., "Effects of Eötvös number and dimensionless liquid volumetric flux on lateral motion of a bubble in a laminar duct flow", Proc. ICMF-2, Kyoto, Japan, 1995.

- [152] Tomiyama A., "A bubble tracking method for the prediction of spatial-evaluation of bubble flow in a vertical pipe", Proc. ICMF-3, Lyon, France, 1998.
- [153] Tomiyama A., et al., "Drag coefficients of single bubbles under normal and microgravity conditions", JSME Int. J. Ser. B: Fluids Thermal Eng., Vol. 41, pp. 472-479, 1998.
- [154] Tomiyama A., et al., "Transverse migration of single bubbles in simple shear flow", Chem. Eng. Sci., Vol. 57, pp. 1849-1858, 2002.
- [155] Tong L., Weisman J., "Thermal analyses of pressurized water reactors", 3rd Edition, ANS, Illinois, USA, 1996.
- [156] Troshko A., Hassan Y., "A two-equation turbulent model of turbulent bubbly flows", Int. J. Multiphase Flow, Vol. 27, pp. 1965-2000, 2001.
- [157] Tu J., Yeoh G., "Development of a numerical model for subcooled boiling flow", 3rd Int. Conf. CFD in the Minerals and Process Industries CSIRO, Australia, 2003.
- [158] VDI-Waermeatlas, "Kritische Siedezustände", Abschnitt Hbc 30, 9. Auflage, 2002.
- [159] VDI-Waermeatlas, "Kritische Siedezustände", Abschnitt Hbc 3, 9. Auflage, 2002.
- [160] Unal H., "Maximum bubble diameter, maximum bubble-growth time and bubble-growth rate during the subcooled nucleate flow boiling of water up to 17.7 MN/m^2 ", Int. J. Heat Mass Transfer, Vol. 19, pp. 643-649, 1976.
- [161] Ustinenko V., et al., "Validation of CFD-BWR, A new two-phase computational fluid dynamics model for boiling water reactor analysis", OECD/NEA Int. Workshop CFD4NRS, Germany, 2006.
- [162] Wallis G., "One-dimensional two-phase flow", McGraw-Hill, New-York, 1969.
- [163] Wang D., "Modelling of bubbly flow in a sudden pipe expansion", Technical Report II-34, Brite/EuRam Project BE-4098, 1994.
- [164] Wang S., et al., "3-D turbulence structure and phase distribution measurements in bubbly two-phase flows", Int. J. Multiphase Flow, Vol. 13, No. 3, pp. 327-343, 1987.
- [165] Wehle F., et al., "Progress in AREVA NP's LWR Thermal Hydraulics Methodology", Workshop on Modeling and Measurements of Two-Phase Flows and Heat Transfer in Nucl. FAs, KTH, 2006.
- [166] Weisman J., Pei B., "Prediction of Critical Heat flux in flow boiling at low qualities", Int. J. Heat Mass Transfer, Vol. 26, No. 10, pp. 1463-77, 1983.
- [167] Whalley P., "Boiling, condensation and gas-liquid flow", Clarendon Press, Oxford, UK, 1987.

Bibliography

- [168] White F., “Viscous Fluid Flow”, McGraw-Hill, New York, 1974.
- [169] Windecker G., Anglart H., “Phase distribution in a BWR fuel assembly and evaluation of a multidimensional multifield model”, Nucl. Technol., Vol. 134, pp. 49-61, 2001.
- [170] Witt P., Perry J., “A study in multiphase modelling of fluidized beds”, Computational Techniques and Applications: CTAC95, World Scientific, 1995.
- [171] Yang S., Chung M., “Spacer grid effects on turbulent flow in rod bundles”, J. Korean Nucl. Soc., Vol. 28, p. 56, 1996.
- [172] Yao S., et al., “Heat-transfer augmentation in rod bundles near grid spacers”, J. Heat Transfer, Vol. 104, pp. 76-81, 1982.
- [173] Yeoh G., Tu J., “A unified model considering force balances for departing vapour bubbles and population balance in subcooled boiling flow”, Nucl. Eng. Des., Vol. 235, pp. 1251-1265, 2005.
- [174] Žun I., “The transverse migration of bubbles influenced by walls in vertical bubbly flow”, Int. J. Multiphase Flow., Vol. 6, pp. 583-588, 1980.

Curriculum vitae

Personal Information

Name: Tatiana Igorevna Salnikova
Date of Birth: 09.11.1980
Birthplace: Moscow, Russia
Parents: Ph.D. Igor Georgievich Salnikov
Ph.D. Irina Petrovna Chaykina
Nationality: Russian
Marital Status: Married

Education

09/1987 – 09/1993 Secondary School N° 1, Moscow: specialization in English
09/1993 – 09/1997 Applied Science Grammar school (Lyceum N° 1502), Moscow
09/1997 – 09/1999 Pre-degree at the Moscow Power Engineering Institute (TU),
Department of Electromechanics with the major in Environmental
Engineering
09/1999 – 06/2000 Preparatory College at University of applied sciences Zittau/Görlitz
(FH), including German language university entrance exam for
foreign students (DSH)
06/2000 – 09/2003 Diploma Study of Energy and Environmental Engineering with a
major in Nuclear Engineering at the University of applied sciences
Zittau/Görlitz (FH)

- Full time scholarship from Saxon State Ministry of
Science and Culture (SMWK)
- Degree: Bachelor of Mechanical Engineering
- DAAD-Reward for brilliant achievement for foreign
students
- Diploma Thesis by AREVA NP, Erlangen, Germany
- Degree: Dipl.-Ing.(FH)

09/2003 – 11/2007 Ph.D. Thesis at the Dresden University of Technology (TUD) in
cooperation with University of applied sciences Zittau/Görlitz (FH)
and AREVA NP GmbH, Erlangen